INVESTIGATIONS OF SOUTHWEST PACIFIC INTRAPLATE AND BACKARC VOLCANISM USING TRADITIONAL AND NON-TRADITIONAL ISOTOPES

A DISSERTATION SUBMITTED TO THE GRADUATE DIVISION OF THE UNIVERSITY OF HAWAIʻI AT MĀNOA IN PARTIAL FULFILLMENT OF THE REQUIREMENTS FOR THE DEGREE OF

DOCTOR OF PHILOSOPHY

IN

GEOLOGY AND GEOPHYSICS

AUGUST 2017

By

Valerie A. Finlayson

Dissertation Committee:

Jasper G. Konter, Chairperson
Ken Rubin
John Sinton
Mike Garcia
Chris Measures

Acknowledgements

This section cannot be started without first mentioning my advisor, Dr. Jasper Konter, with whom I originally started studying under at the University of Texas at El Paso before moving to University of Hawai'i at Mānoa. I would not be the scientist I am today without his guidance, patience, and importantly, humor. As his first PhD student (and my first time as a PhD student), I didn't know what to expect. The benefits far outweighed the risks: I've learned what had proven to be a diverse, incredible set of opportunities with which I could broaden my skillset. This ranges from lab/analytical/seagoing methods, computational analysis, and efficient lab operation, to every possible way in which a workspace can unexpectedly flood. Dr. Bridget Smith-Konter, while not formally my advisor, has always been willing to lend an ear, as well as her advice and support. Dr. Tyrone Rooney at Michigan State University saw potential in me and has never hesitated to in his guidance through this path, whether it's about academia, or life while in academia. The three of you, your mentorship, and your friendship have changed my life for the better. Thank you for these six years.

My dissertation committee: Drs. Ken Rubin, Mike Garcia, John Sinton, and Chris Measures, who provided helpful guidance and comments that improved this dissertation. I am grateful for their input and time, and for working with my somewhat non-traditional path as a transfer student.

Dr. Denys VonderHaar has been an enormous help around the SOEST Isotope Lab facility. Her depth of knowledge about the lab is unparalleled and she was invaluable in helping the transition into the lab at UH.

Many thanks to my collaborators: For Chapter 2, Dr. Lin Ma at the University of Texas at El Paso CEEIR Facility assisted with conceptual development of the method and manuscript structure. For Chapter 3, Dr. Ken Rubin made the Mata Volcanic Field samples available for use. Dr. Nicolas Dauphas allowed me to visit University of Chicago Origins Lab to analyze Fe isotopes. Nicole (Xike) Nie assisted with lab work and analyses during the Origins Lab visit. For Chapter 4, Dr. Kevin Konrad provided age determinations. Dr. Anthony Koppers, Dr. Matt Jackson, and Dr. Tyrone Rooney provided many helpful suggestions to streamline the text. Drs. Tyrone Rooney and Guillame Girard acquired the Rurutu compositional data at Michigan State University. Drs. Janet Becker and Pål Wessel helped develop the concept that became the computational location method crucial to this chapter. Last but not least, Captain Wes Hill and the crewmembers of the Roger Revelle ensured the RR1310 expedition exceeded expectations. Few others can attest to 44 dredge attempts using only one dredge bag. NSF grants OCE# 1433097, OCE# 1153959 , OCE#1433097, OCE# 1154070, and OCE# 1153894 supported research presented in this dissertation.

Finally, friends and family have been an important part of my life throughout the past six years, keeping me at least partly in touch with the rest of the world. There are too many to list, but particularly deserving of a mention are my mom, Grandma Joyce, Hubbell, Justine, Marissa, my sister, my amazing officemates/grad family of the Magma Chamber, my cohorts at UTEP, and the friends/colleagues from CIDER 2014.

Abstract

Volcanic activity in the southwest Pacific Ocean provides ample opportunity to study various tectonic settings spanning as much as ~140 million years. High-precision stable and radiogenic isotopes are powerful geochemical tools capable of identifying melt source contributions and petrological processes in mantle-derived melts in various tectonic settings, expanding our understanding of the dynamics of underlying Pacific mantle domains.

In this dissertation, I present methodological improvements to Fe isotopic measurement methods capable of achieving an analytical precision of ±0.046‰. An accompanying secondary statistical correction can account for instrumental drift between analyses. At such high precision, potential exists to resolve Fe isotope fractionation behavior in response to processes such as melting, fractionation, and metasomatism in ultramafic materials. Predictable Fe isotope behavior can also be used to identify isotopically distinct source compositions contributing to mantle-derived melts. Here, Fe isotope behavior is characterized in a suite of young boninitic melts from the Mata Volcanic Field, located in the northeastern Lau Basin. The combination of δ^{56}Fe and melt compositions suggest that Mata volcanoes see variable input from a subduction fluid-like component, and the degree of its contribution may be influenced by proximity to the Tonga forearc versus nearby backarc basin spreading centers.

The isotopically distinct, long-lived (120+ Myr) Rurutu hotspot track is a third potential constraint to hotspot-based Pacific absolute plate motion models, which are subject to large model uncertainty, particularly after ~47-50 Ma. Located

in a geologically complex region of the southwest Pacific known as the "Hotspot Highway", other hotspot tracks overlap with the Rurutu track, requiring use of radiogenic (Sr-Pb-Nd-Hf) isotope ratios to identify Rurutu-origin seamounts. Paired with ^{40}Ar-^{39}Ar age data, I present evidence of age-progressive (~75-42 Ma), dual track Rurutu volcanism in the Tuvalu chain. Additionally, I present a computational method that identifies the highest-probability location and age of the Rurutu Bend, analogous to the ~47-50 Ma Hawaiian-Emperor Bend. Identification of this ~50-49 Ma Bend in the Rurutu hotspot track confirms the continuity of Rurutu volcanic activity throughout the Pacific ocean basin, establishing its importance as a third major, singly-sourced constraint on Pacific absolute plate motion.

TABLE OF CONTENTS

List of Tables

List of Figures

List of Abbreviations, Variables, and Standards

DMM	Depleted MORB Mantle
DS	Double spike
EM1	Isotopic mantle endmember, Enriched Mantle 1
EM2	Isotopic mantle endmember, Enriched Mantle 2
HIMU	Isotopic mantle endmember, High μ (μ = $^{238}U/^{204}Pb$)
LA-ICP-MS	Laser ablation inductively coupled plasma mass spectrometry
MC-ICP-MS	Multicollector inductively coupled plasma mass spectrometer
MORB	Mid-ocean ridge basalt
μ	μ = $^{238}U/^{204}Pb$
MSU	Michigan State University
OIB	Ocean island basalt
P	Peak center mass
PVF	Potrillo Volcanic Field
REE	Rare earth element
RGR	Rio Grande Rift
TIMS	Thermal ionization mass spectrometer
UHM	University of Hawaii at Manoa
UTEP	The University of Texas at El Paso
XRF	X-ray fluorescence
Variables	
$\delta^{56}Fe$	Permil offset of a $^{56}Fe/^{54}Fe$ relative to IRMM-014
η_{Fe}	Offset of sample Fe cycle peak center mass relative to IRMM-014
η_{Cr}	Offset of sample Cr cycle peak center mass relative to IRMM-014
η_{Ni}	Offset of sample Ni cycle peak center mass relative to IRMM-014
Standards	
Alfa Fe	In-house Fe standard from Alfa SpecPure Fe solution
Alfa Hf	In-house Hf isotopic standard, used for sample-standard bracketing
BCR-2	USGS powdered rock standard, Columbia River Basalt
BIR-1	USGS powdered rock standard, Icelandic Basalt
BHVO-1	USGS powdered rock standard, Kilauea 1919 Basalt
IRMM-014	Fe isotopic standard, used for standard-sample bracketing
JMC475	Hf isotopic standard
JNdi-1	Nd isotopic standard, used for standard-sample bracketing
La Jolla	Nd isotopic standard
SRM 981	National Institute of Standard and Technology (NIST) Pb isotopic standard, used for standard-sample bracketing
SRM 987	NIST Sr isotopic standard, used for standard-sample bracketing
SRM 997	NIST Tl isotopic standard, used for Pb fractionation correction

CHAPTER 1. INTRODUCTION

1.1.Dissertation theme

The southwest Pacific hosts volcanic activity spanning a range of roughly 140 million years, from Cretaceous Era large igneous provinces to modern-day activity at tectonic boundaries and within plates (e.g., Konter et al., 2008; Koppers et al., 2004, 2003; Mahoney et al., 2005; Resing et al., 2011). The region, particularly from the Wake Island chain southward to the Tuvalu chain and Lau Basin (Figure 1.1), has been only partially explored because of its remote location, extremely large area, and commonly deeply submerged volcanoes. Studies of volcanic activity in the southwest Pacific have proven crucial to our understanding of the fundamental principles of mantle dynamics, plate tectonics, and magmatic evolution of seamounts (Nakanishi et al., 1999; Taylor, 2006; Taylor et al., 1996; Wessel and Kroenke, 2008). Central to understanding these dynamics is the ability to evaluate the geochemical and petrogenetic signatures preserved in rocks erupted from these seamounts. Isotopic signatures from stable or radiogenic isotope systems, when combined with other age or geochemical data, become powerful tracers of processes influencing the development of igneous systems (e.g., Konter et al., 2016, 2008; Sossi et al., 2012; Staudigel et al., 1991; Teng et al., 2013; Williams et al., 2005). These signatures also provide clues into compositions of the heterogeneous mantle sources from which melts are generated (e.g., Hanyu and Kaneoka, 1997; Jackson et al., 2007; Salters et al., 2011; Zindler and Hart, 1986). Studying the origins of these mantle heterogeneities expressed at Earth's surface allows extrapolation into Earth's mantle and the dynamic processes driving its evolution, both past and present.

This dissertation presents improvements to Fe isotope analytical methods, statistical approaches, and new isotope data from southwest Pacific volcanoes to investigate contributions to, and evolution of, oceanic volcanism (Figure 1.1). Stable and radiogenic isotope geochemistry are powerful tools capable of tracing processes and sources that are otherwise difficult, if not impossible to trace through other methods. The utility of isotope work is increased by the ability to maximize current instrumental precision and developing methods to improve data quality. Maximizing data quality allows us to identify subtle geochemical patterns in a magmatic dataset. Chapter 2 presents a new high-precision Fe isotope measurement technique and data quality analysis based on robust statistical approaches. Fe isotopes are a relatively new tool used in geochemical investigations of high-temperature environments that require the highest achievable analytical precision to resolve magmatic variations. Chapter 3 uses high-precision Fe isotopes in combination with compositional data to explore magmatic processes in the northern Lau backarc, the site of a rare, early-stage backarc environment that has recently erupted boninitic lavas. Few Fe isotope data exist for subduction zones, and controls on Fe isotope variations in subduction-related melts are not fully understood (Sossi et al., 2016). However, an early-stage subduction environment is the ideal setting to study the response of redox-sensitive Fe isotope ratios to generation of highly oxidized, high-degree flux melts. North of the Vitiaz Lineament bounding the north terminus of the Lau Basin lies the Tuvalu island chain, the site of Chapter 4. In this study, I use a combination of Sr-Pb-Nd-Hf isotopes and age data to identify and characterize a missing segment of the long-lived, yet under-recognized Rurutu hotspot. This work builds on studies of nearby, related volcanic chains (Bonneville et al., 2002; Konter et al., 2008; Koppers et al., 2007, 2003; Staudigel et al.,

1991) to trace the Rurutu hotspot track through the Tuvalu island chain, revealing its ~49 Ma morphological bend (referred to herein as the "Bend"). The Rurutu Bend is akin to the characteristic Hawaiian-Emperor Bend that occurred between ~47-50 Ma, thought to correspond to initiation of subduction along the Izu-Bonin-Mariana arc system (Sharp and Clague, 2006). Besides locating this Bend in the newly-characterized Tuvalu segment, the data define a bilaterally zoned plume. Identification of Tuvalu seamounts belonging to Rurutu confirms an~120 Ma record of Pacific plate motion, restoring Morgan's (1972) forgotten "Austral-Gilbert-Marshall" hotspot track as a major Pacific tectonic feature.

1.2. Isotope geochemistry and applications to magmatic and tectonic processes

This section briefly explains the fundamental principles of stable and radiogenic isotope fractionation, and the utility of these tools in mantle exploration settings. These are included to provide background and a brief literature review of the principles upon which interpretation of isotope data are based.

1.2.1. Stable isotope fractionation (Fe)

Stable isotopes of elements are isotopes whose abundance in the Solar System remain constant, although now-extinct decay systems influenced isotopic abundances of some elements early in Earth's history. Commonly analyzed stable isotope systems include, but are not limited to, the so-called "traditional" light elements – such as N, O, C – and the "non-traditional" heavier elements – such as Fe, Mg, Si, and Cr. While global averages of stable isotope abundances remain constant with time, it is possible to change stable isotope ratios in systems within Earth via several fractionation mechanisms, detailed below. These

mechanisms can be grouped into two categories: 1) Mass-independent and 2) mass-dependent. Mass-independent processes such as nuclear volume (Schauble, 2007) or magnetic isotope (Buchachenko, 2001) effects may fractionate stable isotopes in specific settings. The nuclear volume effect is thought to be significant in very heavy elements such as mercury or uranium (Schauble, 2007; Schauble et al., 2009), and the magnetic isotope effect is not thought to be significant at magmatic temperatures (Buchachenko, 2001). For Fe, redox state produces the most significant fractionation effects in igneous systems (Dauphas et al., 2014) of all known fractionation mechanisms; therefore mass-independent mechanisms will not be discussed further in this dissertation. The second category, mass-dependent fractionation, includes several distinct processes, discussed in more detail below. Mass-dependent fractionation is a kinetic principle; displacing a lighter isotope requires less energy than a heavier isotope, both in chemical bonds and chemical or thermal diffusion gradients (e.g., Huang et al., 2010; Sio et al., 2013; Teng et al., 2011). Equilibrium fractionation is another process common in stable isotope systems. For Fe, equilibrium fractionation is known to occur between oxidation states of Fe (e.g., elevated Fe^{3+}/Fe^{2+} typically correlates with an increase in $\delta^{56}Fe$). This makes stable isotope systems useful tracers of mass-dependent processes affecting an evolving system, particularly with common rock-forming elements that are ubiquitous in most terrestrial environments.

Prior to advances in multicollection mass spectrometry in the early 2000s, stable isotopic fractionation of elements heavier than the traditional light elements was considered to be negligible in high-temperature settings (Beard and Johnson, 1999). Improvements in analytical precision, however, revealed small (<1‰) systematic fractionation patterns in igneous Fe isotopic ratios (e.g., Konter et al., 2016; Schuessler et

al., 2009; Sossi et al., 2012; Teng et al., 2013, 2008; Williams et al., 2005; Zambardi et al., 2014). Further study and modeling of igneous Fe isotopic fractionation processes have since become possible, including the potential to distinguish characteristic signatures of ultramafic mantle mineral phases, and mantle materials affected by changes in oxidation state (Dauphas et al., 2014, 2009a; Sossi et al., 2012; Teng et al., 2008; Williams et al., 2004).

Mechanisms known to fractionate Fe isotope ratios magmatically include assimilation/fractional crystallization (AFC) (Xhu et al., 2002), fractional melting, changes in redox state (as Fe can exist in 2+, 3+, and 0 valence states) (Sossi et al., 2012), and kinetic or equilibrium fractionation between phases (Sio et al., 2013). Typical mass-dependent fractionation occurs as a kinetic effect; the result of heavier isotopes forming stronger bonds than lighter isotopes. Correspondingly, more energy is required to break bonds with heavier isotopes than those with lighter isotopes. More strongly bonded phases (or melts generated from sources where Fe^{3+} is more incompatible, such as mantle peridotite) typically display net heavier Fe isotopic compositions (e.g. Polyakov and Mineev, 2000; Schoenberg and Von Blanckenburg, 2005; Weyer and Ionov, 2007; Williams et al., 2012, 2004). The Fe isotopic effects generated in these settings, though, tend to remain small. The magnitude of fractionation decreases with increasing temperature approximating $\sim 1/T^2$ (Polyakov and Mineev, 2000). As temperature increases, the greater available energy in a system reduces the probability of disrupting a chemical bond with a lighter isotope over a heavier isotope. Similarly, higher temperatures correlate with smaller differences in bond strength between different isotopes, which also factors into relatively small fractionation in magmatic settings. For Fe, this translates to <1‰ variations in igneous materials, making

reliable, precise analysis of stable isotopic variations in igneous systems challenging (e.g., Dauphas et al., 2009; Dideriksen et al., 2006; Millet et al., 2012; Weyer and Schwieters, 2003). However, these challenges can be overcome by, increasing precision of analytical techniques, and for some systems, using isotopic "spikes" or averages of repeated measurements via standard-sample bracketing to correct for instrumental fractionation.

Recent application of techniques such as X-ray Absorption Near Edge Structure (XANES; Cottrell et al., 2009; Cottrell and Kelley, 2013) and Nuclear Resonant Inelastic X-ray Scattering (NRIXS; Dauphas et al., 2014) have provided insight into the mechanisms of crystallization-driven Fe fractionation in igneous systems. Fe^{3+} does not partition in any significant quantity into olivine (Dauphas et al., 2014); thus as olivine fractionates from a melt, Fe^{2+} is depleted, increasing Fe^{3+}/Fe^{2+}_{melt} and correspondingly the melt oxygen fugacity (Sossi et al., 2012). NRIXS measurements of ^{57}Fe in olivine reveals that its bond strength is comparable to that of many host melts in which olivine may precipitate (Dauphas et al., 2014), and produces results in agreement with XANES (Cottrell and Kelley, 2013) and Mössbauer techniques (e.g. Polyakov and Mineev, 2000). This similarity in bond strength indicates that Fe^{2+} incorporation into olivine alone is not a significant source of isotopic fractionation of the melt (Dauphas et al., 2014). Instead, the significant equilibrium fractionation between Fe^{2+} and Fe^{3+} oxidation states, which concentrate heavier isotopes into the more oxidized (higher bond strength) state, drives major isotopic shifts of melts (Dauphas et al., 2014; Sossi et al., 2012). Thus, crystal fractionation indirectly controls melt oxidation state, and therefore Fe isotopic composition (Dauphas et al., 2014).

Changes in redox in igneous systems convert Fe between its 2+ and 3+ oxidation states. Fe isotopic fractionation from oxidation follows a mass-dependent principle, with

oxidized compositions preferentially retaining net heavier Fe during equilibrium fractionation with Fe^{2+}. Several magmatic processes, including metasomatism, melting, and crystallization can affect redox states of mantle domains and mantle-derived melts.

Metasomatic fluids are commonly implicated in the oxidation of mantle domains (Williams et al., 2004). Fe-depletion by metasomatism more easily disrupts the bonds of lighter Fe isotopes, leaving behind a net higher isotopic signature in metasomatized mantle (e.g., Debret et al., 2016; Konter et al., 2016; Su et al., 2015). Accordingly, melt produced from oxidized, higher fO_2 mantle is thought to yield heavier Fe isotopic compositions than lower fO_2 sources (Konter et al., 2016; Sossi et al., 2012).

Assimilation/fractional crystallization (AFC) processes are common in magmatic systems. Assimilation involves digestion of host rock or other pre-existing material by a magma. Fractional crystallization involves the formation and separation of mineral phases that precipitate as a melt evolves. These processes produce predictable mineral-melt fractionation patterns, making it possible to quantitatively model the isotopic evolution of a system (e.g. Dauphas et al., 2009a; Teng et al., 2008; Williams et al., 2004; Konter et al., 2016). This in turn can be used as a predictive tool for Fe isotopic compositions in certain mantle systems and a method by which to identify potential initial isotopic conditions of primary mantle melts and the depleted mantle sources feeding volcanic systems. Mantle Fe isotopic composition, therefore, may be useful as a proxy for oxidation state, useful to infer influence of chemical processes (e.g., metasomatism, assimilation-fractional crystallization, melting, zone refining) and source input (Dauphas et al., 2009a; Teng et al., 2013; Williams et al., 2005; Zambardi et al., 2014).

Fractional melting is another process capable of fractionating Fe isotopes (Dauphas et al., 2009a; Teng et al., 2013). Melt generation preferentially partitions Fe^{3+} into the liquid phase because of its more incompatible nature in many melts compared to Fe^{2+} (Cottrell and Kelley, 2011). Equilibrium fractionation, discussed previously, occurs between Fe^{3+} and Fe^{2+} states, concentrating heavier isotopes in the 3+ redox state (Dauphas et al., 2014). Hence, melting produces a liquid with a net higher Fe^{3+}/Fe^{2+} and correspondingly heavier $\delta^{56}Fe$ composition (Teng et al., 2008). As melt fraction increases, however, melt Fe^{3+}/Fe^{2+} and $\delta^{56}Fe$ increasingly resemble the composition of the source (Dauphas et al., 2009a; Konter et al., 2016; Figure 3.7).

Diffusion between olivine and melt is another possible driver of Fe isotopic fractionation as a function of mineral precipitation, although it requires significant cooling time (~20 years) and a large crystal fraction to produce any measurable effects on a host melt (Dauphas et al., 2014; Sio et al., 2013; Teng et al., 2011). While Mg tends to diffuse out of crystals and into more Fe-rich melt, Fe simultaneously diffuses into the crystal lattice (Teng et al., 2011). Since diffusion is a kinetic process, ^{54}Fe will diffuse into the crystal faster than heavier isotopes of Fe. This may produce a small increase in melt $\delta^{56}Fe$, depending on the crystal fraction present in the melt and timescale of cooling. Other phases, such as orthopyroxene, may take up to an order of magnitude longer than olivine to reach equilibrium (Dauphas et al., 2014; Sio et al., 2013; Teng et al., 2011).

1.2.1.1. Redox, melting, and Fe isotope ratios in subduction zones

Some recent work has been done to evaluate Fe isotope fractionation in subduction zone environments, although the total dataset remains small and cannot account for the

significant variability of Fe behavior (δ^{56}Fe -0.2‰ to +0.2‰) in arc melts throughout time or in a specific location (Dauphas et al., 2009a; Nebel et al., 2014, 2013b; Sossi et al., 2016).

According to simple melting models (e.g., Dauphas et al., 2009a), melts should be isotopically heavier in Fe than their source regardless of tectonic setting (Dauphas et al., 2009a; Teng et al., 2008) due to the relatively incompatible nature of Fe^{3+} in ultramafic source rocks (Cottrell and Kelley, 2011). Multiple melt extraction events, therefore, should deplete the upper mantle of heavy Fe, and arc (and backarc) magmas derived from mantle may carry a Fe signature heavier than their source rocks. However, the history of mantle depletion and/or refertilization, and therefore any influence on Fe isotope signature, is not well characterized.for the MVF. The effect is further enhanced in arcs compared to other tectonic settings because of more oxidizing conditions there (e.g., Evans and Tomkins, 2011). However, this expectation is not consistently observed, and the limited data on Fe isotope behavior in boninitic melts reveals unexpectedly low δ^{56}Fe (Dauphas et al., 2009a). Other arc compositions span a range from isotopically heavy to light (Dauphas et al., 2009a; Debret et al., 2016; Nebel et al., 2015, 2013a; Su et al., 2015).

Subducting crust is thought to have progressively higher δ^{56}Fe as it loses increasing amounts of low-δ^{56}Fe fluids into the overlying mantle (Debret et al., 2016). This is based on δ^{56}Fe changes with increasing metamorphic grade in exhumed, metamorphosed subducted crust that suggests Fe isotope fractionation occurs during dehydration processes (Debret et al., 2016; Su et al., 2015). An isotopically light subduction fluid component provides a potential source of unexpectedly light Fe isotopes in arc magmas (Debret et al., 2016), although a much larger global dataset is required to fully constrain controls on the observed relatively low δ^{56}Fe (Figure 3.5) in subduction zone magmas.

1.2.2. Radiogenic isotope fractionation (Sr, Pb, Nd, and Hf)

1.2.2.1. Radiogenic ingrowth and origin of variations

Radiogenic isotopes (e.g., ^{87}Sr, ^{208}Pb, ^{207}Pb, ^{206}Pb, ^{177}Hf, and ^{143}Nd) are generated by decay of an unstable parent nuclide. In contrast to stable isotope fractionation, radiogenic isotope fractionation is not driven in any significant manner by magmatic processes or redox state. Instead, radiogenic isotope variations are controlled by ingrowth from radioactive parent nuclides. Minerals forming within a melt all have the same initial ratio of a radiogenic isotope (e.g., ^{206}Pb, stable decay product of ^{238}U) of an element relative to a stable or "common" isotope (^{204}Pb). Over time, ^{238}U parent atoms decay and increase the abundance of ^{206}Pb, modifying its ratio relative to ^{204}Pb. Any differences in ratio between minerals crystallized from the same melt represent the time-integrated effect of parent-daughter fractionation that occurred during its formation (e.g., Taylor and McLennan, 1985). This allows us to track radiogenic ingrowth of an isotope in a rock, mineral, or reservoir over time. These time-integrated ratios can also be recycled into different geochemical reservoirs, providing a useful indicator of the source of geochemical provinces with implications for mantle dynamics (Zindler and Hart, 1986).

The amount of radiogenic ingrowth is dependent on the proportion of the radioactive parent isotope to the radiogenic daughter isotope (Zindler and Hart, 1986). In the case of a sample containing large amounts of parent relative to the concentration of its daughter isotope, relatively rapid radiogenic ingrowth occurs relative to the common isotope of the daughter element. Conversely, slow radiogenic ingrowth occurs if large amounts of the daughter element are present relative to parent element abundances. Therefore, the radiogenic isotope ratios (compared to a stable isotope) are a time-

integrated representation of the parent/daughter ratio of a given sample's source material (e.g., Hofmann and White, 1982; Zindler and Hart, 1986). On a larger scale, such time-integrated behavior contributes to our understanding of the evolution of major geochemical reservoirs in the Earth, such as crust-mantle differentiation (e.g., Taylor and McLennan, 1985).

The ability to identify different source reservoirs ultimately relies on the differing partition coefficients of parent and daughter elements between two materials, e.g., mantle and partial melt, and the passage of adequate time for radiogenic ingrowth of daughter isotopes (e.g., Hofmann, 2007 and references therein). Indeed, fractionation of the parent/daughter ratio during melting (or crystallization) produces distinctive signatures in oceanic crust and other materials such as continental crust and sediments that may later be subducted back into the mantle and recycled in mantle plumes (e.g., Zindler and Hart, 1986). Radiogenic ratios are therefore also useful in determining how a source material may have been fractionated and by proxy, which process(es) may have fractionated it prior to being incorporated into a reservoir. The use of multiple isotope systems is important here, as each system has different sensitivity to different processes. Thus, a combination of isotopic systems will best reflect specific processes that have affected a mantle source, in turn inferring its likely origin. This provides evidence for recycling of various crustal, lithospheric, and mantle materials within the dynamic earth system (Zindler and Hart, 1986) in addition to providing a way to distinguish the origins of mantle-derived melts.

1.2.2.2. Mantle plumes

Mantle plumes are buoyant parcels of thermochemically anomalous mantle material (relative to ambient upper and lower mantle compositional averages), in some cases possibly arising from near the core-mantle boundary (CMB; e.g. Hart et al., 1973; Morgan, 1972). Plumes are the likely cause of so-called mantle "hotspots", which represent melting anomalies associated with upwelling mantle (Morgan, 1972). Originally thought to be stationary features in the mantle, some hotspots have been shown to undergo varying degrees of drift over time in response to the flow of ambient mantle (Doubrovine and Tarduno, 2004; Steinberger et al., 2004; Tarduno, 2007; Tarduno et al., 2009, 2003). The combination of plume drift and passage of crust over these hotspots produces volcanic tracks on the seafloor that become progressively older with distance from the current location of the hotspot (Morgan, 1972; Wilson, 1965, 1963). Plumes are typically thought to have a large plume head that, upon impacting the underside of the lithosphere, generate large volumes of basaltic volcanism that form large igneous provinces (LIPs; Head III and Coffin, 1997). Following exhaustion of the plume head, a tail, or column, of hot rock remains (French and Romanowicz, 2014; Hart et al., 1992; Morgan, 1972; White, 2010), producing a mantle "hotspot" below the lithosphere where increased mantle melting takes place.

Mantle plume generation has been linked to large low-shear velocity provinces (LLSVPs) located below the SW Pacific Ocean and continental Africa, detectable via seismic studies and visible in tomographic models (Lekic et al., 2012; Torsvik et al., 2006) just above the CMB. LLSVPs are steep-sided and seismically slow compared to regions of the lower mantle residing just above the CMB (To et al., 2011; Torsvik et al., 2006; Weis et al.,

2011). These regions could be geochemically distinct reservoirs formed by pooled subducted material accumulating at the base of the mantle (Hofmann and White, 1982). Also possible is that LLSVPs are remnants of a basal "magma ocean" formed early in Earth's history (e.g. Labrosse et al., 2007; Li et al., 2014). Using a downward projection model, Torsvik et al. (2006) found that most hotspots correlate with edges of LLSVPs and suggested plumes are generated as thermal instabilities from the steep-sided LLSVP boundaries. Plume ascent, however, may not be vertical; some plumes may be deflected by solid-state flow within the mantle while rising, resulting in a laterally drifting hotspot relative to its source (Doubrovine and Tarduno, 2004; Tarduno, 2007; Tarduno et al., 2009). It is still a matter of debate whether the plumes contain ambient lower mantle compositions, or whether they also entrain material from the LLSVP. Regardless of the origins of these reservoirs in the mantle, volcanism generated from most mantle plumes yields chemically and isotopically distinct signatures, commonly attributed to variable proportions of recycled subducted materials (Zindler and Hart, 1986), as discussed in more detail in the next section.

Alternative models have been proposed to explain hotspot volcanism. Some smaller, "secondary" plumes may arise from shallower boundaries within the mantle (Courtillot et al., 2003). Much of the ocean island basalt (OIB) activity observed in the southwestern Pacific has been associated with a South Pacific Isotope and Thermal Anomaly, or SOPITA, linked to the Pacific LLSVP (Hart, 1984; Staudigel et al., 1991; White, 2015). This anomaly was originally attributed to a high concentration of subducted, compositionally heterogeneous material concentrated in a localized region. The subducted materials were thought to have metasomatized overlying mantle, enhancing plume formation in the SW

Pacific (Staudigel et al., 1991). Other models attempting to explain the unusually high density of volcanism in this region include secondary plumes rising from a "superplume" (Courtillot et al., 2003; McNutt and Fischer, 1987; Menard, 1973) and so-called mantle "hotline" volcanism (Bonatti et al., 1977) to explain complex age progressions and overlapping compositions in regions such as the so-called "Hotspot Highway" (Jackson et al., 2010). In this case, a hotline was proposed as a linear upwelling in the mantle to explain the complicated age progressions in the Easter and possibly Cook-Austral chains (e.g., Barsczus et al., 1994). Some suggest that mantle plumes do not adequately explain hotspot volcanism, instead proposing alternative models such as passive upwelling of ambient mantle (e.g., Anderson, 2006, 2000; Foulger et al., 2005). Most southwest Pacific hotspot volcanism has since been explained by primary mantle plumes, including 3 extant plumes in the Cook-Australs (Chauvel et al., 1997). Recent research using high-resolution tomography (e.g., French and Romanowicz, 2014; Niu et al., 2002), and geochemical evidence in the form of dual-trend volcanism (e.g., Harpp et al., 2014; Huang et al., 2011; O'Connor and Jokat, 2015; Payne et al., 2013; Weis et al., 2011; Workman and Hart, 2004) however, support a deep primary plume origin for many age-progressive Pacific hotspot tracks. The discovery of parallel geochemical-geographic "dual-trend" volcanism in some hotspot tracks is proposed as a consequence of a bilaterally zoned, heterogeneous plume. Plumes are thought to result from convective instabilities from the steep edges of LLSVPs, potentially sampling two different mantle domains (Weis et al., 2011). One side samples an enriched component (possibly LLSVP material) and the other a more depleted component (ambient mantle). Furthermore, plumes have often been found to align with modeled LLSVP boundaries, with enriched hemispheres oriented toward the LLSVP (Figure 1.2; e.g.

Harpp et al., 2014). Dual-trend hotspot tracks include Hawaii, Marquesas, Samoa, Society, Cook-Austral, and Walvis (Abouchami et al., 2005; Hanyu et al., 2013; Harpp et al., 2014; Huang et al., 2011; Nebel et al., 2013b; O'Connor and Jokat, 2015; Payne et al., 2013; Tatsumoto, 1978; Weis et al., 2011). The geographic separations between parallel compositional trends in a hotspot track is typically on the order of ~45 km (Weis et al., 2011), but can be as large as ~400 km (O'Connor and Jokat, 2015). Advances in tomographic resolution show that velocity anomalies under some volcanically active seamount tracks extend to the CMB, rendering them "primary" (sourced from the CMB) mantle plumes (French and Romanowicz, 2014). Previously, resolution was not sufficient to image deep-mantle plume-like features beneath some hotspots (e.g. Montelli et al., 2004).

1.2.2.3. Isotopic fingerprinting and absolute plate motion

Ocean island basalts (OIBs) are products of intraplate volcanism that exhibit characteristic $^{87}Sr/^{86}Sr$, $^{206}Pb/^{204}Pb$, $^{207}Pb/^{204}Pb$, $^{208}Pb/^{204}Pb$, $^{176}Hf/^{177}Hf$, and $^{143}Nd/^{144}Nd$ isotopic signatures representing mixtures of endmember compositions (HIMU, EM1, and EM2). Plotted in isotope space ($^{87}Sr/^{86}Sr$-$^{206}Pb/^{204}Pb$-$^{143}Nd/^{144}Nd$), these endmembers define the extreme values in the known range of magmatic isotopic compositions (e.g. Figure 1.3; adapted from Hart et al., 1992). These are sourced from heterogeneous compositional reservoirs in the lower mantle that mix with a "common" composition ("C" – Hanan et al., 2000; Hanan and Graham, 1996; "FOZO", Hart et al., 1992; Hauri and Hart, 1994; "PREMA", Wörner et al., 1986; Zindler and Hart, 1986; or an ancient, dense, high-$^{3}He/^{4}He$ reservoir, Jackson et al., 2017) thought to be ambient lower mantle (Zindler and

Hart, 1986). These endmembers are chemically and isotopically distinct from mid-ocean ridge basalts (MORB) and their depleted MORB mantle (DMM) source and thought to be derived from a range of recycled subducted materials such as oceanic (HIMU) and continental crust (EM2) and pelagic sediments (EM1), although consensus on origins has not yet been reached (e.g. Blichert-Toft et al., 1999; Eisele et al., 2002; Hanyu and Kaneoka, 1997; Jackson et al., 2007; Panter, 2006; Parai et al., 2009; Weaver, 1991; Workman et al., 2004). OIB compositions display heterogeneity between, and commonly within seamounts, although it should be noted that plumes have often (erroneously) been described in terms of a single specific composition. Compositional variations within plumes form a mixing array (Zindler and Hart, 1986) and/or variations due to time-integrated radiogenic ingrowth (Hofmann and White, 1982) in isotope space between a compositional endmember (or mixture of endmembers), and a common composition such as FOZO. Other compositional shifts between endmembers have also been observed. For example, most seamounts comprising the Macdonald hotspot track in the Cook-Austral islands have a strongly HIMU signature. However, the Macdonald plume transitioned to an EM1-like composition at ~8 Ma, observed in the youngest Macdondald seamounts: Rapa, Marotiri, and Macdonald (Chauvel et al., 1997).

Through a combination of trace element geochemistry and distinctive isotopic signatures generated from parent nuclide decay, it is further possible to identify ("fingerprint") geochemically distinct reservoirs within the mantle. These reservoirs are thought to be formed from subduction of different recycled materials present in hotspot volcanism that act as sources for thermochemical mantle plumes (Zindler and Hart, 1986). The ability to establish age-progressive volcanic tracks and geochemically link them to a

single hotspot source provides the key constraint for absolute plate motion models (e.g., Konter et al., 2008; Morgan, 1972). The semi-fixed nature of hotspots beneath the lithosphere provides an absolute reference frame, rather than relative to a specific plate, by which to characterize plate motion vectors. The discovery of age-progressive volcanism has led to multiple generations of hotspot-constrained plate motion models (e.g., Duncan and Clague, 1985; Morgan, 1972; Wessel and Kroenke, 2008). Paleomagnetic analyses quantified latitudinal drift (but not longitudinal) and inter-hotspot motion of both the Hawaiian-Emperor and Louisville hotspots, likely due to displacement by mantle flow (Doubrovine and Tarduno, 2004; Koppers et al., 2012, 2011; Tarduno, 2007; Tarduno et al., 2009, 2003). This led to development of additional absolute plate motion (APM) models that integrate plume drift and global mantle flow dynamics (e.g. (Doubrovine et al., 2012; Steinberger et al., 2004).

APM models tend to predict ~50-0 Ma plate motion well, but the combination of hotspot drift and mismatches between the different hotspot tracks (e.g., comparing Hawaii-Emperor and Louisville), plate motion uncertainty increases greatly, underscoring the need for additional constraints (Koppers et al., 1998; Wessel and Kroenke, 2008). Furthermore, both Hawaii-Emperor and Louisville tracks extend only to ~80 Ma and plate motion older than that is estimated by piecing together discontinuous volcanic segments (Koppers et al., 2003; Wessel and Kroenke, 2008). A third major hotspot track in the Pacific Ocean basin is required to test fits of existing APM models and develop new models. Previous research has identified volcanic chains up to ~120 Ma in the southwest Pacific that have been linked to the Rurutu hotspot, but an important constraining feature in the Bend had not yet been identified, which is discussed in Chapter 4.

1.3. Dissertation Structure

1.3.1. Chapter 2 – Fe isotope technique development

Chapter 2, published in *Geochemistry, Geophysics, Geosystems* in 2015 (Finlayson et al., 2015), introduces an improved high-precision iron (Fe) isotope analytical method that has potential to distinguish small (<0.1‰) isotopic differences among ultramafic mineral phases (olivine, orthopyroxene, and clinopyroxene) commonly found in mantle xenoliths. Analysis via multicollector inductively-coupled plasma mass spectrometry, however, complicates high-precision determinations of the small Fe isotope fractionation that occurs at magmatic temperatures. In brief, instrumental fractionation produces a predictable shift in measured ratios that requires correction. Although there are several methods to correct this, use of an exponential curve is the most common correction method, and care must be taken to determine the magnitude of fractionation, as this can vary unpredictably with time. Other complications include polyatomic argide interferences present on all Fe masses and isobaric elements that interfere on two Fe masses, all described in detail in Chapter 2. Fe ratio analyses were performed using one of two methods: 1) Standard-sample bracketing (Dauphas et al., 2004), and 2) Analysis with an isotopic "spike" mixed with sample (Finlayson et al., 2015; Konter et al., 2016). In the first method, analyses alternate between repeatedly measuring samples and a standard solution, then calculating the offset of the sample (as δ^{56}Fe) relative to the standard measurements immediately before and after. In this method, most instrumental drift that might affect measurements is accounted for. Multiple sample measurements are averaged together to provide the best estimate of sample composition (e.g. Dauphas et al., 2004). The second method is to "spike", or add an,

artificial, known isotopic composition of the same element (or element of similar mass, such as in the case of using a known $^{203}Tl/^{205}Tl$ composition to track fractionation during measurements of Pb isotopes; Albarède et al., 2004) to the standard and sample aliquots. With the Fe double spike, however, any double spike composition will mix with the natural fraction of the same isotopes in the natural sample, requiring additional solutions to determine instrumental fractionation (e.g. Siebert et al., 2001). Because the spike composition is a known quantity, it can be iteratively "unmixed" from the sample solution while simultaneously correcting for instrumental bias. Solutions for Fe usually involve double and triple spikes (non-natural mixture of two and three Fe isotopes, respectively; Johnson and Beard, 1999) This method is advantageous in that it typically requires fewer repeat analyses of a single solution to achieve high precision.

The method described in Chapter 2 requires use of a ^{57}Fe-^{58}Fe double spike with a precisely known composition to determine sample $^{56}Fe/^{54}Fe$ composition. The iterative double spike correction method is sensitive to the small amounts of ^{58}Ni, an isobaric interference contributing to the total 58 atomic mass unit (amu) signal, which may remain in standards and samples in picogram (pg) quantities. To counter these interferences, the method accounts for ^{58}Ni and ^{54}Cr (another possible isobaric interference on the 54 amu ion beam), by monitoring ^{60}Ni and ^{52}Cr, respectively. In addition, a robust three-dimensional statistical outlier identification method was used to remove any data potentially affected by instrumental drift, which may occur during analysis, improving overall analytical precision by ~10%. This method was tested on olivine, orthopyroxene, and clinopyroxene mineral separates from mantle xenoliths recovered from Kilbourne Hole maar in southern New Mexico, and from rejuvenated lavas on Savaiʻi, Samoa. Results

indicate the technique (including statistical outlier rejection) is capable of achieving 0.046‰ reproducibility, with fewer replicate analyses compared to standard-sample bracketing, providing strong potential to resolve the small isotopic variations between some ultramafic mineral phases.

1.3.2. Chapter 3 – δ^{56}Fe of young SW Pacific boninites

The predictable fractionation behavior of Fe isotopes can be used in combination with compositional data to determine the dominant processes and mantle sources that control petrogenesis of boninite, a rare rock type characterized by high MgO and high SiO_2, in the North Tonga backarc. Of particular interest is the effect of the inferred high oxidation state of subduction-related lavas on Fe isotope fractionation, although limited data has not provided a clear understanding of the fractionation patterns in subduction-related melt (e.g. Dauphas et al., 2009a; Foden et al., 2013; Nebel et al., 2014, 2013a; Sossi et al., 2016). In Chapter 3, intended for *Geochemistry, Geophysics, Geosystems*, the combination of Fe isotopes and major element compositions of glasses, and selected whole rock trace element data can be used to investigate effects of various magmatic processes and source contributions affecting boninites erupted from the Mata Volcanic Field (MVF), located within the northern Lau Basin/Tonga backarc region. The MVF contains a small array of young volcanoes located in the northern Tonga backarc, between the Tonga arc system and the local NE Lau Spreading Center (NELSC). The volcanoes erupt primarily boninitic and boninite-like compositions, thought to be generated by high extents of partial melting of depleted mantle resulting from "fluxing" by subduction-derived fluids, and possibly involving mantle material from the Samoan plume several hundred kilometers NE of the

MVF. The MVF sits near a confluence of tectonic styles and mantle compositions, providing a window into underlying mantle geochemistry and source contributions to early-stage subduction zones, where the processes and contribution to melt generation are a topic of ongoing debate. The combination of glass δ^{56}Fe ratios, and whole rock trace elemental proxies of subduction fluid input reveal systematically different within-volcano trends in δ^{56}Fe and MgO of two well-sampled volcanoes in this study: Mata Tolu and West Mata. Located in the northwest and southeast halves of the MVF, respectively, Mata Tolu is proximal to the NE Lau Spreading Center (NELSC), and West Mata closer to the Tonga Arc. The Mata Tolu trend bears geochemical characteristics resembling a mixture of MVF and NELSC compositions, while West Mata is more Ba-enriched, bearing a more arc-like trace element signature (Lupton et al., 2015). Magmatism at West Mata likely involved slightly greater incorporation of subduction fluid into its melts compared to Mata Tolu. The δ^{56}Fe compositions of MVF volcanoes, however, are considerably lower than ratios expected for mantle-derived melts, instead resembling typical depleted mantle composition. This lower-than-expected signature may be related to a combination of the large degree of melt required to produce boninitic compositions and the incorporation of isotopically light subduction fluids.

1.3.3. Chapter 4 – SW Pacific hotspot tracks and absolute plate motion

Immediately north of the northern terminus of the Tonga Arc lies the so-called "Hotspot Highway" region of the southwest Pacific (Figure 1.1). Chapter 4, submitted to *Earth and Planetary Science Letters,* focuses on the origins of the little-studied Tuvalu island chain within this region. To properly identify the geochemical and mantle provenance of

the volcanoes comprising the Tuvalu chain, we use a combination of Sr, Pb, Nd, and Hf radiogenic ratios. Tuvalu volcanism was generated by several sources: 1) the Rurutu hotspot, 2) the Samoan hotspot, and 3) volcanic activity likely linked to the breakup of Ontong-Java Nui. Tuvalu volcanoes sourced by the Rurutu hotspot are used to find the location of the Rurutu hotspot Bend that might correlate with the archetypal ~47-50 Ma Bend (Sharp and Clague, 2006) first characterized in the Hawaiian-Emperor hotspot track.

The intersection of the Tuvalu chain and western Samoa complicates an otherwise simple visual estimation of the Bend location. To assist location efforts, a statistical technique is used to pinpoint the highest-probability Bend locations for each of three fundamentally different APM models (Doubrovine et al., 2012; Duncan and Clague, 1985; Wessel and Kroenke, 2008). A Monte Carlo simulation was used to estimate the uncertainty of the calculated Bend locations. The combination of age determinations, radiogenic geochemical compositions, and Bend location estimate provide crucial evidence that the Rurutu hotspot persisted up to ~120 Ma. This complete, long-lived hotspot track allows for the development of new APM models that use three major hotspot tracks: the traditional Hawaiian-Emperor and Louisville tracks, and now the Rurutu track.

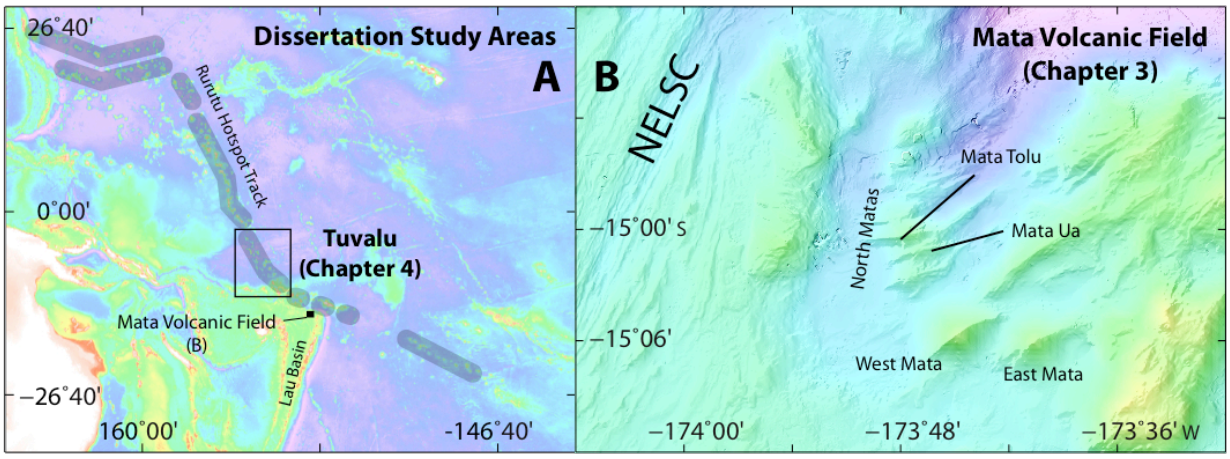

Figure 1.1. Map showing locations of the study areas discussed in this dissertation. **A)** Wide-view map of the southwestern Pacific basin, showing the known extent of the Rurutu hotspot track. The Mata Volcanic Field (MVF; small black square) sits in the northeastern Lau Basin, SE of the Tuvalu segment of the Rurutu track. **B)** Detailed view of the MVF and volcanoes sampled in this dissertation.

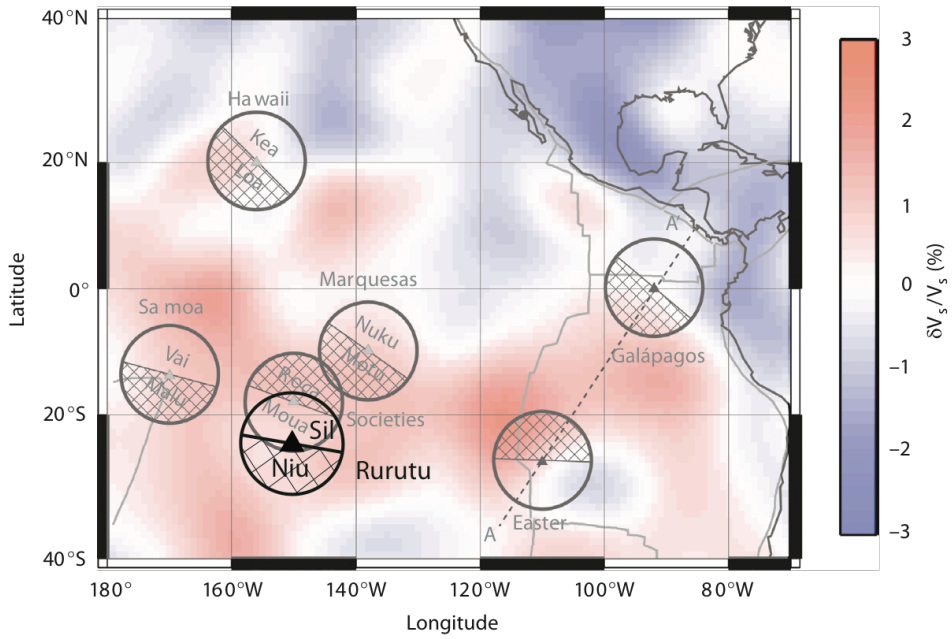

Figure 1.2. Map showing the locations and proposed orientations of bilaterally zoned mantle plumes superimposed over the SAW642AN model (2800 km depth to capture the Pacific LLSVP; Panning and Romanowicz, 2006), adapted from Harpp et al. (2014). Also shown with previously published hotspot locations is the Rurutu hotspot to display similar bilateral heterogeneity with probable N-S orientation (full discussion is found in Chapter 4). The depleted Sil trend (Chapter 4) roughly aligns with a small increase in seismic shear wave velocity anomaly centered around 155°W, 25°S. The same region also aligns with the depleted Moua trend in the Society plume. The enriched Niu trend corresponds with an decrease in seismic shear wave velocity anomaly near 160°W, 40°S.

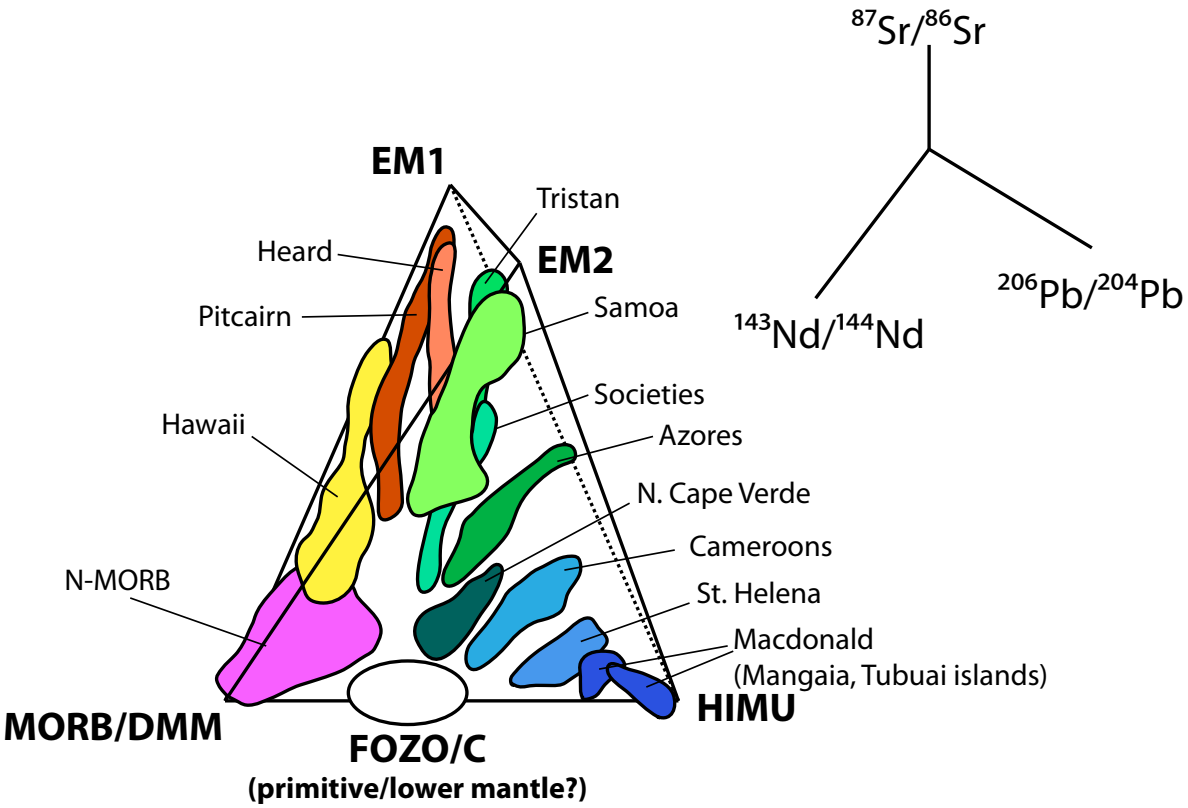

After figure by Stan Hart, published in Hofmann (2007)

Figure 1.3. The mantle tetrahedron (after Hart et al., 1992) formed by mantle-derived compositions in Sr-Pb-Nd isotope space. This illustrates the geochemical variability of various OIBs and their relationship to FOZO, one of the definitions of a "common" geochemical reservoir in the mantle. The corners of the tetrahedron are defined by the most extreme "endmember" compositions observed in OIBs. The space enclosed by the tetrahedron defines the range in which most mantle compositions plot.

1.4. References

Abouchami, W., Hofmann, A.W., Galer, S.J.G., Frey, F.A., Eisele, J., Feigenson, M., 2005. Lead isotopes reveal bilateral asymmetry and vertical continuity in the Hawaiian mantle plume. Nature 434, 851–856. doi:10.1038/nature03402

Albarède, F., Telouk, P., Blichert-Toft, J., 2004. Precise and accurate isotopic measurements using multiple-collector ICPMS. Geochim. Cosmochim. Acta 68, 2725–2744. doi:10.1016/j.gca.2003.11.024

Anderson, D.L., 2000. The thermal state of the upper mantle; no role for mantle plumes. Geophys. Res. Lett. 27, 3623–3626.

Anderson, D.L., 2006. Speculations on the nature and cause of mantle heterogeneity. Tectonophysics 416, 7–22.

Barsczus, H.G., Guille, G., Maury, R., Chauvel, C., Guillou, H., 1994. Two magmatic sources at Rurutu Island (Austral Islands, French Polynesia) and the Austral "hotline." EOS, Trans. Am. Geophys. Union 75, 323.

Blichert-Toft, J., Frey, F.A., Albarède, F., 1999. Hf Isotope Evidence for Pelagic Sediments in the Source of Hawaiian Basalts. Science. 285, 879–883.

Bonatti, E., Harrison, C.G.A., Fisher, D.E., Honnorez, J., Schilling, J.-G., 1977. Easter volcanic chain (southeast Pacific): A mantle hotline. J. Geophys. Res. 82, 2457–2478.

Bonneville, A., Suavé, R. Le, Audin, L., Clouard, V., Dosso, L., Gillot, P.-Y., Janney, P.E., Jordahl, K., Maamaatuaiahutapu, K., 2002. Arago Seamount: The missing hotspot found in the Austral Islands. Geology 30, 1023–1026. doi:10.1130/0091-7613(2002)030<1023

Buchachenko, A.L., 2001. Magnetic Isotope Effect : Nuclear Spin Control of Chemical Reactions. J. Phys. Chem. A 105, 9995–10011.

Chauvel, C., McDonough, W.F., Guille, G., Maury, R., Duncan, R.A., 1997. Contrasting old and young volcanism in Rurutu Island, Austral chain. Chem. Geol. 139, 125–143. doi:10.1016/S0009-2541(97)00029-6

Cottrell, E., Kelley, K.A., 2011. The oxidation state of Fe in MORB glasses and the oxygen fugacity of the upper mantle. Earth Planet. Sci. Lett. 305, 270–282.

Cottrell, E., Kelley, K.A., 2013. Redox heterogeneity in MORB as a function of mantle source. Science. 340, 1314–1317. doi:10.1126/science.1233299.This

Cottrell, E., Kelley, K.A., Lanzirotti, A., Fischer, R.A., 2009. High-precision determination of iron oxidation state in silicate glasses using XANES. Chem. Geol. 268, 167–179.

Courtillot, V., Davaille, A., Besse, J., Stock, J., 2003. Three distinct types of hotspots in the Earth' s mantle. Earth Planet. Sci. Lett. 205, 295–308.

Dauphas, N., Craddock, P.R., Asimow, P.D., Bennett, V.C., Nutman, A.P., Ohnenstetter, D., 2009a. Iron isotopes may reveal the redox conditions of mantle melting from Archean to Present. Earth Planet. Sci. Lett. 288, 255–267. doi:10.1016/j.epsl.2009.09.029

Dauphas, N., Janney, P.E., Mendybaev, R.A., Wadhwa, M., Richter, F.M., Davis, A.M., van Zuilen, M., Hines, R., Foley, C.N., 2004. Chromatographic separation and multicollection-ICPMS analysis of iron. Investigating mass-dependent and independent isotope effects. Anal. Chem. 76, 5855–63. doi:10.1021/ac0497095

Dauphas, N., Pourmand, A., Teng, F.-Z., 2009b. Routine isotopic analysis of iron by HR-MC-ICPMS: How precise and how accurate? Chem. Geol. 267, 175–184. doi:10.1016/j.chemgeo.2008.12.011

Dauphas, N., Roskosz, M., Alp, E.E., Neuville, D.R., Hu, M.Y., Sio, C.K., Tissot, F.L.H., Zhao, J., Tissandier, L., Mèdard, E., Cordier, C., 2014. Magma redox and structural controls on iron isotope variations in Earth's mantle and crust. Earth Planet. Sci. Lett. 398, 127–140.

Debret, B., Millet, M.-A., Pons, M.-L., Bouilhol, P., Inglis, E., Williams, H., 2016. Isotopic evidence for iron mobility during subduction. Geology 44, 215–218.

Dideriksen, K., Baker, J.A., Stipp, S.L.S., 2006. Iron isotopes in natural carbonate minerals determined by MC-ICP-MS with a 58Fe-54Fe double spike. Geochim. Cosmochim. Acta 70, 118–132. doi:10.1016/j.gca.2005.08.019

Doubrovine, P. V., Steinberger, B., Torsvik, T.H., 2012. Absolute plate motions in a reference frame defined by moving hot spots in the Pacific, Atlantic, and Indian oceans. J. Geophys. Res. Solid Earth 117. doi:10.1029/2011JB009072

Doubrovine, P. V., Tarduno, J.A., 2004. Late Cretaceous paleolatitude of the Hawaiian Hot Spot: New paleomagnetic data from Detroit Seamount (ODP Site 883). Geochemistry, Geophys. Geosystems 5. doi:10.1029/2004GC000745

Duncan, R.A., Clague, D.A., 1985. Pacific plate motion recorded by linear volcanic chains, in: The Ocean Basins and Margins. Springer US, Boston MA. doi:10.1007/978-1-4613-2351-8_3

Eisele, J., Sharma, M., Galer, S.J.G., Blichert-Toft, J., Devey, C.W., Hofmann, A.W., 2002. The role of sediment recycling in EM-1 inferred from Os, Pb, Hf, Nd, Sr isotope and trace element systematics of the Pitcairn hotspot. Earth Planet. Sci. Lett. 196, 197–212.

Evans, K.A., Tomkins, A.-G., 2011. The relationship between subduction zone redox budget and arc magma fertility. Earth Planet. Sci. Lett. 308, 401–409.

Finlayson, V.A., Konter, J.G., Ma, L., 2015. The importance of a Ni correction with ion counter in the double spike analysis of Fe isotope compositions using a 57Fe/58Fe double spike. Geochemistry, Geophys. Geosystems 16.

Foden, J.D., Sossi, P.A., Halverson, G.P., 2013. Global variation in Fe-isotopic composition of arc basalts indicate a variably oxidised and metasomatised mantle wedge source? Mineral. Mag. 77, 1097.

Foulger, G.R., Natland, J.H., Anderson, D.L., 2005. Genesis of the Iceland melt anomaly by plate tectonic processes. Plate, Plumes, Paradig. Geol. Soc. Am. Spec. Pap. 388 595–625.

French, S.W., Romanowicz, B. a., 2014. Whole-mantle radially anisotropic shear velocity structure from spectral-element waveform tomography. Geophys. J. Int. 199, 1303–1327. doi:10.1093/gji/ggu334

Hanan, B.B., Blichert-Toft, J., Kingsley, R., Schilling, J.-G., 2000. Depleted Iceland mantle plume geochemical signature: Artifact of multicomponent mixing? Geochemistry, Geophys. Geosystems 1, n/a-n/a. doi:10.1029/1999GC000009

Hanan, B.B., Graham, D.W., 1996. Lead and Helium Isotope Evidence from Oceanic Basalts for a Common Deep Source of Mantle Plumes. Science. 272, 991–995.

Hanyu, T., Dosso, L., Ishizuka, O., Tani, K., Hanan, B.B., Adam, C., Nakai, S., Senda, R., Chang, Q., Tatsumi, Y., 2013. Geochemical diversity in submarine HIMU basalts from Austral Islands, French Polynesia. Contrib. to Mineral. Petrol. 166, 1285–1304. doi:10.1007/s00410-013-0926-x

Hanyu, T., Kaneoka, I., 1997. The uniform and low 3 He/4He ratios of HIMU basalts as evidence for their origin as recycled materials. Nature 390, 273–276.

Harpp, K.S., Hall, P.S., Jackson, M.G., 2014. Galápagos and Easter : A Tale of Two Hotspots, in: Harpp, K.S., Mittelstadt, E., D'Ozouville, N., Graham, D.W. (Eds.), The Galapagos: A Natural Laboratory for the Earth Sciences,Geophysical Monograph 204. American Geophysical Union, pp. 27–40.

Hart, S.R., 1984. A large-scale isotope anomaly in the Southern Hemisphere mantle. Nature 309, 753–757.

Hart, S.R., Hauri, E.H., Oschmann, L.A., Whitehead, J.A., 1992. Mantle plumes and entrainment: Isotopic evidence. Science. 256, 517–520.

Hart, S.R., Schilling, J.-G., Powell, J.L., 1973. Basalts from Iceland and along the Reykjanes Ridge: Sr isotope geochemist. Nature 246, 104–107.

Hauri, E.H., Hart, S.R., 1994. Constraints on melt migration from mantle plumes: A trace element study of peridotite xenoliths from Savai'i, Western Samoa. J. Geophys. Res. 99, 24301–24321. doi:10.1029/94JB01553

Head III, J.W., Coffin, M.F., 1997. Large igneous provinces: A planetary perspective, in: Mahoney, J.J., Coffin, M.F. (Eds.), Large Igneous Provinces: Continental, Oceanic, and Planetary Flood Volcanism, Geophysical Monograph 100, AGU. pp. 411–438. doi:10.1029/GM100p0411

Hofmann, A.W., 2007. Sampling Mantle Heterogeneity through Oceanic Basalts : Isotopes and Trace Elements. Treatise on Geochemistry 1–44.

Hofmann, A.W., White, W.M., 1982. Mantle plumes from ancient oceanic crust. Earth Planet. Sci. Lett. 57, 421–436.

Huang, F., Chakraborty, P., Lundstrom, C.C., Holmden, C., Glessner, J.J.G., Kieffer, S.W., Lesher, C.E., 2010. Isotope fractionation in silicate melts by thermal diffusion. Nature 464, 396–400.

Huang, S., Hall, P.S., Jackson, M.G., 2011. Geochemical zoning of volcanic chains associated with Pacific hotspots. Nat. Geosci. 4, 874–878. doi:10.1038/ngeo1263

Jackson, J.M., Hamecher, E.A., Sturhahn, W., 2009. Nuclear resonant X-ray spectroscopy of (Mg,Fe)SiO3 orthoenstatites. Eur. J. Mineral. 21, 551–560.

Jackson, M.G., Hart, S.R., Konter, J.G., Koppers, A.A.P., Staudigel, H., Kurz, M.D., Blusztajn, J., Sinton, J.M., 2010. Samoan hot spot track on a "hot spot highway": Implications for mantle plumes and a deep Samoan mantle source. Geochemistry, Geophys. Geosystems 11. doi:10.1029/2010GC003232

Jackson, M.G., Hart, S.R., Koppers, A.A.P., Staudigel, H., Konter, J.G., Blusztajn, J., Kurz, M.D., Russell, J.A., 2007. The return of subducted continental crust in Samoan lavas. Nature 448, 684–687. doi:10.1038/nature06048

Jackson, M.G., Konter, J.G., Becker, T.W., 2017. Primordial helium entrained by the hottest mantle plumes. Nature 542, 340–343.

Johnson, C.M., Beard, B.L., 1999. Correction of instrumentally produced mass fractionation during isotopic analysis of Fe by thermal ionization mass spectrometry. Int. J. Mass Spectrom. 193, 87–99.

Konter, J.G., Hanan, B.B., Blichert-Toft, J., Koppers, A.A.P., Plank, T., Staudigel, H., 2008. One hundred million years of mantle geochemical history suggest the retiring of mantle plumes is premature. Earth Planet. Sci. Lett. 275, 285–295. doi:10.1016/j.epsl.2008.08.023

Konter, J.G., Pietruszka, A.J., Hanan, B.B., Finlayson, V.A., Craddock, P.R., Jackson, M.G., Dauphas, N., 2016. Unusual δ56Fe values in Samoan rejuvenated lavas generated in the mantle. Earth Planet. Sci. Lett. 450, 221–232.

Konter, J.G., Pietruszka, A.J., Hanan, B.B., Finlayson, V.A., Craddock, P.R., Jackson, M.G., Dauphas, N., n.d. High δ56Fe values in Samoan rejuvenated lavas generated in the mantle. Earth Planet. Sci. Lett.

Koppers, A.A.P., Gowen, M.D., Colwell, L.E., Gee, J.S., Lonsdale, P.F., Mahoney, J.J., Duncan, R.A., 2011. New 40 Ar/ 39 Ar age progression for the Louisville hot spot trail and implications for inter-hot spot motion. Geochemistry, Geophys. Geosystems 12. doi:10.1029/2011GC003804

Koppers, A.A.P., Staudigel, H., Hart, S.R., Young, C., Konter, J.G., 2004. Vailulu'u Seamount. Oceanography 23, 164.

Koppers, A.A.P., Staudigel, H., Phipps Morgan, J., Duncan, R.A., 2007. Nonlinear 40Ar/39Ar age systematics along the Gilbert Ridge and Tokelau Seamount Trail and the timing of the Hawaii-Emperor Bend. Geochemistry, Geophys. Geosystems 8. doi:10.1029/2006GC001489

Koppers, A.A.P., Staudigel, H., Pringle, M.S., Wijbrans, J.R., 2003. Short-lived and discontinuous intraplate volcanism in the South Pacific: Hot spots or extensional volcanism? Geochemistry, Geophys. Geosystems 4. doi:10.1029/2003GC000533

Koppers, A.A.P., Staudigel, H., Wijbrans, J.R., Pringle, M.S., 1998. The Magellan seamount trail: implications for Cretaceous hotspot volcanism and absolute Pacific plate motion. Earth Planet. Sci. Lett. 163, 53–68.

Koppers, A.A.P., Yamazaki, T., Geldmacher, J., Gee, J.S., Pressling, N., Hoshi, H., Anderson, L., Beier, C., Buchs, D.M., Chen, L.-H., Cohen, B.E., Deschamps, F., Dorais, M.J., Ebuna, D., Ehmann, S., Fitton, J.G., Fulton, P.M., Ganbat, E., Hamelin, C., Hanyu, T., Kalnins, L., Kell, J., Machida, S., Mahoney, J.J., Moriya, K., Nichols, A.R.L., Rausch, S., Sano, S. -i., Sylvan, J.B., Williams, R., 2012. Limited latitudinal mantle plume motion for the Louisville hotspot. Nat. Geosci. 5, 911–917. doi:10.1038/ngeo1638

Labrosse, S., Hernlund, J.W., Coltice, N., 2007. A crystallizing dense magma ocean at the base of the Earth's mantle. Nature 450, 866–9. doi:10.1038/nature06355

Lekic, V., Cottaar, S., Dziewonski, A., Romanowicz, B., 2012. Cluster analysis of global lower mantle tomography: A new class of structure and implications for chemical heterogeneity. Earth Planet. Sci. Lett. 357–358, 68–77.

Li, M., Mcnamara, A.K., Garnero, E.J., 2014. Chemical complexity of hotspots caused by cycling oceanic crust through mantle reservoirs. Nat. Geosci. 7, 366–370. doi:10.1038/NGEO2120

Lupton, J.E., Rubin, K.H., Arculus, R.J., Lilley, M.D., Butterfield, D.A., Resing, J.A., Baker, E.T., Embley, R.W., 2015. Helium isotope, C3/He, and Ba-Nb-Ti signatures in the northern Lau Basin: Distinguishing arc, back-arc, and hotspot affinities. Geochemistry, Geophys. Geosystems 16, 1133–1155. doi:10.1002/2014GC005625

Mahoney, J.J., Duncan, R.A., Tejada, M.L.G., Sager, W.W., Bralower, T.J., 2005. Jurassic-Cretaceous boundary age and mid-ocean-ridge–type mantle source for Shatsky Rise. Geology 33, 185. doi:10.1130/G21378.1

McNutt, M.K., Fischer, K.M., 1987. The South Pacific Superswell, in: Keating, B.H., Fryer, P., Batiza, R., Boehlert, G.W. (Eds.), Seamounts, Islands, and Atolls. American Geophysical Union.

Menard, H.W., 1973. Depth Anomalies and the Bobbing Motion of Drifting Islands. J. Geophys. Res. 78, 5128–5137.

Millet, M.A., Baker, J.A., Payne, C.E., 2012. Ultra-precise stable Fe isotope measurements by high resolution multiple-collector inductively coupled plasma mass spectrometry with a Fe-57-Fe-58 double spike. Chem. Geol. 304, 18–25. doi:10.1016/j.chemgeo.2012.01.021

Montelli, R., Nolet, G., Dahlen, F.A., Masters, G., Engdahl, E.R., Hung, S.-H., 2004. Finite-frequency tomography reveals a variety of plumes in the mantle. Science. 303, 338–343.

Morgan, W.J., 1972. Deep Mantle Convection Plumes and Plate Motions. Am. Assoc. Pet. Geol. Bull. 56, 203–213.

Nakanishi, M., Sager, W.W., Klaus, A., 1999. Magnetic lineations within Shatsky Rise, northwest Pacific Ocean: Implications for hot spot-triple junction interaction and oceanic plateau formation. J. Geophys. Res. 104, 7539–7556.

Nebel, O., Arculus, R.J., Sossi, P.A., Jenner, F.E., Whan, T.H.E., 2013a. Iron isotopic evidence for convective resurfacing of recycled arc-front mantle beneath back-arc basns. Geophys. Res. Lett. 40, 5849–5853.

Nebel, O., Arculus, R.J., Westrenen, W. van, Woodhead, J.D., Jenner, F.E., Nebel-Jacobsen, Y.J., Wille, M., Eggins, S.M., 2013b. Coupled Hf–Nd–Pb isotope co-variations of HIMU oceanic island basalts from Mangaia , Cook-Austral islands, suggest an Archean source component in the mantle transition zone. Geochim. Cosmochim. Acta 112, 87–101.

Nebel, O., Campbell, I.H., Sossi, P.A., Van Kranendonk, M.J., 2014. Hafnium and iron isotopes in early Archean komatiites record a plume-driven convection cycle in the Hadean Earth. Earth Planet. Sci. Lett. 397, 111–120. doi:10.1016/j.epsl.2014.04.028

Nebel, O., Sossi, P.A., Benard, A., Wille, M., Vroon, P.Z., Arculus, R.J., 2015. Redox variability and controls in subduction zones from an iron-isotope perspective. Earth Planet. Sci. Lett. 432, 142–151.

Niu, F., Solomon, S.C., Silver, P.G., Suetsugu, D., Inoue, H., 2002. Mantle transition-zone structure beneath the South Pacific Superswell and evidence for a mantle plume underlying the Society hotspot. Earth Planet. Sci. Lett. 198, 371–380.

O'Connor, J.M., Jokat, W., 2015. Tracking the Tristan-Gough mantle plume using discrete chains of intraplate volcanic centers buried in the Walvis Ridge. Geology 43, 715–718. doi:10.1130/G36767.1

Panning, M., Romanowicz, B., 2006. A three-dimensional radially anisotropic model of shear velocity in the whole mantle. Geophys. J. Int. 167, 361–379.

Panter, K.S., 2006. The Origin of HIMU in the SW Pacific: Evidence from Intraplate Volcanism in Southern New Zealand and Subantarctic Islands. J. Petrol. 47, 1673–1704. doi:10.1093/petrology/egl024

Parai, R., Mukhopadhyay, S., Lassiter, J.C., 2009. New constraints on the HIMU mantle from neon and helium isotopic compositions of basalts from the Cook–Austral Islands. Earth Planet. Sci. Lett. 277, 253–261. doi:10.1016/j.epsl.2008.10.014

Payne, J.A., Jackson, M.G., Hall, P.S., 2013. Parallel volcano trends and geochemical asymmetry of the Society Islands hotspot track. Geology 41, 19–22. doi:10.1130/G33273.1

Polyakov, V.B., Mineev, S.D., 2000. The use of Mössbauer spectroscopy in stable isotope geochemistry. Geochim. Cosmochim. Acta 64, 849–865. doi:10.1016/S0016-7037(99)00329-4

Resing, J.A., Rubin, K.H., Embley, R.W., Lupton, J.E., Baker, E.T., Dziak, R.P., Baumberger, T., Lilley, M.D., Huber, J.A., Shank, T.M., Butterfield, D.A., Clague, D.A., Keller, N.S., Merle, S.G., Buck, N.J., Michael, P.J., Soule, A., Caress, D.W., Walker, S.L., Davis, R., Cowen, J.P., Reysenbach, A.-L., Thomas, H., 2011. Active submarine eruption of boninite in the northeastern Lau Basin. Nat. Geosci. 4, 799–806. doi:10.1038/ngeo1275

Salters, V.J.M., Mallick, S., Hart, S.R., Langmuir, C.E., Stracke, A., 2011. Domains of depleted mantle: New evidence from hafnium and neodymium isotopes. Geochemistry, Geophys. Geosystems 12. doi:10.1029/2011GC003617

Schauble, E.A., 2007. Role of nuclear volume fractionation in driving equilibrium stable isotope fractionation of mercury, thallium, and other very heavy elements. Geochim. Cosmochim. Acta 71, 2170–2189.

Schauble, E.A., Meheut, M., Hill, P.S., 2009. Combining Metal Stable Isotope Fractionation Theory with Experiments. Elements 5, 369–374. doi:10.2113/gselements.5.6.369

Schoenberg, R., Von Blanckenburg, F., 2005. An assessment of the accuracy of stable Fe isotope ratio measurements on samples with organic and inorganic matrices by high-resolution multicollector ICP-MS. Int. J. Mass Spectrom. 242, 257–272. doi:10.1016/j.ijms.2004.11.025

Schuessler, J.A., Schoenberg, R., Sigmarsson, O., 2009. Iron and lithium isotope systematics of the Hekla volcano, Iceland - Evidence for Fe isotope fractionation during magma differentiation. Chem. Geol. 258, 78–91.

Sharp, W.D., Clague, D.A., 2006. 50-Ma initiation of Hawaiian-Emperor Bend records major change in Pacific plate motion. Science. 313, 1281–1284.

Siebert, C., Nägler, T.F., Kramers, J.D., 2001. Determination of molybdenum isotope fractionation by double-spike multicollector inductively coupled plasma mass spectrometry. Geochemistry, Geophys. Geosystems 2.

Sio, C.K.I., Dauphas, N., Teng, F.-Z., Chaussidon, M., Helz, R.T., Roskosz, M., 2013. Discerning crystal growth from diffusion profiles in zoned olivine by in situ Mg–Fe isotopic analyses. Geochim. Cosmochim. Acta 123, 302–321. doi:10.1016/j.gca.2013.06.008

Sossi, P.A., Foden, J.D., Halverson, G.P., 2012. Redox-controlled iron isotope fractionation during magmatic differentiation: an example from the Red Hill intrusion, S. Tasmania. Contrib. to Mineral. Petrol. 164, 757–772.

Sossi, P.A., Nebel, O., Foden, J.D., 2016. Iron isotope systematics in planetary reservoirs. Earth Planet. Sci. Lett. 452, 295–308.

Staudigel, H., Park, K.-H., Pringle, M.S., Rubenstone, J.L., Smith, W.H.F., Zindler, A., 1991. The longevity of the South Pacific isotopic and thermal anomaly. Earth Planet. Sci. Lett. 102, 24–44.

Steinberger, B., Sutherland, R., Connell, R.J.O., 2004. Prediction of Emperor-Hawaii seamount locations from a revised model of global plate motion and mantle flow. Nature 430, 167–173.

Su, B.-X., Teng, F.-Z., Hu, Y., Shi, R.-D., Zhou, M.-F., Zhu, B., Liu, F., Gong, X.-H., Huang, Q.-S., Xiao, Y., Chen, C., He, Y.-S., 2015. Iron and magnesium isotope fractionation in oceanic lithosphere and sub-arc mantle: Perspectives from ophiolites. Earth Planet. Sci. Lett. 430, 523–532.

Tarduno, J.A., 2007. On the motion of Hawaii and other mantle plumes. Chem. Geol. 241, 234–247. doi:10.1016/j.chemgeo.2007.01.021

Tarduno, J.A., Bunge, H.-P., Sleep, N., Hansen, U., 2009. The bent Hawaiian-Emperor hotspot track: inheriting the mantle wind. Science. 324, 50–3. doi:10.1126/science.1161256

Tarduno, J.A., Duncan, R.A., Scholl, D.W., Cottrell, R.D., Steinberger, B., Thordarson, T., Kerr, B.C., Neal, C.R., Frey, F.A., Torii, M., Carvallo, C., 2003. The Emperor Seamounts: Southward Motion of the Hawaiian Hotspot Plume in Earth's Mantle. Science. 301, 1064–1069.

Tatsumoto, M., 1978. Isotopic composition of lead in oceanic basalt and its implication to mantle evolution. Earth Planet. Sci. Lett. 38, 63–87.

Taylor, B., 2006. The single largest oceanic plateau: Ontong Java–Manihiki–Hikurangi. Earth Planet. Sci. Lett. 241, 372–380. doi:10.1016/j.epsl.2005.11.049

Taylor, B., Zellmer, K., Martinez, F., Goodliffe, A., 1996. Sea-floor spreading in the Lau back-arc basin. Earth Planet. Sci. Lett. 144, 35–40.

Taylor, S.R., McLennan, S.M., 1985. The continental crust: Its composition and evolution. Blackwell Scientific Pub., Palo Alto, CA.

Teng, F.-Z., Dauphas, N., Helz, R.T., 2008. Iron isotope fractionation during magmatic differentiation in Kilauea Iki lava lake. Science. 320, 1620–2. doi:10.1126/science.1157166

Teng, F.-Z., Dauphas, N., Helz, R.T., Gao, S., Huang, S., 2011. Diffusion-driven magnesium and iron isotope fractionation in Hawaiian olivine. Earth Planet. Sci. Lett. 308, 317–324. doi:10.1016/j.epsl.2011.06.003

Teng, F.-Z., Dauphas, N., Huang, S., Marty, B., 2013. Iron isotopic systematics of oceanic basalts. Geochim. Cosmochim. Acta 107, 12–26. doi:10.1016/j.gca.2012.12.027

To, A., Fukao, Y., Tsuboi, S., 2011. Evidence for a thick and localized ultra low shear velocity zone at the base of the mantle beneath the central Pacific. Phys. Earth Planet. Inter. 184, 119–133. doi:10.1016/j.pepi.2010.10.015

Torsvik, T.H., Smethurst, M. a., Burke, K., Steinberger, B., 2006. Large igneous provinces generated from the margins of the large low-velocity provinces in the deep mantle. Geophys. J. Int. 167, 1447–1460. doi:10.1111/j.1365-246X.2006.03158.x

Weaver, B.L., 1991. The origin of ocean island basalt end-member compositions: trace element and isotopic constraints. Earth Planet. Sci. Lett. 104, 381–397.

Weis, D., Garcia, M.O., Rhodes, J.M., Jellinek, M., Scoates, J.S., 2011. Role of the deep mantle in generating the compositional asymmetry of the Hawaiian mantle plume. Nat. Geosci. 4, 831–838. doi:10.1038/NGEO1328

Wessel, P., Kroenke, L.W., 2008. Pacific absolute plate motion since 145 Ma: An assessment of the fixed hot spot hypothesis. J. Geophys. Res. 113, B06101. doi:10.1029/2007JB005499

Weyer, S., Ionov, D. a., 2007. Partial melting and melt percolation in the mantle: The message from Fe isotopes. Earth Planet. Sci. Lett. 259, 119–133. doi:10.1016/j.epsl.2007.04.033

Weyer, S., Schwieters, J.B., 2003. High precision Fe isotope measurements with high mass resolution MC-ICPMS. Int. J. Mass Spectrom. 226, 355–368. doi:10.1016/S1387-3806(03)00078-2

White, W.M., 2010. Oceanic Island Basalts and Mantle Plumes: The Geochemical Perspective. Annu. Rev. Earth Planet. Sci. 38, 133–160. doi:10.1146/annurev-earth-040809-152450

White, W.M., 2015. Isotopes, DUPAL, LLSVPs, and Anekantavada. Chem. Geol.

Williams, H.M., McCammon, C.A., Peslier, A.H., Halliday, A.N., Teutsch, N., Levasseur, S., Burg, J.-P., 2004. Iron isotope fractionation and the oxygen fugacity of the mantle. Science. 304, 1656–1659. doi:10.1126/science.1095679

Williams, H.M., Peslier, A.H., McCammon, C.A., Halliday, A.N., Levasseur, S., Teutsch, N., Burg, J.-P., 2005. Systematic iron isotope variations in mantle rocks and minerals: The effects of partial melting and oxygen fugacity. Earth Planet. Sci. Lett. 235, 435–452. doi:10.1016/j.epsl.2005.04.020

Williams, H.M., Wood, B.J., Wade, J., Frost, D.J., Tuff, J., 2012. Isotopic evidence for internal oxidation of the Earth's mantle during accretion. Earth Planet. Sci. Lett. 321–322, 54–63. doi:10.1016/j.epsl.2011.12.030

Wilson, J.T., 1963. A possible origin of the Hawaiian Islands. Can. J. Phys. 41, 863–870.

Wilson, J.T., 1965. Convection current and continental drift: Evidence from ocean islands suggesting movement in the Earth. R. Soc. London, Philos. Trans. Ser. A Math. Phys. Sci. 258, 145–167.

Workman, R.K., Hart, S.R., 2005. Major and Trace Element Composition of the Depleted MORB Mantle (DMM). Earth Planet. Sci. Lett.

Workman, R.K., Hart, S.R., Jackson, M.G., Regelous, M., Farley, K.A., Blusztajn, J., Kurz, M., Staudigel, H., 2004. Recycled metasomatized lithosphere as the origin of the Enriched Mantle II (EM2) end-member: Evidence from the Samoan Volcanic Chain. Geochemistry, Geophys. Geosystems 5. doi:10.1029/2003GC000623

Wörner, G., Zindler, A., Staudigel, H., Schmincke, H.-U., 1986. Sr, Nd, and Pb isotope geochemistry of Tertiary and Quaternary alkaline volcanics from West Germany. Earth Planet. Sci. Lett. 79, 107–119.

Xhu, X.K., Guo, Y., Williams, R.J.P., O'Nions, R.K., Matthews, A., Belshaw, N.S., Canters, G.W., de Waal, E.C., Weser, U., Burgess, B.K., Salvato, B., 2002. Mass fractionation processes of transition metal isotopes. Earth Planet. Sci. Lett. 200, 47–62.

Zambardi, T., Lundstrom, C.C., Li, X., McMurry, M., 2014. Fe and Si isotope variations at Cedar Butte volcano; insight into magmatic differentiation. Earth Planet. Sci. Lett. 405, 169–179.

Zindler, A., Hart, S.R., 1986. Chemical Geodynamics. Annu. Rev. Earth Planet. Sci. 14, 493–571.

CHAPTER 2: THE IMPORTANCE OF A NI CORRECTION WITH ION COUNTER IN THE DOUBLE SPIKE ANALYSIS OF FE ISOTOPE COMPOSITIONS USING A $^{57}FE/^{58}FE$ DOUBLE SPIKE

Finlayson, V.A.[1], Konter, J.G.[1], and Ma, L.[2]

[1]Dept. Geology and Geophysics, School of Ocean and Earth Science and Technology, University of Hawaii at Manoa, 1680 East-West Rd, Honolulu, HI 96822, USA

[2]Dept. Geological Sciences, University of Texas at El Paso, El Paso, TX 79968, USA

Published in Geochemistry, Geophysics, Geosystems vol. 16 (2015)

Abstract

We present a new method capable of measuring iron isotope ratios of igneous materials to high precision by multicollector inductively coupled plasma mass spectrometry (MC-ICP-MS) using a ^{57}Fe-^{58}Fe double spike. After sample purification, near-baseline signal levels of nickel are still present in the sample solution, acting as an isobaric interference on 58 amu. To correct for the interference, the minor ^{60}Ni isotope is monitored and used to subtract a proportional ^{58}Ni signal from the total 58 amu beam. The ^{60}Ni signal is difficult to precisely measure on the Faraday detector due to Johnson noise occurring at similar magnitude. This noise-dominated signal is subtracted from the total 58 amu beam, and its error amplified during the double spike correction. Placing the ^{60}Ni beam on an ion counter produces a more precise measurement, resulting in a near-threefold improvement in $\delta^{56}Fe$ reproducibility, from ±0.145‰ when measured on Faraday to 0.052‰. Faraday detectors quantify the ^{60}Ni signal poorly, and fail to discern the transient $^{20}Ne^{40}Ar$ interference visible on the ion counter, which is likely responsible for poor reproducibility. Another consideration is instrumental stability (defined herein as drift in peak center mass), which affects high resolution analyses. Analyses experiencing large drift relative to bracketing standards often yield non-replicating data. Based on this, we present a quantitative outlier detection method capable of detecting drift-affected data. After outlier rejection, long-term precision on individual runs of our secondary standard improves to ±0.046‰. Averaging 3-4 analyses further improves precision to 0.019‰, allowing distinction between ultramafic minerals.

2.1. Introduction

Iron isotope compositions have recently become more commonplace for tracking a variety of geological, biological, and environmental processes. While iron isotopic ratios tend to vary across fairly large ranges in low-temperature and biological systems, only small variations are observed at high temperatures (e.g., Arnold et al., 2004; Beard and Johnson, 1999; Kehm et al., 2003; Teng et al., 2013, 2008; Williams et al., 2006). Such small signals are now resolvable following a number of improvements in the analytical procedures involved. Particularly, the use of multi-collector inductively coupled plasma mass spectrometry (MC-ICP-MS) for iron isotopic ratios has significantly improved long-term precision (Dauphas and Rouxel, 2006).

While more precise than TIMS, using MC-ICP-MS to measure iron isotopic ratios also increases mass fractionation (Albarède et al., 2004). On an MC-ICP-MS, mass fractionation can be corrected for with sample-standard bracketing or doping with an element of similar mass, or with an isotopic double spike (Albarède and Beard, 2004; Beard and Johnson, 1999; Dideriksen et al., 2006; Rudge et al., 2009; Siebert et al., 2001).

At present, the highest precision for iron isotopic ratios are reported by Dauphas et al. (2009a) and Millet et al. (2012), who report precisions of ±0.02 – 0.03‰ (2σ) and ±0.02‰ (2σ), respectively. Dauphas et al. (2009a) obtain 5-9 analyses per sample normalized by standard-sample bracketing replicated (n=23) analyses of unspiked BHVO-1. Millet et al. (2012) report a 2σ reproducibility of ±0.02 ‰ over 51 replicate analyses of double spiked IRMM-014 (without correction for the isobaric ^{58}Ni interference, while recommending a 50% longer analytical time than we suggest, and specific instrumental

settings). Dideriksen et al. (2006) report reproducibility of ±0.05‰ (2σ) for a ^{58}Fe-^{54}Fe double spiked hematite standard.

In this study, we evaluate the importance of monitoring and correcting the nickel interference in double spiked compositions. By using an ion counter, it becomes possible to obtain high precision measurements of non-interfered ^{60}Ni and therefore correct a proportional amount of ^{58}Ni from the total 58 amu signal prior to implementing the double spike correction. The double spike correction uses the measured spike/sample mixture and the assumption of exponential mass dependent fractionation to derive the ^{56}Fe/^{54}Fe composition of the sample. Use of the ion counter instead of a Faraday detector to measure ^{60}Ni improves precision nearly threefold, from ±0.145‰ to 0.052‰. The relatively high uncertainty on Faraday-corrected analyses may stem from two possibilities: 1) Our choice of double spike composition with lower ^{58}Fe/^{57}Fe than the recommended composition by Rudge et al. (2009) exhibits increased sensitivity to Faraday-corrected Ni. 2) Incorrect ^{58}Ni signal subtraction from contribution to the ^{60}Ni signal of a transient ^{20}Ne^{40}Ar interference detectable by ion counter, but not by Faraday detector. If the interference is present and cannot be discerned from ^{60}Ni by Faraday, it is not possible to confirm that the interference is avoided during analysis and contribute to poor precision.

In addition, we present a statistical outlier detection method capable of identifying most measurements affected by machine instability. Using this method, we can improve our precision from 0.052‰ to a long-term, error-weighted precision of ±0.046‰. Double spiking and ion counter-based Ni correction reduces the amount of time required compared to multiple analyses of an unspiked sample (1 run of 60 ratios vs. 5-9 runs of at least 20 ratios), yet produces comparable precision to recent studies using unspiked

compositions (Craddock and Dauphas, 2010; Dauphas et al., 2009a; Schoenberg and Von Blanckenburg, 2005; Teng et al., 2013, 2008). Below, we provide details on our new analytical technique, and we present results for both extensive tests with standard materials and natural samples.

2.2. Analytical Methods

Measuring high-precision iron isotope ratios presents several analytical challenges that have been described by other authors (Albarède et al., 2004; Beard and Johnson, 1999; Dauphas et al., 2009a, 2004; Millet et al., 2012; Weyer and Schwieters, 2003). These issues include the ability to (partially) resolve iron from polyatomic argides, isobaric elemental interference correction, achieving precision high enough to distinguish variations in igneous samples, and understanding potential sources of error introduced during sample preparation and analysis.

We developed a new technique that manages these issues, and we describe it in detail below. In brief, measurements were performed on a Nu Plasma HR MC-ICP-MS at the University of Texas at El Paso (UTEP) with twelve Faraday detectors and three ion counters on the low mass side of the collector array. The instrument is used in 20V mode for masses 56 and 57 (detector array, see Table 2.1). The Nu Plasma HR at UTEP has been modified to continuously pump the pre-amplifier bin (~0.05 mbar) with a dedicated scroll pump (Varian IDP3), reducing baseline noise. We use a ^{57}Fe-^{58}Fe double spike for both standards and samples to correct for mass fractionation. Due to the collector configuration of the UTEP Nu Plasma HR, measurements are made using a 3-cycle program (1 cycle for Fe isotopes, 2 cycles for interference monitoring). We monitor for isobaric interferences from

^{54}Cr and ^{58}Ni, by monitoring ^{52}Cr on a Faraday and ^{60}Ni on an ion counter. To remove the ^{58}Ni interference from the baseline-corrected 58 amu beam, we calculate the ^{58}Ni signal, using the measured ^{58}Ni/^{60}Ni ratio obtained at the beginning of each analytical session and the ^{60}Ni signal measured each cycle (Equation 1):

$$^{58}Fe = {}^{58}\left(Fe+Ni\right)_m - {}^{60}Ni_m * \left(\frac{^{58}Ni}{^{60}Ni}\right)_m \quad \text{(Equation 1)}$$

^{54}Cr is calculated using the same approach as Equation 1, although an assumed fractionated ratio (^{54}Cr/^{52}Cr = 0.02920) is used in lieu of measuring a natural Cr solution.

Polyatomic interferences (^{40}Ar^{14}N$^+$ on ^{54}Fe$^+$, ^{40}Ar^{16}O$^+$ on ^{56}Fe$^+$, ^{40}Ar^{16}OH$^+$ and ^{40}Ar^{17}O on ^{57}Fe$^+$, and ^{40}Ar^{18}O$^+$ on ^{58}Fe$^+$) are avoided by using a desolvating nebulizer (DSN-100) to boost the Fe signal intensity, and with (pseudo-) high resolution to enable measurements on the non-interfered low-mass peak shoulder (achieving ~300ppm peak flat with a typical resolution of 5000-7000). Data reduction is performed partially offline, where instrument drift is evaluated using peak center mass drift, and blocks with large drift are rejected. Further instrumental settings are provided in Supplemental Table S.2.1.

2.3. Materials analyzed

2.3.1. Standards

For our primary standard, we used an IRMM-014-double spike mixture, and Fe isotope compositions are reported as δ^{56}Fe with respect to IRMM-014 DS as the bracketing standard. A secondary in-house standard (Alfa Aesar Specpure Fe; lot no. 14-19107H) was similarly spiked and also analyzed to assess precision. Double spiking of the standards was performed using gravimetric dilution to obtain standard-spike mixtures with a ^{57}Fe/^{58}Fe

lower than that recommended by Rudge et al. (2009), although still expected to produce a low error from double spike correction (Table 2.2). Determination of an optimal double spike composition is discussed further in Section 4.1. Standard-double spike mixtures were prepared in 0.05N HNO_3 and diluted to approximately 4 ppm stock solutions. Analyses were run with concentrations of approximately 2 ppm (15-18V on ^{56}Fe with a ~80μL/min uptake rate).

2.3.2. Natural materials

Samples used in this study are mineral separates obtained from mantle xenolith samples from Kilbourne Hole, (NM) USA and Savai'i, Samoa (Table 2.3). Mantle xenoliths from Kilbourne Hole are examples of sub-continental lithospheric mantle bearing MORB-like compositions (Takahashi et al., 1993), while the mantle xenoliths from Savai'i are more enriched and metasomatized samples from an oceanic hotspot setting (Hauri et al., 1993). Mineral types analyzed include olivine, orthopyroxene, and clinopyroxene. All three phases were recovered from Kilbourne Hole sample peridotite KH-7, and clinopyroxene only from pyroxenites KH-26 and KH-60B (Perkins and Anthony, 2011; Anthony, unpublished data). Olivine and orthopyroxene were recovered from a suite of five peridotite xenoliths from a cinder cone on the island of Savai'i (SAV09-15 samples; Konter et al., in prep). Crystals were selected for a combination of 1) large size where possible and 2) purity to ensure no isotopic contamination from other mineral phase(s) was present. Each sample represents a batch of five to ten crystals. Samples are digested in 4mL of a 3:1 mixture of concentrated HF (~24N) and concentrated HNO_3 (15.2-15.4M) for ~1 week at >80°C. Once dissolved, samples are dried down and subsequently redissolved for ~24 hours in ~2mL

concentrated HNO_3 to break down insoluble fluoride complexes. This step is repeated multiple times. The sample is then dried and ~2mL of 3-4N HCl is added to dissolve nitrate salts formed during the HNO_3 step. Once the sample is completely dissolved, it is dried down a final time, then dissolved in 0.5mL 9N HCl + 0.001% H_2O_2. Sample Fe separation followed a technique modified from Kehm et al. (2003). The dissolved sample is loaded onto a 0.3mL AG1-X4 column and washed through with 6mL of 9N HCl + 0.001% H_2O_2. Fe is then eluted in 1.5mL of 0.1N HCl. Sample yields were quantitative, assuring no Fe fractionation occurred during separation (Anbar et al., 2000; Kehm et al., 2003). Procedural blanks were <10ng, which, at <0.001% of total sample Fe, do not measurably influence sample δ^{56}Fe. After separation, we tested aliquots of each sample with the Nu Plasma HR to verify concentrations in order to obtain an optimal double spike-sample solution, similar to the spiking method described in Millet et al. (2012). After spiking, each sample was dried down to remove HCl from the double spike solution and redissolved in 0.05N HNO_3. Multiple digestions of single crystals and batch digestions were used to determine variability of the isotopic compositions of individual crystals versus batches of crystals. Additionally, we used USGS powdered standard BCR-2 (recommended δ^{56}Fe is 0.091‰, similar to our value of 0.116‰; Craddock and Dauphas, 2010) to verify that the Fe separation chemistry did not isotopically fractionate samples or introduce contamination.

2.4. Technique development and results

2.4.1. Mass fractionation correction by double spike and Ni interference

Adding an amount of calibrated double spike to a sample solution is a common practice to correct an unknown (sample) iron isotopic composition for mass-dependent

fractionation during analysis. Albarède and Beard (2004) suggest a Newton-Raphson iterative solution for mass-dependent fractionation following the exponential law to solve for the corrected $^{56}Fe/^{54}Fe$ ratio. Siebert et al. (2001) employ an iterative solution and assume that all mass-dependent fractionation (natural and instrumental) follow the exponential law. The correction then applies a linear approximation to estimate the predicted exponential fractionation behavior. For simplicity, we use the Siebert method to reduce our data. In addition, we employ time-corrected standard-sample bracketing with IRMM-014 DS to eliminate variation from instrumental drift.

We employ a ^{57}Fe-^{58}Fe double spike (Table 2.2) for both standard and sample analysis because it allows real-time monitoring of the fractionation factor during a measurement block, instead of relying solely on the bracketing standards for fractionation correction. This double spike composition differs from the optimal composition calculated by Rudge et al. (2009), however the predicted error for double spike corrections stays low across a large range of double spike compositions (~15%-85% ^{57}Fe in a ^{57}Fe-^{58}Fe double spike).

Using the minor ^{57}Fe and ^{58}Fe isotopes in a double spike should lead to small analytical errors (e.g., Rudge et al., 2009), however the ^{58}Fe in the double spike is sensitive to interfering Ni signals. The mass 58 signal consists of both ^{58}Fe and ^{58}Ni. This Ni interference can be reduced by wet separation and purification chemistry; however small amounts may be present from the desolvating membrane, the cones and the blank level in the diluting acid. This is not a factor in fractionation correction of unspiked iron samples that often only include $^{56}Fe/^{54}Fe$ and $^{57}Fe/^{54}Fe$, although (Schoenberg and Von Blanckenburg, 2005) recommended that sample measurements with levels of ^{58}Ni in excess

of 1% of the total signal are rejected. Any ^{57}Fe-^{58}Fe-based double spike correction is sensitive to a small contribution from ^{58}Ni; analytical uncertainty in its correction is amplified throughout the double spike reduction and exerts significant influence on the double spike-corrected ^{56}Fe/^{54}Fe ratio. Thus, with spiked iron compositions, monitoring and correction for nickel in a sample is an important step in the analysis.

Reanalysis of our initial data, including outliers, showed that ignoring the nickel correction had a substantial effect on the corrected ^{56}Fe/^{54}Fe ratio (Table 2.4). This is caused by the poor precision of the beam monitored for ^{58}Ni correction (^{60}Ni) at its usual sub-mV intensity, transient presence of the small ^{20}Ne^{40}Ar interference, and the amplification of the error (to the more abundant ^{58}Ni) propagated through the double spike reduction. More specifically, since the Faraday noise level is approximately 20μV for a 10 second integration (Nu Plasma specifications), a Faraday-based correction for ^{58}Ni is limited to about two significant digits. This error is then propagated, reducing overall precision. Modeling the double spike correction while ignoring the Ni correction results in an average (non-weighted, non-outlier rejected) δ^{56}Fe of our in-house standard (Alfa Fe DS) of 0.392 ±0.384‰, and 0.620 ±0.590‰ for olivine crystals from Kilbourne Hole peridotites (full results found in Table 2.4). These values compare to Ni-corrected values of 0.473 ±0.046‰ and 0.034 ±0.056‰ respectively, and these extreme differences result from a combination of the propagated error of the ^{58}Ni measurement and slight measurement imperfections on mass 54 (seen in raw ^{54}Fe/^{56}Fe). This is likely caused by a peak coincidence setting that is not centered on the flat part of the Fe-only peak-shoulder. The combination of non-corrected Ni and displacements from the true fractionation curve passing through the true composition controlled by the finite amount of error on analyses

and slight daily variations in instrumental behavior cause the double spike geometry in three isotope space to define a different fractionation trend for the analyzed spike-standard mixture. This trend then forces a different best-fit mixing line between the true double spike composition and the fractionation trend through natural Fe. In other words, the effect of ignoring the Ni interference is an amplification of the slight inaccuracies on the measured Fe ratios, which presents as a less reproducible sample or standard $^{56}Fe/^{54}Fe$ estimate that is not observed when Ni is accounted for. The remaining samples behave in a similar fashion without the Ni correction. Turning off only the Cr correction during reanalysis results in a minimal change for all standards and samples, within error of the fully corrected averages. This is due to the low interference levels, and the error demagnification from monitoring the more abundant ^{52}Cr beam to remove ^{54}Cr from the 54 amu signal.

In order to isolate the Ni interference as the primary cause of large analytical uncertainty, we compared Ni measurements collected by Faraday and measurements collected by ion counter. First we established the reproducibility of the Fe standard IRMM-014 DS with six runs in a single analytical session (Supplemental Table S.2.2), using instrumental conditions similar to those used for the whole dataset obtained in this study. The session $\delta^{56}Fe$ of 0.000‰ ±0.145‰ was calculated as offset of individual IRMM-014 DS analyses from the session average. Next, we tested the response of the measurements to small differences in Ni contribution.

The response of the method was tested with small ^{58}Ni and ^{60}Ni signals on the Faraday detectors. Using dilutions of an in-house Ni solution of known concentration, we measured signal levels for Ni over several orders of magnitude, including the levels

normally found in our samples (usually near the detection limits of the Faraday detectors). Our results show the expected linear correlation of signal to concentration above 0.1 ppb (1 mV) Ni on both ^{58}Ni and ^{60}Ni (Figure 2.1, Supplemental Table S.2.3). Below 0.1 ppb concentration (1 mV), the relationship is no longer linear with higher than expected signal levels recorded for a particular concentration on both isotopes. As a result, both the ^{60}Ni and ^{58}Ni intensity vs. Ni concentration correlations break down between the detector noise level (approximately 20μV; Johnson noise) and ~1 mV of ^{60}Ni signal. This is likely related to a change in analyte, not a detector effect (the Ni isotope intensities are different at the breakdown level of the Faraday measurements). The likeliest cause lies in either remaining Ni washing out of the DSN-100 membrane, and/or potentially a small blank in the diluting acid. However, this signal level is representative for sample runs and limits the precision of the Ni ratio to roughly two significant digits, with the same ratio across the measured range. Improvement of this measurement can be achieved using an ion counter, and is particularly important if it results from washout of the introduction system.

To avoid Faraday noise propagation, we place ^{60}Ni on an ion counter, with mass 58 in one of the Faraday detectors (Table 2.1). Prior to analyses, we define a ^{60}Ni/^{58}Ni ratio that includes mass fractionation and ion counter gain by measuring an in-house nickel solution assumed to represent a natural ratio at the attainable precision. It should be noted that calibration of the ion counter will affect the measured nickel ratio, and there may be a long-term drift in the calibration that may be detector-dependent. However, in our case drift in the measured ^{58}Ni/^{60}Ni is not resolvable above the error during daylong tests, so we measured the Ni standard only once at the beginning of each analytical session.

^{54}Cr is similarly corrected via monitoring ^{52}Cr. However, Cr has little effect on the double spike correction and precise measurement of ^{52}Cr by ion counter is not required due to the demagnification of error when monitoring ^{52}Cr for a Cr correction on ^{54}Fe. Modeling of collected data using an artificially increased Cr signal (signal multiplied 2x, 3x, 5x, and 10x) suggests that the corrected ^{56}Fe/^{54}Fe ratio increases at a rate of approximately 0.03-0.05‰ per mV ^{52}Cr (Figure 2.2). When the Cr signal is increased to 5-7 times that of a typical measurement (^{52}Cr = 0.2-0.4 mV), the Δ^{56}Fe ratio ($\delta^{56}Fe_{reanalyzed} - \delta^{56}Fe_{original}$) of most samples and standards increases beyond the ±0.046‰ reproducibility reported for Alfa Fe DS (Supplemental Table S.2.4). Sub-mV variations in the ^{52}Cr signal from processed sample to non-processed standard (such as IRMM-014 DS) will minimally affect the offset between the two; variations are well within error of the best precision currently reported in literature.

2.4.2. Statistical treatment of instrumental drift

The Nu Plasma analysis program uses a peak centering routine prior to measurement of each block of data to determine the optimal magnet setting for a measurement. For Fe analyses, the optimal measurement setting occurs in the middle of the uninterfered Fe peak flat, far enough to avoid contribution from any argide abundance sensitivity while not measuring on the sloped part of the uninterfered Fe beam where signal begins to decrease. This placement is determined by the user setting the “delta M” (M/ΔM) value in the Nu Plasma software. Instrumental drift and instabilities can affect the position of isotopic peaks on a mass range. Typically, this drift is small or negligible (averaging 5 ppm for the Fe cycle, 5 ppm for the Ni cycle, and 2 ppm for the Cr cycle)

between blocks, although occasional periods of relatively large drift (>10 ppm) do occur. While the drift is not enough to affect an interference-free measurement at low resolution, it presents a challenge to iron isotopic measurements because the narrow range of uninterfered Fe peak flat does not accommodate substantial or abrupt instrumental drift. Hence, we use peak center mass as a proxy for instrumental stability.

Acquiring peak centers before each measurement block captures the bulk variations than can occur between measurements, although tracking drift during a measurement is not possible. Similar to the bracketing formula used to calculate δ^{56}Fe values, we calculated ppm-level changes in peak center masses (here referred to as η) of secondary standards and samples as a function of the peak center masses obtained for each of the three cycles of bracketing IRMM-014 DS measurements (Equation 2). *P* is peak center mass of a standard or sample as specified in subscripts. *IRMM-014 DS(1)* and *IRMM-014 DS(2)* are subscripts denoting the two standard measurements bracketing a sample measurement. Since several sample measurements were made between bracketing standards, we assumed a linear approximation of drift between standards and weighted the standard measurements accordingly (*X* and *Y*).

$$\eta = 10^6 * \left(\frac{P_{sample}}{\left(\frac{X * P_{IRMM-014DS(1)} + Y * P_{IRMM-014DS(2)}}{X+Y} \right)} \right) \quad \text{(Equation 2)}$$

Iron, nickel, and chromium peak center offsets from first and second measurement blocks of all secondary standards and samples are used in this analysis (Supplemental Table S.2.5). Plotting η_{Fe}, η_{Ni}, and η_{Cr} of secondary standards and samples shows that most

of the data clusters near the origin, indicating minimal peak center drift relative to bracketing standards (Figure 2.3). Extreme η values plot dominantly above the center of the data, indicating drift typically occurred toward heavier mass during analysis. Samples with δ^{56}Fe values inconsistent with recommended values, or with the average for their mineral type in this study, often plot away from the center of the data, suggesting shifts in peak center mass are coupled to unexpected δ^{56}Fe. We interpret this behavior as a result of the measurement taking place off the measureable peak flat, either at a mass high enough to measure iron plus a small amount of the interfering tail, or low enough that some slope from the peak shoulders slightly lowers measured intensity on one (or more) of the masses.

To determine which points may be considered outliers, we computed the minimum covariance determinant-based (MCD) centroid and covariance matrix of the bracketed iron, nickel, and chromium peak center masses. MCD is preferable to classical covariance in this application because unlike classical covariance, it is not significantly influenced by outlying data. The MCD of the data was computed in MATLAB using an implementation of the FAST-MCD algorithm included in the LIBRA robust analysis library (Rousseeuw and Driessen, 1999; Verboven and Hubert, 2005). The centroid and covariance matrix can then be used to calculate the distance of each point from the average peak center masses. This distance then identifies potentially-outlying data. Since the data cloud does not vary uniformly along all three axes, geometric distance between individual points and the centroid is not a reliable indicator of outlying data. A dimensionless number, Mahalanobis distance, indicates how far a point in a multivariate dataset (in this case, Fe-Ni-Cr space) lies from the centroid while scaling that distance by normalizing the residuals to the variances (from

the covariance matrix). This provides a method in which to identify possible outliers that cannot be easily determined using geometric distance when each axis displays a different variance. Squared Mahalanobis distances (Supplemental Table S.2.5) were calculated (Mahalanobis, 1936) in R using the same centroid and covariance data determined in MATLAB.

Outlier identification is aided by knowing how far each point lies from the centroid and best constrained with a tolerance ellipsoid representing a surface of constant Mahalanobis distance. The 1σ tolerance ellipse is empirically determined to correspond to a squared Mahalanobis distance (D^2) of approximately 4.3. With normally-distributed data, a comparison of a Mahalanobis distance cutoff to χ^2 distribution is recommended. However, in this case, the data is not normally distributed (Supplemental Figure S.2.2) and resulting cutoff value cannot be estimated with a χ^2 comparison; instead, it must be determined by comparing the radius of the 1σ ellipsoid to Mahalanobis values of the dataset. Tests with different tolerance levels (i.e. 2σ) eliminated extreme outliers, but some questionable data remained and little to no improvement of in-house double spiked standard Alfa Fe DS occurred. Similarly, lower tolerance levels rejected acceptable data, and the reproducibility of Alfa Fe DS decreased (Figure 2.4). Any data points with a D^2 greater than 4.3 are identified as outliers and rejected from the data set, with the exception of points outlying only along the chromium axis.

It should be noted that analyses with outlying chromium peak center masses, but within tolerance for iron and nickel, are not rejected because the very low levels of Cr present in the sample do not significantly affect analyses. Hence, outliers in Fe-Ni two-dimensional space are considered. As an example, one outlying USGS rock standard BCR-2

measurement yielded a δ^{56}Fe of 0.022‰ while the recommended value is 0.091‰ (Craddock and Dauphas, 2010). Both blocks for that analysis fall outside of the 1σ ellipsoid. Similarly, this technique identified one block that yielded a high δ^{56}Fe (0.078‰) for an olivine separate from a peridotite from the island of Savai'i (Samoan Islands; SAV09-15.4; Figure 2.3). Removing this block and the other outliers identified in Fe-Ni space improves precision of the δ^{56}Fe data.

The identified Mahalanobis distance and tolerance ellipse can be used to calculate a maximum shift in peak center, and by extension a gauge of the available true peak flat. For the Fe and Ni cycles, this amounts to approximately 60 and 80 ppm of drift respectively (Figure 2.3). Compared to peak-scan estimates of peak flat of ~100-300 ppm (Δm/m; Weyer and Schwieters, 2003); this study), this suggests instrumental drift during a single analysis needs to be limited half or less of the observed peak-scan width estimate to achieve optimal δ^{56}Fe measurements. Any larger amount of drift significantly increases the probability that the measurement includes some amount of an interference or moves off the peak flat and is measuring the low-mass, sloped peak sides. Our suggested 60 ppm drift limit for the Fe cycle agrees with the 60 ppm usable peak flat estimate by Millet et al. (2012), beyond which they report significant reduction in reproducibility.

We suggest that applying standard-sample bracketing to peak center masses and comparing to a 1σ (68%) covariance ellipse will reliably identify data affected by instrumental drift resulting in measurement occurring outside of the ideal peak flat range. Removing outliers identified by this method improves precision of double spiked Alfa Fe DS measurements from δ^{56}Fe = 0.471 ±0.051‰ (2σ, n=19) to δ^{56}Fe = 0.473 ±0.046‰ (2σ, n=17). The averages reported in this study are error-weighted unless otherwise noted.

Similar improvements in precision following outlier rejection occur for the mineral phases with the exception of some Savai'i mineral separates (Table 2.5). However, for natural materials, different values might be expected for distinct dissolutions due to sample heterogeneity or alteration.

2.4.3. Precision and data reduction techniques from other studies

2.4.3.1. Average calculations

In order to compare the precision of our approach to some of the highest reported precisions in the literature, averaging is required. For example, Dauphas et al. (2009a) obtain 5-9 sample runs to average as one δ^{56}Fe, and multiple sets of analyses are used to determine an external precision of 0.02-0.03‰ (2σ). Grouping in-house standard Alfa Fe DS analyses (prior to outlier rejection) in this manner (n=5, n=5, n=5, n=4) and calculating a long-term average of these groups suggests an average non-weighted δ^{56}Fe of 0.471 ±0.029‰ (2σ).

Excluding outlying data, Alfa Fe DS δ^{56}Fe becomes 0.471 ±0.027‰ (n=5, n=4, n=4, n=4). Additional permutations yielded δ^{56}Fe = 0.474 ±0.019‰ (n=4, n=4, n=3, n=3, n=3) and 0.475 ±0.031‰ (n=3, n=2, n=2, n=2, n=2, n=2, n=2, n=2). Given the external precision is effectively the same for averages of 2 through 5 runs, our double spike technique requires fewer repeat analyses of a sample to produce precision similar to the standard-sample bracketing techniques described by (Craddock and Dauphas, 2010; Dauphas et al., 2009a; Millet et al., 2012).

2.4.3.2. Standard-sample bracketing comparison

In order to compare our technique to a standard-sample bracketing approach directly, we also calculate the error from bracketing our collected data without applying the double spike correction routine. This requires knowledge of the true exact composition of the standard-double spike mixture, which we have calculated as the average of all our double spiked IRMM analyses (the double spiked IRMM-014 solution was prepared as one large batch). We then used the measured data for the double spiked IRMM-014 runs to bracket the fractionation on our Alfa Fe DS standard (also prepared as one batch). This results in an average δ^{56}Fe of 0.056 ±0.054‰. Data are reported in Supplemental Table S.2.6. With no double spike correction, the measured ratios represent a mixture of the standard and double spike. The spike:standard ratios of Alfa Fe DS and IRMM-014 DS differ slightly, which changes the expected δ^{56}Fe offset between the two standards. However, the reproducibility should still be representative of the bracketing method. With outlier rejection, this improves approximately 6% to a δ^{56}Fe of 0.059 ± 0.051‰. Compared to standard-sample bracketing without the double spike correction, precision is improved 10% with double spike correction both before and after outlier rejection.

2.5. Results for natural materials

Results are reported in Table 2.6. We analyzed our in-house standard (Alfa Fe DS) 19 times in addition to 24 natural sample analyses and 2 analyses of USGS reference standard BCR-2 before outlier rejection. Two Alfa Fe DS measurements and single blocks from two other measurements were rejected by the outlier analysis and are not considered in the long-term average (n=17). These repeat analyses suggest a 2σ long-term error of

±0.046‰ in δ^{56}Fe (equivalent to ±0.019‰ 2σ if each analysis is calculated as an average of ~3-4 analyses). These values should be considered the limit of attainable precision for the samples reported below.

2.5.1. Mineral Analyses

Results from the mineral samples after double spike correction and outlier rejection are found in Table 2.6. The internal error (1 standard error, or 1SE) on the corrected δ^{56}Fe of all standards and samples averaged ±0.013‰. Kilbourne Hole olivines yielded an average δ^{56}Fe of 0.028 ±0.047‰ (2σ, n=6) and orthopyroxenes had an average δ^{56}Fe of 0.023 ±0.055‰ (2σ, n=2). The clinopyroxenes from pyroxenites KH-26 (n=1) and KH-60B (n=1) yielded δ^{56}Fe values of 0.115±0.019‰ (1SE) and 0.158±0.006‰ (1SE), respectively. Internal precision in standard error is reported since only one analysis of each sample is available except where a duplicate measurement of the same sample preparation is listed. Savai'i xenolith olivines from multiple different hand pieces average a δ^{56}Fe of 0.033 ±0.072‰ (2σ, n=4), and the orthopyroxenes average a δ^{56}Fe of 0.053 ±0.044‰ (n=2). The larger uncertainty of these averages results from the inclusion of multiple xenolith hand pieces in the average. The average olivine and orthopyroxene δ^{56}Fe values for Kilbourne Hole and Savai'i are within error of each other (Table 2.6, Figure 2.6) and not isotopically distinguishable without a far larger number of analyses available for averaging, or further improvement in analytical precision. However, the clinopyroxenes from the pyroxenites are significantly higher in δ^{56}Fe, and particularly δ^{56}Fe values for KH-60B are statistically different from the olivines and orthopyroxenes of peridotite KH-7.

2.6. Caveats and further potential

2.6.1. Possible sources of remaining error

A remaining challenge is to identify the source or sources of error remaining in the measurement method. Instrumental instability that may be insignificant in standard resolution has a measurable effect on data obtained in (pseudo) high resolution mode, given the smaller amount of peak flat available on the low-mass shoulders of the interfered peaks.

Nickel cycle peak centering takes place at the low-mass end of the collector array where beam distortion increases relative to the center of the array. Part of this distortion comes from the unusual mass separation (0.4 amu instead of 0.25 or 0.33) and related high voltages on the quadrupole lenses required to collect mass 60 in IC0 and mass 58 in L5 (Table 2.1). As the nickel-based isobaric correction has a significant influence on the corrected $^{56}Fe/^{54}Fe$ ratio, the greater variation in the nickel cycle peak center mass is likely the dominant cause of remaining variations in the $\delta^{56}Fe$. Unfortunately, the architecture of the collector array prevents a more optimal setup; a high-mass ion counter would be required to place the 58 amu beam into a more central Faraday detector and therefore less distorted beam.

2.6.2. Potential for iron isotopic signatures of mineral phases and applications to understanding mantle processes

Clinopyroxenes from Kilbourne Hole pyroxenite xenoliths yield $\delta^{56}Fe$ values ≥0.1‰ higher than any of the phases from the peridotites (Figure 2.6). These results are very similar to elevated values in pyroxenites reported by Williams et al. (2005) and Williams

and Bizimis (2014). Williams and Bizimis (2014) propose that their elevated $\delta^{57}Fe$ values in pyroxenites relative to peridotites are related to fractional crystallization of pyroxene from a melt. This would be the case if these pyroxenites represent veins of wall-cumulates or replacive pyroxenites from melts interacting with peridotite (e.g., Bodinier and Godard, 2003). In either of these cases the pyroxenites would likely have $\delta^{56}Fe$ values related to melt, which is thought to have higher values than peridotite (Dauphas et al., 2009b; Williams et al., 2004). Our pyroxenite data follows this relationship.

The values we report for mineral phases in peridotite overlap with the values of Williams and Bizimis (2014), but are slightly elevated compared to an estimate for primitive mantle ($\delta^{56}Fe$ ~0.02‰; Weyer and Ionov, 2007). Our samples from Kilbourne Hole are slightly above, but within error of this value, and we can therefore not distinguish their values from a relatively pristine mantle value. The values found in the Samoan xenoliths, in contrast, are nearly all above $\delta^{56}Fe$ ~0.02‰ ranging up to values of ~0.07‰, and likely were affected by an additional process. Weyer and Ionov (2007) suggest that metasomatic action of Si-undersaturated melt will replace orthopyroxene with clinopyroxene and elevate $\delta^{56}Fe$ values. Independently, Hauri et al. (1993) have suggested that orthopyroxene to clinopyroxene replacement has taken place through metasomatism in the set of xenoliths they studied, based on petrography and geochemical compositions. Thus, the simplest interpretation of our elevated peridotite values for Samoa lies in a metasomatic event affecting the $\delta^{56}Fe$ values of the mantle. Alternatively, variability in mantle $\delta^{56}Fe$ values has also been related to variations in oxygen fugacity (e.g., Williams et al., 2004). Since recent work on Samoan lavas has shown extreme fO_2 values (Cottrell and Kelley, 2014), perhaps the $\delta^{56}Fe$ values in the xenoliths reflect a Samoan mantle fO_2.

2.7. Conclusions

We have developed a new measurement technique for MC-ICP-MS that uses a new type of isobaric interference correction and instrument stability assessment for ^{57}Fe-^{58}Fe double spike analyses. We find that the isobaric interference from Ni must be accounted for, in order to obtain the greatest possible precision with our double spike composition. Placing ^{60}Ni on a low-abundance ion counter increases precision of the measurement, which prevents propagation of Faraday noise into the double spike correction. After double spike correction and outlier removal, we can achieve a δ^{56}Fe value of 0.473 ±0.046‰ (2σ) on our secondary standard Alfa Fe DS relative to IRMM-014 DS.

Tracking instrumental stability is valuable for data quality monitoring. Peak center masses are a useful proxy for stability and may be used in statistical outlier detection to reliably remove data points with ratios likely to have been influenced by polyatomic argide tails that interfere with iron isotope beams. Tolerance ellipses and Mahalanobis distances are effective outlier detection tools, as points plotting outside of the ellipse tend to have questionable δ^{56}Fe values and are likely to have been measured outside of the ideal peak flat region where interfering argides may have encroached.

Our technique produces high precision Fe isotope data. Further improvements are possible with multiple analyses and statistical tests of representative crystals of each mineral phase in order to distinguish iron isotopic signatures of the mineral phases. Our data set suggests that different ultramafic rock types may be distinguished with this approach. Our outlier test helps reduce the uncertainty of mineral averages. Potentially, the

technique can be extended to different minerals phases, given enough repeat analyses per sample.

2.8. Acknowledgements

This research was funded by a University Research Institute grant at UTEP, and was supported by the UTEP CEEIR facility. V.A.F. was also partially supported by NSF-OCE grant 1433097. We thank Elizabeth Anthony for sharing the Kilbourne Hole samples and compositional data. We would like to thank John Rudge and two anonymous reviewers for their suggestions, which considerably improved the manuscript. Additional data can be found in the Supplemental Material for this manuscript.

Table 2.1. Cup Configuration of masses (amu) measured during the three cycles.

Cycle	H6	gap	H5	gap	H4	H3	H2	H1	Ax	L1	L2	IC0	L3	IC1	L4	IC2	L5
1 (Ni)												60					58
2 (Fe)			58			57			56						54		
3 (Cr)					54						52						

Table 2.2. Concentrations and masses of standards and double spike used to make spiked standard solutions.

Double spike composition (ratio)	Ratio
$^{58}Fe/^{56}Fe$	4.7671
$^{57}Fe/^{56}Fe$	36.473
$^{54}Fe/^{56}Fe$	0.000154
Ideal $^{57}Fe/^{56}Fe$ of spike/sample mix	0.834533
Double spike composition (wt%)	**Percent**
^{58}Fe	11.286%
^{57}Fe	2.3674%
^{56}Fe	86.347%
^{54}Fe	3.6E-6%

Table 2.3. Sample information.

Sample Name	Location	Host sample type	Mineral Type	Mass (mg)
OL-2	Kilbourne Hole, NM	KH-7 peridotite xenolith	Olivine (single crystal)	14.76
OL-3	Kilbourne Hole, NM	KH-7 peridotite xenolith	Olivine (single crystal)	14.40
B-OL	Kilbourne Hole, NM	KH-7 peridotite xenolith	Olivine (batch)	52.09
B-OL.1	Kilbourne Hole, NM	KH-7 peridotite xenolith	Olivine (batch)	44.34
B-OL.3	Kilbourne Hole, NM	KH-7 peridotite xenolith	Olivine (batch)	26.57
B-OPX	Kilbourne Hole, NM	KH-7 peridotite xenolith	Olivine (batch)	31.77
B-OPX.1.2	Kilbourne Hole, NM	KH-7 peridotite xenolith	Olivine (batch)	22.96
B-OPX.3	Kilbourne Hole, NM	KH-7 peridotite xenolith	Orthopyroxene (batch)	15.43
SAV09-15	Savai'i	peridotite xenolith	Olivine (batch)	65.48
SAV09-15NI	Savai'i	peridotite xenolith	Olivine (batch)	35.50
SAV09-15.1	Savai'i	peridotite xenolith	Olivine (batch)	45.91
SAV09-15.2	Savai'i	peridotite xenolith	Olivine (batch)	33.22
SAV09-15.3	Savai'i	peridotite xenolith	Olivine (batch)	37.08
SAV09-15.4	Savai'i	peridotite xenolith	Olivine (batch)	38.45
SAV09-15OPX	Savai'i	peridotite xenolith	Orthopyroxene (batch)	41.38
SAV09-15.1OPX	Savai'i	peridotite xenolith	Orthopyroxene (batch)	9.93
B-CPX	Kilbourne Hole, NM	KH-7 peridotite xenolith	Clinopyroxene (batch)	39.18
KH-26	Kilbourne Hole, NM	KH-26 pyroxenite	Clinopyroxene (batch)	18.66
KH-60B	Kilbourne Hole, NM	KH-60B pyroxenite	Clinopyroxene (batch)	13.74

Table 2.4. Behavior of results (averages, when given, are non-error weighted, prior to outlier rejection) with and without interference corrections[a].

Sample	Type	δ^{56}Fe Ni correction on Cr correction on	δ^{56}Fe Ni correction off Cr correction on	δ^{56}Fe Ni correction on Cr correction off	δ^{56}Fe Ni correction off Cr correction off
Alfa Fe DS	Standard	0.439	0.584	0.440	0.585
Alfa Fe DS	Standard	0.478	0.826	0.497	0.846
Alfa Fe DS[b]	*Standard*	*0.452*	*0.582*	*0.450*	*0.582*
Alfa Fe DS	Standard	0.450	0.562	0.448	0.563
Alfa Fe DS	Standard	0.469	0.543	0.471	0.545
Alfa Fe DS	Standard	0.501	0.274	0.502	0.275
Alfa Fe DS	Standard	0.487	0.270	0.488	0.271
Alfa Fe DS	Standard	0.491	0.267	0.492	0.269
Alfa Fe DS	Standard	0.448	0.151	0.448	0.155
Alfa Fe DS	Standard	0.516	0.221	0.518	0.220
Alfa Fe DS	Standard	0.454	0.166	0.456	0.165
Alfa Fe DS	Standard	0.477	0.188	0.479	0.188
Alfa Fe DS[b]	*Standard*	*0.420*	*0.302*	*0.420*	*0.303*
Alfa Fe DS[b]	*Standard*	*0.458*	*0.325*	*0.458*	*0.325*
Alfa Fe DS	Standard	0.496	0.376	0.497	0.376
Alfa Fe DS	Standard	0.486	0.333	0.485	0.336
Alfa Fe DS	Standard	0.511	0.297	0.511	0.297
Alfa Fe DS	Standard	0.464	0.474	0.459	0.466
Alfa Fe DS	Standard	0.445	0.697	0.440	0.693
Average Alfa		**0.471**	**0.392**	**0.472**	**0.393**
2σ		**0.052**	**0.384**	**0.055**	**0.387**
Average (no outliers)		**0.473**	**0.389**	**0.477**	**0.391**
2σ		**0.046**	**0.405**	**0.051**	**0.409**
USGS Rock Standard[c]					
BCR-2[b]		*0.022*	*0.604*	*0.024*	*0.605*
BCR-2		0.116	0.913	0.120	0.916

[a]Data is presented with nickel and chromium corrections (recommended), no nickel correction (chromium corrected), no chromium correction (nickel corrected), and with neither correction. The nickel correction exerts significant control on δ^{56}Fe, particularly when comparing processed samples with low Ni levels to unprocessed standards with slightly higher Ni levels. Non-weighted averages are calculated for in-house standard Alfa Fe DS. Data are also presented for USGS Reference standard BCR-2, Kilbourne Hole olivines (KHol), Kilbourne Hole orthopyroxenes (KHopx), Kilbourne Hole peridotite and pyroxenite clinopyroxenes (KHcpx), Savai'i olivines (SAVol), and Savai'i orthopyroxenes (SAVopx).

[b]Italicized Samples had one or more blocks are identified as outliers in Fe-Ni space (see discussion in Section 2.4).

[c]BCR-2 average is not calculated because one of the analyses was identified as an outlier and rejected.

Table 2.4 (continued)

Sample	Type	δ^{56}Fe Ni correction on Cr correction on	δ^{56}Fe Ni correction off Cr correction on	δ^{56}Fe Ni correction on Cr correction off	δ^{56}Fe Ni correction off Cr correction off
OL-2	KHol	0.030	0.556	0.034	0.560
OL-3[b]	*KHol*	*0.069*	*0.648*	*0.067*	*0.652*
B-OL	KHol	-0.012	0.318	-0.007	0.322
duplicate	KHol	0.025	0.350	0.032	0.357
B-OL.1	KHol	0.056	1.126	0.059	1.130
B-OL.3	KHol	0.037	0.720	0.040	0.723
B-OPX	KHopx	-0.005	-0.400	-0.016	-0.409
B-OPX.1.2	KHopx	0.019	0.928	0.000	0.912
duplicate[b]	*KHopx*	*0.025*	*0.572*	*0.008*	*0.555*
B-OPX.3	KHopx	0.050	0.748	0.055	0.754
B-CPX[b]	*KHcpx*	*0.088*	*0.756*	*0.047*	*0.715*
duplicate[b]	*KHcpx*	*0.004*	*0.679*	*-0.040*	*0.636*
KH-26[b]	*KHcpx*	*0.125*	*0.674*	*0.130*	*0.679*
KH-60b[b]	*KHcpx*	*0.170*	*0.065*	*0.177*	*0.072*
SAV09-15	SAVol	0.046	0.998	0.047	1.001
SAV09-15NI	SAVol	0.043	1.041	0.045	1.044
duplicate[b]	*SAVol*	*-0.060*	*0.553*	*-0.055*	*0.554*
SAV09-15.1	SAVol	-0.019	0.997	-0.017	1.002
duplicate[b]	*SAVol*	*-0.005*	*0.602*	*-0.001*	*0.602*
SAV09-15.2	SAVol	0.047	0.544	0.048	0.545
SAV09-15.3	SAVol	0.070	0.421	0.072	0.423
SAV09-15.4[b]	*SAVol*	*0.040*	*0.707*	*0.041*	*0.709*
SAV09-15OPX[b]	*SAVopx*	*0.035*	*0.386*	*0.038*	*0.389*
SAV09-15.1OPX	SAVopx	0.073	0.776	0.075	0.776

Table 2.5. Comparison of iron isotopic data before and after outlier rejection[a]

	Without outlier rejection		With outlier rejection	
	Average $\delta^{56}Fe$[b]	2σ	Average $\delta^{56}Fe$[b]	2σ
Alfa	0.471	0.051	0.473	0.046
KHol	0.033	0.052	0.028	0.047
SAVol	0.025	0.087	0.033	0.072
KHopx	0.023	0.045	0.023	0.055
SAVopx	0.052	0.037	0.053	0.044
KHcpx	0.103	0.165	0.149	0.051
BCR-2	0.061	0.132	0.116	N/A[c]

[a]Explanations of sample types can be found in Table 3.
[b]Averages and 2σ are error-weighted.
[c]BCR-2 n=1 after outlier rejection.

Table 2.6. Iron isotopic data for secondary standard Alfa Fe DS, USGS powdered standard BCR-2 and mineral samples after outlier rejection. "Duplicate" analyses are a re-measurement of the same dissolution of the previously listed sample. 1SE is the internal error reported for the double spike-corrected $^{56}Fe/^{54}Fe$ ratio.

Sample	Type	$\delta^{56}Fe$ (‰)	1SE
Alfa Fe DS	Standard	0.439	1.66E-02
Alfa Fe DS	Standard	0.478	1.59E-02
Alfa Fe DS	Standard	0.450	1.66E-02
Alfa Fe DS	Standard	0.469	9.55E-03
Alfa Fe DS	Standard	0.501	1.31E-02
Alfa Fe DS	Standard	0.487	1.11E-02
Alfa Fe DS	Standard	0.491	1.20E-02
Alfa Fe DS	Standard	0.448	9.87E-03
Alfa Fe DS	Standard	0.516	1.13E-02
Alfa Fe DS	Standard	0.454	1.10E-02
Alfa Fe DS	Standard	0.477	1.13E-02
Alfa Fe DS	Standard	0.443	1.54E-02
Alfa Fe DS	Standard	0.496	1.48E-02
Alfa Fe DS	Standard	0.486	1.31E-02
Alfa Fe DS	Standard	0.505	1.33E-02
Alfa Fe DS	Standard	0.464	8.34E-03
Alfa Fe DS	Standard	0.445	9.56E-03
Weighted average		**0.475**	
Weighted 2σ		**0.045**	
BCR-2	USGS Ref.	0.116	1.19E-02
OL-2	KHol	0.030	1.10E-02
OL-3	KHol	0.023	1.75E-02
B-OL	KHol	-0.012	1.01E-02
duplicate	KHol	0.025	8.41E-03
B-OL.1	KHol	0.056	9.56E-03
B-OL.3	KHol	0.037	1.13E-02
Weighted average		**0.028**	
Weighted 2σ		**0.047**	
B-OPX	KHopx	-0.004	1.13E-02
B-OPX.1.2	KHopx	0.018	1.10E-02
B-OPX.3	KHopx	0.049	1.03E-02
Weighted average		**0.023**	
Weighted 2σ		**0.055**	

Table 2.6 (continued)

Sample	Type	δ^{56}Fe (‰)	1SE
KH-26	KHcpx	0.115	1.80E-02
KH-60b	KHcpx	0.158	9.43E-03
SAV09-15	SAVol	0.046	1.08E-02
SAV09-15NI	SAVol	0.043	1.11E-02
SAV09-15.1	SAVol	-0.019	1.06E-02
duplicate	SAVol	-0.018	1.77E-02
SAV09-15.2	SAVol	0.047	1.20E-02
SAV09-15.3	SAVol	0.070	8.86E-03
SAV09-15.4	SAVol	0.002	1.64E-02
SAV09-15OPX	SAVopx	0.018	1.80E-02
SAV09-15.1OPX	SAVopx	0.073	1.34E-02

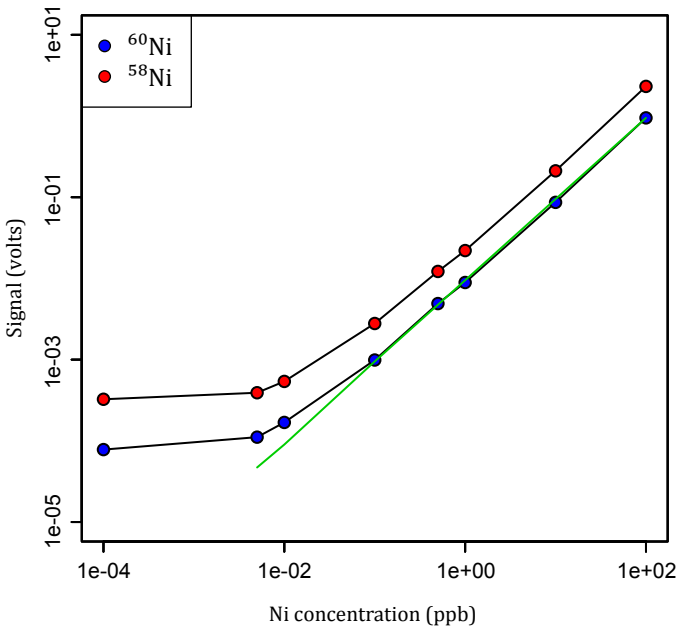

Figure 2.1. Behavior of nickel signal with concentration on the Faraday detectors. Below 0.1 ppb, signal is dominated by background levels of Ni in the diluting acid and the relationship of signal to concentration is no longer linear (green trendline).

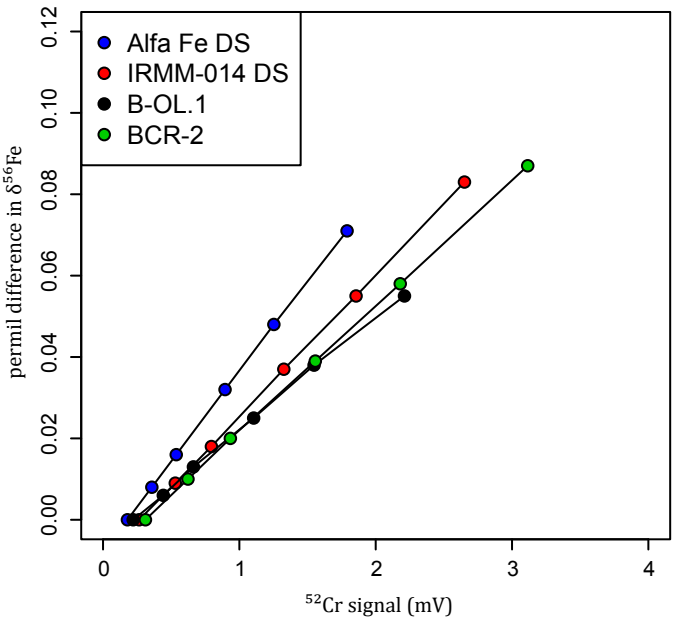

Figure 2.2. Change in $\delta^{56}Fe$ of selected standard and sample analyses with modeled increases in ^{52}Cr signal. 2σ uncertainty of Alfa Fe DS is shown.

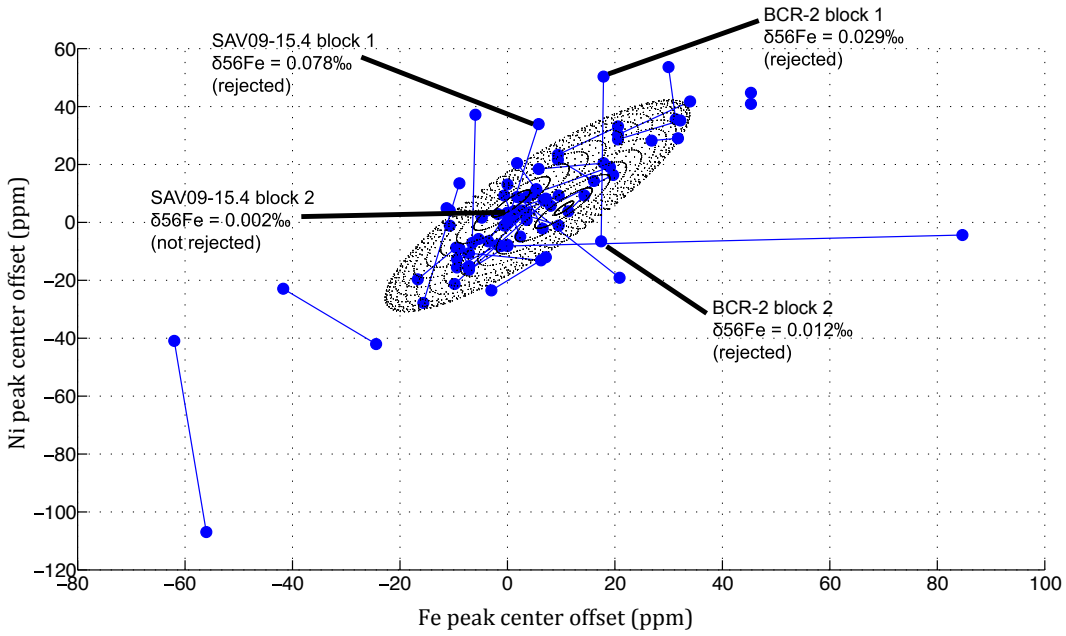

Figure 2.3. Sample data plotted as peak center offsets for iron, nickel, and chromium. The plot is oriented to look down the Cr axis since data points plotting as outliers are not rejected from analysis (additional projections provided in Supplementary Data). Points plotting outside of the 1σ ellipsoid in this projection are considered to be outlying data and are rejected from the average. Points joined by a line are paired blocks representing one sample measurement. In the case where only one block of a measurement is identified as an outlier, that block is rejected. To compensate for single-block measurements, the measurements are weighted by error when calculating long-term Alfa Fe DS average and mineral averages. Several rejected points are identified. One measurement of USGS reference standard BCR-2 yielded a low δ^{56}Fe. Both blocks plot outside of the ellipsoid and are rejected. Similarly, one block of Savai'i olivine plots outside of the ellipsoid while the other plots within the ellipsoid. The outlying block has a δ^{56}Fe = 0.078‰, somewhat higher than the average Savai'i xenolith olivine (δ^{56}Fe = 0.033‰). Conversely, the inlying block has a δ^{56}Fe = 0.002‰, closer to the average value.

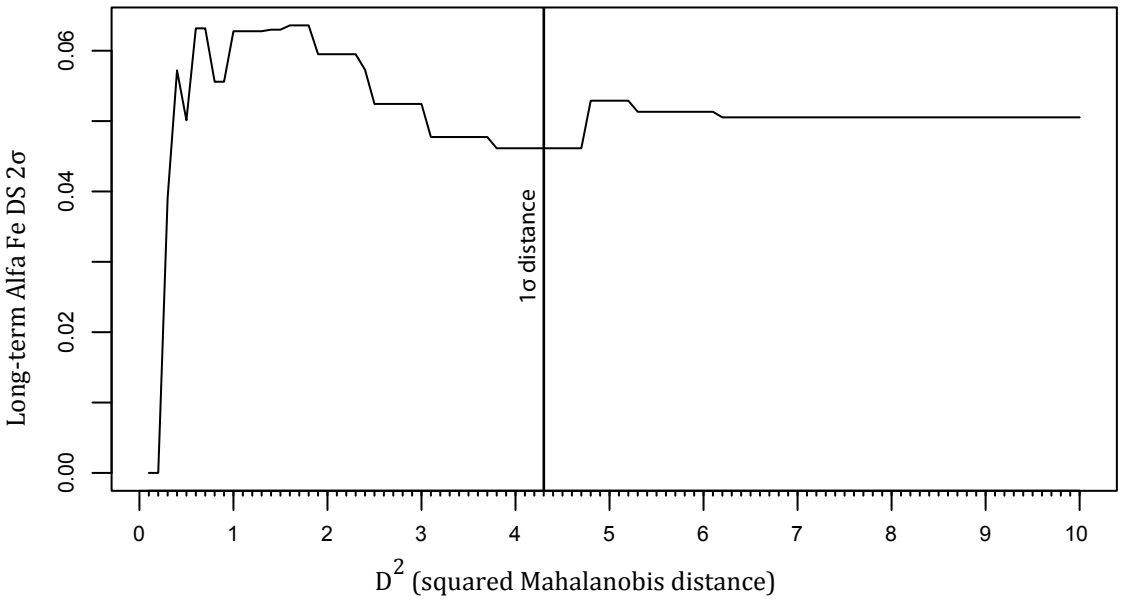

Figure 2.4. Plot of Alfa Fe DS 2σ (unweighted) versus squared Mahalanobis distance. Varying the Mahalanobis distance of the ellipsoid allows an ideal ellipsoid size to be determined. Too small an ellipsoid eliminates too many measurements (that are also likely valid); too large an ellipsoid fails to exclude a majority of measurement that may not be valid. Hence, we expect elevated error at small Mahalanobis distance and small sample size, and large Mahalanobis distances where potentially bad data is included. An error minimum occurs between D^2 values of 3.8 and 4.7, corresponding well with the proposed 1σ tolerance ellipsoid. Data outlying only along the Cr-axis are considered included when squared Mahalanobis distance is greater than 3.

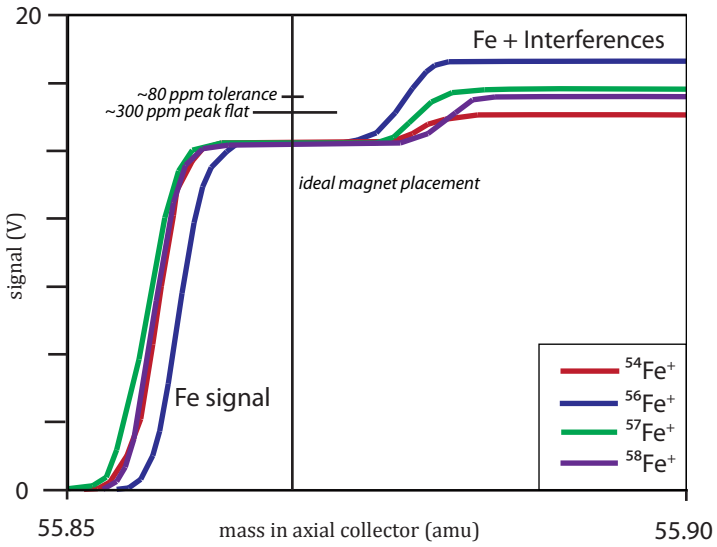

Figure 2.5. Ideal magnet placement on interference-free peak flat. Width and estimated tolerances are plotted with magnet placement.

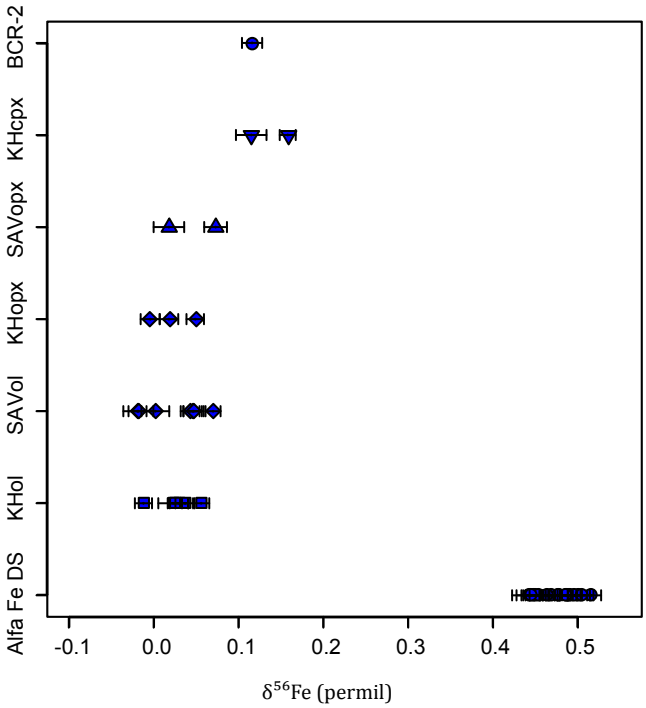

Figure 2.6. Distribution of δ^{56}Fe values sorted by mineral phase. KHol is Kilbourne Hole olivine, KHopx is Kilbourne Hole orthopyroxene, cpx is Kilbourne Hole clinopyroxene, SAVol is Savai'i olivine, and SAVopx is Savai'i orthopyroxene. Error bars represent internal precision of measurements (permil 1SE).

2.9. References

Albarède, F., Beard, B.L., 2004. Analytical methods for non-traditional isotopes. Rev. Mineral. Geochemistry 55, 113–152.

Albarède, F., Telouk, P., Blichert-Toft, J., 2004. Precise and accurate isotopic measurements using multiple-collector ICPMS. Geochim. Cosmochim. Acta 68, 2725–2744. doi:10.1016/j.gca.2003.11.024

Arnold, G.L., Weyer, S., Anbar, A.D., 2004. Fe isotope variations in natural materials measured using high mass resolution multiple collector ICPMS. Anal. Chem. 76, 322–327.

Beard, B.L., Johnson, C.M., 1999. High precision iron isotope measurements of terrestrial and lunar materials. Geochim. Cosmochim. Acta 63, 1653–1660.

Bodinier, J.-L., Godard, M., 2003. Orogenic, Ophiolitic, and Abyssal Peridotites. Treatise on Geochemistry 2, 103–170.

Craddock, P.R., Dauphas, N., 2010. Iron Isotopic Compositions of Geological Reference Materials and Chondrites. Geostand. Geoanalytical Res. 35, 101–123. doi:10.1111/j.1751-908X.2010.00085.x

Dauphas, N., Craddock, P.R., Asimow, P.D., Bennett, V.C., Nutman, A.P., Ohnenstetter, D., 2009b. Iron isotopes may reveal the redox conditions of mantle melting from Archean to Present. Earth Planet. Sci. Lett. 288, 255–267. doi:10.1016/j.epsl.2009.09.029

Dauphas, N., Janney, P.E., Mendybaev, R.A., Wadhwa, M., Richter, F.M., Davis, A.M., van Zuilen, M., Hines, R., Foley, C.N., 2004. Chromatographic separation and multicollection-ICPMS analysis of iron. Investigating mass-dependent and independent isotope effects. Anal. Chem. 76, 5855–63. doi:10.1021/ac0497095

Dauphas, N., Pourmand, A., Teng, F.-Z., 2009a. Routine isotopic analysis of iron by HR-MC-ICPMS: How precise and how accurate? Chem. Geol. 267, 175–184. doi:10.1016/j.chemgeo.2008.12.011

Dauphas, N., Rouxel, O., 2006. Mass spectrometry and natural variations of iron isotopes. Mass Spectrom. Rev. 25, 515–550. doi:10.1002/mas.20078

Dideriksen, K., Baker, J.A., Stipp, S.L.S., 2006. Iron isotopes in natural carbonate minerals determined by MC-ICP-MS with a 58Fe-54Fe double spike. Geochim. Cosmochim. Acta 70, 118–132. doi:10.1016/j.gca.2005.08.019

Hauri, E.H., Shimizu, N., Dieu, J.J., Hart, S.R., 1993. Evidence for hotspot-related carbonatite metasomatism in the oceanic upper mantle. Nature 365, 221–227.

Kehm, K., Hauri, E.H., Alexander, C.M.O., Carlson, R.W., 2003. High precision iron isotope measurements of meteoritic material by cold plasma ICP-MS. Geochim. Cosmochim. Acta 67, 2879–2891. doi:10.1016/S0016-7037(03)00080-2

Mahalanobis, P.C., 1936. On the generalized distance in statistics. Proc. Natl. Inst. Sci. 2, 49–55.

Millet, M.A., Baker, J.A., Payne, C.E., 2012. Ultra-precise stable Fe isotope measurements by high resolution multiple-collector inductively coupled plasma mass spectrometry with a Fe-57-Fe-58 double spike. Chem. Geol. 304, 18–25. doi:10.1016/j.chemgeo.2012.01.021

Perkins, D., Anthony, E.Y., 2011. The evolution of spinel lherzolite xenoliths and the nature of the mantle at Kilbourne Hole, New Mexico. Contrib. to Mineral. Petrol. 162, 1139–1157. doi:10.1007/s00410-011-0644-1

Rousseeuw, P.J., Driessen, K. Van, 1999. A Fast Algorithm for the Minimum Covariance Determinant Estimator. Technometrics 41, 212–223.

Rudge, J.F., Reynolds, B.C., Bourdon, B., 2009. The double spike toolbox. Chem. Geol. 265, 420–431. doi:10.1016/j.chemgeo.2009.05.010

Schoenberg, R., Von Blanckenburg, F., 2005. An assessment of the accuracy of stable Fe isotope ratio measurements on samples with organic and inorganic matrices by high-resolution multicollector ICP-MS. Int. J. Mass Spectrom. 242, 257–272. doi:10.1016/j.ijms.2004.11.025

Siebert, C., Nägler, T.F., Kramers, J.D., 2001. Determination of molybdenum isotope fractionation by double-spike multicollector inductively coupled plasma mass spectrometry. Geochemistry, Geophys. Geosystems 2.

Takahashi, E., Shimazaki, T., Tsuzaki, Y., Yoshida, H., 1993. Melting Study of a Peridotite KLB-1 to 6.5 GPa, and the Origin of Basaltic Magmas. Philos. Trans. R. Soc. A Math. Phys. Eng. Sci. 342, 105–120. doi:10.1098/rsta.1993.0008

Teng, F.-Z., Dauphas, N., Helz, R.T., 2008. Iron isotope fractionation during magmatic differentiation in Kilauea Iki lava lake. Science. 320, 1620–2. doi:10.1126/science.1157166

Teng, F.-Z., Dauphas, N., Huang, S., Marty, B., 2013. Iron isotopic systematics of oceanic basalts. Geochim. Cosmochim. Acta 107, 12–26. doi:10.1016/j.gca.2012.12.027

Verboven, S., Hubert, M., 2005. LIBRA: a MATLAB library for robust analysis. Chemom. Intell. Lab. Syst. 75, 127–136. doi:10.1016/j.chemolab.2004.06.003

Weyer, S., Ionov, D. a., 2007. Partial melting and melt percolation in the mantle: The message from Fe isotopes. Earth Planet. Sci. Lett. 259, 119–133. doi:10.1016/j.epsl.2007.04.033

Weyer, S., Schwieters, J.B., 2003. High precision Fe isotope measurements with high mass resolution MC-ICPMS. Int. J. Mass Spectrom. 226, 355–368. doi:10.1016/S1387-3806(03)00078-2

Williams, H.M., Bizimis, M., 2014. Iron isotope tracing of mantle heterogeneity within the source regions of oceanic basalts. Earth Planet. Sci. Lett. 404, 396–407. doi:10.1016/j.epsl.2014.07.033

Williams, H.M., Markowski, A., Quitté, G., Halliday, A.N., Teutsch, N., Levasseur, S., 2006. Fe isotope fractionation in iron meteorites: New insights into metal-sulphide segregation

and planetary accretion. Earth Planet. Sci. Lett. 250, 486–500. doi:10.1016/j.epsl.2006.08.013

Williams, H.M., McCammon, C.A., Peslier, A.H., Halliday, A.N., Teutsch, N., Levasseur, S., Burg, J.-P., 2004. Iron isotope fractionation and the oxygen fugacity of the mantle. Science. 304, 1656–1659. doi:10.1126/science.1095679

Williams, H.M., Peslier, A.H., McCammon, C.A., Halliday, A.N., Levasseur, S., Teutsch, N., Burg, J.-P., 2005. Systematic iron isotope variations in mantle rocks and minerals: The effects of partial melting and oxygen fugacity. Earth Planet. Sci. Lett. 235, 435–452. doi:10.1016/j.epsl.2005.04.020

CHAPTER 3: SOLVING THE PARADOX OF HIGH-fO_2 BONINITIC MELTS WITH LOW δ^{56}FE: SOURCE INPUT VS. MAGMATIC PROCESSES IN THE YOUNG LAU BASIN BACKARC

Abstract

The Fe isotopic compositions of magmatic systems may relate to the fO_2 of the evolving melts, resulting in high $\delta^{56}Fe$ values for closed systems that evolve to high fO_2. If indeed fO_2 plays such a vital role in generating high $\delta^{56}Fe$ values, magmas with known high fO_2 should also display unusual $\delta^{56}Fe$ values. Such high fO_2 conditions are present in subduction zone environments and expected to be characteristic for boninites, which are thought to form from fluid-flux melting. Therefore, the $\delta^{56}Fe$ composition of boninites may improve our understanding of the relationship between $\delta^{56}Fe$ and fO_2.

The Northeast Lau Basin backarc hosts the Mata Volcanic Field (MVF), a cluster of small, young volcanoes that recently erupted boninitic lavas related to early stages of subduction. Here we present the first Fe isotopic data for a suite of MVF high-Ca boninitic glasses. These melts are derived directly from underlying mantle and have short crustal residence times, preserving geochemical characteristics reflecting parental melt compositions. Furthermore, elevated redox state in the MVF compared to typical mid-ocean ridge settings provides an ideal location to evaluate the known correlation between redox and Fe isotope composition. Coupling of redox-sensitive Fe isotope ratios to compositional data can therefore provide clues into the relationships between redox state, magmatic processes, source contributions and Fe isotope composition of a melt.

MVF $\delta^{56}Fe$ values (average ~+0.013‰) are unusually low for a mantle-derived melt (average ~+0.1‰), instead resembling depleted upper mantle $\delta^{56}Fe$ (~0.0‰). High redox state has often been associated with elevated $\delta^{56}Fe$ in literature, rendering low $\delta^{56}Fe$ values of boninites paradoxical considering their elevated redox states. Notably, MVF $\delta^{56}Fe$ values display geochemical correlations not previously observed in boninites. Specifically, the

northwestern part of the MVF proximal to the NE Lau Spreading Center, particularly Tolu Volcano, have higher glass MgO and δ^{56}Fe, and lower whole-rock Ba/Nb. To the southeast, lower glass MgO and δ^{56}Fe and higher whole rock Ba/Nb, particularly in West Mata Volcano, are dominant. This suggests West Mata, which sits closer to the Tonga arc, may reflect incorporation of greater amount of a low- δ^{56}Fe, LILE-enriched, lower Mg# subduction-derived fluid component that metasomatized mantle wedge. Furthermore, such a mechanism offers a possible explanation of high-fO_2 melts with low δ^{56}Fe. In contrast, Mata Tolu-type compositions more closely resemble compositions enriched in some elements similarly to the nearby Northeast Lau Spreading Center and likely contain less of the subduction fluid component. This indicates that Fe isotopes may be a useful tracer of subduction fluid input in arc-generated, mantle-derived melts.

3.1. Introduction

The Lau Basin is a young ocean basin that has been the subject of many geophysical and geochemical studies because of its widespread volcanic activity and complex ridge system (Figure 3.1). The northeastern part of the Lau backarc in particular has generated interest due to the discovery of active submarine volcanic eruptions in 2008 during the TN227 expedition (R/V Thompson) and has since been revisited during Northeast Lau Response Cruises (Resing et al., 2011). The eastern Lau Basin hosts the Tonga backarc, where the production of mantle-derived melts serves as a window into the geochemical makeup of underlying heterogeneous mantle domains that act as controls on the geochemistry of Lau Basin volcanism (e.g., Falloon et al., 1992). This discovery of these backarc compositions has provided the basis for understanding the petrological conditions present in young subduction settings as well as the influence of different geochemical domains on the genesis of melt in subduction settings.

Early studies (Falloon and Crawford, 1991; Sinton and Fryer, 1987) demonstrated the uniqueness of backarc basin basaltic compositions in the North Tonga region and discussed general boninite petrogenesis. These studies also revealed the relatively complex source contributions to Tongan boninites, including identification of at least three major source components, their redox states, and characterization of regional chemical heterogeneities. As boninites are thought to be a product of fluid flux in an oxidizing environment, they provide a useful setting to study igneous processes capable of fractionating Fe isotopes in early stages of subduction. Melt sources in subduction zones have elevated redox states compared to intraplate and mid-ocean ridge settings (Kelley and Cottrell, 2009), providing ideal settings to evaluate the relationship between redox and Fe

isotope composition. Additionally, Fe isotopes have potential as a useful tool to determine the cumulative effect of different magmatic processes and contributions on melt compositions. While cumulative Fe fractionation behaviors have been fairly well studied in other magmatic environments, the outcome of these processes on δ^{56}Fe in subduction zones currently remains inconclusive. The small global subduction zone dataset for δ^{56}Fe suggests a large degree of variation exists in arc and backarc melts, which is not well understood at this time (Sossi et al., 2016). We present new Fe isotopic data for a set of 25 fresh glass samples recovered from the Mata Volcanic Field (MVF). The sensitivity of Fe isotopic composition to source oxidation state and magmatic processes allows further exploration of boninite melt petrogenesis.

3.2. The Tonga Trench and-Lau Basin backarc system

The Lau Basin began opening at ~6.5-4 Ma in response to rollback of the Tonga Trench, with opening accommodated across the Australian, Tongan, and Niuafo'ou plates (Taylor et al., 1996; Yan and Kroenke, 1993; Zellmer and Taylor, 2001). The Vitiaz Lineament comprises the northern boundary of the Lau Basin and is thought to be a fossil convergent zone prior to initiation of slab rollback (Calmant et al., 2003). This feature converted to a strike-slip boundary that accommodates slip past the tear in Pacific lithosphere at the northern terminus of the Tonga trench and Tofua Arc, which forms the eastern boundary of the Lau Basin. Immediately north of the Vitiaz Lineament is the Samoan hotspot track. Some Samoan plume material may be "leaking" or channeling into the northern Lau Basin, providing the enriched signature common in the NW Lau Basin region (Danyushevsky et al., 1995; Falloon et al., 2007; Price et al., 2014; Turner and

Hawkesworth, 1998), but not in the northeastern Lau Basin (Lupton et al., 2015). Volcanic activity occurs throughout the northern Lau Basin, with small volumes of boninites and boninite-like melts with variable TiO_2 contents and multiple source contributions produced primarily in the northern part of the basin (Falloon et al., 2008, 2007). This study focuses on the North Tonga backarc near the intersection of the Vitiaz Lineament and the Tonga Trench, which hosts the Mata Volcanic Field (MVF). This field lies between the arc and the Northeast Lau Spreading Center (NELSC; Lupton et al., 2015; Resing et al., 2011), and is comprised of young, en echelon boninitic volcanoes. The presence of disequilibrium textures, xenocrysts and antecrysts, and compositional variations within individual volcanoes suggests that the MVF melts have short crustal residence times and lack a large, well-developed magma chamber. Melts therefore may not have had time to homogenize or equilibrate with the source or crust prior to eruption (Rubin et al., 2013), contributing to compositional variations found throughout MVF volcanoes. Additionally, it has been found (Michael et al., 2009; Rubin et al., 2013) that crystal fractionation processes control trends in major element data – such as CaO/Al_2O_3 versus MgO – in MVF melts, providing evidence of how melt compositions were affected prior to eruption.

3.3. Boninite petrogenesis

Boninites *sensu stricto* are rare, mantle-derived melts with unusual chemical compositions usually associated with early-stage subduction. Characterized by high whole-rock SiO_2, low TiO_2, and high H_2O (formally requiring $SiO_2 > 52$ wt. %, MgO > 8 wt. % and $TiO_2 < 0.5$ wt. %; Le Bas, 2000). Boninites from the North Tonga backarc region require

specific petrogenetic conditions (high T at ~1300°C and low P at ~10 kbar) exclusive to early-stage subduction settings (Danyushevsky et al., 1995; Falloon and Crawford, 1991).

Crawford et al. (1989) propose a boninite subtype classification scheme based on multiple boninite suites including samples from the type locality in the Izu-Bonin arc, based on relative Ca and Al abundance: 1) High-Ca boninites, and 2) low-Ca boninites. The latter subtype may be further classified into three types (see discussion in Crawford et al., 1989). High-Ca boninites are thought to require a less-depleted, or somewhat more pyroxene-rich lherzolite source (Crawford et al., 1989). In contrast, low-Ca boninites are thought to be derived from clinopyroxene-poor lherzolite or harzburgite (e.g., Cooper et al., 2010; Stern and Bloomer, 1992). Typical boninite extended trace element patterns reflect concave-upward "spoon-shaped" profiles with some heavy rare earth element (HREE) enrichment due to melt depletion followed by later-stage re-enrichment of LREE (e.g., Hickey and Frey, 1982). North Tongan boninites do not reflect this pattern, instead showing enrichment in HREE compared to boninite *sensu stricto* (Rubin, 2017; personal communication).

Up to three components are thought to contribute to boninite petrogenesis in the North Tongan region: 1) Mantle wedge previously depleted by basaltic melt extraction, or refractory OIB mantle (Crawford et al., 1989), 2) an OIB (pyroxenite) component for high-Ca boninites (Cooper et al., 2010; Danyushevsky et al., 1995; Falloon and Crawford, 1991; Turner and Hawkesworth, 1998), and 3) a slab-derived fluid with very high H_2O/K_2O and LILE (Danyushevsky et al., 1995; Sobolev and Danyushevsky, 1994). This fluid component fluxes the depleted mantle wedge, lowering its solidus temperature to produce boninitic melts. Variable mixtures of these components may produce compositional enrichments and depletions (indicated by variations in ratios such as CaO/Al_2O_3; e.g., Crawford et al., 1989;

Falloon and Crawford, 1991). Hydrous conditions were typically considered a requirement for boninite melt generation, however, an anhydrous model has been proposed (Cooper et al., 2010). In this model, the authors argue that high-Ca boninite compositions can be generated by multistage anhydrous (high temperature) melting of fertile peridotite. Later stages of melt generation were then thought to include slab-derived fluids, imparting the elevated water content characteristic of boninites.

North Tonga backarc volcanism produces both low-Ca and high-Ca boninite compositions (Falloon et al., 2008), but this study presents data only from high-Ca samples. North Tongan high-Ca boninites are generated under redox conditions near or slightly above the NNO fO_2 buffer (a reference point defined by stable mineral phase assemblages at a given redox state, where NNO = nickel-nickel oxide and FMQ = fayalite-magnetite-quartz), as determined by equilibrium olivine-spinel pairs (Danyushevsky and Sobolev, 1996). Recent work by Glancy (2014) on MVF boninites also suggests highly oxidizing conditions during melt generation (Fe^{3+}/Fe^{2+} = 0.357-1.32; fO_2 = FMQ + 1.8-4.8). Within the North Tonga region, Danyushevsky et al. (1995) noted that "eastern" and "western" boninite have slight chemical differences controlled by differences in either melt composition or oxidation state. The eastern melts, sampled near the MVF, may also be more magnesian. This is evidenced by slightly more magnesian eastern olivines (Fo_{94}) compared to western ones (Fo_{93}), and higher Fe content in eastern spinels compared to western. If the regional variability in North Tonga is a function of changing redox state, corresponding shifts in Fe isotopic composition throughout the backarc region can be expected.

Magma mixing and assimilation also appear to be an important feature of North Tongan boninites. Zoned olivine phenocrysts from Volcano A in the Tonga Arc preserve a complex history of recharge of magmas with differing compositions (Cooper et al., 2010). Similarly, Resing et al. (2011) find both equilibrium and antecryst/xenocryst populations in West Mata samples. Sampling at West Mata was more extensive than at other MVF volcanoes, characterizing several different, geochemically distinct eruptions (Rubin et al., 2014, 2013). Lavas from different eruptions at West Mata show variations in elements such as CaO/Al_2O_3, MgO, and TiO_2 that are interpreted as reflecting differing parental melt compositions and short residence times in the crust (Glancy, 2014; Michael et al., 2009; Resing et al., 2011; Rubin et al., 2014, 2013).

3.3.1. MVF boninites and magmatic evolution

Previously published major (glass) and limited trace element (whole rock) data (Glancy, 2014; Lupton et al., 2015; Michael et al., 2009; Rubin et al., 2013), are reported in Tables 3.1 and 3.2, respectively. The glass samples do not plot within the boninite field (Figure 3.2; Le Bas, 2000), although whole rock compositions classify as boninites. All but one of the samples are considered "low TiO_2" samples (TiO_2 < 0.70 wt. %), plus one "medium TiO_2" (0.70 < TiO_2 < 1.0 wt. %) and three "evolved" (SiO_2 = 68-70 wt%) boninitic compositions, following the classification scheme and nomenclature presented in Glancy (2014). The low-TiO_2 group includes samples with heterogeneous MgO and SiO_2 wt. % potentially traceable to different parental melts (Michael et al., 2009; Rubin et al., 2013).

Major element behavior in this sample set (Figure 3.3) agrees with a melt evolution path controlled largely by fractionation of clinopyroxene and olivine (Michael et al., 2009)

from a high-MgO parental melt (see Section 3.6.4 for discussion of parental melt estimates). However, earlier stages of the crystallization sequence were probably controlled by some combination of olivine and orthopyroxene precipitation (Michael et al., 2009). Mata Ua and Mata Tolu samples roughly parallel the differentiation trend formed by East and West Mata samples in SiO_2 vs. MgO and CaO/Al_2O_3 vs. MgO (Figure 3.3A, 3.3D). Crystallizing only olivine (or orthopyroxene and olivine) from the melts would not substantially fractionate CaO/Al_2O_3 because olivine incorporates only very small amounts of Ca (Figure 3.3D). In contrast, clinopyroxene incorporates Ca into its structure, depleting the melt of CaO relative to Al_2O_3 (which is not part of pyroxene stoichiometry).

In addition to crystal fractionation, variations in source composition are also important, and southeastern West Mata and northeastern Mata Tolu volcanoes provide the best examples of compositional variability due to both factors. These volcanoes form parallel evolutionary paths in MgO vs. SiO_2 and MgO vs. CaO/Al_2O_3 (Figure 3.3A, 3.3D), suggesting similar crystal fractionation, but West Mata is more incompatible-enriched (K_2O = 0.65-1.00 wt. %; Mg# = 0.4-0.58; CaO/Al_2O_3 = 0.59-0.77; compared to Mata Tolu K_2O = 0.50-0.85 wt. %; Mg# = 0.53-0.63; CaO/Al_2O_3 = 0.70-0.82). In MgO vs. FeO, West and East Mata cluster toward more differentiated (higher FeO, lower MgO) compositions compared to Tolu and Ua, which have higher MgO and lower FeO.

Previously published whole rock trace element data are available for a subset of the MVF samples evaluated in this study (Table 3.2; Glancy, 2014; Lupton et al., 2015). No trace element data was obtained for the high-MgO East Mata compositions evaluated for Fe isotopes in this study. Mata Ua compositions have variable TiO_2 contents compared to other MVF volcanoes and therefore are not easily characterized with the few data available.

For East Mata, trace elements are only available for evolved samples. As such, most interpretation based on these data focuses on Tolu and West Mata. Variations in fluid-mobile elements such as Ba, and relatively immobile elements such as Nb can be used to track influence of slab-derived fluids versus other local domains, such as the Nb-enriched NELSC (Elliot, 2003; Lupton et al., 2015). West Mata and Mata Ua samples are enriched in Ba and depleted in Nb, but do not plot within the arc field defined in Figure 3.4A. Thus, MVF melts appear to incorporate less of the slab-derived fluid component in the backarc region than arc melts generated closer to the Tonga Trench. Compared to West Mata, Tolu is less enriched in Ba and has higher Nb, more closely resembling the NELSC than arc compositions (Figure 3.4A, 3.4B).

3.3.2. Boninites and Fe isotopes as a proxy for source oxidation state

A suite of Izu-Bonin and New Caledonia boninites has shown that boninitic whole-rock $\delta^{56}Fe$ values are similar to average global MORB values despite their differences in MgO and SiO_2, with little to no systematic variations with whole rock major elements (Dauphas et al., 2009). The New Caledonia samples are low-Ca classification and the Izu-Bonin samples are high-Ca. The Izu-Bonin and New Caledonia boninites yield Fe isotopic ratios similar to or slightly above typical mantle ($\delta^{56}Fe_{mantle}$ = ~+0.00-0.01‰; Craddock et al., 2013; Dauphas et al., 2009; Weyer and Ionov, 2007), in contradiction to observations that mantle-derived melts have a $\delta^{56}Fe$ value elevated ~0.1‰ relative to their source (e.g., Teng et al., 2013). This elevated signal in mantle melts is a function of Fe^{3+} behaving moderately incompatibly during melting (Teng et al., 2013). Equilibrium fractionation between Fe^{3+} and Fe^{2+} is expected to produce a higher isotopic ratio in Fe^{3+} than Fe^{2+}

(Dauphas et al., 2009; Polyakov and Mineev, 2000). To explain this discrepancy between oxidation state and $\delta^{56}Fe$, Dauphas et al. (2009) proposed a large fraction of the mantle source melted to generate boninitic compositions. These melts then isotopically equilibrated with their depleted sources, adopting a lower, mantle-like ratio.

In contrast, metasomatic processes can preferentially remove light Fe isotopes from mantle material, leaving behind elevated $\delta^{56}Fe$ in the mantle (Debret et al., 2016). Konter et al. (2016) show that unusually high $\delta^{56}Fe$ in Samoan rejuvenated lavas cannot be reasonably explained by common fractionation processes alone, assuming a typical upper mantle signature of ~0.0-0.02‰. Instead, elevated $\delta^{56}Fe$ must be a feature of the source, and Konter et al., (2016) suggest metasomatism is one possible cause. Evidence for this exists in metasomatized mantle xenolith minerals recovered from rejuvenated lavas on Savai'i, that display Fe isotopic signatures elevated as much as ~0.1‰ above average mantle (Finlayson et al., 2015). Other metasomatized mantle xenoliths have shown similar behavior (Williams et al., 2005, 2004; Williams and Bizimis, 2014). Boninites are highly oxidized with high Fe^{3+}/Fe^{2+} and associated with metasomatic fluid flux, yet have lower $\delta^{56}Fe$ than most other, lower-redox oceanic igneous rocks. We find similarly low $\delta^{56}Fe$ values in North Tongan boninite samples studied here, which would imply rather low $\delta^{56}Fe$ mantle source values (~-0.10‰ vs. ~0.00‰; Nebel et al., 2013). We explore the potential reasons for this paradoxical combination of high oxidation state and low $\delta^{56}Fe$ of boninites in this study.

The unique combination of tectonic setting, heterogeneous mixtures of mantle compositions within a relatively small area and within individual MVF volcanoes potentially preserve source signatures and effects of magmatic processes. Accordingly,

variations in Fe isotopic ratios may be preserved within and among individual volcanoes. Coupling $\delta^{56}Fe$ to existing compositional data (Glancy, 2014; Lupton et al., 2015) allows an evaluation of common magmatic fractionation processes, redox state, and source contributions as possible controls on the unusual combination of low $\delta^{56}Fe$ ratios in high-fO_2 magmas.

3.4. Methods

3.4.1. Sample selection and preparation

Samples in this study were selected from a suite recovered from multiple cruises: TN-234 (R/V Thomas Thompson), KM1024 and KM1129a (R/V Kilo Moana), and RR1211 (R/V Roger Revelle) (Lupton et al., 2015). Samples are a mixture of mantle-derived boninitic, high-Ti boninitic, and basaltic compositions.

Previously published major element data for sample glasses used in this study were obtained by microprobe at the University of Tulsa and the University of Hawai‘i at Mānoa (Table 3.1). We also report selected whole-rock trace element data corresponding to a subset of samples used in this study, collected via XRF at the University of Hawai‘i at Mānoa. We determined Fe isotope data on fresh glass samples selected from dredge and ROV sampling sites within the MVF, that provide an opportunity to study effects of various controls on Fe isotope fractionation in several different volcanoes, differing parent compositions, and across a range of compositional variations.

3.4.2. Processing and separation technique

Glass (180-260 mg) was picked from each sample for dissolution. Phenocryst phases were removed in order to better preserve the Fe isotopic signature of the melt rather than the crystal fractions. Samples were placed in a 1:1 mixture of concentrated HF and concentrated HNO_3 and heated on a hot plate for a minimum of 24 hours until digested, then sonicated in this mixture to break down the remaining insoluble fraction as completely as possible and left to digest further if necessary. After the dissolutions were complete, samples were treated twice with 200-300 μL concentrated HNO_3, with a complete drydown after each step. Next, samples were dissolved in ~6 mL of an ~6N HCl solution.

Sample splits (~5-10 mg) were taken from the dissolutions and were purified for Fe using the method described in Finlayson et al. (2015). In brief, sample splits were loaded onto a bed of Eichrom AG1-x4 100-200 mesh in 9N HCl + 0.001% H_2O_2 and washed in the same reagent to remove matrix. Fe was collected in 0.1N HCl, with yields exceeding 97%. A subset of the samples were also processed in ~10 mg split sizes for analysis at the University of Chicago Origins Lab using the separation technique described by Dauphas et al. (2004), which uses a similarly high normality HCl separation on AG1-x8 resin. Samples were analyzed at the University of Chicago Origins Lab via standard-sample bracketing on a ThermoFinnigan Neptune Plus MC-ICP-MS. Rock standards BCR-2, BIR-1, and KIL1919 were also included to determine sample and instrumental reproducibility and track day-to-day analytical variations.

3.5. Results

Fe isotopic results are given in Table 3.1, reported as $\delta^{56}Fe = 1000*[(^{56}Fe/^{54}Fe_{sample}/^{56}Fe/^{54}Fe_{standard})-1]$, referenced to the IRMM-014 standard. The weighted average values for each sample ($\delta^{56}Fe$ = -0.038 ‰ ± 0.099 to +0.051 ‰ ± 0.046; 2σ) display a compositional range similar to the boninitic $\delta^{56}Fe$ values (-0.01‰ ± 0.029 to 0.057‰ ± 0.039; 95% ci) published in Dauphas et al. (2009). Glass data are not available for the samples studied by Dauphas et al. (2009), but their whole rock compositions (MgO = 12-22 wt%) are similar to the range of whole rock compositions displayed in the MVF (6-20 wt. %; Glancy, 2014; Resing et al., 2011).

The majority of the MVF Fe isotopic compositions (average $\delta^{56}Fe$ = 0.009‰ ± 0.055 2σ, n=25) cluster at or slightly below whole-rock boninite $\delta^{56}Fe$ (Figure 3.5) from the Izu-Bonin and New Caledonia arcs (+0.031‰ ± 0.036, n=21; Dauphas et al., 2009), with a total $\delta^{56}Fe$ (weighted average) variation of ~0.09‰. The MVF data, and boninites in general, have low $\delta^{56}Fe$ compared to the global basaltic $\delta^{56}Fe$ compositions (~0.1‰) reported in many studies (e.g., Hibbert et al., 2012; Schuessler et al., 2009; Sossi et al., 2012; Teng et al., 2013; Zambardi et al., 2014). Instead $\delta^{56}Fe$ values in boninites resemble depleted or residual mantle $\delta^{56}Fe$ (e.g., Teng et al., 2013; Figure 3.5).

3.6. Discussion

3.6.1. Geochemical correlations with $\delta^{56}Fe$

Although glass compositions best represent evolving liquid compositions, boninite compositions in the literature are usually obtained on whole rocks due to a lack of fresh glass. It is therefore necessary to consider whole rock data for the MVF as well. The glasses

of this study have much lower MgO, slightly decreased TiO_2, and slightly higher SiO_2 contents than associated whole rocks (Glancy, 2014; Resing et al., 2011). This was attributed to the glass rinds reflecting effects of low-pressure differentiation relative to the whole rocks (Resing et al., 2011). However, inclusion of phenocrysts and more primitive xenocrysts and/or antecrysts in the whole rock compositions would have the same effect compared to the melt fraction represented by the glass.

Whole rock major element data for MVF samples (Glancy, 2014) highlight the compositional differences between the high-Ca MVF boninite lavas (average glass CaO/Al_2O_3 = 0.69) and the largely low-Ca (average CaO/Al_2O_3 = 0.48) Izu-Bonin and New Caledonia boninites. The Ca-based subcategories are commonly attributed to presence (high-Ca) or absence (low-Ca) of pyroxenite in source compositions (e.g., Falloon and Crawford, 1991). Whole rock MgO contents of both datasets, have significant compositional overlap (MVF $MgO_{\text{whole rock}}$ = 6.08-20.04 wt. % vs. Izu-Bonin/New Caledonia $MgO_{\text{whole rock}}$ = 12.27-22.12 wt. %), although the New Caledonia boninites, unlike the MVF and Izu-Bonin samples discussed herein, classify as the low-Ca subtype. MVF whole rock Al_2O_3 is also somewhat elevated relative to Izu-Bonin (Figure 3.3E), which probably results from the lack of plagioclase precipitation during melt evolution. The Izu-Bonin whole rock data overall suggest similar source compositions to the Lau Basin boninites. These data, unlike our glass compositions, only show correlation between $\delta^{56}Fe$ and TiO_2, attributed to changes in melting and water flux with depth (Dauphas et al., 2009). Critically, presence of xenocrysts and antecrysts indicates that whole rock compositions are unlikely to represent liquid compositions. The variable crystallinity and phenocryst assemblages in whole rock data may obscure any correlations. Unfortunately, glass fractions are not present for the

Izu-Bonin/New Caledonia samples, rendering a direct comparison of Izu-Bonin/New Caledonia and MVF melt fractions impossible.

The MVF data is on average slightly lower in δ^{56}Fe, although individual samples overlap in error compared to the Izu-Bonin/New Caledonia sample suite. With decreasing MgO in MVF samples δ^{56}Fe increases slightly, appearing to define trends in West Mata and Mata Tolu (Figure 3.5) that parallel differentiation patterns displayed in other igneous systems (e.g., Konter et al., 2016; Schuessler et al., 2009; Sossi et al., 2012; Teng et al., 2013, 2008; Zambardi et al., 2014). Given that the isotopic ranges is small compared to the analytical uncertainty on Fe isotope analyses, statistical evaluations are required to determine the robustness of this parallelism.

To test the parallelism, we focus on the Tolu δ^{56}Fe vs. MgO data (n=4), which show a negative correlation with a slope of ~-0.0195. With a Pearson product-moment correlation test we test the null hypothesis that the δ^{56}Fe and MgO are not related, but find a high correlation of -99.7% and a low probability ($p = 2.7e-3$ at 99% confidence) that the null hypothesis is correct (i.e., the variables are correlated). However, this test ignores analytical uncertainty for each measurement and the sample size is low. To further test the correlation, we calculate MSWD of the Tolu samples (~0.14). Such a low value (<1) suggests a much better fit to the trend line than would be expected given the magnitude of the analytical errors, and therefore the errors may be overestimated. Thus, both statistical tests and the parallelism with other magmatic systems imply that the Tolu data display a robust trend.

Similar tests performed on the West Mata data (n=13) also produce a low MSWD (0.034 for δ^{56}Fe-MgO), and a Pearson product-moment correlation that suggests δ^{56}Fe and

MgO are correlated (-80.9% correlation with a slope of -0.021; probability of non-correlation = 8e-4 at 99% confidence). Overall, West Mata data is slightly more scattered due to the likely influence of significantly different parental melt compositions for the various lavas sampled across this volcano (Rubin et al., 2013). However, it does suggest similarly robust, parallel behavior to that of the Tolu samples.

Thus, statistically there are two parallel trends in $\delta^{56}Fe$ vs. MgO, and these show great similarity to other magmatic systems, which are thought to reflect the evolution of $\delta^{56}Fe$ during magmatic processes (e.g., Sossi et al., 2012).

3.6.2. Constraining influences on evolution of boninitic melts

The evolution of the boninitic melts likely involves processes such as assimilation or magma recharge and mixing, given the presence of xenocrysts and antecrysts in the samples (Resing et al., 2011; see Section 3.6.4). We explore the effects of several magmatic processes and source variables on boninite melts in the following sections. The competing effects and unknown extents of these processes on melt $\delta^{56}Fe$ makes estimates of their contributions non-unique, but a first-order evaluation of their effects is made below.

3.6.3. Crystal-melt interaction and controls on Fe isotope ratios

Analytical precision has only recently revealed Fe isotope fractionation in igneous systems and although multiple processes might contribute, redox state plays an important role (Dauphas et al., 2014). Olivine crystallization removes Fe^{2+} from the melt, enriching the melt in isotopically heavier, more incompatible Fe^{3+} (e.g., Sossi et al., 2012; Dauphas et al., 2014). Thus, in a magmatic system that is closed to oxygen exchange, olivine

fractionation will considerably increase melt fO_2 values that result in increasing Fe^{3+} content and higher melt $\delta^{56}Fe$ (Dauphas et al., 2014). This type of evolution has been observed at Kilauea Iki (Hawaii), Society Islands, Samoa Islands, and Red Hill instrusion (Australia) (Teng et al., 2008; 2013; Sossi et al., 2012; Konter et al., 2016). Alternatively, if the system is open to oxygen, Fe^{3+} will not show the same strong increase in the melt, and the melt will not evolve to high $\delta^{56}Fe$ values. This process results in a relatively flat to slightly negative MgO vs. $\delta^{56}Fe$ fractionation trend, followed by an exponential increase in $\delta^{56}Fe$ at very low MgO, as suggested for Cedar Butte (Zambardi et al., 2014). Hekla volcano (Schuessler et al., 2009) also follows this evolution. Thus two evolutionary patterns are possible in igneous systems, depending on the occurrence or lack of oxygen exchange, combined with crystal fractionation (Sossi et al., 2012).

In the MVF melts, major element evolution is mainly controlled by olivine and clinopyroxene crystallization, despite the dominant occurrence of orthopyroxene phenocrysts (Michael et al., 2009; Rubin et al., 2013). For example, at West Mata major element patterns versus Mg# reflect control by olivine and clinopyroxene (Michael et al., 2009). However, the exact Fe isotope fractionation for each mineral is not yet well established. Instead magmatic trends for $\delta^{56}Fe$ have recently been modeled using an effective bulk fractionation factor describing the evolution of $\delta^{56}Fe_{melt}$ as mafic phases are removed from the melt (e.g. Konter et al., 2016).

Multiple igneous systems with extensive differentiation have been identified showing increasing $\delta^{56}Fe$ with decreasing MgO, attributed to differentiation under conditions closed to oxygen exchange (e.g., Kilauea Iki (Hawaii), Society, Samoa, Red Hill (Tasmania); Teng et al., 2008; 2013; Sossi et al., 2012; Konter et al., 2016). Their trends in

MgO vs. $\delta^{56}Fe$ are virtually identical to the MVF lavas, and have been relatively successfully modeled with a simple Rayleigh fractionation model describing bulk mineral fractionation from a primary melt using a fractionation factor of -0.3‰ (Teng et al., 2008; Figure 3.5), although the true control on fractionation may actually result from enrichment of isotopically heavy Fe^{3+} in the melt (e.g., Dauphas et al., 2014; Sossi et al., 2012).

Although the MVF lavas show parallel trends to these other locations, a Rayleigh model through the West Mata and Mata Tolu data would require a primary melt with a rather negative $\delta^{56}Fe$ value (Figure 3.5). However, establishing the exact composition of the primary melt is difficult, as this is usually accomplished through olivine back-addition until the melt composition is in equilibrium with mantle olivine (Fo=91-92%). Unfortunately, the MVF lavas are controlled by more than simple olivine fractionation, phenocrysts and xenocrysts may have had a hard-to-quantify effect, and more importantly a very depleted mantle such as a boninite source may have Fo=94%. Thus, simple olivine back-addition oversimplifies the likely history of these melts and it is unclear at what Fo value back-addition should stop.

Since the modeling is underconstrained in this case, an example fractionation pattern is shown in Figure 3.5 (see Section 3.6.4) that is not a unique solution, but it illustrates the main components of any solution; (1) the primary melt and original source had a rather low $\delta^{56}Fe$ value, (2) there is no single fractionation trend that passes through both West Mata and Mata Tolu; instead two parallel trends are needed. Eventual crystallization of magnetite in this type of evolution should cause a reversal in the Fe^{3+} and $\delta^{56}Fe$ increase (e.g., Sossi et al., 2012), and this might explain the lowest MgO samples with their low $\delta^{56}Fe$ values (average -0.022‰ ± 0.026, n=3). It cannot be ruled out that these

samples were formed by evolution in an open (to oxygen) magmatic system, however that would require both open and closed magmatic evolution in the general area. Therefore, we prefer explaining the data with a single process: Differentiation under closed conditions, where the offset between the West Mata and Mata Tolu data might be explained by: 1) Assimilation or magma mixing (Section 3.6.4), 2) diffusion-based kinetic Fe isotope fractionation, and 3) differences in primary melt compositions (Section 3.6.6).

3.6.4. Assimilation and magma mixing

Some of the crystal cargo in MVF magmas are xenocrysts and antecrysts (Resing et al., 2011), suggesting that assimilation and or crystal accumulation affected magma compositions and potentially $\delta^{56}Fe_{melt}$. This severely complicates estimations of the parental melt compositions. However, for a first-order compositional estimate, we assume a simplified system that does not assimilate crystals and only precipitates phases that are in equilibrium with the melt. This estimate is calculated by stepwise back-addition of equilibrium crystal phases to the melt, starting with the composition of the most magnesian glass reported here (Mata Tolu sample KM 1129a D07-R01; MgO = 7.34 wt. %). Stepwise equilibrium clinopyroxene and olivine are added to each sample composition in equal proportions until MgO = 8 wt. %, above which only olivine is assumed to control melt evolution. Additionally, ~8 wt. % MgO sits roughly at the intersection of the liquid line of descent defined by MVF compositional data and an olivine-controlled liquid line of descent from estimates of North Tongan parental melt compositions (e.g., Danyushevsky et al., 1995). Therefore, we assume that clinopyroxene fractionated CaO/Al_2O_3 relative to MgO when MgO < 8 wt. %. When glass MgO > 8 wt. %, only equilibrium olivine is added to the

melt until composition of equilibrium olivine reaches $Fo_{91.5}$, the composition of the most magnesian olivines found in MVF samples (Glancy, 2014). We assume a Kd=0.3 for melt-olivine MgO/FeO fractionation (Roeder and Emslie, 1970) and Kd=0.4 for clinopyroxene (Bedard, 2010). This approach is modeled after similar estimates by Danyushevsky et al. (1995), although their "PM1" primary estimate was determined using stepwise addition of only olivine to a whole rock composition to Fo_{94}.

Stepwise modeling suggests that a parental melt for KM1129a D07-R01 glass has an MgO of 15.4 wt. % in equilibrium with $Fo_{91.5}$. Comparatively, measured whole-rock compositions from the MVF are as high as ~20 wt. % MgO (Glancy, 2014), suggesting accumulation of the identified xenocrysts likely affected the high-MgO whole rocks. These xenocrysts would need to be high-Fo (probably mantle) olivine and/or pyroxene, and a significant mass fraction is required to drive the parental whole-rock composition high enough to produce the magnesian compositions erupted by MVF volcanoes.

A simple mass balance exercise suggests a minimum addition of 20% olivine ($Fo_{91.5}$) to the parental melt estimate is required to bring the parental whole-rock composition to ~20 wt. % MgO. If olivines are slightly less magnesian or more pyroxene is involved, a larger fraction must be added. Consequently, this exercise demonstrates that the evolution of MVF boninites requires petrogenetic conditions that cannot be reproduced by simple crystal fractionation mechanisms. Addition of a large volume of mantle olivine with a mantle-like $\delta^{56}Fe$ signature may also serve to lighten the Fe isotopic composition of a melt while also increasing MgO (Figure 3.6A).

In addition to an unknown mass of accumulated minerals, their compositions and relative proportions are not tightly constrained either. For example, the proportions of

xenocrysts in the rocks may not perfectly reflect the proportions of the accumulated minerals, if the crystal mush was not representatively sampled upon eruption. Without the mass and exact composition, a truly representative model is not possible. Furthermore, the timing of an assimilation or mixing event during magmatic evolution cannot be constrained either, while the resultant increase in MgO and decrease in δ^{56}Fe of the system could either partially or fully "reset" the evolution trend (Figure 3.6A). We argue here that the potential wide variety actually provides an argument against the importance of all these factors in the melt δ^{56}Fe evolution.

If the processes above were all critical to the evolution of West Mata and Mata Tolu, it is exceedingly unlikely that both groups would have developed parallel slopes at a given MgO range, not only to each other, but also to the available continental and oceanic igneous systems in the literature. Consequently, it appears most likely that the observed trends are mainly controlled by other processes, and two other explanations need to be considered for the offset between the two groups; diffusion-based kinetic fractionation, or a different starting composition.

3.6.5. Diffusion, equilibrium fractionation, and effect on melt δ^{56}Fe

Olivine, orthopyroxene and clinopyroxene all crystallize from these melts (Michael et al., 2009; Resing et al., 2011), therefore isotopic fractionation by kinetic diffusion between mineral and melt must be considered. Sio et al. (2013) suggests that Fe-Mg kinetic interdiffusion between olivine and melt has an isotopic effect that may fractionate the Fe isotopic content of both olivine and melt if cooling occurs over a long enough time period (up to ~20 years; Sio et al., 2013; Teng et al., 2011). Fe-Mg interdiffusion is also possible in

orthopyroxenes, although the diffusion rate is considerably slower (by as much as an order of magnitude) than that of olivine (Klügel, 2001). Any fractionating effect from presence of orthopyroxene, therefore, may be minimal. Geochemical evidence of syn-eruptive magma recharge indicates relatively short MVF residence times (e.g., Rubin et al., 2014), providing little to no time for significant mass exchange between mineral and melt. Similarly, nearby North Tongan boninites have also been shown to have very short residence times, often less than 3-5 months (Danyushevsky et al., 2002).

Diffusion of Fe^{2+} into high Mg# olivines preferentially incorporates the faster-diffusing lighter Fe isotopes (Dauphas et al., 2014), while Mg diffuses out of the crystal and into the melt. This would produce a net increase in $\delta^{56}Fe_{melt}$ and Mg#, assuming a large olivine fraction is present in the melt, and a storage/cooling time on the order of decades (Dauphas et al., 2010; Teng et al., 2011). While MVF melt residence times have not been fully quantified, olivine-driven diffusion may not be a significant control on $\delta^{56}Fe_{melt}$ because of the minimum decades-long exchange times required for olivine and orthopyroxene in melt, versus the likely months-scale residence times of MVF magmas.

3.6.6. Fe isotope ratios as source tracers

The final, and most likely control on $\delta^{56}Fe_{melt}$ variations in the MVF lies is primary magma heterogeneity. It has been shown in several igneous systems that Fe isotope ratios tend to follow predictable major element-stable isotope fractionation patterns during melt differentiation, despite complexities in the individual magmatic systems. The observation that boninites have considerably lower $\delta^{56}Fe$ than many other oceanic systems may reflect the relatively large degree of melting (>20%) required for boninitic melt petrogenesis.

Large melt fractions are capable of lowering $\delta^{56}Fe_{melt}$ to mantle-like ratios (Dauphas et al., 2009; Teng et al., 2013), although increasing the system Fe^{3+}/Fe^{2+} ratio increases the melt fraction required to achieve low primary $\delta^{56}Fe_{melt}$. Arc settings generally have high Fe^{3+}/Fe^{2+} in the source mantle (up to 0.3; Kelley and Cottrell, 2009), and this is conservative for relevant melts here (sample Fe^{3+}/Fe^{2+} = 0.36-1.62; Glancy, 2014). At arc redox conditions, in excess of 50% melting is required to produce $\Delta^{56}Fe_{melt\text{-}source}$ of ~0.04‰ or less, similar in magnitude to Izu-Bonin and New Caledonia boninites (Dauphas et al., 2009). An even greater melt fraction >50% is required to reproduce MVF compositions (Figure 3.7). While Kushiro (2007) suggests that boninite compositions probably require >20% mantle melting, the deduced value of >50% melting is unreasonably high. Alternative solutions to lower $\delta^{56}Fe_{melt}$ include boninitic melt equilibrating with isotopically lighter source mantle (Dauphas et al., 2009), or incorporation of an isotopically light component derived from the subducted slab during melting.

Variations in source geochemistry may be invoked here to explain the offset between West Mata and Mata Tolu, not unlike the "source effect" argued in Konter et al. (2016). Material "leaking" into the Lau Basin mantle from the nearby Samoan plume is capable of enriching melt compositions and has been invoked as a likely component of North Tongan melts (Falloon et al., 2007; Price et al., 2014; Turner and Hawkesworth, 1998). However, input from a relatively enriched, more alkalic (e.g., Natland, 1980) Samoan component would likely enrich the major element chemistry of MVF melts in the pattern we observe here. However, OIBs tend to have $\delta^{56}Fe$ similar to or heavier than typical depleted mantle (e.g., Teng et al., 2013), and therefore are unlikely to produce the Fe

isotope ratios we see here. Therefore, the presence of an OIB component in North Tonga is likely not a major control over $\delta^{56}Fe_{melt}$. Instead, an alternative LILE- and Fe-enriched component could be present in slab-derived fluid.

The mantle wedge in an arc setting undergoes metasomatism, a process expected to elevate $\delta^{56}Fe$ in the refractory peridotite (Su et al., 2015). However, high-degree melt production is required for boninitic compositions to maintain the observed unusually low isotopic ratios at the high fO_2 conditions found in arc systems. If a Rayleigh model accurately describes the evolution of the system, the source $\delta^{56}Fe$ composition must be below average mantle values (~0.00‰) as shown in Figure 3.5. This signature is opposite of the expected redox-driven effect of metasomatic processes on depleted mantle (Finlayson et al., 2015; Konter et al., 2016; Williams et al., 2004), although these studies have looked at melts and xenoliths derived from previously metasomatized residual mantle. Here, we evaluate the boninitic melts likely generated by a metasomatic event, which presumably includes the volatile phase that escaped the residual mantle described above. Therefore, it is likely that during melting, oxidizing subduction fluids carrying light $\delta^{56}Fe$ extracted from the downgoing slab are incorporated into boninitic melt compositions. Presence of a subduction component is further evidenced by enrichment of incompatible elements and some trace element ratios as seen in Figures 3.3 and 3.4.

To further explore the possibility of subduction fluid control on Fe isotopic composition, we employ the only available trace element data (whole rock) for some of our samples (Table 3.2). Because assimilated material may affect whole rock compositions, we only focus on comparing the general pattern between West Mata and Mata Tolu in subduction-sensitive trace elements, glass TiO_2, and glass $\delta^{56}Fe$. West Mata whole rock

Ba/Nb vs. 1/Nb (Figure 3.4A; after Lupton et al., 2015) are somewhat depleted relative to arc compositions, but relative to Mata Tolu they are enriched in Ba, a fluid-mobile element often elevated relative to immobile elements in subduction melts (Elliot, 2003). In contrast, Mata Tolu Ba/Nb plots between most of the other Mata volcanoes and the NELSC (Figure 3.4; Lupton et al., 2015). Additionally, slight enrichment in Mata Tolu whole rock Nb vs. glass TiO_2 is in agreement with a lower subduction signal and NELSC-like (high Nb) composition in Mata Tolu melts (Figure 3.4B). In contrast, the West Mata melts may be slightly Nb-depleted as a result of Nb mobility in fluids, a common signature in arc melts (e.g., Green, 1995; Figure 3.4B). Therefore, in this case, we argue that LILE-enriched, isotopically light subduction fluids (e.g., Danyushevsky et al., 1995; Su et al., 2015) fluxed depleted mantle wedge and may exert considerable control over $\delta^{56}Fe$.

This process is capable of driving the resultant high-fO_2 melt to low $\delta^{56}Fe$, thus explaining the paradoxical combination of low $\delta^{56}Fe$ and extremely high oxidation state (as high as FMQ + 4.8; Glancy, 2014) of these melts (Figure 3.7). The slightly depleted whole rock Ba/Nb ratios, higher glass Mg#, and lower glass $(Na_2O+K_2O)/MgO$ ratios of Mata Tolu samples relative to West Mata suggests that the NELSC and Tolu volcanic systems incorporate less of the subduction fluid component than the West Mata melts that are closer to the backarc axis. Differing fractions of subduction fluid in a volcanic system would also be capable of generating near-parallel differentiation trends between Mata Tolu and West Mata (Figure 3.6B). While quantifying the amount of subduction fluid contributing to melt genesis at each volcano is difficult at best, it is apparent that Fe isotopes may be useful tracers of slab-derived fluid input to metasomatic melts.

Considering the potential difference in input of subduction fluids across the Lau Basin, volcanoes closer to the NELSC may see a lower proportion of a LILE-enriched subduction fluid than volcanoes closer to the arc. Therefore, Mata Tolu might be expected to contain a smaller contribution from the subduction fluid than West Mata, and this is supported by lower whole rock Ba/Nb ratios in Mata Tolu, which geochemically resembles a mixture of MVF and the nearby NELSC (e.g., Elliot, 2003 and references therein; Figure 3.4). Mata Tolu could potentially reflect melting of a more depleted, oxidized, MORB-like source with high Mg# (Workman and Hart, 2005), lower Ba/Nb, and elevated δ^{56}Fe relative to mantle infiltrated with subduction-derived fluids. Mata Tolu trace element behavior is somewhat more like that published for the NELSC, while West Mata looks more arc-like (Lupton et al., 2015). If so, the chemical and stable isotopic characteristics of Mata Tolu may mark a transition in melts generated from mid-backarc to rear-backarc spreading corresponding to a decrease in subduction fluid input to melts generated in the northwestern part of the MVF (Figure 3.8).

3.7. Conclusions

Mata Tolu data define a negative trend in δ^{56}Fe vs. MgO, weakly paralleled by West Mata. Offset between the parallel Tolu and West Mata trends can be explained by different source compositions supplying the volcanoes, which are then affected by similar fractionation processes. The expression of nearly parallel differentiation trends in two volcanoes suggests boninite melt compositions evolve along predictable pathways despite the complexity of melt generation in subduction zones. Furthermore, the differentiated

East Mata compositions provide a potential constraint with low $\delta^{56}Fe$ values relative to the higher MgO composition, suggesting closed fO_2 fractionation pathways control $\delta^{56}Fe$.

Major and trace element data define a broad geographic pattern of major compositional characteristics (Figure 3.8). Lower melt $\delta^{56}Fe$ and Mg# also tend to correspond with elevated Na and K in glasses and high Ba/Nb ratios in whole rocks. These compositions are found dominantly in volcanoes from the southeastern part of the MVF, which sits closer to the Tonga arc, where a larger proportion of subduction fluid may be incorporated into SE MVF melts. Conversely, more depleted compositions found in Tolu volcano feature higher Mg# and $\delta^{56}Fe$, lower Na and K in glasses, and lower whole rock Ba/Th, and Ba/Nb. Generally, Tolu melts exhibit enriched geochemical characteristics, such as elevated Nb, compared to other MVF volcanoes. Simultaneously, Tolu samples display lower levels of Ba and higher Mg# suggestive of less subduction fluid input than other MVF volcanoes such as West Mata.

The processes controlling this compositional difference cannot be uniquely constrained at present, but source composition and magmatic differentiation that indirectly controls melt Fe^{3+}/Fe^{2+} are likeliest to have any significant influence on boninite $\delta^{56}Fe$. The repetition of only two distinct differentiation trends (relatively flat versus increasing) in $\delta^{56}Fe$ vs. MgO in the literature suggests that magmatic processes may only exert minimal control on Fe isotope compositions of these melts. Instead, changes in fO_2 in response to open- or closed-system fractional crystallization appear to control $\delta^{56}Fe$, producing the Tolu and West Mata differentiation trends, but not the offset between the two volcanoes. No other magmatic process we explore here is likely to produce the relationship between compositional enrichment and low $\delta^{56}Fe$ between Mata Tolu and

West Mata. Therefore, the likeliest explanation for offset parallelism between offset trends in MVF volcanoes is isotopic variation in mantle source components. The source component responsible for this offset may also effectively explain why boninites carry a light $\delta^{56}Fe$ signature at high fO_2 compared to other igneous systems.

The discrepancy between boninite $\delta^{56}Fe$ composition and most other oceanic basalts can be explained in part by the subduction fluid flux process invoked as a key mechanism in boninite generation. The light Fe isotopic signature of boninites may be derived from low $\delta^{56}Fe$ fluids extracted from the subducting slab. The effect may be enhanced if these fluids overprinted an already-light refractory mantle wedge signature (Debret et al., 2016; Su et al., 2015) compared to previously metasomatized (higher $\delta^{56}Fe$) mantle wedge. Fluxing by subduction fluids is a process crucial to boninitic melt generation, and these enriched, isotopically light fluids may be incorporated into the melt fraction derived from the mantle wedge (Danyushevsky et al., 1995). Thus, a lower-than-expected $\delta^{56}Fe$ signature is imparted to the resulting boninitic melts despite the probability of elevating $\delta^{56}Fe_{melt}$ during melting. The contribution of slab-derived, isotopically light fluid to boninite may explain the unusually light isotopic signature coexisting with high Fe^{3+}/Fe^{2+} in boninites compared to mantle-derived volcanism in other settings.

3.8. Acknowledgements

This research was carried out in collaboration with Jasper Konter and Ken Rubin at the University of Hawai‘i at Mānoa, and Nicole X. Nie, and Nicolas Dauphas and the University of Chicago Origins Lab. Glass and whole-rock data were analyzed by Eric

Hellebrand and Sarah Glancy at University of Hawai‘i at Mānoa, and Peter Michael at University of Tulsa.

Table 3.1. Sample information and major element data.

Sample	Cruise	SiO_2	TiO_2	Al_2O_3	FeO	MnO	MgO	CaO	Na_2O	K_2O	P_2O_5	sum	Cl	F	S	CaO/ Al_2O_3	Na_2O +K_2O	Petrologic Group	$\delta^{56}Fe$	2WSD	n	Mg#
West Mata - 2009 eruption																						
J2-413-R13	TN-234	55.60	0.57	14.10	8.58	0.15	5.83	10.16	1.92	0.73	0.18	98.00	0.16		0.016	0.72	2.65	low TiO_2	-0.024	0.046	1	0.5493
J2-417-R09	TN-234	55.79	0.54	13.75	8.80	0.17	6.71	10.59	1.90	0.65	0.17	99.07	0.13	0.04	0.004	0.77	2.55	low TiO_2	-0.040	0.099	2	0.5778
J2-418-R18	TN-234	55.77	0.57	13.99	8.54	0.15	6.02	10.29	1.88	0.72	0.17	98.29	0.16		0.009	0.74	2.60	low TiO_2	-0.027	0.032	1	0.5585
J2-420-R17	TN-234	55.70	0.53	14.43	8.96	0.14	6.04	10.51	1.94	0.66	0.09	99.01	0.13	0.04	0.005	0.73	2.60	low TiO_2	-0.001	0.043	1	0.5474
West Mata - low Ti, low Si																						
J2-418-R01	TN-234	58.69	0.48	14.51	8.88	0.14	3.24	8.31	1.98	0.94	0.15	97.54	0.19		0.012	0.57	2.92	low TiO_2	0.034	0.065	4	0.3958
J2-418-C02	TN-234	57.40	0.50	14.66	8.90	0.15	3.99	8.54	2.14	0.99	0.17	97.70	0.24		0.004	0.58	3.13	low TiO_2	0.048	0.011	2	0.4455
J2-418-R04	TN-234	57.54	0.54	14.41	8.85	0.13	4.15	8.82	2.11	1.00	0.19	98.00	0.24		0.012	0.61	3.11	low TiO_2	0.047	0.046	4	0.4566
J2-418-R05	TN-234	57.70	0.51	14.28	8.97	0.13	4.26	8.87	2.04	0.96	0.17	98.13	0.23		0.005	0.62	3.00	low TiO_2	0.045	0.018	3	0.4599
J2-420-R01	TN-234	57.26	0.46	14.64	8.83	0.14	3.52	8.59	2.13	0.95	0.18	97.00	0.30		0.01	0.59	3.08	low TiO_2	0.034	0.005	2	0.4171
J2-420-R02	TN-234	57.06	0.46	14.37	8.85	0.15	4.00	8.87	2.06	0.91	0.15	97.14	0.25		0.01	0.62	2.96	low TiO_2	0.040	0.038	2	0.4479
West Mata - low Ti, high Si																						
KM1024 D12-R01	KM1024	58.36	0.42	14.34	8.96	0.15	3.63	8.63	2.05	0.91	0.15	97.87	0.26		0.01	0.60	2.96	low TiO_2	0.010	0.043	1	0.4210
KM1024 D12-R06	KM1024	58.12	0.42	14.33	8.80	0.14	4.01	9.08	2.03	0.83	0.12	98.11	0.23		0.01	0.63	2.86	low TiO_2	0.008	0.043	1	0.4496
KM1024 D12-R08	KM1024	58.34	0.43	14.46	8.89	0.14	3.69	8.65	2.05	0.89	0.14	97.94	0.25		0.01	0.60	2.94	low TiO_2	0.020	0.043	1	0.4270
North Mata (Ua)																						
RR1211 Q325-R01	RR1211	57.90	0.47	14.69	8.04	0.13	4.72	9.21	1.77	0.77	0.16	98.03	0.17		0.00	0.63	2.54	low TiO_2	-0.013	0.043	1	0.5127
RR1211-Q325-R03	RR1211	54.00	0.85	13.06	8.68	0.16	6.77	11.08	1.86	1.17	0.22	98.02	0.18		0.00	0.85	3.03	med TiO_2	-0.008	0.045	3	0.5832
KM1129a D10-R01	KM1129 a	57.18	0.70	13.39	8.22	0.15	6.28	9.85	1.67	1.08	0.15	98.81	0.15		0.01	0.74	2.75	med TiO_2	0.003	0.043	1	0.5779
North Mata (Tolu)																						
KM1129a D07-R01	KM1129 a	56.72	0.41	13.01	7.79	0.14	7.34	10.70	1.85	0.50	0.21	98.79	0.11		0.01	0.82	2.35	low TiO_2	0.011	0.036	3	0.6283
KM1129a D07-R02	KM1129 a	56.91	0.44	13.70	7.90	0.14	6.52	10.43	1.96	0.55	0.20	98.88	0.12		0.00	0.76	2.52	low TiO_2	0.025	0.047	3	0.5970
KM1129a D08-R07	KM1129 a	57.49	0.50	14.25	8.46	0.14	5.39	9.93	1.82	0.85	0.18	99.20	0.17		0.01	0.70	2.67	low TiO_2	0.049	0.060	3	0.5333
KM1129a D08-R08	KM1129 a	56.00	0.51	14.49	8.22	0.14	6.21	10.68	1.90	0.70	0.24	99.24	0.13		0.01	0.74	2.60	low TiO_2	0.031	0.014	2	0.5756

Table 3.1. (continued)

Sample	Cruise	SiO_2	TiO_2	Al_2O_3	FeO	MnO	MgO	CaO	Na_2O	K_2O	P_2O_5	sum	Cl	F	S	CaO/ Al_2O_3	Na_2O +K_2O	Petrologic Group	$\delta^{56}Fe$	2WSD	n	Mg#
East Mata																						
KM1024 D14-R02	KM1024	57.41	0.42	12.36	8.76	0.17	5.57	9.76	1.80	0.98	0.19	97.62	0.21		0.01	0.79	2.78	low TiO_2	0.010	0.030	2	0.5330
KM1024 D14-R05	KM1024	57.66	0.44	13.01	8.87	0.15	4.94	9.55	1.84	1.01	0.18	97.87	0.22		0.01	0.73	2.85	low TiO_2	-0.008	0.058	2	0.4995
East Mata - differentiated																						
KM1129a D02-R01	KM1129 a	70.69	0.64	11.97	6.37	0.09	0.49	3.65	2.28	2.44	0.32	99.36	0.41		0.01	0.31	4.71	evolved	-0.036	0.032	1	0.1221
KM1129a D02-R03	KM1129 a	68.56	0.53	12.53	6.92	0.11	1.10	4.67	2.33	2.09	0.31	99.52	0.35		0.01	0.37	4.42	evolved	-0.011	0.032	1	0.2223
KM1129a D02-R04	KM1129 a	68.69	0.53	12.53	6.89	0.10	1.13	4.68	2.34	2.08	0.30	99.63	0.36		0.00	0.37	4.42	evolved	-0.019	0.032	1	0.2275
Estimated parental melt composition from stepwise equilibrium phase addition																						
KM1129a D07-R01 (parent)		53.95	0.34	10.61	8.52	0.14	15.38	8.98	1.50	0.41	0.17	100.0				0.85			-0.077			0.7629

Standards for Fe analysis

	Separation procedure used																					
BCR-2	UC																		0.064	0.056		
BCR-2	UC																		0.071	0.042		
BCR-2	UC																		0.085	0.044		
BCR-2	UHM																		0.065	0.037		
BCR-2	UHM																		0.055	0.046		
Average																			**0.068**	**0.022**	5	
BIR-1	UC																		0.006	0.056		
BIR-1	UC																		0.030	0.042		
BIR-1	UC																		0.062	0.044		
BIR-1	UC																		0.080	0.032		
BIR-1	UHM																		0.023	0.037		
Average																			**0.047**	**0.064**	5	
KIL1919	UC																		0.066	0.056		
KIL1919	UC																		0.107	0.042		
KIL1919	UC																		0.077	0.053		
KIL1919	UHM																		0.048	0.046		
KIL1919	UHM																		0.040	0.037		
KIL1919	UC																		0.119	0.032		
KIL1919	UC																		0.096	0.043		
Average																			**0.083**	**0.057**	7	

Glass major elements and Fe isotope compositions (weighted mean and 2*standard deviations are reported where n > 1). Fe isotope standard data are also given with weighted averages and weighted 2*standard deviations. Compositional and Fe isotope estimate for a parental liquid is also given, based on the most magnesian sample in the dataset. The method used to calculate composition is given in Section 3.6.4, and Fe isotope ratio in Figure 3.5.

Table 3.2. Selected whole rock trace element data for the sample set, obtained via XRF at University of Hawai'i at Mānoa. All data are given in ppm.

Sample	Nb	Zr	Y	Sr	U	Rb	Th	Pb	Co	Cr	V	Ba	Zn	Cu	Ni	Sc	Mn
West Mata - 2009 eruption																	
J2-413-R13	7	34	8	216	1.5	9	1.3	1.6	50	984	242	127	70		216	45	1312
J2-417-R09	6	32	7	194	1.5	8	1.3	1.6	57	1114	223	107	68	70	251	43	1341
J2-418-R18	6	35	8	225	1.5	10	1.3	1.6	52	928	252	126	70		209	46	1327
J2-420-R17	6	30	7	186	1.5	9	1.3	1.6	54	1021	233	105	68	72	221	44	1336
West Mata - low Ti, high Si																	
J2-418-R01	6	30	7	218	1.5	14	1.8	3.3	40	413	260	137	72	72	71	51	1358
J2-418-C02																	
J2-418-R04																	
J2-418-R05																	
J2-420-R01	6	30	7	204	1.5	12	1.3	2.2	45	695	250	123	70	72	113	47	1362
J2-420-R02	6	31	7	212	1.5	13	1.8	1.7	44	634	252	124	72	73	110	46	1348
West Mata - low Ti, high Si																	
KM1024 D12-R01	5	29	6	206	2.1	12	1.8	2.4	43	583	255	119	71	83	100	48	1342
KM1024 D12-R06																	
KM1024 D12-R08																	
North Mata (Ua)																	
RR1211 Q325-R01	7	35	8	227	1.5	14	2.2	3	41	582	258	148	72	83	133	42	1233
RR1211 Q325-R03	30	44	11	287	1.6	20	1.4	2	131	605	264	274	75	76	144	41	1306
KM1129a D10-R01	4	20	5	162.44	1.52	13	1.38	1.65	63	1508.33	201.38	123.17	70	59.78	419.03	38	1325.97
North Mata (Tolu)																	
KM1129a D07-R01	13	36	8	298	1.5	8	2.5	2	57	1250	214	222	74	79	292	37	1268
KM1129a D07-R02	13	34	8	272.34	2.28	9	2.6	1.66	57	1378.98	213.87	200.76	70	84.69	314.61	39	1292.1
KM1129a D08-R07	8	33	7	198.62	1.85	12	1.23	1.68	55	930.66	237.77	140.5	73	76.25	196.67	43	1346.45
KM1129a D08-R08																	
East Mata																	
KM1024 D14-R02																	
KM1024 D14-R05																	
East Mata Differentiated Lavas																	
KM1129a D02-R04	14	52	8	335.39	2.32	25	2.17	2.79	26	260.11	230.99	272.99	68	104.11	28.04	36	1109.59
KM1129a D02-R01																	
KM1129a D02-R03	13	50	8	328.37	2.04	24	1.73	2.05	29	287.35	237.3	262.41	69	92.7	25.01	39	1174.59

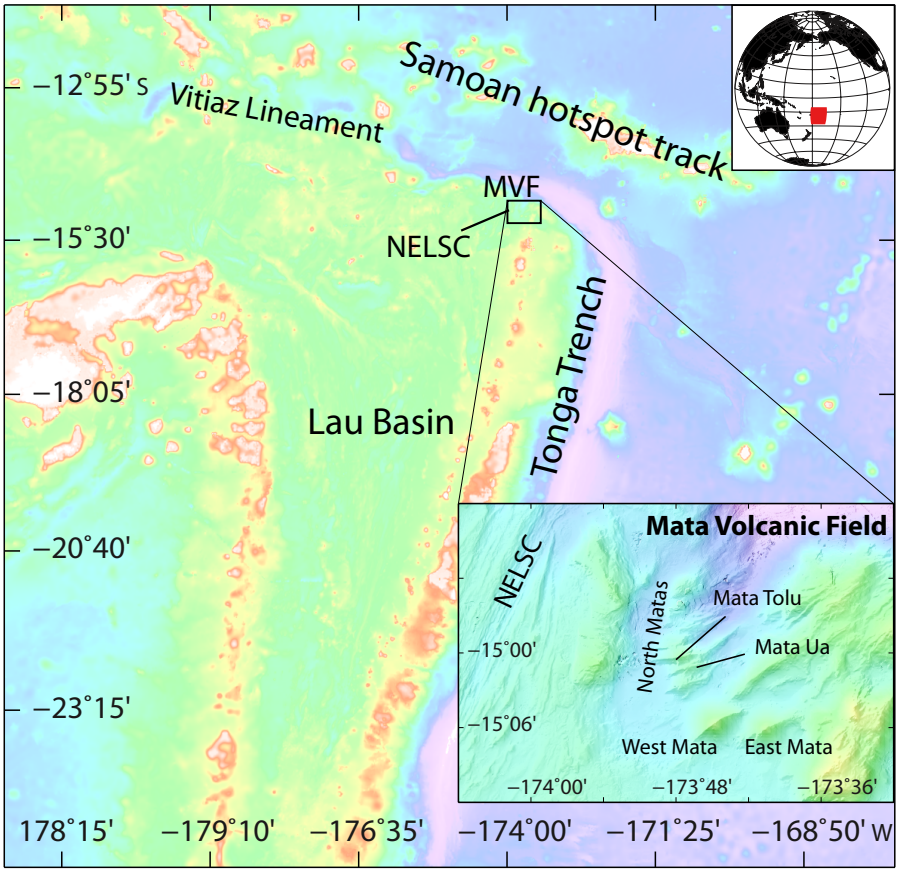

Figure 3.1. Map of the greater Lau Basin and Tonga arc region, SW Pacific. Inset shows the Mata Volcanic Field (MVF) and northern segment of the NE Lau Spreading Center (NELSC).

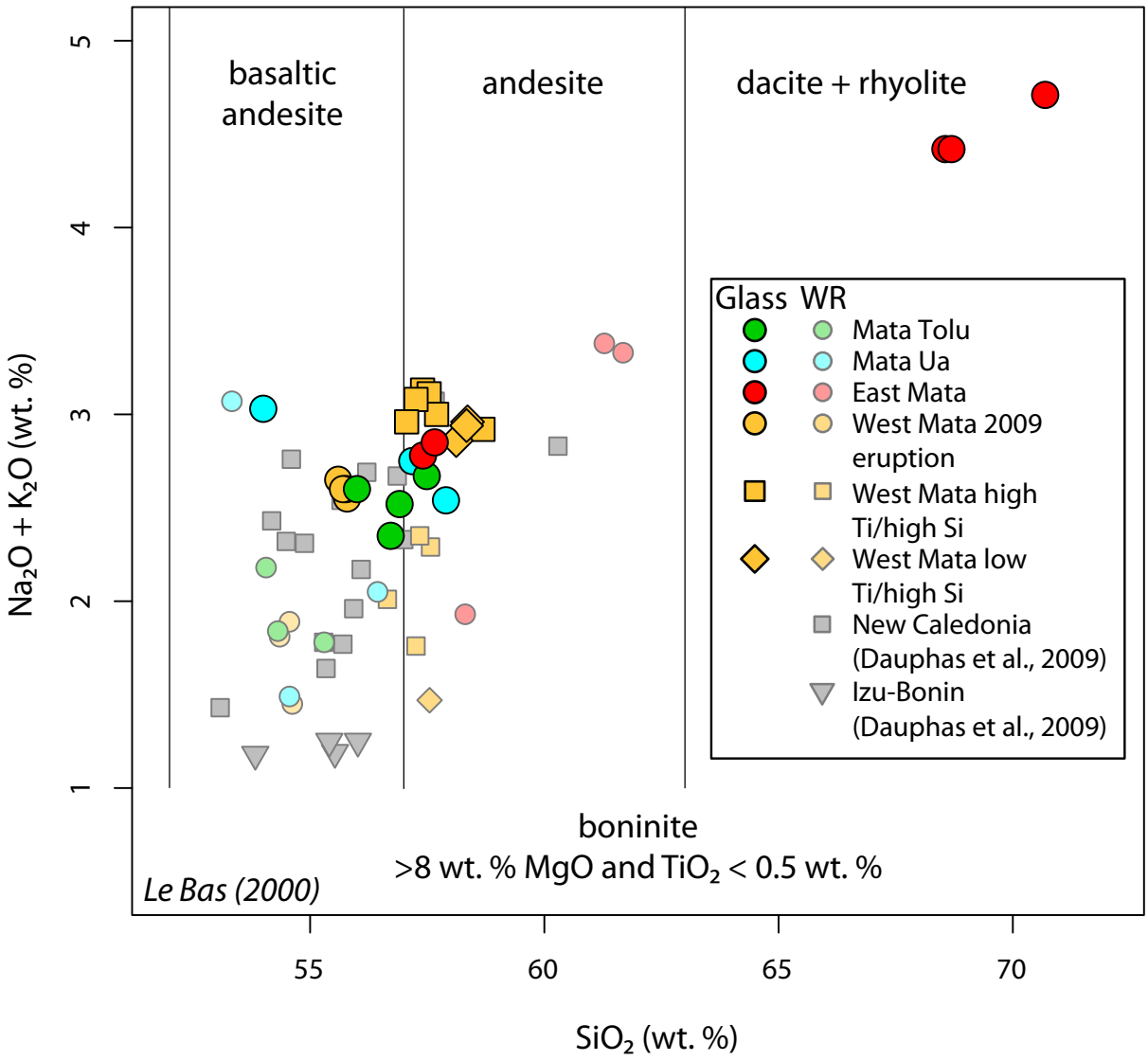

Figure 3.2. TAS diagram from Le Bas (2000) showing compositions of the samples used in this study vs. previously published whole-rock and glass data (Resing et al., 2011). Boninitic compositions in this study do not fit the published definition of a boninite; however, they are directly derived from boninite compositions.

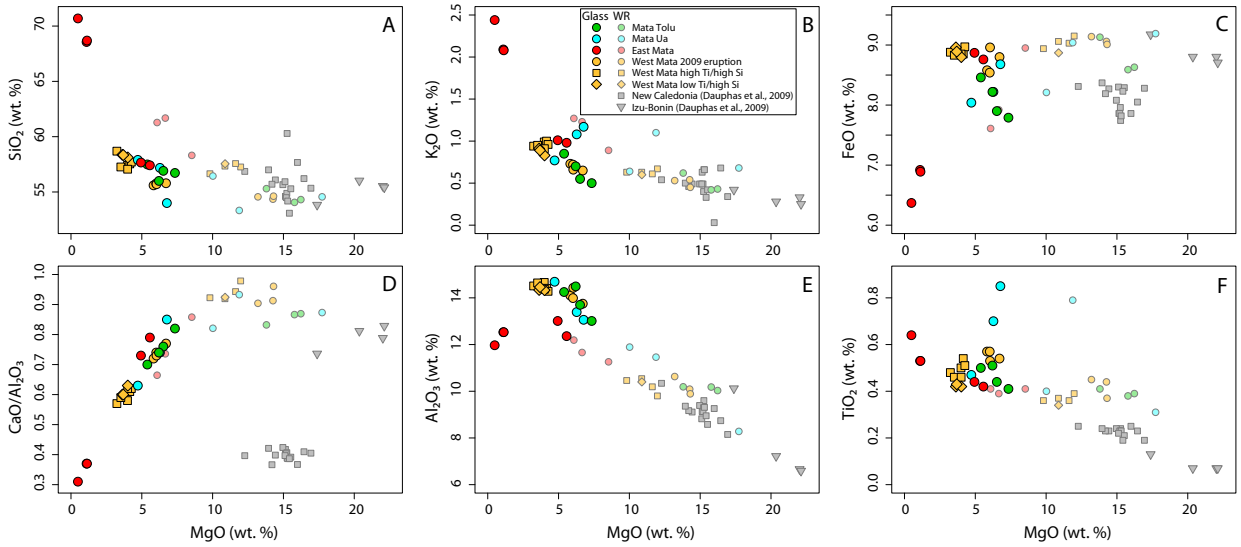

Figure 3.3. MgO vs. major element plots characterizing general behavior of the MVF and patterns within individual volcanoes. Whole data available for most MVF samples are also plotted, as well as the Izu-Bonin/New Caledonia data from Dauphas et al. (2009). All data are given as wt. %. **A)** MgO vs. SiO_2. The general differentiation pattern shows that all MVF volcanoes follow a similar differentiation slope. **B)** MgO vs K_2O. While the data display somewhat more scatter than with SiO_2, this is largely limited to more compositionally variable Mata Ua samples. **C)** MgO vs. FeO. West Mata and Mata Tolu compositions vary along a direction orthogonal to the differentiation trend suggested by the low MgO East Mata evolved samples. Given the limited variability in FeO of the boninitic compositions (~1 wt. %) and large variability in MgO, this offset between volcanoes is likely due to different parental melt compositions. Offsets are also observed in samples from various eruptive episodes in West Mata, suggesting different parental compositions are erupting from a single volcano. **D)** MgO vs. CaO/Al_2O_3 provides a marker for mineral precipitation. In this case, CaO is being removed from the melt relative to Al_2O_3, indicating clinopyroxene was precipitating from the melt. Despite the differing parental compositions between West Mata and Mata Tolu, the glass compositions fall on the same trendline, indicating the melts were being fractionated by identical crystallization processes. Crystallization, therefore, is not capable of producing the offsets seen in C. **E)** MgO vs. Al_2O_3, showing some offset between West Mata and Mata Tolu, although this behavior follows a more typical fractionation pattern. East Mata boninites, however, have lower Al_2O_3 than boninites from the other volcanoes, the origin of which is currently unconstrained. **F)** MgO vs. TiO_2 shows that TiO_2 for most samples remains fairly uniform. Two Mata Ua samples have higher TiO_2 than the rest of the sample set, and the East Mata evolved samples have slightly elevated average TiO_2 compared to the rest of the group, suggested that oxide fractionation may have removed primarily Fe from the melts, rather than Ti.

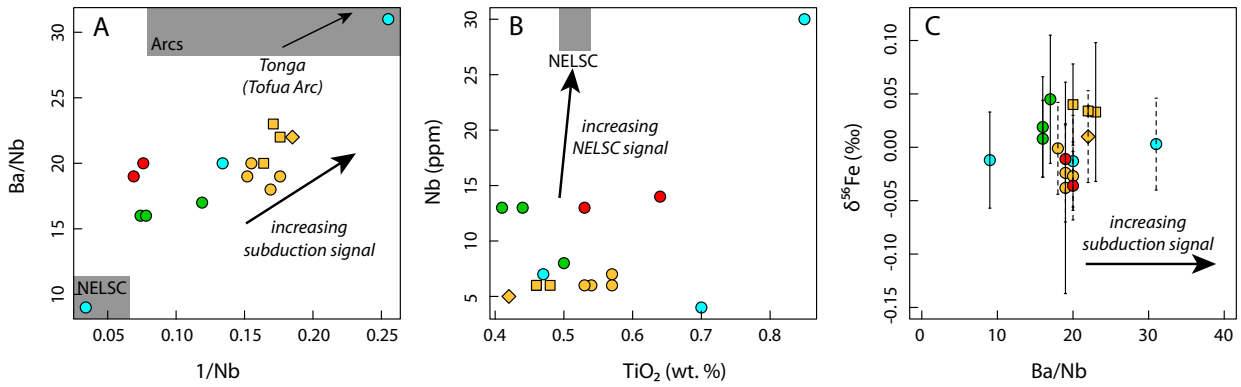

Figure 3.4. Selected trace elements as proxies for subduction input, after Lupton et al. (2015). Grey fields are labeled with representative source compositions (NELSC vs. arc-like) **A)** Ba/Nb vs. 1/Nb showing the relative depletion of Ba, a subduction fluid tracer relative to HFSE (Nb) in Tolu melts. Slightly Ba-enriched West Mata melts are still more depleted than arc melts, but have a stronger arc-like signal than Tolu. **B)** Nb/TiO_2, adapted from Lupton et al. (2015). Ti may be used to approximate behavior of Yb in the absence of REE data. NELSC melts are more Nb-enriched relative to TiO_2 than MVF melts (Lupton et al., 2015). Our Tolu samples plot between West Mata and the NELSC field. The influence of the subduction fluid component on East Mata compositions is unclear, as trace element data is only available for the differentiated subgroup, but not any of the more primitive compositions. **C)** Ba/Nb vs. $\delta^{56}Fe$, showing the slight negative correlation between Fe isotopic composition and presence of the subduction fluid component.

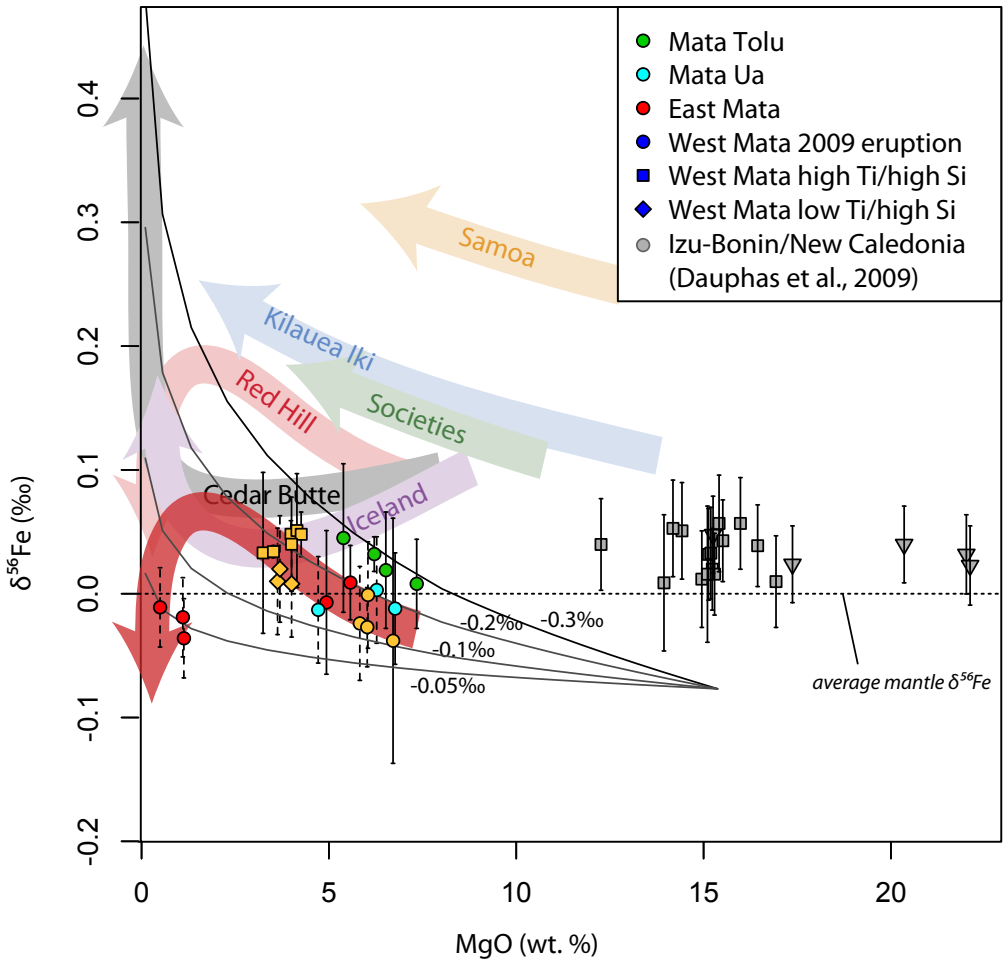

Figure 3.5. MgO vs. $\delta^{56}Fe$ of the sample set compared to other magmatic systems, adapted from Konter et al. (2016). Rayleigh curves are shown using fractionation factors of -0.05, -0.1, -0.2, and -0.3‰, assuming a boninitic parental melt with MgO = 15.4 wt. % (Table 3.1). The $\delta^{56}Fe_{initial}$ of -0.077‰ for the parental melt estimate was calculated using KM1129a D07-R01 $\delta^{56}Fe_{measured}$ and estimates of melt fraction along the boninite liquid line of descent. Melt fraction can be estimated by assuming a general relationship between measured KM1129a D07-R01 K_2O and FeO and K_2O and FeO of the estimated parent composition (Teng et al., 2008, 2013). The red arrow shows the approximate differentiation pattern shown by the sample set during melt evolution, which reflects a closed-system differentiation pattern similar to Red Hill- or Society-style differentiation.

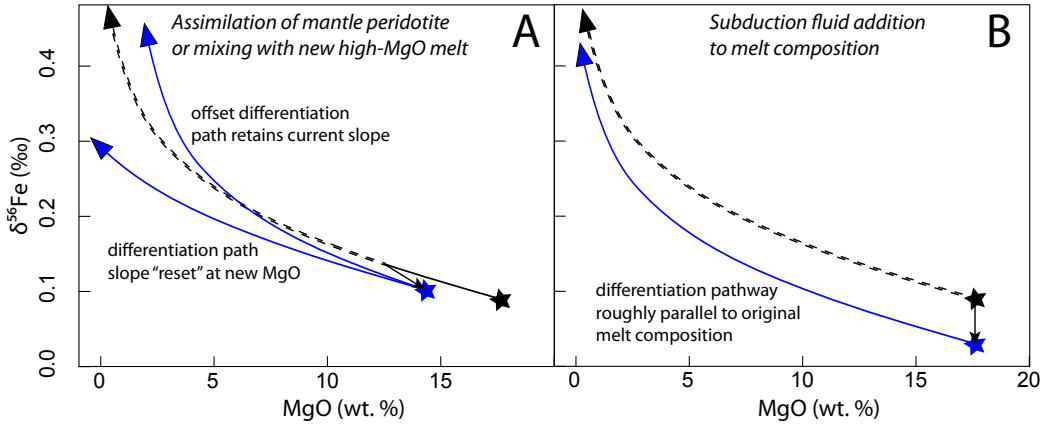

Figure 3.6. Conceptual models showing effects of magma mixing or assimilation processes on Fe isotope Rayleigh differentiation pathways. Black dashed lines show the expected fractionation pathway without subduction fluid modification. Arrows indicate the expected shift in composition with addition of a component, and blue lines are new, modified pathways. MgO and δ^{56}Fe values are arbitrary. **A)** Effect of adding a primitive or mantle-like assimilant to an existing melt composition (high MgO) along its differentiation pathway. The point at which the assimilant is added is arbitrary, as this is not presently a constrainable parameter. This composition will have both lower δ^{56}Fe and higher MgO, shifting the path backward. Depending on the system response and change in oxidation state of the melt, δ^{56}Fe fractionation may "reset", producing less overall fractionation, or the pathway may merely be displaced. The latter is less likely as the assimilant likely has a lower fO_2, particularly if it is olivine-rich. Additionally, a "reset" occurring further along the original evolutionary pathway will decrease the chances of parallel evolutionary slopes between compositions. **B)** Addition of a subduction component during melt generation. The effect on MgO content may be minimal; instead, Mg# of these melts is altered by incorporation of Fe (likely transported as fluid-mobile Cl complexes, e.g., Debret et al. (2016), which in this schematic is reflected by lower δ^{56}Fe than the original composition. In this case, the differentiation slopes between the two compositions remain roughly parallel, providing a possible explanation of the offset in the West Mata and Tolu trends.

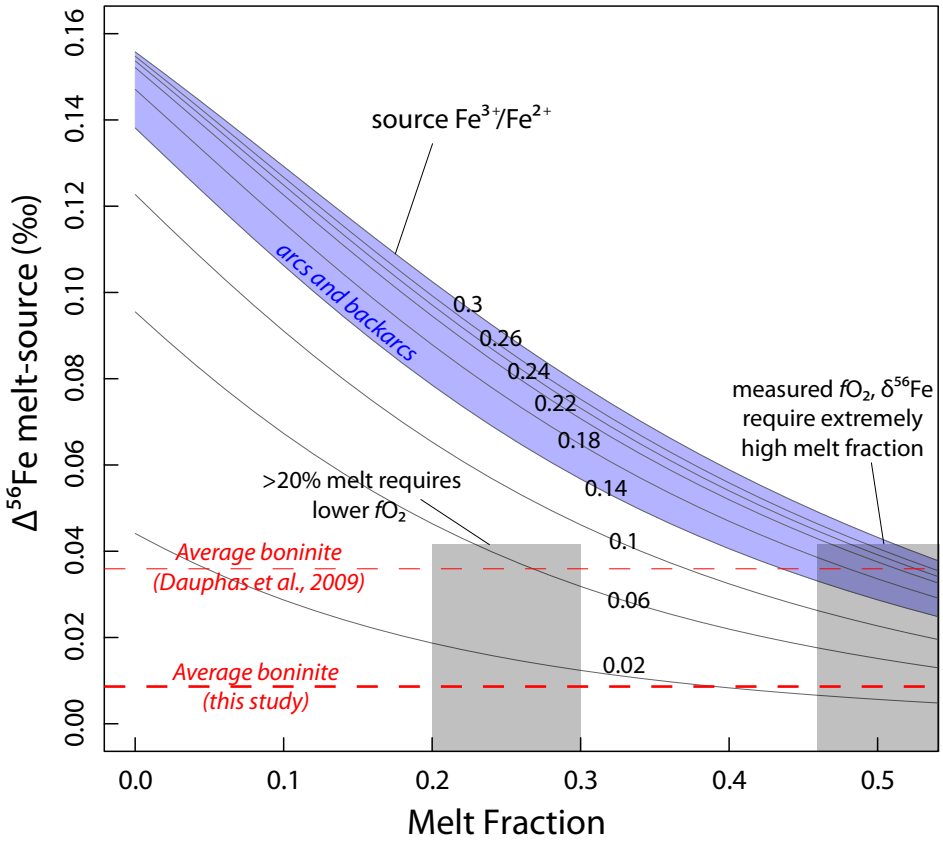

Figure 3.7. Non-buffered fractional melting modeling of expected Fe isotope fractionation between melt and source (after Dauphas et al., 2009; Konter et al., 2016). Various Fe^{3+}/Fe^{2+}source compositions are shown; the light blue field defines the range of backarc to arc oxidation states (Kelley and Cottrell, 2009). Grey boxes indicate proposed degrees of melt for boninites (>20%; Kushiro, 2007) and the minimum melt degree suggested by measured data. At highly oxidized arc settings, melt fractions in excess of 50% are required to produce the $\Delta^{56}Fe_{(melt\text{-}source)}$ found in Izu-Bonin/New Caledonia boninites, assuming typical mantle $\delta^{56}Fe$ (~0.0‰). An even larger melt fraction (calculated ~80%, not plotted) is required to achieve average MVF glass values (excluding the evolved East Mata subset). Such a large melt fraction may be unreasonable even for boninitic melts. Instead, another mechanism or addition of an isotopically light component is required to explain the low $\delta^{56}Fe$ in boninites.

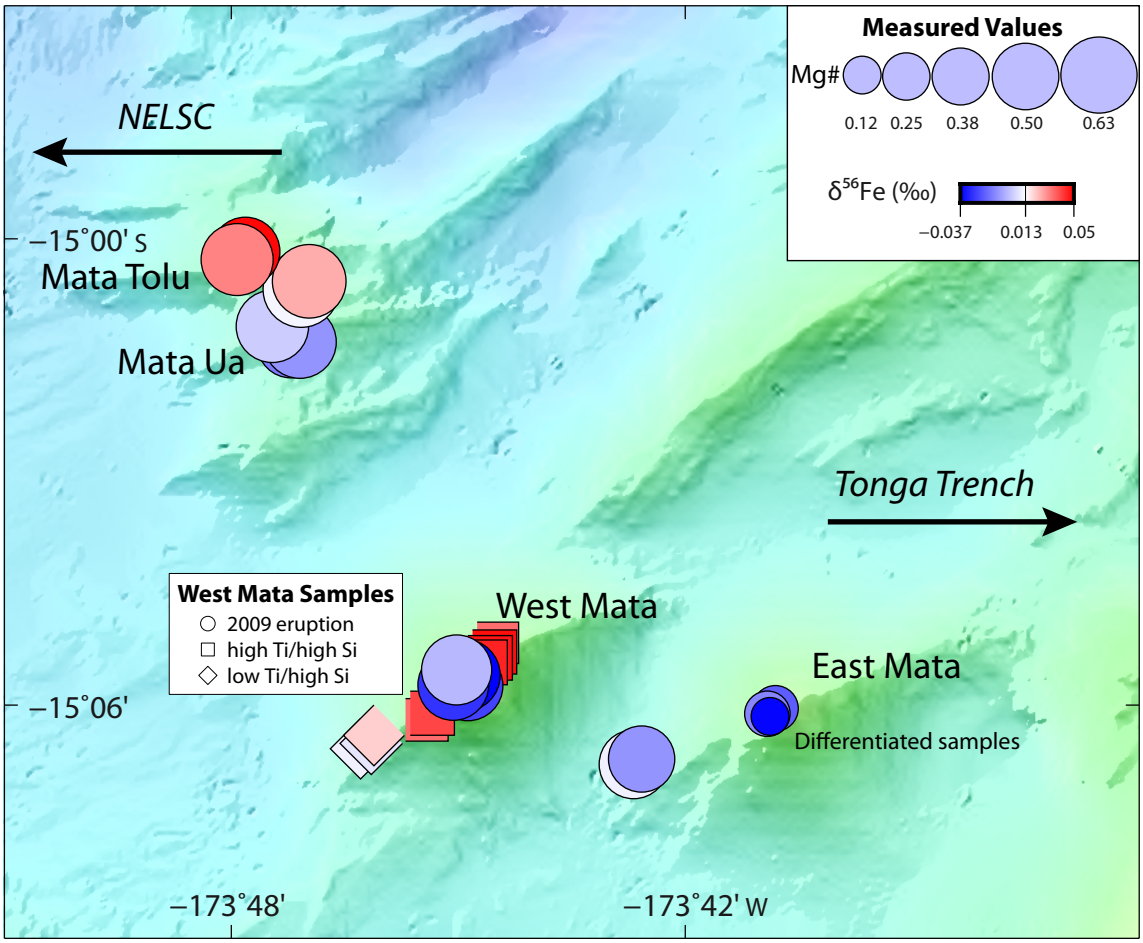

Figure 3.8. δ^{56}Fe vs. Mg# of melt compositions mapped at each sampled Mata volcano, showing the spatial distribution of compositions throughout the MVF. At a certain Mg# (symbol size), a simple, single-parent system should have similar δ^{56}Fe. As Mg# decreases, δ^{56}Fe should decrease until very low Mg#. However, comparably-sized West Mata and Mata Tolu symbols have different δ^{56}Fe. Mata Ua suggests some similarity to West Mata despite its proximity to Mata Tolu, suggesting differing levels of subduction fluid input at juxtaposed volcanoes.

3.9. References

Bedard, J.H., 2010. Parameterization of the Fe=Mg exchange coefficient (Kd) betwen clinopyroxene and silicate melts. Chem. Geol. 274, 169–176.

Calmant, S., Pelletier, B., Lebellgard, P., 2003. New insights on the tecotnics along the New Hebrides subduction zone based on GPS results. J. Geophys. Res. 108.

Cooper, L.B., Plank, T., Arculus, R.J., Hauri, E.H., Hall, P.S., Parman, S.W., 2010. High-Ca boninites from the active Tonga Arc. J. Geophys. Res. 115.

Craddock, P.R., Warren, J.M., Dauphas, N., 2013. Abyssal peridotites reveal the near-chondritic Fe isotopic composition of the Earth. Earth Planet. Sci. Lett. 365, 63–76.

Crawford, A.J., Falloon, T.J., Green, D.H., 1989. Classification, petrogenesis, and tectonic setting of boninites, in: Boninites and Related Rocks. pp. 1–49.

Danyushevsky, L. V., Sobolev, A. V., 1996. Ferric-ferrous ratio and oxygen fugacity calculations for primitive mantle-derived melts: calibration of an empirical technique. Mineral. Petrol. 57, 229–241.

Danyushevsky, L. V., Sobolev, A. V., Falloon, T.J., 1995. North Tongan high-Ca boninite petrogenesis: The role of Samoan plume and subduction zone-transform fault transition. J. Geodyn. 20, 219–241.

Danyushevsky, L.V., Sokolov, S., Falloon, T.J., 2002. Melt inclusions in olivine phenocrysts: Using diffusive re-equilibration to determine the cooling history of a crystal, with implications for the origin of olivine-phyric volcanic rocks. J. Petrol. 43, 1651-1671.

Dauphas, N., Craddock, P.R., Asimow, P.D., Bennett, V.C., Nutman, A.P., Ohnenstetter, D., 2009. Iron isotopes may reveal the redox conditions of mantle melting from Archean to Present. Earth Planet. Sci. Lett. 288, 255–267. doi:10.1016/j.epsl.2009.09.029

Dauphas, N., Janney, P.E., Mendybaev, R.A., Wadhwa, M., Richter, F.M., Davis, A.M., van Zuilen, M., Hines, R., Foley, C.N., 2004. Chromatographic separation and multicollection-ICPMS analysis of iron. Investigating mass-dependent and independent isotope effects. Anal. Chem. 76, 5855–63. doi:10.1021/ac0497095

Dauphas, N., Roskosz, M., Alp, E.E., Neuville, D.R., Hu, M.Y., Sio, C.K., Tissot, F.L.H., Zhao, J., Tissandier, L., Mèdard, E., Cordier, C., 2014. Magma redox and structural controls on iron isotope variations in Earth's mantle and crust. Earth Planet. Sci. Lett. 398, 127–140.

Dauphas, N., Teng, F.-Z., Arndt, N.T., 2010. Magnesium and iron isotopes in 2.7 Ga Alexo komatiites: Mantle signatures, no evidence for Soret diffusion, and identification of diffusive transport in zoned olivine. Geochim. Cosmochim. Acta 74, 3274–3291. doi:10.1016/j.gca.2010.02.031

Debret, B., Millet, M.-A., Pons, M.-L., Bouilhol, P., Inglis, E., Williams, H., 2016. Isotopic evidence for iron mobility during subduction. Geology 44, 215–218.

Elliot, T., 2003. Tracers of the slab, in: Inside the Subduction Factory. pp. 23–45.

Falloon, T.J., Crawford, A.J., 1991. The petrogenesis of high-calcium boninite lavas dredged

from the northern Tonga ridge. Earth Planet. Sci. Lett. 102, 375–394. doi:10.1016/0012-821X(91)90030-L

Falloon, T.J., Danyushevsky, L. V., Crawford, A.J., Meffre, S., Woodhead, J.D., Bloomer, S.H., 2008. Boninites and adakites from the northern termination of the Tonga Trench: Implications for adakite petrogenesis. J. Petrol. 49, 697–715.

Falloon, T.J., Danyushevsky, L. V., Crawford, T.J., Maas, R.A., Woodhead, J.D., Eggins, S.M., Bloomer, S.H., Wright, D.J., Zlobin, S.K., Stacey, A.R., 2007. Multiple mantle plume components involved in the petrogenesis of subduction-related lavas from the northern termination of the Tonga Arc and northern Lau Basin: Evidence from the geochemistry of arc and backarc submarine volcanics. Geochemistry, Geophys. Geosystems 8, 1–45.

Falloon, T.J., Malahoff, A., Zonenshain, L.P., Bogdanov, Y., 1992. Petrology and geochemistry of back-arc basin basalts from Lau Basin spreading ridges at 15°, 18°, and 19°S. Mineral. Petrol. 47, 1–35.

Finlayson, V.A., Konter, J.G., Ma, L., 2015. The importance of a Ni correction with ion counter in the double spike analysis of Fe isotope compositions using a 57Fe/58Fe double spike. Geochemistry, Geophys. Geosystems 16.

Glancy, S., 2014. Petrology and geochemistry of boninites and related lavas from the Mata volcanoes, NE Lau Basin. University of Hawaii at Manoa.

Green, T.H., 1995. Significance of Nb/Ta as an indicator of geochemical processes in the crust-mantle system. Chem. Geol. 120, 347–359.

Hibbert, K.E.J., Williams, H.M., Kerr, A.C., Puchtel, I.S., 2012. Iron isotopes in ancient and modern komatiites: Evidence in support of an oxidised mantle from Archean to present. Earth Planet. Sci. Lett. 321–322, 198–207. doi:10.1016/j.epsl.2012.01.011

Hickey, R.L., Frey, F.A., 1982. Geochemical characteristics of boninite series volcanics: implications for their source. Geochim. Cosmochim. Acta 46, 2099-2115.

Jackson, J.M., Hamecher, E.A., Sturhahn, W., 2009. Nuclear resonant X-ray spectroscopy of (Mg,Fe)SiO3 orthoenstatites. Eur. J. Mineral. 21, 551–560.

Kelley, K.A., Cottrell, E., 2009. Water and the oxidation state of subduction zone magmas. Science. 325.

Klügel, A., 2001. Prolonged reaction between harzburgite xenoliths and silica-undersaturated melt: implications for dissolution and Fe-Mg interdiffusion rates of orthopyroxene. Contrib. to Mineral. Petrol. 141, 1–14.

Konter, J.G., Pietruszka, A.J., Hanan, B.B., Finlayson, V.A., Craddock, P.R., Jackson, M.G., Dauphas, N., 2016. Unusual δ56Fe values in Samoan rejuvenated lavas generated in the mantle. Earth Planet. Sci. Lett. 450, 221–232.

Kushiro, I., 2007. Origin of magmas in subduction zones: a review of experimental studies. Proc. Japan Acad. Ser. B 83, 1–15.

Le Bas, M.J., 2000. IUGS Reclassification of the High-Mg and Picritic Volcanic Rocks. J. Petrol. 41, 1467–1470.

Lupton, J.E., Rubin, K.H., Arculus, R.J., Lilley, M.D., Butterfield, D.A., Resing, J.A., Baker, E.T., Embley, R.W., 2015. Helium isotope, C3/He, and Ba-Nb-Ti signatures in the northern Lau Basin: Distinguishing arc, back-arc, and hotspot affinities. Geochemistry, Geophys. Geosystems 16, 1133–1155. doi:10.1002/2014GC005625

Michael, P.J., Escrig, S., Rubin, K.H., Cooper, L.B., Langmuir, C.H., Clague, D.A., Keller, N.S., Plank, T., 2009. Major and trace elements and volatiles in glasses from the 2009 rapid response expedition to West Mata Volcano and Northeast Lau Spreading Center (NELSC), #V51D-1720, in: AGU Fall Meeting. San Francisco, CA.

Natland, J.H., 1980. The progression of volcanism in the Samoan linear volcanic chain. Am. J. Sci. 280–A, 709–735.

Nebel, O., Arculus, R.J., Sossi, P.A., Jenner, F.E., Whan, T.H.E., 2013. Iron isotopic evidence for convective resurfacing of recycled arc-front mantle beneath back-arc basns. Geophys. Res. Lett. 40, 5849–5853.

Nebel, O., Campbell, I.H., Sossi, P.A., Van Kranendonk, M.J., 2014. Hafnium and iron isotopes in early Archean komatiites record a plume-driven convection cycle in the Hadean Earth. Earth Planet. Sci. Lett. 397, 111–120. doi:10.1016/j.epsl.2014.04.028

Polyakov, V.B., Mineev, S.D., 2000. The use of Mössbauer spectroscopy in stable isotope geochemistry. Geochim. Cosmochim. Acta 64, 849–865. doi:10.1016/S0016-7037(99)00329-4

Price, A.A., Jackson, M.G., Blichert-Toft, J., Hall, P.S., Sinton, J.M., Kurz, M.D., Blusztajn, J., 2014. Evidence for a broadly distributed Samoan-plume signature in the northern Lau and North Fiji Basins. Geochemistry, Geophys. Geosystems 15. doi:10.1002/2013GC005061.Received

Resing, J.A., Rubin, K.H., Embley, R.W., Lupton, J.E., Baker, E.T., Dziak, R.P., Baumberger, T., Lilley, M.D., Huber, J.A., Shank, T.M., Butterfield, D.A., Clague, D.A., Keller, N.S., Merle, S.G., Buck, N.J., Michael, P.J., Soule, A., Caress, D.W., Walker, S.L., Davis, R., Cowen, J.P., Reysenbach, A.-L., Thomas, H., 2011. Active submarine eruption of boninite in the northeastern Lau Basin. Nat. Geosci. 4, 799–806. doi:10.1038/ngeo1275

Roeder, P.L., Emslie, R.F., 1970. Olivine-liquid equilibrium. Contrib. to Mineral. Petrol. 29, 275–289.

Rubin, K.H., Michael, P.J., Gill, J.B., Clague, D.A., Plank, T., Escrig, S., Glancy, S., Todd, E., Cooper, L., Keller, N., Langmuir, J., Embley, R.W., 2013. Timescale and petrogenesis of 2009 and older W. Mata boninite magmas. Mineral. Mag. 77, 2094.

Rubin, K.H., Michael, P.J., Perfit, M., Sinton, J.M., 2014. Magma dynamics from temporal and spatial compositional variations within and between eruptions. Goldschmidt Conf. Abstr. 2014, 2125.

Schuessler, J.A., Schoenberg, R., Sigmarsson, O., 2009. Iron and lithium isotope systematics of the Hekla volcano, Iceland - Evidence for Fe isotope fractionation during magma differentiation. Chem. Geol. 258, 78–91.

Sinton, J.M., Fryer, P., 1987. Mariana Trough lavas from 18 N: Implications for the origin of

back arc basin basalts. J. Geophys. Res. 92, 12782–12802.

Sio, C.K.I., Dauphas, N., Teng, F.-Z., Chaussidon, M., Helz, R.T., Roskosz, M., 2013. Discerning crystal growth from diffusion profiles in zoned olivine by in situ Mg–Fe isotopic analyses. Geochim. Cosmochim. Acta 123, 302–321. doi:10.1016/j.gca.2013.06.008

Sobolev, A. V., Danyushevsky, L. V., 1994. Petrology and geochemistry of boninites from the north termination of the Tonga Trench: Constraints on the generation conditions of primary high-Ca boninite magmas. J. Petrol. 35, 1183–1211.

Sossi, P.A., Foden, J.D., Halverson, G.P., 2012. Redox-controlled iron isotope fractionation during magmatic differentiation: an example from the Red Hill intrusion, S. Tasmania. Contrib. to Mineral. Petrol. 164, 757–772.

Stern, R.J., Bloomer, S.H., 1992. Subduction zone infancy: Examples from the Eocene Izu-Bonin-Mariana and Jurassic California arcs. Geol. Soc. Am. Bull. 104, 1621–1636.

Su, B.-X., Teng, F.-Z., Hu, Y., Shi, R.-D., Zhou, M.-F., Zhu, B., Liu, F., Gong, X.-H., Huang, Q.-S., Xiao, Y., Chen, C., He, Y.-S., 2015. Iron and magnesium isotope fractionation in oceanic lithosphere and sub-arc mantle: Perspectives from ophiolites. Earth Planet. Sci. Lett. 430, 523–532.

Taylor, B., Zellmer, K., Martinez, F., Goodliffe, A., 1996. Sea-floor spreading in the Lau back-arc basin. Earth Planet. Sci. Lett. 144, 35–40.

Teng, F.-Z., Dauphas, N., Helz, R.T., 2008. Iron isotope fractionation during magmatic differentiation in Kilauea Iki lava lake. Science. 320, 1620–2. doi:10.1126/science.1157166

Teng, F.-Z., Dauphas, N., Helz, R.T., Gao, S., Huang, S., 2011. Diffusion-driven magnesium and iron isotope fractionation in Hawaiian olivine. Earth Planet. Sci. Lett. 308, 317–324. doi:10.1016/j.epsl.2011.06.003

Teng, F.-Z., Dauphas, N., Huang, S., Marty, B., 2013. Iron isotopic systematics of oceanic basalts. Geochim. Cosmochim. Acta 107, 12–26. doi:10.1016/j.gca.2012.12.027

Turner, S., Hawkesworth, C., 1998. Using geochemistry to map mantle flow beneath the Lau Basin. Geology 26, 1019–1022.

Weyer, S., Ionov, D. a., 2007. Partial melting and melt percolation in the mantle: The message from Fe isotopes. Earth Planet. Sci. Lett. 259, 119–133. doi:10.1016/j.epsl.2007.04.033

Williams, H.M., Bizimis, M., 2014. Iron isotope tracing of mantle heterogeneity within the source regions of oceanic basalts. Earth Planet. Sci. Lett. 404, 396–407. doi:10.1016/j.epsl.2014.07.033

Williams, H.M., McCammon, C.A., Peslier, A.H., Halliday, A.N., Teutsch, N., Levasseur, S., Burg, J.-P., 2004. Iron isotope fractionation and the oxygen fugacity of the mantle. Science. 304, 1656–1659. doi:10.1126/science.1095679

Williams, H.M., Peslier, A.H., McCammon, C.A., Halliday, A.N., Levasseur, S., Teutsch, N., Burg, J.-P., 2005. Systematic iron isotope variations in mantle rocks and minerals: The effects of partial melting and oxygen fugacity. Earth Planet. Sci. Lett. 235, 435–452.

doi:10.1016/j.epsl.2005.04.020

Workman, R.K., Hart, S.R., 2005. Major and Trace Element Composition of the Depleted MORB Mantle (DMM). Earth Planet. Sci. Lett. 231, 53–72.

Yan, C.Y., Kroenke, L.W., 1993. A plate tectoni reconstruction of the southwest Pacific, 0-100 Ma. Proc. Ocean Drill. Program, Sci. Results 130.

Zambardi, T., Lundstrom, C.C., Li, X., McMurry, M., 2014. Fe and Si isotope variations at Cedar Butte volcano; insight into magmatic differentiation. Earth Planet. Sci. Lett. 405, 169–179.

Zellmer, K.E., Taylor, B., 2001. A three-plate kinematic model for Lau Basin opening. Geochemistry, Geophys. Geosystems 2.

CHAPTER 4: A HAWAIIAN-EMPEROR STYLE BEND IN THE HEMISPHERICALLY-ZONED RURUTU HOTSPOT REVEALED BY SR-PB-ND-HF ISOTOPES

V.A. Finlayson[a]*, J.G. Konter[a], K. Konrad[b], A.A.P. Koppers[b], M.G. Jackson[c], T.O. Rooney[d]

[a]Dept. Geology and Geophysics, School of Ocean and Earth Science and Technology, University of Hawai'i at Mānoa, Mānoa, Honolulu, HI 96822, USA

[b]Dept. Geology and Geophysics, College of Earth, Ocean, and Atmospheric Sciences, Oregon State University, Corvallis, OR 97331, USA

[c]Dept. Earth Science, University of California Santa Barbara, Santa Barbara, CA 93106, USA

[d]Dept. Geological Sciences, Michigan State University, East Lansing, MI 48824, USA

Abstract

Current Pacific absolute plate motion (APM) models include two major, long-lived hotspot tracks: the ~80 Ma Hawaiian-Emperor and the ~79 Ma Louisville tracks. Prior to ~50 Ma, these two tracks appear to show significant inter-hotspot drift, possibly due to southern motion of the Hawaiian plume. With the addition of a third long-lived hotspot track featuring a well-constrained hotspot location and a Hawaiian-Emperor-style Bend (herein referred to as the "Bend"), a more robust evaluation of the relationship between APM models and inter-hotspot drift becomes possible. Such a candidate exists in the Rurutu hotspot track. The youngest volcanism (~10-0.2 Ma) associated with the Rurutu hotspot is located in the Cook-Austral Islands. Here we show that Rurutu hotspot-related islands and seamounts along the older portion of the hotspot track can be related to compositions and APM model predictions, using $^{40}Ar/^{39}Ar$ ages and Sr-Pb-Nd-Hf "isotopic fingerprints".

The Rurutu hotspot has a distinctive composition that trends toward the HIMU mantle endmember, characterized in $^{206}Pb/^{204}Pb$ (≥20.0) and $^{87}Sr/^{86}Sr$ (≤0.704) ratios. This is a rare composition, and only two other hotspots worldwide have a similar composition. Rurutu is the only HIMU hotspot that continues into the West Pacific, allowing its effective use as a fingerprint. This HIMU signature can be traced through Samoa, through a Bend in the south Tuvalu Islands, continuing through the ~63-74 Ma Gilbert Ridge and the ~78-120 Ma Wake seamounts. The new data also reveal that this hotspot track consists of dual trend volcanism, possibly a consequence of bilateral plume heterogeneity. This is most clearly reflected in the Tuvalu Islands, just north of the Bend that is located where Tuvalu and Samoa volcanoes intersect. However, precisely locating the Rurutu Bend is complicated

because of the presence of two intersecting hotspot tracks. Therefore, we present a computational Bend location method that tests a range of APM models, all producing similar Bend locations within error of the models. Our new results confirm the presence of a third major hotspot track in the Pacific as originally proposed by Morgan, with a ~50.5-49 Ma Bend at 178.48°E and 8.56°S, in closer age agreement with the Hawaiian-Emperor Bend than the Louisville Bend.

4.1. Introduction

Pacific hotspot tracks were the early basis for absolute plate motion (APM) estimates. Under the initial assumption of hotspots as fixed locations of upwelling in Earth's mantle, APM modeling relied heavily on the long tracks of the Hawaiian-Emperor and Louisville hotspots (Figure 4.1). Large uncertainty exists in these models for Pacific plate motion older than ~50 Ma (e.g. Wessel and Kroenke, 2008), underscoring the need for additional APM constraints from a third long-lived Pacific hotspot.

Recent work suggests that the thermochemical anomalies sourcing hotspot volcanism may not remain stationary beneath tectonic plates; instead these sources might drift within the mantle over time (Koppers et al., 2011a; Tarduno, 2007; Tarduno et al., 2003). This adds uncertainty to fixed-hotspot APM models as the Hawaiian-Emperor plume possibly underwent southerly drift during formation of the Emperor track segment (>47 Ma), producing a sharper Hawaiian-Emperor Bend than suggested by comparison to the Indo-Atlantic hotspot reference frame (Cande et al., 1995). In contrast, the Louisville plume underwent a lesser degree of latitudinal drift and an unknown, possibly large, amount of longitudinal drift prior to ~55 Ma (Koppers et al., 2012; Wessel and Kroenke, 2008).

Pacific APM models are hampered by a mismatch of Bend ages between Louisville (50-51 Ma; Koppers et al., 2011a) and Hawaii (47 Ma, bending initiated at ~50 Ma according to Sharp and Clague, 2006), uncertainty in the present-day location of the Louisville plume (Koppers et al., 2011a), and the use of a patchwork of short-lived, age-progressive volcanic tracks distributed throughout the Pacific plate (e.g., Koppers et al., 2001; Wessel and Kroenke, 2008).

Finally, the absence of a hotspot track traceable beyond 80 Ma introduces significant uncertainty into tectonic reconstructions into the Mesozoic. With a lack of known seamount tracks older than 100 Ma, Large Igneous Provinces (LIPs), such as the Mid-Pacific Mountains, have been used to estimate Mesozoic APM (Wessel and Kroenke, 2008). However, large eruptive volumes of LIPs and their poorly understood eruption modes do not place tight constraints on plate motion, hence a well-defined hotspot track traceable beyond 80 Ma is needed to test existing APM models. Morgan (1972) originally proposed a long-lived "Austral-Gilbert-Marshall" hotspot track, based solely on Pacific Ocean seamount track morphologies. This is now considered part of the Rurutu hotspot track (e.g., Konter et al., 2008), but until this study, a Bend in the Rurutu track corresponding to the archetypal 47-50 Ma Hawaiian-Emperor Bend had not been located. Thus, new data are needed to fully trace this hotspot and integrate it with ages, , ~47-50 Ma Bends for Louisville and Hawaii, and existing Pacific APM models.

Evidence for a long-lived Rurutu hotspot track in the western Pacific Ocean was previously reported by Konter et al. (2008), Koppers et al. (2003), and Staudigel et al. (1991), but these studies were limited to volcanoes older than ~63 Ma. In this study, we characterize the section that includes the Bend and connects existing data sets. We present new elemental abundance and Pb-Sr-Nd-Hf isotope data from recently dredged samples in the Tuvalu and western Samoan (WESAM) seamounts (*R/V Roger Revelle*, expedition RR1310; Figure 4.1 inset). These data are used to first identify multiple compositional groups. We use compositions and new age determinations (Konrad et al., submitted) to distinguish a group of isolated Cretaceous seamounts formed at an extinct mid-ocean ridge and another group of younger volcanoes related to the Samoan hotspot. More importantly,

we identify another group of volcanoes that fits the expected Rurutu composition and age progression. Sampling density within the Rurutu-related volcanoes is high enough to distinguish two parallel trends that explain scatter in the compositional data and age progression of the hotspot. Having identified the locations of Rurutu volcanoes, we then locate the Rurutu Bend. The complex volcanic history of the Tuvalu area prevents straightforward identification of the Bend location, which we instead locate via a computational method reliant on newly-identified Rurutu volcanoes in the Tuvalu chain. The Rurutu Bend, occurring at ~49 Ma, is a key morphological feature in the chemically distinct Rurutu hotspot track, which we show continues from the Cook-Austral islands to the Samoan and Tuvalu chains, through the Gilbert Ridge, and into the Western Pacific.

4.2. Geologic History of the Southwest Pacific

4.2.1. Pacific Cretaceous Activity and Large Igneous Provinces

Volcanic activity in the Western Pacific increased during the early Cretaceous (starting ~140-120 Ma) with the development of the Pacific-Izanagi-Farallon triple junction and formation of multiple LIPs (Nakanishi et al. 1999; Neal et al. 1997), including the Ontong Java Nui "super plateau". Hochmuth et al. (2015) and Taylor (2006) suggest that Ontong Java Nui formed around 122 Ma, then rifted into three separate oceanic plateaux (Ontong-Java, Manihiki, and Hikurangi) shortly thereafter. Manihiki Plateau and Ontong Java Plateau (OJP) rifting possibly initiated by 119 Ma, forming the short-lived Ellice Basin (Taylor, 2006), which ceased spreading at ~86 Ma (Chandler et al., 2012). Late-stage OJP volcanic activity flared up at ~95-90 Ma (Taylor, 2006) and plate reconstructions suggest that by ~60 Ma, the Rurutu hotspot formed volcanoes in the northern Ellice Basin

(Konter et al., 2008; Koppers et al., 2003), producing the NNW-SSE trending Tuvalu chain and the projected Rurutu Bend near the intersection of the Tuvalu chain and WESAM.

4.2.2. The Hotspot Highway

The central South Pacific hosts a number of hotspot tracks that each define a limited but unique region of isotopic space, yet together they span the largest compositional range in the Pacific basin (e.g., $^{87}Sr/^{86}Sr$ = 0.7025-0.7205; $^{206}Pb/^{204}Pb$ = 17.4-22.0; $^{143}Nd/^{144}Nd$ = 0.5123-0.5132; e.g., Staudigel et al., 1991, Jackson et al., 2007). Some hotspots define extreme "endmember" compositions that represent geochemically distinct mantle reservoirs: HIMU, EM1, EM2, and MORB (Zindler and Hart, 1986). The endmembers, when plotted in $^{87}Sr/^{86}Sr$ -$^{143}Nd/^{144}Nd$ -$^{206}Pb/^{204}Pb$ isotopic space, anchor each apex of the so-called "mantle tetrahedron" and enclose the range of all known mantle isotopic compositions. Hotspot tracks plotted on these axes tend to form distinct arrays that radiate away from a common composition central to the tetrahedron ('FOZO'; Hart et al., 1992 or 'C'; Hanan and Graham, 1996).

These distinct seamount isotopic compositions and radiometric ages are used as a "fingerprint" to uniquely identify individual hotspot tracks in areas where multiple episodes of hotspot activity have overlapped (Konter et al., 2008; Koppers et al., 2003; Staudigel et al., 1991). During the last ~60 Myr, for example, the Ellice Basin region (Figure 4.1, Supplemental Figure S.4.1) passed over multiple isotopically distinct mantle plumes, each separated by at least 950 km –Samoa, Rarotonga, Rurutu and Macdonald. The plumes left overlapping hotspot tracks, resulting in areas of juxtaposed seamounts with different ages and geochemical signatures. This swath of the Pacific with the highest density of

overlapping hotspot tracks was consequently dubbed the "Hotspot Highway" (Jackson et al., 2010). The Samoan track bears strong EM2 signatures ($^{87}Sr/^{86}Sr > 0.704$ and $^{206}Pb/^{204}Pb \sim 18.5\text{-}19.5$; Jackson et al., 2007) and some EM1-like rejuvenation stage lavas (Konter and Jackson, 2012), both of which are distinct from the less radiogenic Sr and more radiogenic Pb, Nd and Hf compositions characteristic of Rurutu. Rurutu hotspot isotopic compositions range from HIMU ($^{206}Pb/^{204}Pb \geq 20.0$ from high μ – $^{238}U/^{204}Pb$ – ratios in the mantle source; $^{87}Sr/^{86}Sr < 0.7035$), dominant in the older volcanoes, to FOZO, found primarily in more recent volcanism (Chauvel et al., 1997). Similarly, the Rarotonga track is distinguished by an EM1 isotopic signature ($^{206}Pb/^{204}Pb < 18.0$, $^{143}Nd/^{144}Nd < 0.5126$) largely distinct from Rurutu and overlapping with rejuvenated Samoa (Jackson et al., 2010).

In addition, APM projections indicate that the Rurutu, Samoa, and Rarotonga tracks overlap in the Samoan chain (Figure 4.1), but along the Hotspot Highway, Rurutu hotspot volcanoes are ~10 Ma and ~20 Ma older than Rarotonga hotspot and Samoan hotspot volcanoes, respectively. The Macdonald hotspot produced the type HIMU signature similar to Rurutu, but it is located too far east to overlap in the Ellice Basin (Supplementary Figure S.4.1). Thus, the locations, ages and geochemistry of seamounts along the Hotspot Highway can be used to assign each volcano to the Rurutu, Rarotonga, or Samoa hotspot.

4.2.3. Tracing the Rurutu Hotspot

The Rurutu hotspot track can be broken up into several different segments, extending as far back as ~120 Ma in the Northern Wake chain, where the track is lost due to low sampling density (Konter et al., 2008; Koppers et al., 2003). A younger Rurutu

segment comprises the Gilbert Ridge (73-64 Ma; Koppers et al., 2007). Within the Samoan chain, “interloper” seamounts like Rose Atoll and Malulu bear non-Samoan HIMU- to FOZO-like signatures that contrast with the characteristically Samoan EM2 signature (Jackson et al., 2010). While age determinations for these interlopers could not be obtained, thick ferromanganese rinds and advanced alteration of recovered samples suggests these volcanoes are older than adjacent Samoan seamounts, consistent with formation by an older hotspot (Jackson et al., 2010). East of Rose Atoll in the easternmost region of the Samoan chain lies a swath of unsampled seafloor extending to the western Cook Islands that hosts relatively little volcanic activity. Further east still, the Young Rurutu trend in the Cook-Austral islands (10-0 Ma; Chauvel et al., 1997) has modern activity near Arago Seamount (Bonneville et al., 2002).

Between the Gilbert Ridge and the interloper-hosting Samoan chain lies the Tuvalu chain. The southern end of the Gilbert Ridge was investigated as the Bend, but found to be an older intersection of volcanic tracks with widely varying compositions (~66, 75, and 115 Ma; Koppers and Staudigel, 2005; Konter et al., 2008). In this study, we argue that the Rurutu Bend is located in the southern part of the Tuvalu chain. A Tuvalu-based Bend is consistent with existing APM models and the Gilbert Ridge ages (Figure 4.1). This suggests that Morgan's (1972) “Austral-Gilbert-Marshall” track is now finally confirmed, with its expected Bend in Tuvalu, and its active eruptive center at Arago seamount in the Cook-Austral Islands.

In this study, we focus on identifying the Rurutu hotspot Bend and linking all known Rurutu segments into a single long hotspot track by using its distinctive isotopic signature and expected age progression to trace the hotspot through the Tuvalu and WESAM study

area. Because the origins of Tuvalu volcanoes have not been extensively studied in prior work, we first assess the mantle source signatures. Tuvalu volcanoes with a Rurutu signature are then used to identify the most probable Rurutu hotspot track morphology, using fundamentally different APM models to assess the potential error in Bend location.

4.3. Samples

Most samples analyzed in this study were obtained during the 2013 *R/V Roger Revelle* RR1310 cruise. We evaluate a total of 42 samples (Table 4.1), representing 27 RR1310 dredges, two dredges from KK820316 (*R/V Kana Keoki*; Sinton et al., 1985), two MW8602 samples (*R/V Moana Wave*; Keating, 1996), and one from the SO66/59DSR cruise (*F/S Sonne*; Bau et al., 1996). Samples are mainly basaltic pillow and tube fragments with variable degrees of alteration (altered olivine phenocrysts and groundmass; some veins). The area represented by this sample set is largely limited to the Tuvalu chain, extending slightly southward into WESAM to capture the predicted Rurutu Bend (Figure 4.1 inset).

4.4. Methods

The RR1310 samples were analyzed for major and trace element groundmass compositions (Supplemental Tables S.4.1, S.4.2) and Sr, Pb, Nd, and Hf isotopes (Supplemental Table S.3). In brief, samples were crushed with metal free techniques. Major and trace element analyses were performed using XRF and LA-ICP-MS at Michigan State University (Rooney et al., 2015) on unleached rock chips that were handpicked to minimize the effects of alteration. Samples analyzed for radiogenic isotopes were acid-leached following the protocol modified from Koppers et al. (2003) and analyzed from single

dissolutions for Pb-Sr-Nd isotopes following Konter and Storm (2014) and Hf isotopes following Connelly et al. (2006). Age corrected isotope data and correction methods are presented in Supplemental Table S.4.4. A leaching experiment was performed on two samples to evaluate the removal of secondary Pb isotopic signatures (see Section 4.6). All separations used Eichrom resins, purifying Sr by Sr-Spec, Pb by Sr-Spec and AG1-x8, Nd by TRU and LN-resin, and Hf by AG50-x8 and DGA resin. Pb was analyzed by MC-ICP-MS using standard-sample bracketing and monitoring fractionation with Tl doping. Sr, Nd and Hf were analyzed by MC-ICP-MS (Konter and Storm, 2014), with a subset of Sr analyses duplicated via TIMS. Full sample separation and analytical details are provided in the supplement.

$^{40}Ar/^{39}Ar$ plateau ages for a subset of seamounts in this study were obtained at the Oregon State University Argon Geochronology Laboratory via laser step-heating (Konrad et al., submitted). All $^{40}Ar/^{39}Ar$ age determinations discussed herein are normalized to a Fish Canyon Tuff standard age of 28.201 ± 0.046 Ma (Kuiper et al., 2008) and errors are reported with 2σ uncertainties. For convenience, age data relevant to this study are found in Supplemental Table S.4.4 and Supplemental Age Data.

4.5. Results

4.5.1. Major and Trace Elements

Sample compositions show relatively enriched concentrations of incompatible elements relative to more compatible elements (Supplemental Table S.4.2, Supplemental Figures S.4.2, S.4.3, S.4.4). Samples show a range in absolute (unnormalized) concentration ratios La/Yb (~5-35) vs. La/Sm (~2-10) that is typical of OIB compositions (e.g., Weaver,

1991). Primitive mantle-normalized trace element patterns (Sun and McDonough, 1989; Figure 4.2) for different geochemical groups occurring in Tuvalu, best defined in isotope space (Section 4.5.2), show both subtle differences between the groups and the effects of post-eruptive alteration. Trace element variations reflecting alteration are discussed in Section 4.6. Compositional differences between volcanic groups are most clearly displayed in the slopes of the trace element patterns. Group 1 trace element patterns are generally steepest, falling within the expected HIMU range (Weaver, 1991), and within the field defined by Young Rurutu samples from the Cook-Austral region (Figure 4.2A). Group 2 samples (89 to 95 Ma) exhibit intermediate slopes and isotopic behavior, similar to previously documented ~90 Ma late-stage OJP volcanism in the region, in particular the Sigana Alkalic Suite, which is distinct from the relatively flat patterns of the main 120 Ma phase of OJP activity (Tejada et al., 1996; Figure 4.2B). Group 3 has relatively flat trace element patterns (Figure 4.2C) and tholeiitic to alkalic major element composition (Supplemental Figure S.4.2), which agree well with depleted WESAM compositions such as those from Alexa Bank (Hart et al., 2004; Figure 4.1). The Group 4 sample, while similar in age to Group 3, displays a much steeper trace element pattern with geochemical signatures similar to those of some eastern Samoan lavas.

4.5.2. Radiogenic Isotopes and Geochemical Groups

The radiogenic isotopic compositions reported here cover nearly a third of the isotopic ranges defining MORB and OIB. However, Rurutu-related volcanoes are clearly distinguished from other sources when also incorporating age data. Relying on the combination of isotopic compositions and ages, we distinguish four groups; 1) similar to

present-day Rurutu hotspot, 2) similar to the Sigana Alkalic Suite (late-stage OJP), 3) similar to tholeiitic Samoan samples from Alexa Bank, 4) similar to common alkalic Samoan lavas. Below, present-day as well as age-corrected isotope ratios are presented (Supplemental Table S.4.4), using parent/daughter ratios calculated from the trace element data.

4.5.2.1 Group 1: Similar to Rurutu

Group 1 lavas (including samples from dredges D02-D11, D13-D16, D18, D22, D23, D24, D27 older series) have ages 75-42 Ma (Supplemental Table S.4.4) and geochemical and isotopic compositions consistent with Rurutu hotspot track predictions. The samples plot between the FOZO and HIMU endmembers (Supplemental Table S.4.3). Two seamounts (D02, D22) plot near FOZO, similar to some Rurutu hotspot-related Gilbert volcanoes (Konter et al., 2008). Overall, measured $^{206}Pb/^{204}Pb$ covers a wide range from 19.256 to 21.654, $^{207}Pb/^{204}Pb$ ranges from 15.418 to 15.800, and $^{208}Pb/^{204}Pb$ varies 38.840-42.059. Similar to Pb isotopes, $^{87}Sr/^{86}Sr$ is variable (0.70269-0.70366), as are $^{143}Nd/^{144}Nd$ (0.51280-0.51304), and $^{176}Hf/^{177}Hf$ (0.28283-0.28309); these values align with expectations for the Rurutu hotspot (e.g., Konter et al., 2008).

Group 1 volcanoes split into two distinct radiogenic isotopic compositions that form parallel volcanic tracks: the incompatible-depleted "Sil" (more radiogenic $^{143}Nd/^{144}Nd$ and $^{176}Hf/^{177}Hf$) and incompatible-enriched "Niu" (less radiogenic $^{143}Nd/^{144}Nd$ and $^{176}Hf/^{177}Hf$) trends. These are most distinct in $^{143}Nd/^{144}Nd$ vs. $^{206}Pb/^{204}Pb$ (Figure 4.3A), although visible in all other isotopic axes except for $^{207}Pb/^{204}Pb$ vs. $^{206}Pb/^{204}Pb$ (Figure 4.3D). Measured $^{206}Pb/^{204}Pb$ values for the Niu trend range from 19.301-21.654, while $^{87}Sr/^{86}Sr$ ranges from 0.70282-0.70366. $^{143}Nd/^{144}Nd$ (0.51279-0.51290) and $^{176}Hf/^{177}Hf$ (0.28284-

0.28301) for Niu-trend lavas are both relatively unradiogenic. The Sil trend also displays a wide range in $^{206}Pb/^{204}Pb$ (19.254-20.454). $^{87}Sr/^{86}Sr$ is less radiogenic and more MORB-like (0.70269-0.70285) than the Niu trend. Similarly, $^{143}Nd/^{144}Nd$ (0.51293-0.51304) and $^{176}Hf/^{177}Hf$ (0.28299-0.28310) are more depleted (radiogenic), also trending toward MORB-like ratios. The Niu and Sil trends remain after age correction to initial ratios and forward modeling to present day compositions using modeled reservoir parent-daughter ratios, suggesting the trends reflect true compositional heterogeneity in the plume, rather than an effect of radiogenic ingrowth (Supplemental Table S.4.4, Supplemental Figure S.4.5, Supplemental Figure S.4.6).

4.5.2.2 Group 2: Similar to Sigana Alkalic Suite (OJP)

Group 2 (D12, D19, D20) features more evolved major element chemistry (MgO < 1.5 wt. %) than the other groups, large ion lithophile element (LILE)-enriched trace element chemistry, and moderately to highly radiogenic isotopic compositions. The samples predate (95-89 Ma; Supplemental Table S.4.4) the predicted age range for Rurutu volcanoes in Tuvalu by ~30 Myr (Supplemental Figure S.4.1), and their mismatch in composition and age suggests they are not related to the Rurutu hotspot.

Group 2 samples have high $^{143}Nd/^{144}Nd$ (0.51294-0.51322), high $^{206}Pb/^{204}Pb$ (19.761-20.603), and intermediate $^{208}Pb/^{204}Pb$ and $^{207}Pb/^{204}Pb$ (38.054-39.297; 15.541-15.702). Overall, the sample ratios plot within HIMU and MORB compositional ranges although deviations occur: $^{87}Sr/^{86}Sr$ (0.70278-0.70478) and $^{176}Hf/^{177}Hf$ (0.28288-0.28303), for example, plot within the range defined by MORB and HIMU, but $^{176}Hf/^{177}Hf$ is decoupled from $^{143}Nd/^{144}Nd$ (Figure 4.3C, 4.3E). In $^{208}Pb/^{204}Pb$ vs. $^{206}Pb/^{204}Pb$ (Figure 4.3B), these

samples form a scattered subhorizontal trend well below the Northern Hemisphere Reference Line (NHRL; Hart, 1984), while in $^{207}Pb/^{204}Pb$ vs. $^{206}Pb/^{204}Pb$ (Figure 4.3D), these samples plot with Group 1 in the HIMU field.

4.5.2.3 Group 3: Similar to Alexa Bank Samoan tholeiites

Group 3 (D21, D26, D27 younger series, D33) samples were obtained from seamounts in southern Tuvalu and WESAM with compositions that do not fit the combined geochemical characteristics and ages expected for the Rurutu hotspot. Instead, sample compositions ($^{143}Nd/^{144}Nd$ ranges 0.51293-0.51301; $^{206}Pb/^{204}Pb$ 18.614-19.033; $^{87}Sr/^{86}Sr$ 0.70355-0.70417; $^{176}Hf/^{177}Hf$ 0.28307-0.28314) match closely with the depleted signatures characteristic of Alexa Bank in the Samoan WESAM province (Hart et al., 2004). Dated samples are much younger (15-9 Ma) than the age range reported for Group 1, falling within the age range expected for the WESAM province (Supplemental Figure S.4.1, S.4.7). Notably, this group includes a 14.8 Ma sample from D27, which also yielded older (46-42 Ma) Group 1-type samples, suggesting the seamount underwent two distinct periods of activity.

4.5.2.4 Group 4: Similar to alkalic Samoan lavas

The single Group 4 sample has an age and geochemistry consistent with an EM2 origin and lacks the depleted component characteristic of Group 3 (D32-02/Lafetoga, 11.1 Ma; Supplemental Table S.4.4). The sample displays radiogenic $^{87}Sr/^{86}Sr$ (0.705108), moderately radiogenic $^{206}Pb/^{204}Pb$ (19.0508) and relatively unradiogenic $^{143}Nd/^{144}Nd$ and $^{176}Hf/^{177}Hf$ (0.512662, 0.282879), plotting within the Samoan field. Compared to Group 3,

this sample has a steeper trace element pattern, and an isotopic composition further from FOZO, and closer to the EM2 end-member, also defined by Samoan lavas.

4.6. Alteration and Non-Rurutu Sources

4.6.1 Alteration Signatures

4.6.1.1 Trace Elements

Seawater alteration visible in hand sample and thin section indicates that alteration processes may have overprinted some major and trace element data, particularly data for fluid-mobile elements. Both elemental and isotopic compositions of samples are subject to secondary alteration. For isotopes, this is addressed through acid leaching samples, discussed further in Supplemental Methods. Since leaching may fractionate the original magmatic trace element ratios, however, these values consequently are usually measured on unleached samples (e.g., Koppers et al., 2003) where alteration effects are readily observed. Alteration effects are clearest in fluid-mobile elements, which show significant scatter compared to more immobile elements such as the high field strength elements (HFSE; Figure 4.2). Alteration in fluid-mobile elements can be quantified by the Ba/Rb ratio, which is commonly ~12 for both OIB and MORB; altered submarine samples have lower values because of Rb enrichment (e.g., Hart et al., 1999). Half of the Tuvalu samples have ratios below 12, down to 2.5, implying caution should be exercised in the interpretation of trace elements with respect to magmatic processes.

Secondary carbonates, ferromanganese crust, and clay contribute seawater compositions to the samples, while marine phosphate can enrich rocks in elements that are typically low abundance in seawater (e.g., Cheng et al., 1987; Grandjean et al., 1987). On

mantle-normalized diagrams, several samples show a small positive anomaly in Y, as well as nearly flat heavy rare earth element (HREE) pattern, features previously interpreted to indicate marine phosphate addition (e.g., Vanderkluysen et al., 2014). Given these effects, we emphasize isotopic compositions, although below we discuss specific circumstances in which alteration effects remain after leaching.

4.6.1.2 Isotopic Compositions

In combination with leaching, hand-picking the samples removes obvious ferromanganese crust and carbonate. Although seemingly effective for ferromanganese crust, elevated $^{87}Sr/^{86}Sr$ ratios and $^{206}Pb/^{204}Pb$ ratios – the result of Sr exchange and U enrichment, summarized in Bach et al. (2003) – are clearly present in unleached rocks, while leached samples often still display scatter in $^{87}Sr/^{86}Sr$ ratios (e.g., Koppers et al., 2003). In this case, despite the aggressive acid leaching during sample preparation, some effects remain. We identify two sets of outlying compositions in radiogenic isotopes, and these two groups are distinguished by differing isotopic signatures; 1) elevated $^{143}Nd/^{144}Nd$ and $^{206}Pb/^{204}Pb$ ratios, and 2) elevated $^{208}Pb/^{204}Pb$ ratios. We discuss these cases below. However, the majority of the samples (particularly <75 Ma) do not display any outlier compositions for single isotope ratios, suggesting that leaching was effective.

The first outlier group, with elevated $^{143}Nd/^{144}Nd$ and $^{206}Pb/^{204}Pb$ ratios, are found in Group 2 samples, which differ from Group 1 (Rurutu volcanoes) in their radiogenic $^{143}Nd/^{144}Nd$ and unradiogenic $^{87}Sr/^{86}Sr$ (Figure 4.3). The Nd-Sr composition is characteristic of MORB, despite their OIB-like, LILE-enriched trace element patterns. However, the outlying Group 2 $^{143}Nd/^{144}Nd$ values are clearly unusual compared to

$^{206}Pb/^{204}Pb$ and $^{176}Hf/^{177}Hf$, plotting outside most known mantle compositions. Leaching studies have shown that marine phosphate is a common alteration phase with high Sm/Nd that can be removed from old seafloor basalts (Cheng et al., 1987), and it is probably the cause of unusual Group 2 Nd isotopic compositions. Marine phosphate Sm/Nd ratios up to three times higher than most rocks (e.g., Grandjean et al., 1987) can result from phosphate recrystallization during which Sm and Nd are exchanged with seawater (Reynard et al., 1999). Thus, remobilized phosphate deposited shortly after rock formation could disrupt the primary signature and cause the observed radiogenic $^{143}Nd/^{144}Nd$ over time, even after leaching. Moreover, phosphates may have extremely high U/Th values (Baturin, 2001), and the low $^{208}Pb^*/^{206}Pb^*$ present in Group 2 might reflect this process. Thus, Group 2 samples have likely high time-integrated Nd and Pb isotope compositions due to phosphate that have offset their present-day compositions from the FOZO/C side of the MORB field.

The second outlier group, consisting of three samples from this study and the studies of Konter et al. (2008) and Koppers et al. (2003), contain elevated $^{208}Pb/^{204}Pb$ ratios plotting significantly above the NHRL, unlike other Rurutu volcanoes and HIMU compositions in general (Figure 4.3). Given the unusual isotopic composition of D05-08, a duplicate analysis of the sample was obtained. Unlike duplicates of other samples the Pb isotope compositions did not reproduce within error (Supplemental Table S.4.3). Consequently, this sample was subjected to a more aggressive stepwise leaching test. The leach compositions progressively approached the final leached composition (Supplemental Table S.4.5), which again, did not reproduce previous isotope values for the sample. In contrast, leaches from our other test sample (D20-15) replicated the original Pb isotope values (see Supplement). This suggests that alteration effects are not limited to secondary

products removed by leaching; rather they can be hosted in a more resistant phase. The isotopic compositions provide some insight into possible causes.

Since both $^{206}Pb/^{204}Pb$ and $^{208}Pb/^{204}Pb$ values are high for D05-08, its composition must represent high time-integrated parent/daughter ratios. Particularly, the high κ ($^{232}Th/^{238}U$) necessary to produce the observed $^{208}Pb/^{204}Pb$ (κ > 4; Supplemental Figure S.4.8) is unusual for mantle-derived melts. Typical alteration processes instead increase U (and Th, to an extent) content, lowering the κ (e.g., Fowler and Zierenberg, 2016; Macdougall et al., 1979; Valsami-Jones and Ragnarsdottir, 1997). Thorium is usually immobile during alteration, but large κ values are possible in ocean crust gabbros representing the deep, high temperature section of a hydrothermal cell. These gabbros can have κ values up to ~20, with Th likely hosted in either allanite (epidote) or monazite (phosphate) (Hart et al., 1999). Since sample D05-08 is a fine-grained volcanic rock lacking either mineral phase, we interpret the sample's high κ of ~4.9, and elevated κ of several other samples, to result from assimilation of small amounts of hydrothermally altered gabbro into the parental magma. Elevated Sr/Sr* (>1; Supplemental Table S.4.2) is consistent with this process, although it also could be attributed to seawater alteration. Assimilation into parental melt also explains our inability to remove the signature by leaching. Furthermore, the significant $^{208}Pb/^{204}Pb$ ingrowth suggests assimilation of Cretaceous oceanic crust is likelier than younger intrusives from the seamount interior that had less time for ingrowth. In all other isotopic compositions, this sample resembles other Rurutu volcanoes in the area, which is predicted by simple assimilation-fractional crystallization modeling. It thus appears that Rurutu magmas sample this crustal

component, and perhaps localized hydrothermal alteration pathways are only locally incorporated.

4.6.2 Non-Rurutu Sources: Ontong-Java and Samoa

In addition to Rurutu volcanoes, two other geologic provinces appear to be present in Tuvalu; one related to the break-up of Ontong Java Nui (Taylor, 2006) and subsequent seafloor generation, and the other related to the Samoan hotspot.

4.6.2.1. A link between Group 2 and Ontong-Java Nui breakup?

Given its 95-90 Ma age, Group 2 may be related to the waning stages of the Cretaceous Ontong-Java Nui activity and opening of the Ellice Basin between Ontong-Java Plateau (OJP) and Manihiki Plateau. The main ~120 Ma volcanic phase of the OJP is generally C/FOZO-like in composition and may be sourced by an ancient primitive reservoir, although other compositions also occur (e.g., Jackson and Carlson, 2011; Tejada et al., 1996). A smaller, second volcanic pulse at ~90 Ma includes the Sigana basalts and Sigana Alkalic Group on Santa Isabel in the Solomon Islands (Tejada et al., 1996) and late-stage activity on the Hikurangi Plateau (Hoernle et al., 2010). The Sigana basalts have OJP-like isotopic compositions, while the Sigana Alkalic Group are rare alkalic basalt dikes bearing weakly HIMU-like ($^{206}Pb/^{204}Pb \geq 20.0$) signatures. Trace element patterns and isotopic compositions of these dikes are similar to the Tuvalu Group 2 lavas (Figure 4.2B), with the exception of phosphate-contaminated radiogenic $^{143}Nd/^{144}Nd$ and low $^{208}Pb^*/^{206}Pb^*$ (Section 4.6.1; Supplemental Table S.4.3). Consequently, Group 2 lavas may have the same source as the late-stage Ontong-Java and Hikurangi lavas.

Alternatively, Group 2 seamounts may be generated by off-axis ridge magmatism related to the opening of the Ellice Basin. Few age constraints exist for the Ellice Basin, where models are based on the assumption of a constant opening rate from ~120-86 Ma (e.g., Chandler et al., 2012), although a crustal sample recovered from the southern part of the basin (near 46-Ma sample D22-29) dates to ~83 Ma (Taylor, 2006). OIB-like trace element geochemistry paired with MORB-like isotopic signatures have been previously documented in off-axis ridge magmatism (White, 2014 and references therein), supporting the hypothesis that Group 2 samples may have been generated in response to Ontong-Java Nui breakup.

4.6.2.2. Samoan hotspot activity in Southern Tuvalu

Groups 3 and 4 carry a Samoan plume signature, and at least one dredge (D27, E. Niulakita) has two sample groups with ages and compositions that match the Rurutu (45-42 Ma) and the Samoan (15 Ma) hotspots. This suggests that, in some cases, older Rurutu volcanoes may have been reactivated by the Samoan hotspot. Age and location relationships suggest that one of the seamounts in this group (D21/Nukulaelae Atoll) is younger than APM-based Samoan age progression models (Supplemental Figure S.4.7). Nukulaelae yielded ages of 10.4-8.6 Ma, postdating the predicted age by ~5 Ma. However, this discrepancy is within the time span of activity at the Samoan island of Savaiʻi (Konter and Jackson, 2012). This volcano and the rest of Group 3, plotting between EM2 and MORB in isotope space, resemble Alexa Bank, the most depleted WESAM seamount (Figures 4.1, 4.4; Hart et al., 2004; Jackson et al., 2010), and Bayonnaise and Favavesi (Koppers et al., 2011b). Unlike other Samoan volcanoes, Nukulaelae lies ~250 km north of the east-west

trending Samoan hotspot track, suggesting a parallel to the rejuvenated-composition North Arch volcanic field from the Hawaiian Islands (Frey et al., 2005). However, Samoan-sourced rejuvenated volcanism normally carries an EM1 component (e.g., Konter and Jackson, 2012) not seen in Nukulaelae. Instead, it may simply represent a rare component in Samoan volcanism formed well off-axis of the hotspot track.

Finally, the single Group 4 sample, dredged from Lafetoga seamount (~11 Ma), exhibits an EM2 isotopic composition lacking any evidence of a depleted component diagnostic of Group 3. Its geographic location and age match the expected behavior of Samoan plume-sourced volcanoes.

4.7. Rurutu Hotspot Composition and Track

Rurutu hotspot compositions span a limited range, and the densely sampled Tuvalu chain reveals a geographic pattern to compositional variations. The combination of composition and ages allows the Rurutu hotspot track to be identified as the dominant magmatic source for the volcanic chain.

4.7.1. Compositional and Geographic Patterns in Rurutu Volcanism

Our new data reveals a geographic pattern in the isotopic compositions that suggests bilateral isotopic heterogeneity defined by the Niu and Sil compositional groups. Hawaii, Samoa, Society, Marquesas, Walvis, Easter, and Galapagos hotspots exhibit similar bilateral heterogeneity reflected in enriched and depleted trends in $^{208}Pb^*/^{206}Pb^*$ and ε_{Nd} isotopes that are geographically separated (Harpp et al., 2014; Huang et al., 2011; O'Connor and Jokat, 2015; Payne et al., 2013; Weis et al., 2011). The enriched trends (high

$^{208}Pb^*/^{206}Pb^*$, low ε_{Nd}), are attributed to an ancient subducted crustal component and thought to sample the Pacific large low-shear velocity province (LLSVP; e.g., Harpp et al., 2014; Huang et al., 2011). When Tuvalu Group 1 isotopic data are recalculated as $^{208}Pb^*/^{206}Pb^*$ and ε_{Nd} (Supplemental Table S.4.3), the Niu and Sil trends display trends similar to other dual-trend hotspots (Figure 4.4).

An endmember mixing model (Supplemental Table S.4.6) suggests that the geochemically-enriched Niu trend is generated by mixing between HIMU and a FOZO/EM1 mixture (Supplemental Figure S.4.9). The depleted Sil trend features a kinked pathway in isotope space, requiring up to four components mixing in a specific sequence: HIMU compositions mix with a depleted, MORB-influenced composition before interacting with a 5% EM1/95% FOZO mixture (Supplemental Figure S.4.9). Depending on the exact compositions used, the MORB-HIMU mixture requires up to 80% MORB (e.g., D22-23).

The Cook-Austral compositions used as background data in this study were previously identified as hosting two geochemical trends similar to the Sil and Niu trends we describe (Hanyu et al., 2013; Nebel et al., 2013; Figure 4.3), suggesting longevity of both trends in the Rurutu track. Previously unrecognized, both Niu and Sil trends (Supplemental Table S.4.3) also occur in the Wake Seamounts and Samoan interlopers (Jackson et al., 2010; Konter et al., 2008; Koppers et al., 2003; Staudigel et al., 1991), while the Gilbert Ridge samples (Konter et al., 2008) are Niu composition except for Tuba seamount at the southern terminus of the chain.

The cause of the shift to dominantly Niu trend compositions along the Gilbert Ridge remains speculative at best. The data are currently lacking to test for any volume-composition relationship, since many samples in the Gilbert segment were taken from

smaller satellite seamounts in areas where the large atolls lacked suitable exposures. Alternatively, the Rurutu plume conduit may have a roughly N-S-elongated horizontal cross-section (rather than circular), resulting in the wide across-track spacing seen in Wake and Tuvalu. This could mean that large N-S-oriented Gilbert seamounts were Niu-composition during their early stages, then capped by later Sil-composition activity, if Sil is present in the large Gilbert volcanoes. However, because of the previously mentioned sampling bias, this possibility remains untested.

Compared to morphological characteristics of other dual-trend hotspot tracks, Rurutu displays relatively wide across-track scatter. While forming an array offset to the NE side of the Tuvalu chain (Figure 4.5A), Sil-trend seamounts also sit 85-330 km directly north of similarly-aged Niu-trend seamounts. Assuming simple plume geometry and purely vertical transport, the Sil-Niu trend orientations suggest compositional hemispheres with a N-S orientation within the plume (Figure 4.5B). This is possibly mirrored by the Wake seamounts, although low sampling density prevents thorough geographic-geochemical characterization. The Walvis Ridge in the Atlantic Ocean shows an even wider spacing of hundreds of km, presumed related to control on eruptive sites by weaknesses in the underlying plate (e.g., O'Connor and Jokat, 2015). Perhaps a similar control played a more limited role as the Ellice Basin moved over the hotspot.

4.7.2. APM-based backtracking and a Rurutu Bend in southern Tuvalu

Different APM model projections of the Rurutu hotspot track from its present location under Arago Seamount (Bonneville et al., 2002) suggest that its Bend occurs in the southern Ellice Basin, approximately halfway between the southern boundaries of the OJP

and Manihiki plateaux. In this area, Samoa and Rurutu volcanoes overlap, making a visual estimate of the Bend location difficult (Figure 4.1). The paucity of Rurutu-related volcanoes in the WESAM region may be due to subduction of part of the Rurutu hotspot track beneath Tonga (e.g., Price et al., 2016), or due to overprinting ~20 Myr later by the Samoan hotspot. Instead, the Bend identification is augmented using APM projections of the Rurutu track using age-dated Tuvalu seamounts with HIMU- and FOZO-like Group 1 compositions to estimate the highest-probability location of the Rurutu Bend (see Supplement for details).

The analysis is limited to Rurutu-sourced Tuvalu volcanoes, since uncertainty in APM models increases with age. Furthermore, any plume motion becomes increasingly important in analyses that include the older Gilbert and Wake volcanoes. In fact, when Rurutu-origin Gilbert and Wake volcanoes are backtracked, or restored backward in time through APM stage poles, to their original eruptive locations, they scatter ~15° (~2000 km) from Arago Seamount (Figure 4.6). APM-seamount track mismatch was originally thought to suggest a more complex, discontinuous record of short-lived, "secondary" hotspot volcanism in the southwest Pacific, and in particular, older tracks were considered "orphaned" (Koppers et al., 2003). For example, the formerly-orphaned Wake seamounts had been associated with a different, extinct hotspot that produced a "bend" in southern Gilbert Ridge through a combination of plume drift deceleration and localized short-term crustal extension before dying out (Koppers et al., 2007; Koppers and Staudigel, 2005; Wessel and Kroenke, 2008). Since these seamounts are now linked to the Rurutu hotspot (Konter et al., 2008) the mismatch between model and hotspot track may simply be due to poor APM fit to oldest Rurutu segments. Therefore, limiting the input range of seamounts reduces error arising from model misfits and lack of plume fixity. However, as a finite

number of samples are required as input to ensure the robustness of a quantitative approach, this study uses all available Rurutu age data from Tuvalu volcanoes to construct one best-fit Bend location.

In order to limit an effect on the outcome by any specific model, we use the "WK08" (Wessel and Kroenke, 2008), "D12" (Doubrovine et al., 2012), and "DC85" (Duncan and Clague, 1985) APM models. Kernel density estimates of the track projections through each volcano then pinpoint each model's Bend location, which fall within ~100 km of each other, surrounded by three ~50.5-49 Ma HIMU Tuvalu seamounts (Figure 4.7). The final location estimate is determined from a combination of all three estimates.

Using the new Tuvalu Group 1 data, our model results are consistent with the Bend for the Rurutu track located near the intersection of the Tuvalu chain and WESAM (Figure 4.1) where the trend of ~50 Ma HIMU volcanism changes from NW-SE in the Tuvalu islands to WNW-ESE in the Samoan islands with a bend of ~135°, shallower than the Hawaiian-Emperor Bend (120°), yet greater than Louisville (155°). We propose that, based on new isotopic fingerprinting, age data, and the kernel density estimation, that the Rurutu Bend lies near Funafuti (D18) and Nukufetau (D14) islands, at 178.48°E and 8.56°S (Figure 4.7).

Konrad et al. (submitted) report an age of ~49 Ma for Nukufetau and Funafuti and 50.5 Ma for Tayasa, in good agreement with the 50-47 Ma Hawaii and Louisville Bends (Koppers et al., 2011a; Wessel and Kroenke, 2008). One Nukufetau sample has a 43.6 Ma age, ~6 Ma younger than the ages obtained on another sample from the same dredge. However, seamounts can remain volcanically active for 7 (or more) Myr (e.g., Konter et al., 2009), and this younger age may represent rejuvenated-stage volcanism. Consequently, the bend in Rurutu hotspot occurred at ~50.5-49 Ma. Volcanism in this area continued for a

significant amount of time afterward, which is important to recognize for APM modeling efforts that plot age against opening angle. Thus, with a third long-lived hotspot placing new constraints on plate motion around the time of the Bend and the period prior, new APM models are now possible. This hotspot specifically holds the promise of tracking a single, geochemically distinct volcanic track well past the age limitations of Hawaii and Louisville, as volcanoes that may be associated with the Rurutu hotspot extend back to 120 Ma (Koppers et al., 2003; Konter et al., 2008). Some of the implications for plate, plume and global mantle motion are assessed further in Konrad et al. (submitted). However, with current APMs, the uncertainty of backtracked eruptive locations is significant for the oldest Rurutu hotspot volcanoes in particular (Wake Seamounts; Figure 4.6), with a ~15° spread away from present-day Rurutu, and much less so earlier. This is of similar magnitude to the shift in paleomagnetic latitude suggested in the Emperor stage of the Hawaiian hotspot (Tarduno et al., 2003), which may be partly explained with N-S plume motion (e.g., Doubrovine et al., 2012). However, if Rurutu hotspot indeed underwent little drift, mismatch between modeled and actual Rurutu tracks may be controlled by APM uncertainty prior to 60 Ma, suggesting significant model revisions may be required.

4.8. Conclusions

Most volcanoes in Tuvalu represent ~75-42 Ma Rurutu hotspot volcanism, although other regional volcanic events and alteration signatures are recognized. The new data supplement an existing body of data supporting the longevity and continuity of the Rurutu hotspot. The new Tuvalu data clearly define hemispherically distributed compositions

within the source, as one hemisphere interacted with a depleted component prior to exposure to the FOZO component common to most hotspots.

With a kernel density-based computational method, Rurutu-related Tuvalu volcanoes constrain the location and age of a previously-uncharacterized segment of the Rurutu hotspot track, including its ~50.5-49 Ma Bend. When combined with a known current hotspot location and ~120 Ma of eruptive history, the Rurutu hotspot track represents a third long-lived Pacific hotspot track with a longer eruptive record than Hawaii-Emperor, re-establishing the importance of Morgan's "Austral-Gilbert-Marshall" track as a major constraint on Pacific APM.

4.9. Acknowledgements

This study was funded by NSF OCE# 1153959 and 1433097 to JK, OCE# 1154070 to AAPK, and OCE# 1153894 to MJ. We would like to thank Captain Wes Hill and the ship and science crews of the *R/V Roger Revelle*, without whom the RR1310 expedition and resulting studies would not have been possible. We also thank Andrea Koschinsky and John Sinton for sharing samples from prior cruises. VAF thanks Janet Becker and Paul Wessel for suggestions instrumental to developing the Rurutu Bend location error estimates.

Table 4.1. Sample information.

Sample	Seamount	Longitude	Latitude	Sample type
D02-06	Manu Lele Vai	175.63 E	3.9 S	leached gm
D03-24	Taring Nui	176.6 E	4.75 S	leached gm
D04-01D	Logotau	175.65 E	5.66 S	leached gm
D05-08	Nanumanga	176.31 E	6.43 S	leached gm
D05-08dup	Nanumanga	176.31 E	6.43 S	leached gm
D06-14	Maumau	176.75 E	6.35 S	leached gm
D07-22b	Tefolaha	176.9 E	5.98 S	leached gm
D07-30	Tefolaha	176.9 E	5.98 S	leached gm
D08-27	Niutao Atoll	177.22 E	6.12 S	leached gm
D09-14	Na Kaa	176.71 E	6.55 S	leached gm
D10-16	Nui Island	177.24 E	7.7 S	leached gm
D10-32	Nui Island	177.24 E	7.7 S	leached gm
D10-32dup	Nui Island	177.24 E	7.7 S	leached gm
D11-06	Laupapa	177.02 E	8.25 S	leached gm
D12-01	Fialua	177.27 E	8.46 S	leached gm
D12-04	Fialua	177.27 E	8.46 S	leached gm
D13-01	Tayasa	177.9 E	8.66 S	leached gm
D14-01	Nukufetau	178.39 E	8.19 S	leached gm
D15-12	Vaitupu	178.6 E	7.22 S	leached gm
D15-17	Vaitupu	178.6 E	7.22 S	leached gm
D16-38cpx	Telematua	179.27 E	7.42 S	leached cpx
D18-11	Funafuti	178.99 E	8.32 S	leached gm
D19-03	Pae	178.87 E	9.44 S	leached gm
D19-08	Pae	178.87 E	9.44 S	leached gm
D20-15	Foumatua	178.85 E	9.8 S	leached gm
D21-19	Nukulaelae Atoll	179.67 E	9.3 S	leached gm
D21-26	Nukulaelae Atoll	179.67 E	9.3 S	leached gm
D22-23	Silaga	179.82 W	10.31 S	leached gm
D23-05	Macaw Bank	179.25 W	10.77 S	leached gm
D24-04	Kosciusko	179.67 E	10.36 S	leached gm
D24-14A	Kosciusko	179.67 E	10.36 S	leached gm
D26-02	Niulakita	179.34 E	10.81 S	leached gm
D27-31	Bayonnaise	179.88 E	11.33 S	leached gm
D27-35	Bayonnaise	179.88 E	11.33 S	leached gm
D27-57	Bayonnaise	179.88 E	11.33 S	leached gm
D28B-06	Bustard	179.7 W	11.52 S	leached gm
D32-02	Lafetoga	178.04 W	12.94 S	leached gm
D33-32	Tuscarora	178.45 W	12.06 S	leached gm
TUV-1	Fialua	177.32 E	8.39 S	leached WR
TUV-2	near Silaga	179.41 W	10.002 S	leached WR
TUV-3	near Silaga	179.41 W	10.002 S	leached WR
TUV-4	Telematua	179.04 E	7.4 S	leached cpx separates
TUV-5	Telematua	179.04 E	7.4 S	leached WR

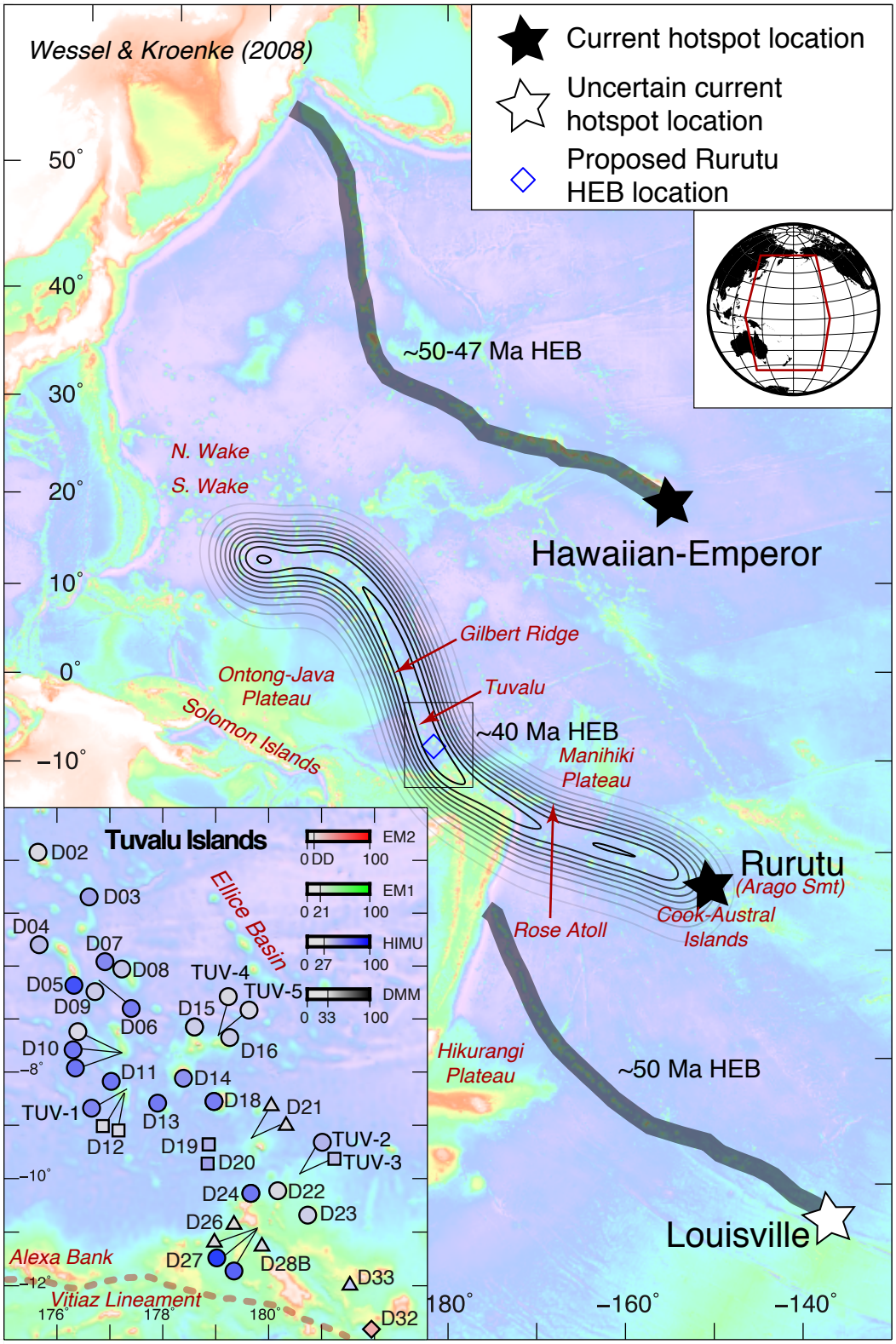

Figure 4.1. Map of the west Pacific showing the Hawaiian-Emperor and Louisville hotspot tracks. The estimated Rurutu track is shown as density contours (see Supplemental

Methods) and likely Bend location marked by the diamond. The inset shows names and locations of all Tuvalu and WESAM seamounts discussed in this study. Track reconstructions use the following hotspot locations: 150.73°W, 23.44°S (Rurutu/Arago Seamount; Bonneville et al., 2002), 155.25°W, 18.93°N (Hawai'i/Loihi Seamount, Seamount Catalog at https://earthref.org); 137.2°W, 52.4°S (Louisville/Hollister Ridge; Wessel and Kroenke, 2008). **Inset:** Dredge locations in the Tuvalu islands. Symbol color is defined by isotopic composition after Konter et al. (2008).. Circles are Group 1, Squares are Group 2, Triangles are Group 3, and the diamond is Group 4. See Sections 4.5 and 4.6 for discussion of Group geochemistry and interpretations.

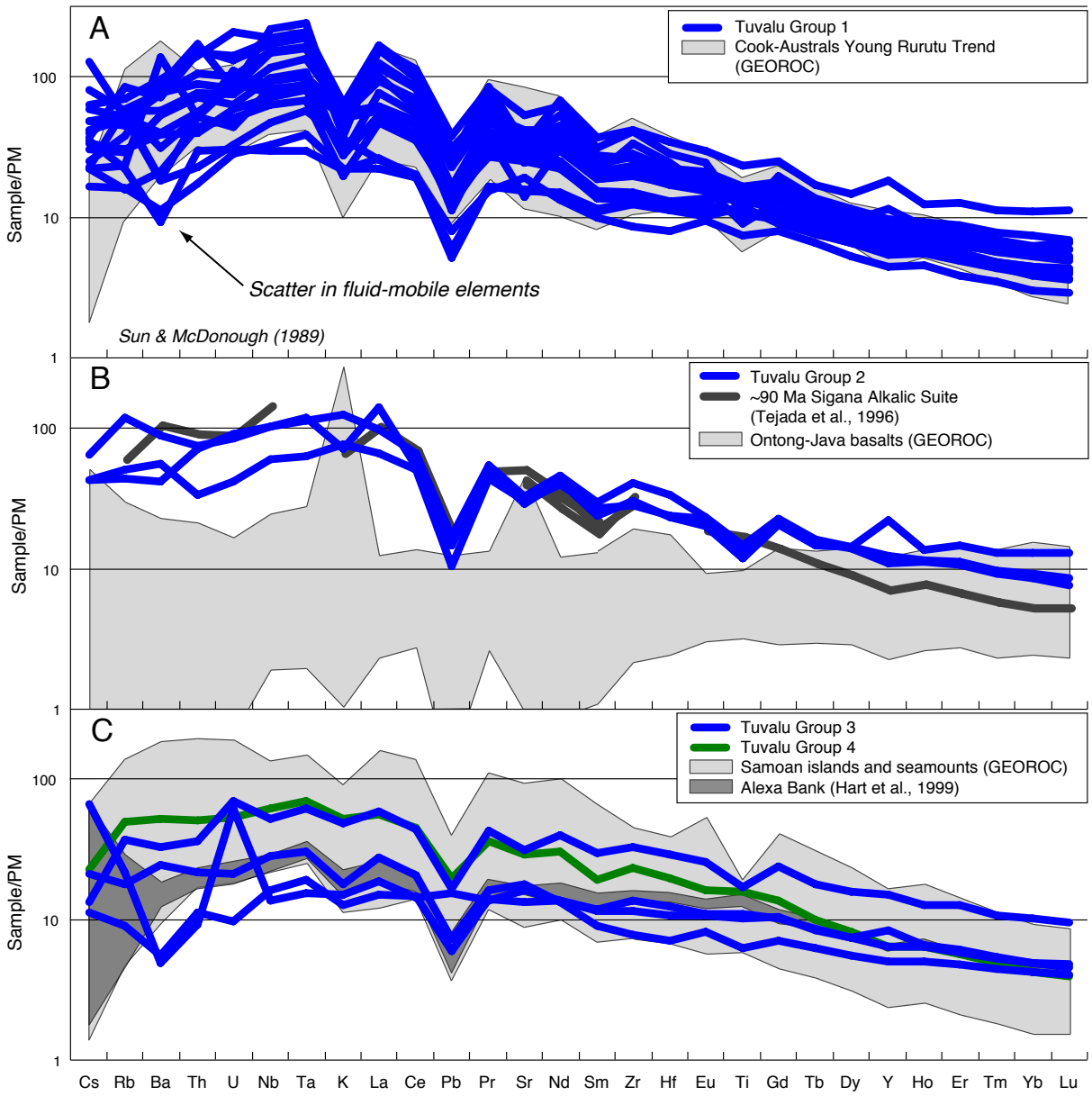

Figure 4.2. Primitive mantle (PM)-normalized extended trace element diagrams after Sun and McDonough (1995). Background data (grey fields) are from compositionally filtered (see Supplemental Methods) GEOROC and PetDB datasets. A) Group 1 (Rurutu) samples with Cook-Austral Atiu samples as background. B) Group 2 (95-90 Ma) samples with Ontong-Java background data, including ~90 Ma Sigana alkalic suite data (Tejada et al., 1996). C) Groups 3 and 4 samples against Samoan seamount background data.

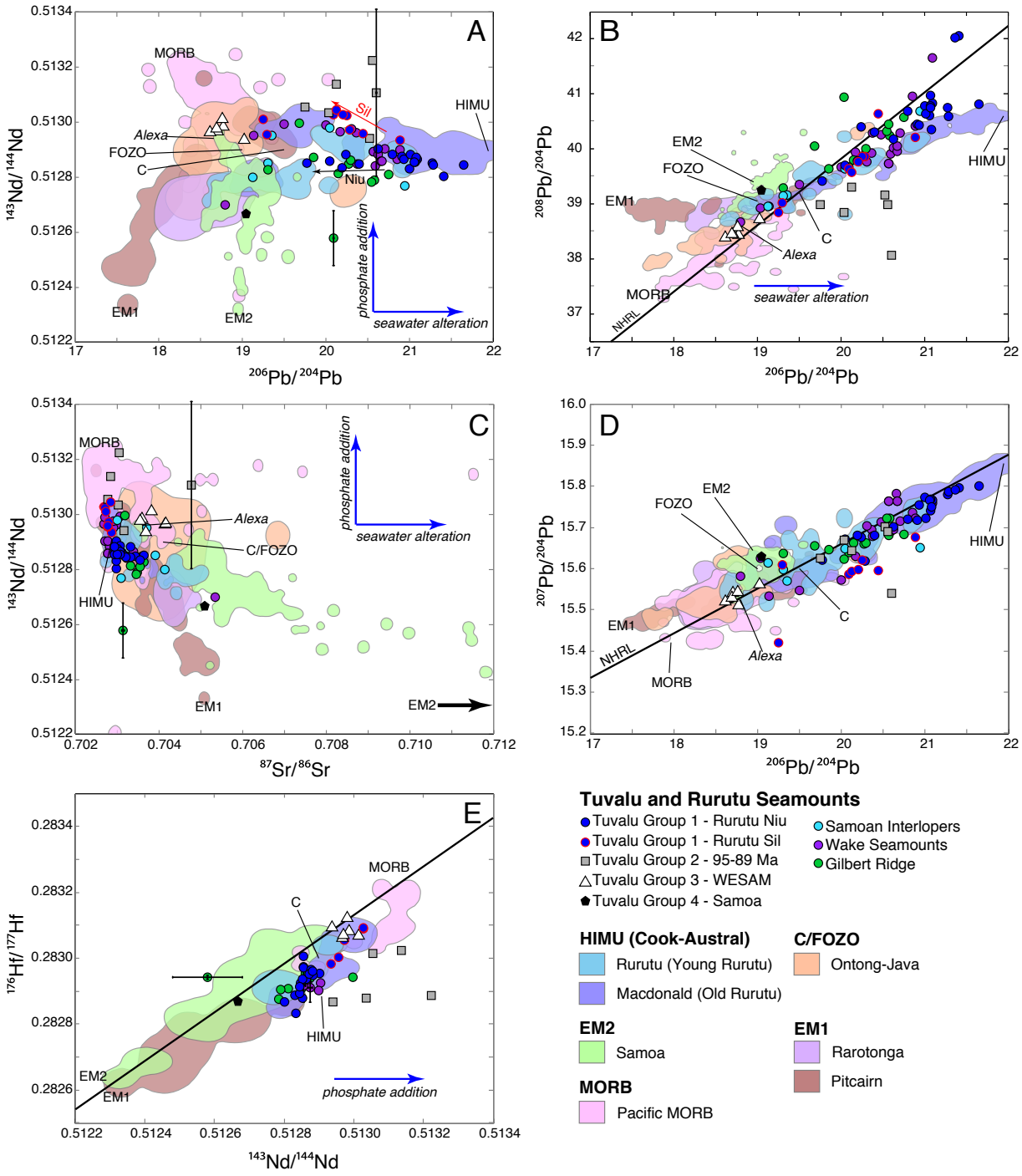

Figure 4.3. Isotopic data. A) $^{143}Nd/^{144}Nd$ vs. $^{206}Pb/^{204}Pb$. B) $^{143}Nd/^{144}Nd$ vs. $^{87}Sr/^{86}Sr$. C) $^{207}Pb/^{204}Pb$ vs. $^{206}Pb/^{204}Pb$ D) $^{208}Pb/^{204}Pb$ vs. $^{206}Pb/^{204}Pb$. E) $^{176}Hf/^{177}Hf$ vs. $^{143}Nd/^{144}Nd$. Background data fields were generated using two-dimensional kernel density estimates (see Supplement for methods and data/endmember sources).

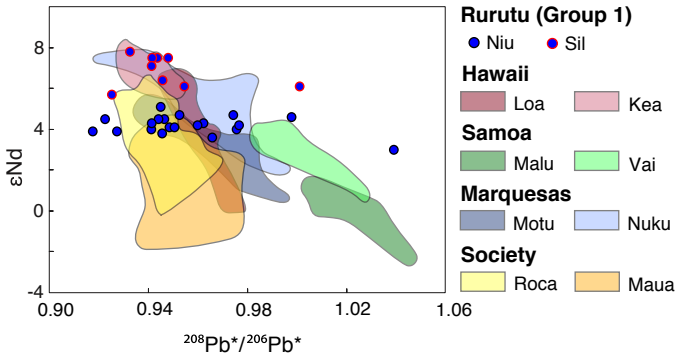

Figure 4.4. Comparison of $^{208}Pb^*/^{206}Pb^*$ vs. εNd data (after Huang et al., 2011) from Hawaii, Marquesas, and Samoa hotspots displaying dual trend patterns and Tuvalu (Group 1/Rurutu data only). The hand-drawn fields for other hotspot tracks were sourced from Huang et al. (2011) and Payne et al. (2013).

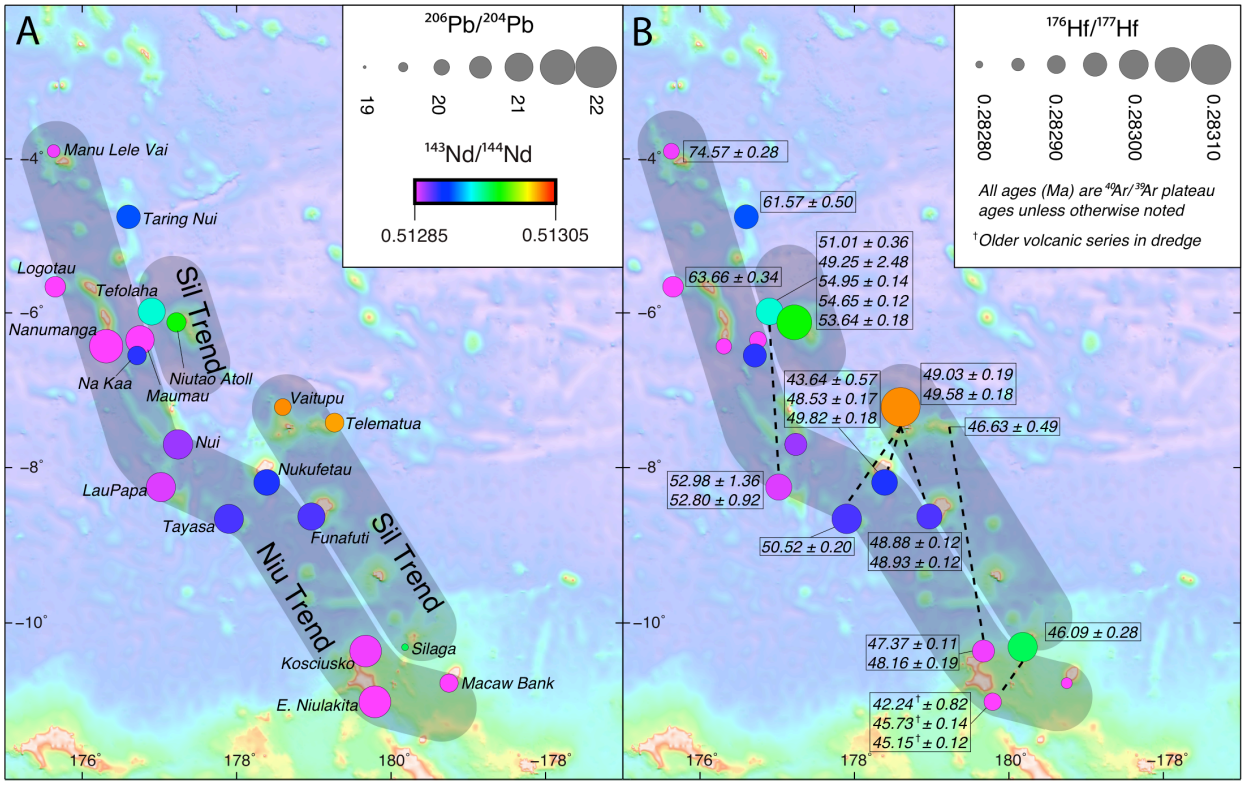

Figure 4.5. Geographic distribution of isotopic data in Tuvalu (Group 1/Rurutu data only) isotopic data $^{143}Nd/^{144}Nd$ (color) and $^{206}Pb/^{204}Pb$ (size), or $^{176}Hf/^{177}Hf$ (size), delineating the Niu and Sil trends. Ages, where present, are plotted next to seamounts. Only Group 1 seamount names are shown. Dashed lines between Niu and Sil seamounts indicate where seamounts of similar age are found between enriched and depleted compositions, showing the N-S, en echelon orientation of the geochemical hemispheres in the plume.

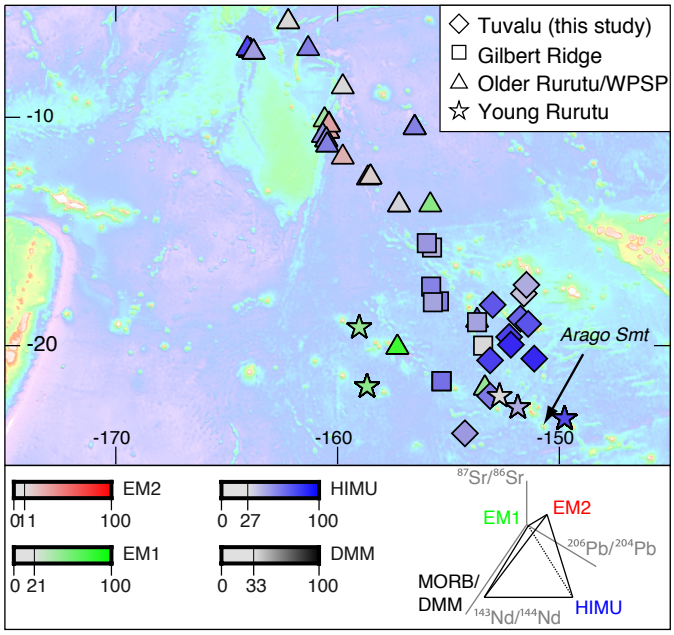

Figure 4.6. Backtracked Rurutu-related seamounts (Tuvalu, Cook-Austral Young Rurutu, Gilbert, and Wake seamounts with isotopic signatures of Rurutu hotspot) to original eruptive locations using the Doubrovine et al. (2012) APM model without compensating for hotspot drift. While Samoan and younger (<64 Ma) Rurutu seamounts are restored to a cloud clustering around a single location, the projected points for older Rurutu seamounts plot to the northwest, near the Manihiki Plateau. Note that the main Rurutu cluster does not actually converge near Arago Seamount, instead clustering closer to the Society hotspot. This could be a consequence of this model attempting to fit a globally averaged hotspot reference frame with moving plumes, while the Pacific-only fixed-plume models WK08 and DC85 restore these seamounts closer to Arago/Rurutu Island. Sample color is same as in Figure 4.1 (inset) and shows relative relative proportion of the various isotopic endmembers.

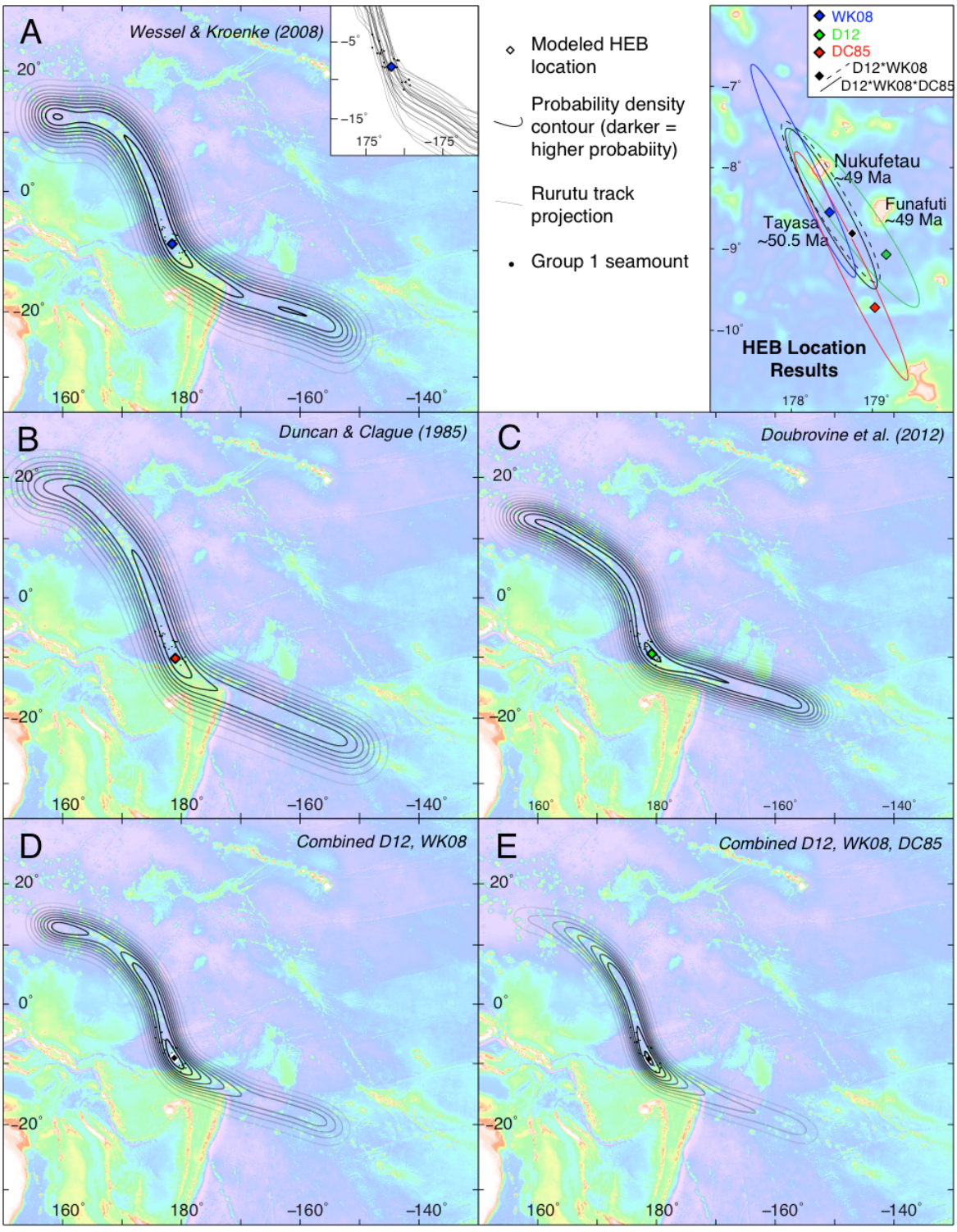

Figure 4.7. Results of the Bend locator approach using the APM models **A:** Wessel and Kroenke (2008), of **B:** Duncan and Clague (1985), and **C:** Doubrovine et al. (2012). Individual model results are shown as combined contours and individual projected tracks

from each dated Group 1 seamount; contours only are displayed for combined models. Combined models (**D** and **E;** WK08 & D12, all three, respectively) are also provided, showing the average of the models. A 2- and 3-model combination provides identical results; WK08 and D12 are more influential than DC85. **Upper right:** The final Rurutu Bend location estimate of 178.76°W, 8.82°S is taken from the combined models, sitting between D14 and D18 with an estimated age of ~50-49 Ma. Individual model results give 178.48°W, 8.56°S (WK08), 179.18°W, 9.08°S (D12), and 179.04°W, 9.73°S (DC85). Error ellipses are calculated using a Monte Carlo simulation, discussed further in the supplement. **Inset:** Example of trackline clustering at the Bend, which is used to calculate kernel density estimate (KDE) contours and likeliest Bend location using each model.

4.10. References

Bach, W., Peucker-Ehrenbrink, Hart, S.R., Blusztajn, J., 2003. Geochemistry of hydrothermally altered oceanic crust: DSDP/ODP Hole 504B - Implications for seawater-crust exchange budgets and Sr-Pb-isotopic evolution of the mantle. Geochemistry, Geophys. Geosystems 4, 40–55.

Baturin, G.N., 2001. Uranium and Thorium in Phosphatic Bone Debris from the Ocean Bottom. Lithol. Miner. Resour. 36, 99–108.

Bau, M., Koschinsky, A., Dulski, P., Hein, J.R., 1996. Comparison of the partitioning behaviours of yttrium, rare earth elements, and titanium between hydrogenetic marine ferromanganese crusts and seawater. Geochim. Cosmochim. Acta 60, 1709–1725.

Bonneville, A., Suavé, R. Le, Audin, L., Clouard, V., Dosso, L., Gillot, P.-Y., Janney, P.E., Jordahl, K., Maamaatuaiahutapu, K., 2002. Arago Seamount: The missing hotspot found in the Austral Islands. Geology 30, 1023–1026. doi:10.1130/0091-7613(2002)030<1023

Cande, S.C., Raymond, C.A., Stock, J., Haxby, W.F., 1995. Cenozoic Geophysics of the Pitman Fracture Zone and Pacific-Antarctic Plate Motions During the Cenozoic. Science. 270, 947–953.

Chandler, M.T., Wessel, P., Taylor, B., Seton, M., Kim, S.-S., Hyeong, K., 2012. Reconstructing Ontong Java Nui: Implications for Pacific absolute plate motion, hotspot drift and true polar wander. Earth Planet. Sci. Lett. 331–332, 140–151. doi:10.1016/j.epsl.2012.03.017

Chauvel, C., McDonough, W.F., Guille, G., Maury, R., Duncan, R.A., 1997. Contrasting old and young volcanism in Rurutu Island, Austral chain. Chem. Geol. 139, 125–143. doi:10.1016/S0009-2541(97)00029-6

Cheng, Q., Park, K.-H., Macdougall, J.D., Zindler, A., Lugmair, G.W., Staudigel, H., Hawkins, J.W., Lonsdale, P.F., 1987. Isotopic evidence for a hotspot origin of the Louisville Seamount Chain, in: Keating, B.H., Fryer, P., Batiza, R., Boehlert, G.W. (Eds.), Seamounts, Islands, and Atolls.

Connelly, J.N., Ulfbeck, D.G., Thrane, K., Bizzarro, M., Housh, T., 2006. A method for purifying Lu and Hf for analyses by MC-ICP-MS using TODGA resin. Chem. Geol. 233, 126–136. doi:10.1016/j.chemgeo.2006.02.020

Doubrovine, P. V., Steinberger, B., Torsvik, T.H., 2012. Absolute plate motions in a reference frame defined by moving hot spots in the Pacific, Atlantic, and Indian oceans. J. Geophys. Res. Solid Earth 117. doi:10.1029/2011JB009072

Duncan, R.A., Clague, D.A., 1985. Pacific plate motion recorded by linear volcanic chains, in: The Ocean Basins and Margins. Springer US, Boston MA. doi:10.1007/978-1-4613-2351-8_3

Fowler, A.P.G., Zierenberg, R.A., 2016. Elemental changes and alteration recorded by basaltic drill core samples recovered from in situ temperatures up to 345°C in the

active, seawater-recharged Reykjanes geothermal system, Iceland. Geochemistry, Geophys. Geosystems 17, 4772–4801.

Frey, F.A., Huang, S., Blichert-Toft, J., Regelous, M., Boyet, M., 2005. Origin of depleted components in basalt related to the Hawaiian hot spot: Evidence from isotopic and incompatible element ratios. Geochemistry, Geophys. Geosystems 6. doi:10.1029/2004GC000757

Grandjean, P., Cappetta, H., Albarède, F., 1987. The assessment of REE patterns and 143Nd/144Nd ratios in fish remains. Earth Planet. Sci. Lett. 84, 181–196.

Hanan, B.B., Graham, D.W., 1996. Lead and Helium Isotope Evidence from Oceanic Basalts for a Common Deep Source of Mantle Plumes. Science. 272, 991–995.

Hanyu, T., Dosso, L., Ishizuka, O., Tani, K., Hanan, B.B., Adam, C., Nakai, S., Senda, R., Chang, Q., Tatsumi, Y., 2013. Geochemical diversity in submarine HIMU basalts from Austral Islands, French Polynesia. Contrib. to Mineral. Petrol. 166, 1285–1304. doi:10.1007/s00410-013-0926-x

Harpp, K.S., Hall, P.S., Jackson, M.G., 2014. Galápagos and Easter : A Tale of Two Hotspots, in: Harpp, K.S., Mittelstadt, E., D'Ozouville, N., Graham, D.W. (Eds.), The Galapagos: A Natural Laboratory for the Earth Sciences,Geophysical Monograph 204. American Geophysical Union, pp. 27–40.

Hart, S.R., 1984. A large-scale isotope anomaly in the Southern Hemisphere mantle. Nature 309, 753–757.

Hart, S.R., Blusztajn, J., Dick, H.J.B., Meyer, P.S., Muehlenbachs, K., 1999. The fingerprint of seawater circulation in a 500-meter section of ocean-crust gabbros. Geochim. Cosmochim. Acta 63, 4059–4080.

Hart, S.R., Coetzee, M., Workman, R.K., Blusztajn, J., Johnson, K.T.M., Sinton, J.M., Steinberger, B., Hawkins, J.W., 2004. Genesis of the Western Samoa seamount province: age, geochemical fingerprint and tectonics. Earth Planet. Sci. Lett. 227, 37–56. doi:10.1016/j.epsl.2004.08.005

Hart, S.R., Hauri, E.H., Oschmann, L.A., Whitehead, J.A., 1992. Mantle plumes and entrainment: Isotopic evidence. Science. 256, 517–520.

Hochmuth, K., Gohl, K., Uenzelmann-Neben, G., 2015. Playing jigsaw with Large Igneous Provinces - a plate tectonic reconstruction of Ontong Java Nui, west Pacific. Geochemistry, Geophys. Geosystems.

Hoernle, K., Hauff, F., van den Bogaard, P., Werner, R., Mortimer, N., Geldmacher, J., Garbe-Schönberg, D., Davy, B., 2010. Age and geochemistry of volcanic rocks from the Hikurangi and Manihiki oceanic Plateaus. Geochim. Cosmochim. Acta 74, 7196–7219. doi:10.1016/j.gca.2010.09.030

Huang, S., Hall, P.S., Jackson, M.G., 2011. Geochemical zoning of volcanic chains associated with Pacific hotspots. Nat. Geosci. 4, 874–878. doi:10.1038/ngeo1263

Jackson, M.G., Carlson, R.W., 2011. An ancient recipe for flood-basalt genesis 21. doi:10.1038/nature10326

Jackson, M.G., Hart, S.R., Konter, J.G., Koppers, A.A.P., Staudigel, H., Kurz, M.D., Blusztajn, J., Sinton, J.M., 2010. Samoan hot spot track on a "hot spot highway": Implications for mantle plumes and a deep Samoan mantle source. Geochemistry, Geophys. Geosystems 11. doi:10.1029/2010GC003232

Jackson, M.G., Hart, S.R., Koppers, A.A.P., Staudigel, H., Konter, J.G., Blusztajn, J., Kurz, M.D., Russell, J.A., 2007. The return of subducted continental crust in Samoan lavas. Nature 448, 684–687. doi:10.1038/nature06048

Keating, B.H., 1996. Side-scan sonar and seismic reflection evidence of volcanic reactivation within the Line Island Seamount Chain. Fifth Circum-Pacific Energy Miner. Resour. Conf. Trans.

Konter, J.G., Hanan, B.B., Blichert-Toft, J., Koppers, A.A.P., Plank, T., Staudigel, H., 2008. One hundred million years of mantle geochemical history suggest the retiring of mantle plumes is premature. Earth Planet. Sci. Lett. 275, 285–295. doi:10.1016/j.epsl.2008.08.023

Konter, J.G., Jackson, M.G., 2012. Large volumes of rejuvenated volcanism in Samoa: Evidence supporting a tectonic influence on late-stage volcanism. Geochemistry, Geophys. Geosystems 13. doi:10.1029/2011GC003974

Konter, J.G., Jackson, M.G., Koppers, A.A.P., 2011. Tracking Long-lived Hotspots to Constrain Temporal Mantle Compositional Evolution, in: American Geophysical Union Fall Meeting. p. #DI22A-04.

Konter, J.G., Staudigel, H., Blichert-Toft, J., Hanan, B.B., Polvé, M., Davies, G.R., Shimizu, N., Schiffman, P., 2009. Geochemical stages at Jasper Seamount and the origin of intraplate volcanoes. Geochemistry, Geophys. Geosystems 10. doi:10.1029/2008GC002236

Konter, J.G., Storm, L.P., 2014. High precision 87Sr/86Sr measurements by MC-ICP-MS, simultaneously solving for Kr interferences and mass-based fractionation. Chem. Geol. 385, 26–34. doi:10.1016/j.chemgeo.2014.07.009

Koppers, A.A.P., Gowen, M.D., Colwell, L.E., Gee, J.S., Lonsdale, P.F., Mahoney, J.J., Duncan, R.A., 2011a. New 40 Ar/ 39 Ar age progression for the Louisville hot spot trail and implications for inter-hot spot motion. Geochemistry, Geophys. Geosystems 12. doi:10.1029/2011GC003804

Koppers, A.A.P., Phipps, J., Morgan, J.W., Staudigel, H., 2001. Testing the fixed hotspot hypothesis using 40Ar/39Ar age progressions along seamount trails. Earth Planet. Sci. Lett. 185, 237–252.

Koppers, A.A.P., Russell, J.A., Roberts, J., Jackson, M.G., Konter, J.G., Wright, D.J., Hart, S.R., 2011b. Age systematics of two young en echeleon Samoan volcanic trails. Geochemistry, Geophys. Geosystems 12. doi:10.1029/2010GC003438

Koppers, A.A.P., Staudigel, H., 2005. Asynchronous bends in Pacific seamount trails: a case for extensional volcanism? Science. 307, 904–907. doi:10.1126/science.1107260

Koppers, A.A.P., Staudigel, H., Phipps Morgan, J., Duncan, R.A., 2007. Nonlinear 40Ar/39Ar age systematics along the Gilbert Ridge and Tokelau Seamount Trail and the timing of the Hawaii-Emperor Bend. Geochemistry, Geophys. Geosystems 8. doi:10.1029/2006GC001489

Koppers, A.A.P., Staudigel, H., Pringle, M.S., Wijbrans, J.R., 2003. Short-lived and discontinuous intraplate volcanism in the South Pacific: Hot spots or extensional volcanism? Geochemistry, Geophys. Geosystems 4. doi:10.1029/2003GC000533

Koppers, A.A.P., Yamazaki, T., Geldmacher, J., Gee, J.S., Pressling, N., Hoshi, H., Anderson, L., Beier, C., Buchs, D.M., Chen, L.-H., Cohen, B.E., Deschamps, F., Dorais, M.J., Ebuna, D., Ehmann, S., Fitton, J.G., Fulton, P.M., Ganbat, E., Hamelin, C., Hanyu, T., Kalnins, L., Kell, J., Machida, S., Mahoney, J.J., Moriya, K., Nichols, A.R.L., Rausch, S., Sano, S. -i., Sylvan, J.B., Williams, R., 2012. Limited latitudinal mantle plume motion for the Louisville hotspot. Nat. Geosci. 5, 911–917. doi:10.1038/ngeo1638

Kuiper, K.F., Deino, A., Hilgen, F.J., Krijgsman, W., Renne, P.R., Wijbrans, J.R., 2008. Synchronizing Rock Clocks of Earth History. Science. 320, 500–504. doi:10.1126/science.1154339

Macdougall, J.D., Finkel, R.C., Carlson, J., Krishnaswami, S., 1979. Isotopic evidence for uranium exchange during low-temperature alteration of oceanic basalt. Earth Planet. Sci. Lett. 42, 27–34.

Morgan, W.J., 1972. Deep Mantle Convection Plumes and Plate Motions. Am. Assoc. Pet. Geol. Bull. 56, 203–213.

Nakanishi, M., Sager, W.W., Klaus, A., 1999. Magnetic lineations within Shatsky Rise, northwest Pacific Ocean: Implications for hot spot-triple junction interaction and oceanic plateau formation. J. Geophys. Res. 104, 7539–7556.

Neal, C.R., Mahoney, J.J., Kroenke, L.W., Duncan, R.A., Petterson, M.G., 1997. The Ontong Java Plateau. Geophys. Monogr. 100 183–216.

Nebel, O., Arculus, R.J., Westrenen, W. van, Woodhead, J.D., Jenner, F.E., Nebel-Jacobsen, Y.J., Wille, M., Eggins, S.M., 2013. Coupled Hf–Nd–Pb isotope co-variations of HIMU oceanic island basalts from Mangaia, Cook-Austral islands, suggest an Archean source component in the mantle transition zone. Geochim. Cosmochim. Acta 112, 87–101.

O'Connor, J.M., Jokat, W., 2015. Tracking the Tristan-Gough mantle plume using discrete chains of intraplate volcanic centers buried in the Walvis Ridge. Geology 43, 715–718. doi:10.1130/G36767.1

Payne, J.A., Jackson, M.G., Hall, P.S., 2013. Parallel volcano trends and geochemical asymmetry of the Society Islands hotspot track. Geology 41, 19–22. doi:10.1130/G33273.1

Price, A.A., Jackson, M.G., Blichert-Toft, J., Blusztajn, J., Conatser, C.S., Konter, J.G., Koppers, A.A.P., Kurz, M.D., 2016. Geochemical evidence in the Northeast Lau Basin for Subduction of the Cook-Austral Volcanic Chain in the Tonga Trench. Geochemistry, Geophys. Geosystems 17, 1694–1724.

Reynard, B., Lecuyer, C., Grandjean, P., 1999. Crystal-chemical controls on rare-earth element concentrations in fossil biogenic apatites and implications for paleoenvironmental reconstructions. Chem. Geol. 155, 233–241.

Rooney, T.O., Morell, K.D., Hidalgo, P., Fraceschi, P., 2015. Magmatic consequences of the transition from orthogonal to oblique subduction in Panama. Geochemistry, Geophys. Geosystems 16, 4178–4208. doi:10.1002/2015GC006150.Received

Sharp, W.D., Clague, D.A., 2006. 50-Ma initiation of Hawaiian-Emperor Bend records major change in Pacific plate motion. Science. 313, 1281–1284.

Sinton, J.M., Johnson, K.T.M., Price, R.C., 1985. Petrology and geochemistry of volcanic rocks from the northern Melanesian borderland, in: Brocher, T.M. (Ed.), Geological Investigations of the Northern Melanesian Borderland, Circum-Pacific Council for Energy and Mineral Resources for Earth Science Series, Vol. 3. Circum-Pacific Council for Energy and Mineral Resources.

Staudigel, H., Park, K.-H., Pringle, M.S., Rubenstone, J.L., Smith, W.H.F., Zindler, A., 1991. The longevity of the South Pacific isotopic and thermal anomaly. Earth Planet. Sci. Lett. 102, 24–44.

Sun, S.S., McDonough, W.F., 1989. Chemical and isotopic systematics of oceanic basalts: implications for mantle composition and processes. Geol. Soc. Am. Spec. Publ. 42, 313–345.

Tarduno, J.A., 2007. On the motion of Hawaii and other mantle plumes. Chem. Geol. 241, 234–247. doi:10.1016/j.chemgeo.2007.01.021

Tarduno, J.A., Duncan, R.A., Scholl, D.W., Cottrell, R.D., Steinberger, B., Thordarson, T., Kerr, B.C., Neal, C.R., Frey, F.A., Torii, M., Carvallo, C., 2003. The Emperor Seamounts: Southward Motion of the Hawaiian Hotspot Plume in Earth's Mantle. Science. 301, 1064–1069.

Taylor, B., 2006. The single largest oceanic plateau: Ontong Java–Manihiki–Hikurangi. Earth Planet. Sci. Lett. 241, 372–380. doi:10.1016/j.epsl.2005.11.049

Tejada, M.L.G., Mahoney, J.J., Duncan, R.A., Hawkins, M.P., 1996. Age and Geochemistry of Basement and Alkalic Rocks of Malaita and Santa Isabel, Solomon Islands, Southern Margin of Ontong Java Plateau. J. Petrol. 37, 361–394.

Valsami-Jones, E., Ragnarsdottir, K.V., 1997. Controls on uranium and thorium behaviour in ocean-floor hydrothermal systems: examples from the Pindos ophiolite, Greese. Chem. Geol. 135, 263–274.

Vanderkluysen, L., Mahoney, J.J., Koppers, A.A.P., Beier, C., Regelous, M., Gee, J.S., Lonsdale, P.F., 2014. Louisville Seamount Chain: Petrogenetic processes and geochemical evolution of the mantle source. Geochemistry, Geophys. Geosystems 15. doi:10.1002/2014GC005288.Received

Weaver, B.L., 1991. The origin of ocean island basalt end-member compositions: trace element and isotopic constraints. Earth Planet. Sci. Lett. 104, 381–397.

Weis, D., Garcia, M.O., Rhodes, J.M., Jellinek, M., Scoates, J.S., 2011. Role of the deep mantle in generating the compositional asymmetry of the Hawaiian mantle plume. Nat. Geosci. 4, 831–838. doi:10.1038/NGEO1328

Wessel, P., Kroenke, L.W., 2008. Pacific absolute plate motion since 145 Ma: An assessment of the fixed hot spot hypothesis. J. Geophys. Res. 113, B06101. doi:10.1029/2007JB005499

White, W.M., 2014. Composition of the Oceanic Crust, in: Treatise on Geochemistry. Elsevier Ltd., pp. 457–496. doi:10.1016/B978-0-08-095975-7.00315-6

Zindler, A., Hart, S.R., 1986. Chemical geodynamics. Annu. Rev. Earth Planet. Sci. 14, 493–571.

APPENDIX: SUPPLEMENTAL MATERIAL FOR RESEARCH CHAPTERS

SUPPLEMENTAL MATERIAL FOR:THE IMPORTANCE OF A NI CORRECTION WITH ION COUNTER IN THE DOUBLE SPIKE ANALYSIS OF FE ISOTOPE COMPOSITIONS USING A ^{57}FE/^{58}FE DOUBLE SPIKE

V. A. Finlayson[1], J. G. Konter[1], and L. Ma[2]

[1]Department of Geology and Geophysics, University of Hawai'i at Mānoa, Honolulu, Hawaii

[2]Department of Geological Sciences, University of Texas at El Paso, El Paso Texas

Published in Geochemistry, Geophysics, Geosystems vol. 16 (2015)

A.2.1. Introduction

This material contains information about instrumental settings used for the Nu Plasma HR, peak center mass data, modeled isotopic data, and additional projections of the outlier analysis ellipsoid. Peak center masses were determined at the time of sample analysis using the software interface with the Nu Plasma HR. Isotopic modeling was performed with the reanalysis routine and double spike correction code using the same software. Outlier rejection ellipsoid was generated in MATLAB using FAST-MCD implementations of the LIBRA robust software package.

Supplemental Table S.2.1. Nu Plasma instrumental settings

RF Power	1300 W
Coolant gas flow	13 L/min
Auxiliary gas flow	0.9 L/min
High voltage	6000V
Interface Pressure	~0.7 mbar
Variable slit width	0.03 mm
Sample uptake rate	~0.1 mL/min (100uL neb)
Neb pressure	34.7
Preamp bin backing	Varian IDP-3 scroll pump

Supplemental Table S.2.2. IRMM-014 DS analyses with ^{60}Ni monitored on a Faraday collector instead of ion counter.

	$^{56}Fe/^{54}Fe$ ratio	SE	$\delta^{56}Fe$ from average IRMM-014
IRMM-014 DS	15.6920	4.49E-03	0.058
IRMM-014 DS	15.6897	2.43E-04	-0.090
IRMM-014 DS	15.6906	3.79E-04	-0.034
IRMM-014 DS	15.6928	2.66E-04	0.110
IRMM-014 DS	15.6910	2.98E-04	-0.008
IRMM-014 DS	15.6905	2.57E-04	-0.037
Average IRMM-014 DS	**15.6911**		**0.000**
2σ	**0.00227**		**0.145**
No. analyses	**6**		

Supplemental Table S.2.3. Results of Faraday response test with dilutions of an in-house Ni test solution

Concentration (ppb)	^{60}Ni (V)	^{58}Ni (V)	^{58}Ni/^{60}Ni
100	0.949	2.32	2.44
10	8.65E-2	0.211	2.44
1	8.91E-3	2.20E-2	2.47
0.5	4.90E-3	1.22E-2	2.49
0.1	9.89E-4	2.79E-3	2.82
0.01	1.69E-4	5.39E-4	3.20
0.005	1.11E-4	3.91E-4	3.52
0.0001	7.8E-5	3.25E-4	4.17

Supplemental Table S.2.4. Data modeled with artificially altered Cr signal (No Cr signal subtraction, 2x, 3x, 5x, 7x, and 10x)[a]

Name	$^{56}Fe/^{54}Fe$ (1x ^{52}Cr)	^{52}Cr (mV)	No Cr correction	$\Delta^{56}Fe_{noCr}$	$^{56}Fe/^{54}Fe$ (2x ^{52}Cr)	$\Delta^{56}Fe_{2xCr}$	$^{56}Fe/^{54}Fe$ (3x ^{52}Cr)	$\Delta^{56}Fe_{3xCr}$	$^{56}Fe/^{54}Fe$ (5x ^{52}Cr)	$\Delta^{56}Fe_{5xCr}$	$^{56}Fe/^{54}Fe$ (7x ^{52}Cr)	$\Delta^{56}Fe_{7xCr}$	$^{56}Fe/^{54}Fe$ (10x ^{52}Cr)	$\Delta^{56}Fe_{10xCr}$
IRMM-014 DS	15.6893	0.286	15.6892	-0.008	15.6895	0.008	15.6896	0.017	15.6899	0.034	15.6901	0.050	15.6905	0.075
IRMM-014 DS	15.6899	0.268	15.6897	-0.008	15.6900	0.008	15.6901	0.016	15.6904	0.033	15.6906	0.048	15.6901	0.016
IRMM-014 DS	15.6900	0.270	15.6902	0.009	15.6904	0.025	15.6906	0.034	15.6908	0.051	15.6911	0.068	15.6915	0.093
IRMM-014 DS	15.6901	0.205	15.6900	-0.008	15.6902	0.008	15.6903	0.015	15.6905	0.030	15.6908	0.045	15.6911	0.068
IRMM-014 DS	15.6901	0.221	15.6899	-0.013	15.6903	0.008	15.6904	0.017	15.6907	0.034	15.6909	0.050	15.6913	0.076
IRMM-014 DS	15.6899	0.243	15.6897	-0.008	15.6900	0.008	15.6901	0.017	15.6904	0.033	15.6906	0.049	15.6910	0.074
IRMM-014 DS	15.6902	0.249	15.6901	-0.009	15.6903	0.009	15.6905	0.018	15.6908	0.035	15.6910	0.053	15.6914	0.075
IRMM-014 DS	15.6900	0.245	15.6899	-0.008	15.6902	0.009	15.6903	0.018	15.6906	0.035	15.6908	0.052	15.6913	0.078
IRMM-014 DS	15.6901	0.231	15.6899	-0.008	15.6902	0.008	15.6903	0.017	15.6906	0.034	15.6909	0.050	15.6913	0.076
IRMM-014 DS	15.6893	0.231	15.6891	-0.009	15.6894	0.008	15.6896	0.017	15.6898	0.034	15.6901	0.052	15.6905	0.077
Alfa Fe DS	15.6970	0.222	15.6968	-0.008	15.6971	0.008	15.6972	0.017	15.6975	0.032	15.6977	0.049	15.6981	0.073
IRMM-014 DS	15.6910	0.479	15.6907	-0.018	15.6913	0.018	15.6916	0.036	15.6921	0.072	15.6927	0.108	15.6936	0.169
IRMM-014 DS	15.6908	0.668	15.6904	-0.022	15.6911	0.022	15.6915	0.044	15.6921	0.087	15.6928	0.131	15.6938	0.196
IRMM-014 DS	15.6901	0.864	15.6896	-0.029	15.6905	0.029	15.6910	0.059	15.6919	0.118	15.6928	0.177	15.6941	0.258
IRMM-014 DS	15.6904	1.388	15.6896	-0.048	15.6911	0.048	15.6919	0.097	15.6934	0.194	15.6950	0.298	15.6973	0.444
Alfa Fe DS	15.6977	0.243	15.6975	-0.010	15.6978	0.010	15.6980	0.019	15.6983	0.038	15.6986	0.057	15.6990	0.086
IRMM-014 DS	15.6900	0.254	15.6898	-0.009	15.6901	0.009	15.6903	0.018	15.6905	0.035	15.6908	0.053	15.6912	0.080
Alfa Fe DS*	15.6972	0.217	15.6970	-0.009	15.6973	0.009	15.6974	0.018	15.6977	0.036	15.6980	0.054	15.6984	0.082

Permil (‰) differences ($\Delta^{56}Fe$) are calculated from the 1x Cr signal correction. Raw ^{52}Cr signal is provided; note the deviation of an analysis is greater when a higher initial signal is present. When the signal is multiplied 5-7 times that of the original measurement, most analyses are shifted to a higher ratio outside of the long-term reproducibility for Alfa Fe DS. Processed samples generally have a lower Cr content than IRMM-014 DS and Alfa Fe DS, and as a result, typically change less than those standards. Within the measured Cr signal levels, however, Cr variations are not expected to significantly influence $\delta^{56}Fe$ offsets. Based on the modeling results, this tolerance should extend out to ^{52}Cr levels as high as approximately 1 mV. When the signal is increased further, the measurement may no longer capture the true offset.

Supplemental Table S.2.4 (continued)

Name	$^{56}Fe/^{54}Fe$ (1x ^{52}Cr)	^{52}Cr (mV)	No Cr correction	$\Delta^{56}Fe_{noCr}$	$^{56}Fe/^{54}Fe$ (2x ^{52}Cr)	$\Delta^{56}Fe_{2xCr}$	$^{56}Fe/^{54}Fe$ (3x ^{52}Cr)	$\Delta^{56}Fe_{3xCr}$	$^{56}Fe/^{54}Fe$ (5x ^{52}Cr)	$\Delta^{56}Fe_{5xCr}$	$^{56}Fe/^{54}Fe$ (7x ^{52}Cr)	$\Delta^{56}Fe_{7xCr}$	$^{56}Fe/^{54}Fe$ (10x ^{52}Cr)	$\Delta^{56}Fe_{10xCr}$
IRMM-014 DS	15.6901	0.253	15.6901	-0.005	15.6903	0.009	15.6904	0.018	15.6907	0.036	15.6910	0.055	15.6914	0.082
Alfa Fe DS	15.6971	0.184	15.6969	-0.009	15.6972	0.009	15.6974	0.018	15.6976	0.036	15.6979	0.054	15.6984	0.081
IRMM-014 DS	15.6899	0.249	15.6898	-0.010	15.6901	0.010	15.6902	0.019	15.6905	0.038	15.6908	0.057	15.6913	0.087
IRMM-014 DS	15.6902	0.237	15.6901	-0.010	15.6904	0.010	15.6905	0.019	15.6908	0.038	15.6911	0.057	15.6915	0.085
IRMM-014 DS	15.6916	0.402	15.6914	-0.013	15.6918	0.013	15.6920	0.026	15.6924	0.052	15.6928	0.078	15.6933	0.110
IRMM-014 DS	15.6915	0.414	15.6913	-0.012	15.6917	0.012	15.6919	0.024	15.6923	0.048	15.6926	0.072	15.6932	0.108
IRMM-014 DS	15.6906	0.385	15.6904	-0.011	15.6907	0.011	15.6909	0.023	15.6913	0.046	15.6916	0.069	15.6922	0.103
IRMM-014 DS	15.6908	0.310	15.6907	-0.011	15.6910	0.011	15.6912	0.021	15.6915	0.043	15.6918	0.064	15.6923	0.096
IRMM-014 DS	15.6917	0.207	15.6915	-0.013	15.6918	0.008	15.6920	0.021	15.6924	0.046	15.6928	0.071	15.6934	0.108
IRMM-014 DS	15.6916	0.284	15.6915	-0.009	15.6917	0.008	15.6919	0.017	15.6921	0.034	15.6924	0.054	15.6928	0.080
Alfa Fe DS	15.6990	0.240	15.6988	-0.007	15.6991	0.007	15.6992	0.014	15.6994	0.031	15.6997	0.045	15.7000	0.066
IRMM-014 DS	15.6947	0.258	15.6946	-0.009	15.6949	0.008	15.6950	0.017	15.6953	0.035	15.6956	0.053	15.6960	0.080
IRMM-014 DS	15.6938	0.252	15.6936	-0.009	15.6939	0.009	15.6941	0.018	15.6943	0.036	15.6947	0.057	15.6951	0.083
IRMM-014 DS	15.6934	0.248	15.6933	-0.009	15.6935	0.008	15.6937	0.017	15.6939	0.034	15.6942	0.052	15.6946	0.078
Alfa Fe DS	15.7012	0.258	15.7011	-0.008	15.7013	0.008	15.7014	0.016	15.7017	0.032	15.7020	0.048	15.7023	0.073
Alfa Fe DS	15.7009	0.239	15.7008	-0.008	15.7010	0.008	15.7011	0.015	15.7014	0.031	15.7016	0.046	15.7020	0.070
OL-2	15.6936	0.138	15.6936	-0.004	15.6937	0.004	15.6938	0.009	15.6939	0.018	15.6941	0.027	15.6943	0.041
IRMM-014 DS	15.6931	0.229	15.6929	-0.009	15.6932	0.009	15.6934	0.018	15.6936	0.036	15.6939	0.054	15.6943	0.080
OL-3**	15.6939	0.149	15.6939	-0.005	15.6940	0.006	15.6941	0.011	15.6943	0.022	15.6944	0.032	15.6947	0.048
B-OL	15.6926	0.150	15.6925	-0.005	15.6927	0.006	15.6928	0.011	15.6930	0.022	15.6931	0.032	15.6934	0.048
IRMM-014 DS	15.6927	0.230	15.6925	-0.010	15.6928	0.009	15.6929	0.018	15.6932	0.037	15.6935	0.055	15.6940	0.083
Alfa Fe DS	15.7005	0.245	15.7003	-0.009	15.7006	0.008	15.7007	0.017	15.7010	0.032	15.7012	0.049	15.7016	0.076

Supplemental Table S.2.4 (continued)

Name	$^{56}Fe/^{54}Fe$ (1x ^{52}Cr)	^{52}Cr (mV)	No Cr correction	$\Delta^{56}Fe_{noCr}$	$^{56}Fe/^{54}Fe$ (2x ^{52}Cr)	$\Delta^{56}Fe_{2xCr}$	$^{56}Fe/^{54}Fe$ (3x ^{52}Cr)	$\Delta^{56}Fe_{3xCr}$	$^{56}Fe/^{54}Fe$ (5x ^{52}Cr)	$\Delta^{56}Fe_{5xCr}$	$^{56}Fe/^{54}Fe$ (7x ^{52}Cr)	$\Delta^{56}Fe_{7xCr}$	$^{56}Fe/^{54}Fe$ (10x ^{52}Cr)	$\Delta^{56}Fe_{10xCr}$
B-OL	15.6932	0.127	15.6932	-0.002	15.6933	0.005	15.6934	0.010	15.6935	0.020	15.6937	0.033	15.6940	0.048
IRMM-014 DS	15.6929	0.245	15.6928	-0.010	15.6931	0.009	15.6932	0.018	15.6935	0.037	15.6938	0.055	15.6942	0.083
IRMM-014 DS	15.6917	0.239	15.6916	-0.009	15.6918	0.009	15.6920	0.018	15.6923	0.036	15.6926	0.058	15.6930	0.085
IRMM-014 DS	15.6914	0.216	15.6912	-0.008	15.6915	0.008	15.6916	0.017	15.6919	0.037	15.6922	0.057	15.6926	0.082
IRMM-014 DS	15.6916	0.233	15.6915	-0.008	15.6917	0.008	15.6918	0.015	15.6921	0.031	15.6923	0.047	15.6927	0.070
Alfa Fe DS	15.6982	0.196	15.6981	-0.008	15.6984	0.008	15.6985	0.017	15.6988	0.033	15.6990	0.050	15.6994	0.075
Alfa Fe DS	15.6989	0.201	15.6988	-0.008	15.6991	0.008	15.6992	0.016	15.6994	0.031	15.6997	0.047	15.7000	0.071
IRMM-014 DS	15.6905	0.195	15.6903	-0.011	15.6905	0.005	15.6907	0.013	15.6909	0.029	15.6912	0.046	15.6916	0.070
Alfa Fe DS	15.6976	0.173	15.6975	-0.008	15.6978	0.008	15.6979	0.016	15.6981	0.032	15.6984	0.047	15.6988	0.071
Alfa Fe DS	15.6980	0.179	15.6979	-0.008	15.6982	0.008	15.6983	0.016	15.6985	0.032	15.6988	0.048	15.6992	0.071
IRMM-014 DS	15.6906	0.204	15.6905	-0.008	15.6907	0.008	15.6909	0.017	15.6911	0.033	15.6914	0.050	15.6917	0.071
IRMM-014 DS	15.6907	0.213	15.6905	-0.008	15.6908	0.009	15.6909	0.018	15.6912	0.036	15.6915	0.057	15.6920	0.083
IRMM-014 DS	15.6900	0.209	15.6898	-0.009	15.6901	0.008	15.6902	0.017	15.6905	0.031	15.6907	0.048	15.6911	0.075
IRMM-014 DS	15.6902	0.290	15.6900	-0.009	15.6903	0.009	15.6904	0.017	15.6907	0.035	15.6910	0.053	15.6914	0.079
Alfa Fe DS	15.6969	0.255	15.6968	-0.009	15.6970	0.009	15.6972	0.018	15.6975	0.036	15.6977	0.054	15.6982	0.080
Alfa Fe DS*	15.6977	0.242	15.6975	-0.010	15.6978	0.009	15.6979	0.018	15.6982	0.036	15.6985	0.054	15.6989	0.081
IRMM-014 DS	15.6906	0.258	15.6905	-0.010	15.6907	0.009	15.6909	0.018	15.6912	0.037	15.6915	0.055	15.6919	0.083
Alfa Fe DS	15.6977	0.253	15.6975	-0.009	15.6978	0.009	15.6979	0.018	15.6982	0.036	15.6985	0.054	15.6989	0.080
IRMM-014 DS	15.6899	0.265	15.6897	-0.010	15.6900	0.009	15.6902	0.018	15.6905	0.037	15.6907	0.055	15.6912	0.083
IRMM-014 DS	15.6890	0.276	15.6889	-0.009	15.6892	0.010	15.6893	0.018	15.6896	0.037	15.6899	0.055	15.6903	0.083
Alfa Fe DS	15.6967	0.238	15.6966	-0.010	15.6969	0.009	15.6970	0.018	15.6973	0.036	15.6976	0.054	15.6980	0.082
Alfa Fe DS*	15.6972	0.250	15.6970	-0.010	15.6973	0.010	15.6975	0.019	15.6978	0.038	15.6981	0.057	15.6985	0.085
IRMM-014 DS	15.6892	0.294	15.6891	-0.010	15.6894	0.010	15.6895	0.019	15.6898	0.039	15.6901	0.058	15.6906	0.087

Supplemental Table S.2.4 (continued)

Name	$^{56}Fe/^{54}Fe$ (1x ^{52}Cr)	^{52}Cr (mV)	No Cr correction	$\Delta^{56}Fe_{noCr}$	$^{56}Fe/^{54}Fe$ (2x ^{52}Cr)	$\Delta^{56}Fe_{2xCr}$	$^{56}Fe/^{54}Fe$ (3x ^{52}Cr)	$\Delta^{56}Fe_{3xCr}$	$^{56}Fe/^{54}Fe$ (5x ^{52}Cr)	$\Delta^{56}Fe_{5xCr}$	$^{56}Fe/^{54}Fe$ (7x ^{52}Cr)	$\Delta^{56}Fe_{7xCr}$	$^{56}Fe/^{54}Fe$ (10x ^{52}Cr)	$\Delta^{56}Fe_{10xCr}$
IRMM-014 DS	15.6911	0.271	15.6910	-0.010	15.6913	0.009	15.6914	0.018	15.6917	0.038	15.6920	0.056	15.6925	0.084
IRMM-014 DS	15.6905	0.255	15.6904	-0.009	15.6907	0.009	15.6908	0.018	15.6911	0.036	15.6914	0.054	15.6918	0.081
IRMM-014 DS	15.6917	0.290	15.6915	-0.010	15.6918	0.010	15.6920	0.018	15.6923	0.038	15.6926	0.057	15.6930	0.085
IRMM-014 DS	15.6907	0.284	15.6905	-0.010	15.6908	0.010	15.6910	0.019	15.6913	0.039	15.6916	0.058	15.6920	0.087
B-OL.1	15.6916	0.221	15.6915	-0.007	15.6917	0.006	15.6918	0.013	15.6920	0.025	15.6922	0.038	15.6925	0.055
B-OPX	15.6907	0.668	15.6904	-0.021	15.6910	0.022	15.6914	0.043	15.6920	0.085	15.6927	0.128	15.6937	0.192
SAV09-15	15.6915	0.297	15.6914	-0.009	15.6917	0.009	15.6918	0.018	15.6921	0.036	15.6924	0.054	15.6928	0.082
IRMM-014 DS	15.6908	0.303	15.6907	-0.010	15.6910	0.010	15.6911	0.020	15.6915	0.040	15.6918	0.059	15.6922	0.088
SAV09-15.1	15.6901	0.205	15.6899	-0.007	15.6902	0.008	15.6903	0.015	15.6906	0.033	15.6908	0.048	15.6912	0.071
B-OPX.1.2	15.6902	0.757	15.6897	-0.029	15.6906	0.029	15.6911	0.057	15.6920	0.114	15.6929	0.171	15.6942	0.257
SAV09-15NI	15.6901	0.191	15.6900	-0.007	15.6902	0.008	15.6903	0.015	15.6905	0.029	15.6908	0.043	15.6910	0.062
IRMM-014 DS	15.6889	0.267	15.6888	-0.010	15.6891	0.010	15.6892	0.020	15.6896	0.041	15.6899	0.061	15.6904	0.091
SAV09-15.3	15.6899	0.251	15.6898	-0.008	15.6901	0.008	15.6902	0.017	15.6905	0.034	15.6907	0.051	15.6911	0.077
B-OL.3	15.6893	0.258	15.6892	-0.008	15.6894	0.008	15.6896	0.017	15.6898	0.033	15.6900	0.045	15.6905	0.073
SAV09-15.4*	15.6893	0.312	15.6891	-0.010	15.6894	0.009	15.6895	0.018	15.6898	0.036	15.6901	0.054	15.6905	0.082
IRMM-014 DS	15.6885	0.332	15.6884	-0.011	15.6887	0.011	15.6889	0.022	15.6892	0.043	15.6896	0.064	15.6901	0.097
B-CPX*	15.6899	1.702	15.6891	-0.052	15.6907	0.053	15.6915	0.106	15.6932	0.211	15.6948	0.316	15.6973	0.474
SAV09-15.2	15.6892	0.309	15.6890	-0.010	15.6893	0.010	15.6895	0.020	15.6898	0.039	15.6901	0.059	15.6906	0.087
IRMM-014 DS	15.6884	0.343	15.6882	-0.011	15.6886	0.011	15.6888	0.022	15.6891	0.045	15.6895	0.067	15.6900	0.101
IRMM-014 DS	15.6908	0.288	15.6907	-0.010	15.6910	0.010	15.6911	0.019	15.6914	0.038	15.6917	0.057	15.6922	0.086
IRMM-014 DS	15.6905	0.278	15.6903	-0.010	15.6906	0.010	15.6908	0.018	15.6910	0.034	15.6913	0.050	15.6917	0.078
IRMM-014 DS	15.6897	0.280	15.6895	-0.010	15.6898	0.010	15.6900	0.020	15.6903	0.039	15.6905	0.055	15.6910	0.084

Supplemental Table S.2.4 (continued)

Name	$^{56}Fe/^{54}Fe$ (1x ^{52}Cr)	^{52}Cr (mV)	No Cr correction	$\Delta^{56}Fe_{noCr}$	$^{56}Fe/^{54}Fe$ (2x ^{52}Cr)	$\Delta^{56}Fe_{2xCr}$	$^{56}Fe/^{54}Fe$ (3x ^{52}Cr)	$\Delta^{56}Fe_{3xCr}$	$^{56}Fe/^{54}Fe$ (5x ^{52}Cr)	$\Delta^{56}Fe_{5xCr}$	$^{56}Fe/^{54}Fe$ (7x ^{52}Cr)	$\Delta^{56}Fe_{7xCr}$	$^{56}Fe/^{54}Fe$ (10x ^{52}Cr)	$\Delta^{56}Fe_{10xCr}$
B-CPX*	15.6896	1.536	15.6887	-0.053	15.6904	0.054	15.6912	0.106	15.6929	0.214	15.6946	0.320	15.6971	0.480
B-OPX.1.2*	15.6898	0.994	15.6893	-0.027	15.6902	0.026	15.6906	0.053	15.6914	0.105	15.6922	0.158	15.6935	0.237
IRMM-014 DS	15.6892	0.317	15.6891	-0.010	15.6894	0.010	15.6895	0.020	15.6899	0.040	15.6902	0.060	15.6906	0.090
BCR-2*	15.6895	0.243	15.6894	-0.008	15.6896	0.007	15.6898	0.015	15.6900	0.029	15.6902	0.045	15.6906	0.067
SAV09-15.1OPX	15.6903	0.264	15.6902	-0.008	15.6904	0.008	15.6905	0.015	15.6908	0.031	15.6910	0.046	15.6914	0.069
SAV09-15.1*	15.6890	0.214	15.6900	-0.006	15.6891	0.006	15.6892	0.013	15.6894	0.025	15.6896	0.038	15.6899	0.056
IRMM-014 DS	15.6891	0.278	15.6889	-0.010	15.6892	0.010	15.6894	0.020	15.6897	0.040	15.6900	0.059	15.6905	0.089
SAV09-15NI*	15.6880	0.204	15.6879	-0.006	15.6881	0.007	15.6882	0.014	15.6885	0.028	15.6887	0.042	15.6890	0.062
Alfa Fe DS	15.6961	0.518	15.6958	-0.017	15.6964	0.017	15.6966	0.034	15.6972	0.068	15.6977	0.103	15.6985	0.154
IRMM-014 DS	15.6887	0.325	15.6885	-0.013	15.6889	0.010	15.6890	0.020	15.6893	0.040	15.6896	0.061	15.6901	0.091
IRMM-014 DS	15.6892	0.424	15.6890	-0.014	15.6894	0.013	15.6896	0.027	15.6900	0.054	15.6905	0.080	15.6911	0.120
IRMM-014 DS	15.6891	0.451	15.6889	-0.013	15.6893	0.013	15.6895	0.027	15.6899	0.054	15.6904	0.080	15.6910	0.120
IRMM-014 DS	15.6905	0.456	15.6903	-0.013	15.6908	0.013	15.6910	0.027	15.6914	0.054	15.6918	0.081	15.6924	0.121
KH-26*	15.6923	0.264	15.6922	-0.008	15.6925	0.008	15.6926	0.017	15.6928	0.033	15.6931	0.050	15.6935	0.074
KH-60B*	15.6929	0.227	15.6928	-0.006	15.6930	0.006	15.6931	0.013	15.6933	0.025	15.6934	0.038	15.6937	0.057
BCR-2	15.6918	0.311	15.6917	-0.010	15.6920	0.010	15.6922	0.020	15.6925	0.039	15.6928	0.058	15.6932	0.087
IRMM-014 DS	15.6898	0.422	15.6896	-0.013	15.6901	0.013	15.6903	0.027	15.6907	0.054	15.6911	0.080	15.6917	0.120
SAV09-15OPX*	15.6907	0.325	15.6905	-0.010	15.6909	0.010	15.6910	0.020	15.6914	0.041	15.6917	0.062	15.6922	0.092
B-OPX.3	15.6912	0.267	15.6911	-0.008	15.6914	0.008	15.6915	0.015	15.6917	0.031	15.6920	0.047	15.6923	0.069
Alfa Fe DS	15.6977	0.597	15.6975	-0.017	15.6980	0.017	15.6983	0.034	15.6988	0.069	15.6994	0.103	15.7002	0.155
IRMM-014 DS	15.6911	0.370	15.6909	-0.012	15.6913	0.012	15.6914	0.024	15.6918	0.047	15.6922	0.071	15.6927	0.106

Supplemental Table S.2.5. Blocks 1 and 2 D^2 (squared Mahalanobis distances) values and peak center offsets (η) for the secondary standards and samples

Sample Name	Type	η_{Fe} block 1	η_{Ni} block 1	η_{Cr} block 1	Block 1 D^2	η_{Fe} block 2	η_{Ni} block 2	η_{Cr} block 2	Block 2 D^2
Alfa Fe DS[a]	Standard	-10.73	-11.46	-18.07	**3.08**	--	--	--	**--**
Alfa Fe DS	Standard	0.00	13.09	4.75	**3.76**	--	--	--	**--**
Alfa Fe DS	Standard	-10.73	4.09	5.70	***18.09***[b]	--	--	--	**--**
Alfa Fe DS	Standard	3.58	0.82	3.80	**0.13**	--	--	--	**--**
Alfa Fe DS	Standard	0.00	-8.19	-1.90	**0.94**	-7.16	-16.38	-17.12	**5.23**
Alfa Fe DS	Standard	-1.79	2.87	-5.23	**0.91**	--	--	--	**--**
Alfa Fe DS	Standard	-7.16	-10.65	-78.98	**217.93**[c]	6.26	-13.11	-15.23	**24.16**[c]
Alfa Fe DS	Standard	1.19	1.64	-1.90	**0.36**	-0.60	-1.09	-2.54	**0.26**
Alfa Fe DS	Standard	-3.58	-6.55	2.54	**2.48**	0.00	3.28	0.00	**0.35**
Alfa Fe DS	Standard	0.00	3.28	3.17	**0.99**	5.37	11.47	-1.90	**2.31**
Alfa Fe DS	Standard	6.56	-2.18	10.78	**1.87**	3.58	8.74	4.44	**0.45**
Alfa Fe DS	Standard	11.33	3.82	13.96	**1.34**	14.31	9.28	6.98	**3.02**
Alfa Fe DS	Standard	7.16	-12.02	5.07	***4.71***[b]	-2.98	-23.50	1.90	***6.17***[b]
Alfa Fe DS	Standard	1.79	8.75	0.63	**0.71**	20.87	-19.13	-3.81	***49.71***[b]
Alfa Fe DS	Standard	7.16	8.20	43.76	**59.32**[c]	--	--	--	**--**
Alfa Fe DS	Standard	9.54	-1.09	6.98	**1.82**	1.19	3.83	-2.54	**0.60**
Alfa Fe DS	Standard	-5.96	37.17	-142.06	***802.30***[b]	-6.56	-7.11	-3.17	**1.52**
Alfa Fe DS	Standard	19.08	19.10	18.39	**0.95**	4.77	9.82	3.80	**0.31**
Alfa Fe DS	Standard	17.89	20.47	17.60	**0.76**	5.81	18.42	15.69	**6.72**[c]
OL-2	KHol	-1.79	-7.78	-8.09	**1.99**	-9.39	-15.56	-7.61	**1.65**
OL-3	KHol	84.68	-4.37	-10.78	***566.60***[b]	-1.19	-8.19	-9.52	**3.28**
B-OL	KHol	-9.54	-8.74	-15.86	**2.44**	-16.70	-19.66	-19.03	**2.54**

[a]Bracketing peak center mass has been estimated based on a stable drift throughout analysis day.
[b]Outliers in Fe-Ni space.
[c]Outliers along the Cr axis only; measurement is not removed from average.

Supplemental Table S.2.5 (continued)

Sample Name	Type	Fe block 1 offsets	Ni block 1 offsets	Cr block 1 offsets	Block 1 D^2	Fe block 2 offsets	Ni block 2 offsets	Cr block 2 offsets	Block 2 D^2
B-OL	KHol	-4.77	1.64	-236.00	**2284.34[c]**	9.54	9.28	4.44	**1.03**
B-OL.1	KHol	9.39	21.68	3.33	**2.97**	16.09	14.32	18.06	**0.87**
B-OL.3	KHol	2.68	4.09	4.75	**0.39**	7.15	7.36	8.56	**0.17**
B-OPX	KHopx	20.56	28.63	16.16	**2.30**	32.18	35.18	36.13	**4.13**
B-OPX.1.2	KHopx	-7.15	-15.54	-1.90	**2.93**	3.58	3.27	0.00	**0.41**
B-OPX.1.2	KHopx	-62.00	-40.92	-52.62	***39.02[b]***	-56.04	-106.94	-54.53	***42.05[b]***
B-OPX.3	KHopx	19.68	16.37	10.46	**4.88[c]**	8.05	5.73	-0.95	**3.29**
B-CPX	KHcpx	--	--	--	**--**	-11.32	4.91	-8.24	***6.15[b]***
B-CPX	KHpx	-41.73	-22.92	-34.87	***21.66[b]***	-24.44	-42.01	-32.97	***9.29[b]***
KH-26	KHcpx	29.97	53.64	23.79	***9.53[b]***	31.31	35.62	24.74	**5.21[c]**
KH-60B	KHcpx	20.58	30.30	22.83	**2.13**	34.00	41.76	38.06	***4.90[b]***
SAV09-15	SAVol	31.73	29.04	38.50	**5.64[c]**	26.82	28.22	33.27	**4.03**
SAV09-15.1	SAVol	-7.15	-15.13	-8.56	**1.35**	-8.94	-9.00	-10.46	**1.09**
SAV09-15.1	SAVol	-8.94	13.50	-2.85	***10.32[b]***	-15.65	-27.83	-15.69	**3.42**
SAV09-15NI	SAVol	0.00	-7.77	2.85	**1.28**	-5.36	-5.73	-2.85	**1.08**
SAV09-15NI	SAVol	45.31	44.74	44.38	***8.27[b]***	45.31	40.92	45.65	***8.84[b]***
SAV09-15.2	SAVol	-0.60	9.27	-9.51	**4.27**	2.38	-4.91	8.24	**2.37**
SAV09-15.3	SAVol	-9.39	-12.68	-8.08	**1.35**	0.00	-0.41	0.48	**0.21**
SAV09-15.4	SAVol	5.81	33.95	15.69	***14.48[b]***	0.00	0.41	9.03	**4.24**
SAV09-15OPX	SAVopx	1.79	20.47	1.43	**4.39**	6.71	7.78	9.04	**0.36**
SAV09-15.1OPX	SAVopx	7.15	7.37	3.80	**0.36**	-9.84	-21.28	-10.46	**2.32**
BCR-2	USGS Ref.	17.89	50.33	21.87	***13.10[b]***	17.44	-6.55	25.20	***10.90[b]***
BCR-2	USGS Ref.	9.39	23.33	10.46	**2.34**	20.57	33.16	17.12	**2.89**

Supplemental Table S.2.6. Iron isotopic data without double spike correction.

Name	Type	$\delta^{56}Fe$	block 1 $\delta^{56}Fe$	block 2 $\delta^{56}Fe$
Alfa Fe DS	Standard	0.070		
Alfa Fe DS	Standard	0.060		
Alfa Fe DS[a]	*Standard*	*0.029*		
Alfa Fe DS	Standard	0.027		
Alfa Fe DS	Standard	0.057		
Alfa Fe DS	Standard	0.079		
Alfa Fe DS	Standard	0.065		
Alfa Fe DS	Standard	0.070		
Alfa Fe DS	Standard	0.027		
Alfa Fe DS	Standard	0.098		
Alfa Fe DS	Standard	0.035		
Alfa Fe DS	Standard	0.057		
Alfa Fe DS[a]	*Standard*	*0.011*		
Alfa Fe DS[b]	*Standard*	*0.049*	0.034	
Alfa Fe DS	Standard	0.093		
Alfa Fe DS	Standard	0.080		
Alfa Fe DS[b]	*Standard*	*0.101*		0.095
Alfa Fe DS	Standard	0.040		
Alfa Fe DS	Standard	0.023		

	All analyses	Outliers removed
Average Alfa	0.056	0.059
2σ	0.054	0.050

[a]Entire measurement was identified as an outlier and discarded
[b]One block identified as an outlier and discarded. For these measurements, the non-outlying block $\delta^{56}Fe$ value is listed.

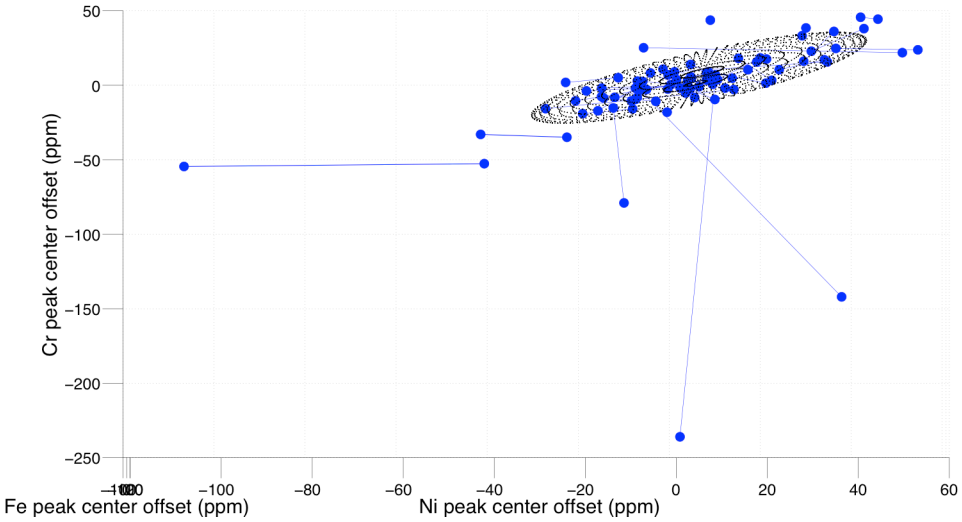

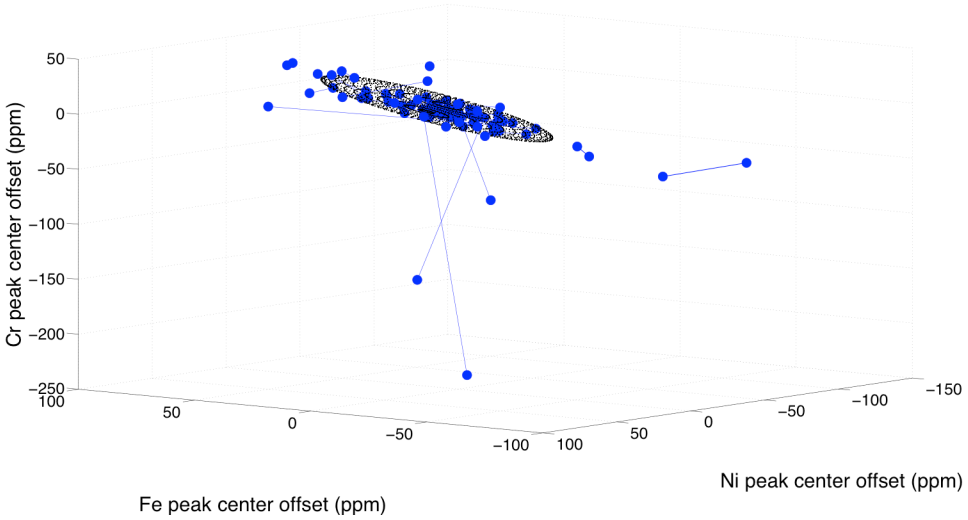

Supplemental Figure S.2.1. Additional projections of the outlier detection ellipsoid showing variation along the Cr axis.

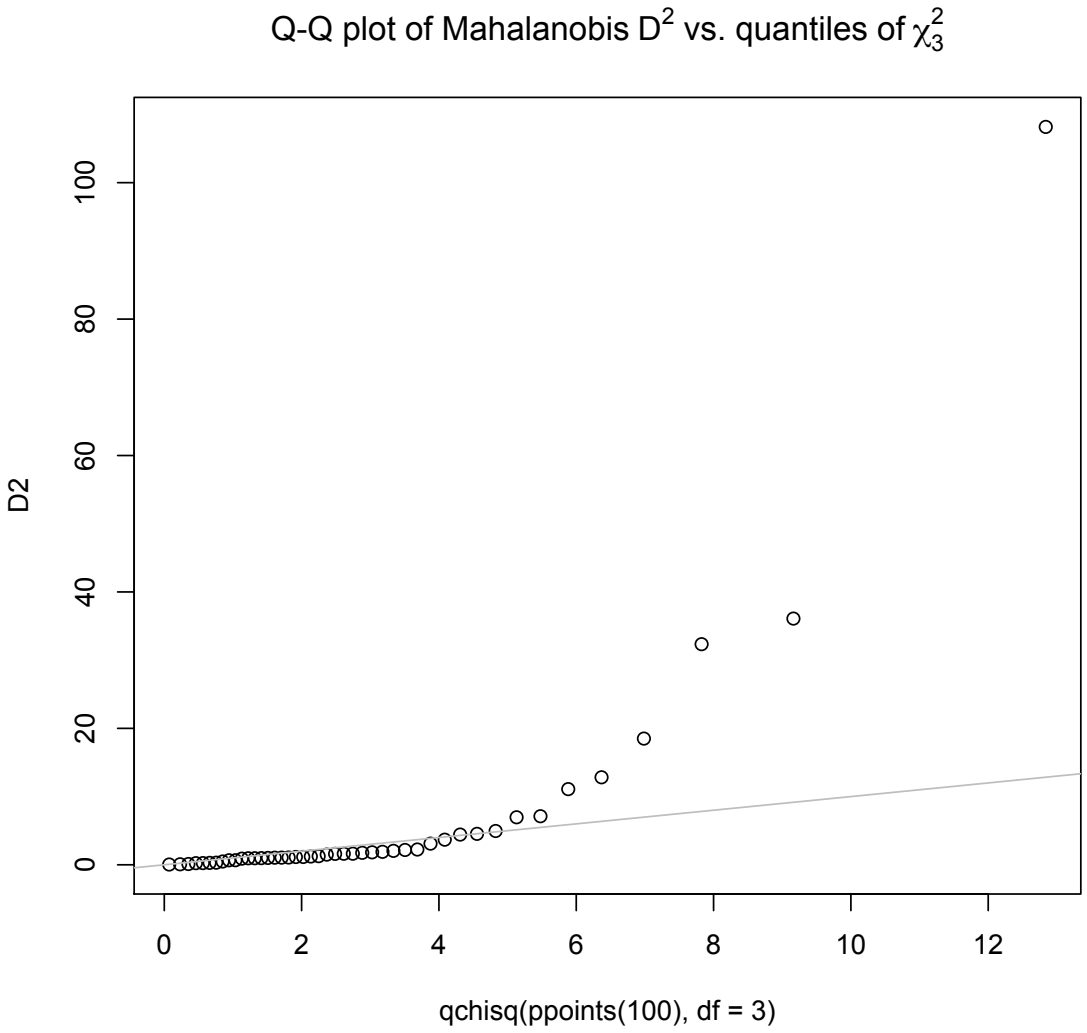

Supplemental Figure S.2.2. Q-Q plot of dataset Mahalanobis distances (given in Table S.6) showing the non-normal distribution of the data.

SUPPLEMENTAL METHODS AND DISCUSSION FOR "A HAWAIIAN-EMPEROR STYLE BEND IN THE HEMISPHERICALLY-ZONED RURUTU HOTSPOT REVEALED BY SR-PB-ND-HF ISOTOPES"

V.A. Finlayson, J.G. Konter, K. Konrad, A.A.P. Koppers, M.G. Jackson, T.O. Rooney

A.4.1. Sample preparation

Initial sample processing took place during the RR1310 cruise. After recovery from the dredge, samples were cut with a diamond-tipped rock saw, cleaned with fresh water, and prepared for petrographic descriptions via microscope. Thin section-sized billets were prepared for groundmass major element estimates by portable laser-induced breakdown spectroscopy (LIBS). Using a combination of onboard petrography and compositional data, multiple (where possible) representative samples from each dredge were selected as candidates for geochemical and isotopic analyses.

From onboard sample selections, the smaller subset of samples ultimately presented in this study was later selected to represent bulk dredge/seamount behavior across the length of the Tuvalu chain and into western Samoa. Selection criteria emphasized samples with the least alteration and secondary mineralization while including as many unique seamounts as possible along the track to best capture and define the Rurutu Bend region (Figures 4.1 and 4.7 in main text).

Prior to geochemical analyses, samples were trimmed with a diamond-tipped saw to remove visibly altered rinds and secondary mineralization in veins and fractures, then crushed in a ceramic jaw crusher to <1mm pieces. Prior to crushing each sample, the ceramic plates were precontaminated with the alteration rinds trimmed from each sample, and then the plates and collection tray were thoroughly cleaned with metal-free tools. The sample was then crushed and collected, and the equipment cleaned again. The crushed sample was then split, with one fraction reserved for compositional analyses and the other for isotopic analyses.

A.4.2. Major and trace element chemistry

Each sample was picked under a microscope to separate phenocryst phases and secondary mineralization from groundmass. Although groundmass was altered by seawater and, for some samples, subaerial weathering processes, it is the rock fraction that best preserves the geochemical profiles of the melt at the time of eruption. Secondary minerals were removed to reduce the influence of open-system and alteration/weathering behavior on groundmass composition. Phenocryst phases such as clinopyroxene were also removed as completely as possible to reduce the chance of phenocryst over-representation, skewing the major element geochemistry toward mineral compositions.

10-15 grams of sample were hand-picked, then hand-powdered with an agate mortar and pestle. These powders were then combined with lithium tetraborate at Michigan State University in a low dilution flux fusion procedures that is detailed elsewhere (Rooney et al., 2012). One sample (D04-01D) was prepared by high-dilution fusion. Major element analysis of the flux-fused discs also took place at the Michigan State University using a Bruker S4 Pioneer X-Ray Fluorescence (XRF). Major elements were used as an internal standard for trace element analysis, which was carried out on the same flux fused disks analyzed for major elements. The trace element analysis was carried out using a Laser Ablation Inductively Coupled Plasma Mass Spectrometry (LA-ICPMS) system comprised of a Photon Machines Analyte G2 laser coupled to a Thermo iCap-Q ICPMS. LA-ICP-MS methods and standards used for calibration are described in Rooney et al. (2015). Each disk was analyzed in triplicate with drift correction being applied throughout the day. The results of these analyses and the standards run as unknowns are presented in the Supplemental Tables S.4.1 and S.4.2.

The majority of the samples in this study are alkalic or transitional basalts or basalt differentiates, and three are tholeiitic basalts (Supplemental Figure S.4.2; Supplemental Table S.4.1). All three RR1310 Group 2 samples have MgO < 1.5%, suggesting the parental magmas underwent more differentiation than the other three groups (2.1-7.6 wt%; Supplemental Figure S.4.3). Two of the three Group 2 samples also display the highest SiO_2 contents of the sample set, up to 49.8 wt%. The third Group 2 sample, however, has SiO_2 indistinguishable (43.9 wt%) from the main cluster of samples. All other samples have similar compositions, such that the four compositional groups described in Sections 5 and 6 of the main text cannot be reliably distinguished based on major element composition alone.

A.4.3. Isotopic separations

The Pb-Nd-Hf-Sr isotope analyses were performed on the Nu Plasma HR multicollector inductively coupled plasma mass spectrometer (MC-ICPMS) at the University of Hawai‘i at Mānoa (UHM) Department of Geology and Geophysics. Sr replicate analyses were performed on the UHM VG Sector thermal ionization mass spectrometer (TIMS). Elements analyzed for isotopic ratios, particularly Sr and Pb, may be subject to seawater alteration processes. Splits of crushed sample, described previously, that were reserved for isotopic analysis underwent a series of leaches of increasing strength to remove any secondary isotopic overprint and the majority of any secondary isotopic overprinting (modified after Koppers et al., 2003). This leaching approach is generally successful at removing the seawater contribution to our rocks, reflected by the correspondence of isotopic ratios in leached whole rocks and mineral separates (Konter et

al., 2008; Koppers et al., 2003). However, there are some exceptions, discussed in Section 4 of this Supplemental Methods document and Section 6 of the main text.

Crushed samples are leached on a hot plate for approximately one hour in 2N HCl, then rinsed three times in 18MΩ H_2O to stop the leach. This sequence is repeated using 6N HCl, then once more with 4N HNO_3. Samples are then dried under a heating lamp. Next, 500-600 mg cuts of crushed and leached sample underwent a final overnight leach, lasting ~16 hours, in 1 mL ~6N HCl immediately prior to dissolution to remove any altered or secondary material that the first leach did not remove. After leaching was complete, the samples were inspected for any remaining secondary minerals. If present, secondary minerals were picked out with clean metal-free tools. After the overnight leach, samples were digested in a mixture of concentrated HF and 8N or concentrated HNO_3 for approximately one week. Once completely broken down, the sample set underwent a series of seven separation procedures to isolate Sr, Pb, Nd, and Hf for analysis (Supplemental Figure S.4.10) described in more detail below.

Sr and Pb primary separations were performed on a single Sr-Spec resin column using a procedure discussed in detail by (Konter and Storm, 2014). The remaining bulk sample was retained for Nd and Hf separation. Secondary column separations for Sr and Pb separates are necessary for further purification and removal of potential interfering elements. The secondary Sr separation procedure was identical to the primary separation, except that the Pb separation step was not included. Sr analyses on the Nu Plasma were performed in wet plasma mode, using a multidynamic program with online Kr interference correction was used to collect isotopic data and the reported results were normalized to a

recommended $^{86}Sr/^{88}Sr$ ratio of 0.1194 (Konter and Storm, 2014). Selected Sr samples and processed USGS standards were replicated via VG Sector TIMS.

The secondary Pb separation uses 100-200 mesh AG1-X8 resin (after Hanan and Schilling, 1989) to remove any matrix still remaining after the primary separation procedure. Pb was analyzed using the desolvating nebulizer (DSN), monitoring fractionation with a Tl spike (NIST SRM 997; $^{205}Tl/^{203}Tl = 2.3889$) and standard-sample bracketing against reference standard NIST SRM 981 (following White et al., 2000). Pb blanks ranged from 37-78 pg.

Nd is separated from the matrix wash collected from the first (Sr and Pb) column, following Horwitz et al. (1993), Konter and Storm (2014), and Pin et al. (1997). The first of two steps separates REEs from the matrix on Eichrom TRU resin. To reduce Fe^{3+} to Fe^{2+}, ascorbic acid is added to each sample prior to being placed on the column, preventing overloading of the TRU resin. The REE cut is placed on an Eichrom LN resin bed for chromatographic REE separation, from which Nd was collected. Nd analysis on the Nu Plasma used a multidynamic program with online REE interference correction and exponential mass bias-correction to an assumed $^{146}Nd/^{144}Nd$ ratio of 0.7219. Sample analyses were standard-sample bracketed with runs of Nd standard JNdi-1 analyzed every 2-3 sample analyses. Several analyses of the La Jolla Nd standard averaged 0.511865 ± 6e-6 (2σ), but all analyses were normalized to La Jolla $^{143}Nd/^{144}Nd = 0.511859$. Nd blanks ranged from 26-121 pg.

Hafnium was separated from the matrix left over from Sr, Pb, and Nd separations following a technique modified from (Connelly et al., 2006). First, the remaining sample was loaded on 13 mL AG50-x8 (100-200 mesh) in a mixture of 0.5M HCl/0.15M HF, and

subsequently the HFSE are eluted in 15 mL of 0.5M HCl/0.15M HF. This cut is dried down and redissolved in 3.5M HNO_3/0.06M H_3BO_3. A cleanup procedure using Eichrom DGA resin (normal, 50-100 μm) separates Hf from Ti. The sample was loaded on the column in 3.5M HNO_3 and Ti was washed off in 13.125 mL 3.5M HNO_3, then Hf was eluted in 22 mL 1M HNO_3/0.35M HF. The Hf cut was then dried down and prepared for analysis. Hf blanks ranged from 50-87 pg.

$^{176}Hf/^{177}Hf$ was run with a static analytical program using an internal correction to a $^{179}Hf/^{177}Hf$ ratio of 0.7325. Ratios were drift-corrected by standard-sample bracketing against in-house standard "Alfa Hf" prepared from an Alfa Aesar Hf concentration standard (10000 ppm, lot no. 02-12722F). In addition, Hf standard JMC 475 averaged 0.282160 ±3e-6 (2σ, n=3), after all values were normalized to JMC 475 $^{176}Hf/^{177}Hf$ = 0.282160.

A.4.4. Leaching experiment results and probable contamination of HIMU melts by hydrothermally altered lower oceanic crust

A stepwise leaching experiment performed on replicates of D05-08 and D20-15 provided insight into the influence of secondary mineralization (Supplemental Table S.4.5). The replicate sample fractions were subjected to the final 16 hour leach in a series of four hour-long increments, plus a ~12 hour step to bring the total time spent in leach to ~16 hours, best replicating conditions of the main sample set.. After each step, the leachate fraction was collected in a separate clean beaker, except for the final 12 hour leach step, which was not expected to contain significant amounts of Pb and was discarded. 1 mL fresh ~6N HCl was added to the sample to continue the leach process during each step. After ~16

hours of total leach time, the leach was stopped and the samples were processed for Pb isotopes using the described separation procedures.

The earliest D20-15 leach step yielded a composition most similar to the rock composition. Later leachates bear progressively lighter compositions, suggesting the composition of the secondary phase – probably marine phosphate – exerted a significant control on the Pb composition of the rock itself. The isotopically lighter secondary phases that dissolved in the later steps, however, do not appear to have heavily influenced the Pb signature remaining in the rock.

In contrast, the stepwise D05-08 leaches showed a substantial difference between Pb isotope compositions of the secondary minerals removed by the leach versus the composition of the rock residue. The first leachate step removed the largest Pb fraction, yielding the lowest Pb ratios and subsequent leachates drifted higher, as magmatic Pb comprised an increasingly larger fraction of the leachate signature.

The difference in degree of leaching between a stepwise approach and the single-step approach used for the main sample set becomes obvious with the D05-08 replicate. Our stepwise leaching ultimately removed more Pb than 16 hours of single-step leaching due to the repeated addition of fresh HCl. In this case, the extreme difference in ratio between secondary alteration signatures and primary (presumably magmatic) signature in the rock makes sample replication challenging and the leaching experiment produces a far higher set of Pb ratios than the D05-08 replicates leached using the standard approach. This agrees with similar observations in OIB samples reported by Hanano et al. (2009) and Silva et al. (2009), which were also attributed to incomplete removal of secondary phases by leaching.

The $^{208}Pb/^{204}Pb$ ratio provided in Supplemental Table S.6 is the most extreme thorogenic Pb ratio ever obtained in a terrestrial igneous sample, but probably is not directly representative of plume material. The Th/U initial ratio required to produce the observed $^{208}Pb/^{204}Pb$ vs. $^{206}Pb/^{204}Pb$ is far higher than any Bulk Earth estimates (e.g. Chauvel et al., 1992 and references therein) and many common processes capable of fractionating Th/U (subduction, shallow hydrothermal alteration, and differentiation of various Earth reservoirs) tend to lower the Th/U ratio of a potential source (e.g. Alt, 1995; Bach et al., 2003; Hanyu et al., 2014; Staudigel et al., 1996).

However, a possible explanation for this behavior exists in assimilation of hydrothermally altered gabbros from lower oceanic crust into ascending Rurutu magmas. At higher P-T conditions, hydrothermal alteration systems are thought to deplete Pb from the crust, similar to the depletion found in the shallower parts of a hydrothermal system. Unlike shallower alteration processes, though, hydrothermal alteration processes at depth do not appear to remobilize seawater U into the crust, producing Th/U ratios as high as ~20 (e.g. Hart et al., 1999).

Indeed, measured (unleached) groundmass data suggest melt Th/U was as high as ~8 in some of our samples (compared to Bulk Earth estimated at 4.2-4.3; e.g. Allègre et al., 1986; Liew and Hofmann, 1990). These ratios cannot be produced from post-eruptive alteration of the U-Th-Pb systematics, as addition of secondary phases, such as discussed for the Group 2 rocks, will decrease Th/U. Epidosite is a common secondary rock type produced from the hydrothermal alteration of plagioclase-rich gabbros. Allanite, a Th-rich epidote group mineral, may concentrate in enough quantity in epidosite zones or veins in

these altered, lower crustal gabbros to increase the Th/U signature of the magma generating a given seamount.

This would also explain the larger degree of scatter in $^{208}Pb/^{204}Pb$ vs. $^{206}Pb/^{204}Pb$ of the Rurutu data compared to the data from the net younger Macdonald seamounts. The general Rurutu $^{208}Pb/^{204}Pb$ vs. $^{206}Pb/^{204}Pb$ systematics generally indicate Rurutu Pb is more thorogenic than in the relatively young Mangaia and Tubuai samples that define the HIMU endmember. Most likely, this is probably a function of age. Older (40-60 Ma) seamounts comprising the Tokelau chain (linked to the Macdonald hotspot) also exhibit more thorogenic Pb signatures than expected for HIMU. This probably reflects a similar assimilation of altered, thorium-rich crustal gabbro that is reflected to varying degree by the greater Rurutu hotspot dataset, which is not yet seen in the young Cook-Austral volcanoes because of the slow ingrowth of ^{208}Pb.

A.4.5. Plotting background isotopic data

Isotopic results are plotted with background data sourced from GEOROC and PetDB precompiled datasets for various OIBs, LIPs, and Pacific MORB that represent a range of isotopic compositions and mantle endmembers. The Nd-Hf reference line is from Vervoort and Blichert-Toft (1999). Endmember compositions were sourced from multiple publications. HIMU (Mangaia Suite): Nebel et al. (2013) and Woodhead (1996); EM2 (dredge D115-18 data): Jackson et al. (2007) and Salters et al. (2011); EM1: Eisele et al. (2002); MORB Chauvel and Blichert-Toft (2001); FOZO: Hart et al. (1992) and Hauri and Hart (1994), C: (Hanan et al., 2000; Hanan and Graham, 1996). No $^{176}Hf/^{177}Hf$ estimate exists for FOZO and the composition is not plotted on Hf axes. Background data used in

isotopic plots was sourced from the GEOROC and PetDB online databases, and additional Young Rurutu trend Nd-Hf isotopic was sourced from Salters et al. (2011).

To objectively present background data in isotopic figures instead of arbitrary hand-drawn fields, we used MATLAB to produce two-dimensional kernel density estimates (2D KDE) of each dataset, which are then used to generate the fields. The 2D KDE matrix characterizes the probability density function of a dataset, which we then treat as a three-dimensional density "surface" in order to consider the volume. The volume under the surface, acting as a proxy for confidence level, can be used to generate a contour that represents a 95% confidence level by contouring around the upper 95% of the volume of the KDE matrix. The resulting distribution after filtering leaves KDE matrices for each of the datasets close to a lognormal distribution. Multimodal datasets (from sampling bias or natural behavior) may not exhibit a perfect lognormal fit, but yield a contour level close to that calculated from the actual volume.

Rather than using the more computationally expensive approach of calculating volume under a surface and determining the contour, we instead find that taking the lognormal 2SD of the matrix produces a quantitatively equivalent contour. Calculating the contour level in this manner, while efficient, leaves it vulnerable to skew from zero values in the matrix, which otherwise would not be counted during a true volume calculation. If these zero values are left in the matrix, the resulting incorrect contour level is too low and over-represents the 2D KDE of the dataset. To avoid skewing the contour, any grid values less than <0.0001 are replaced with a "NaN" value (Not a Number), which are not considered in the calculation.

A.4.6. Bend Location

When quantitatively determining a Bend of a hotspot track obscured by volcanism from other sources, the Bend location method must be constructed in such a way as to avoid introducing any age bias that might influence the Bend location. We assume that 1) the Rurutu hotspot did not drift substantially while erupting its Tuvalu phase, and 2) that APM models correctly estimate the hotspot track from ~60 Ma, through the bend, and into the younger track segments. Rurutu plume motion has not been accounted for in this approach, but APM model projections of the Tuvalu volcanoes to their estimated 0 Ma location results in a reasonably tight cluster (see Figure 4.7 in main text), so Assumption 1 is likely valid. Furthermore, Assumption 2 is likely valid, given the WK08 track projection from Arago seamount, the modern location of the Rurutu hotspot, matches reasonably well with the known Rurutu track through Tuvalu, before deviating from the Gilbert segment. In accordance with Assumption 1, we limit input to the Bend locator to age-dated Tuvalu Group 1 seamounts.

To avoid introducing any age biases or other cutoffs that could influence the Bend location estimate, we employ an approach that relies on changes in motion between stage poles to produce local increases in overlap, and therefore density, of Rurutu track projections estimated for each age-dated seamount. While high densities will also occur as a result of a dense cluster of track projections, the highest will occur at stage pole changes capturing the most pronounced changes in APM, such as the Bend.

Using the GMT backtracker function (Wessel et al., 2013), which allows the user to project "tracklines" along a model APM track for any age-dated seamount, we projected the modeled 120-0 Ma Rurutu hotspot track from each age-dated seamount in the Tuvalu

chain, assuming hotspot drift was negligible during the segment of Rurutu activity preserved in Tuvalu. Track projections using age dates for Rurutu-sourced seamounts were determined using the Global Moving Hotspot Reference Frame (GMHRF, referred to herein as "D12"; Doubrovine et al., 2012), WK08 (Wessel and Kroenke, 2008), and DC85 (Duncan and Clague, 1985) APM models, as a series of densely-spaced coordinates defining the modeled tracklines. Once plotted on a map, the projections produce a cluster of projected Bends capable of providing an estimate of the likeliest actual Bend location.

The GMT backtracker function outputs projected tracks as a series of coordinates and age estimates for each seamount. From the location output, we calculate 2D kernel density estimates of all seamount projections calculated via each APM model. The resulting 2D KDE matrices for each model and combinations of models provide the coordinates for the highest density in the matrix, at which we place the Bend for that particular APM model.

A.4.6.1. Error estimates

The Bend location estimate is a simple exercise in finding a density high corresponding to the likeliest location where the Rurutu track bends. The drawback to this approach is that it does not provide an estimate of uncertainty on the location. Instead, we employ a Monte Carlo approach (n=1000) to simulate uncertainties on results for all models (Figure 4.7 in main text). To determine error, all age data are assumed to represent mean seamount ages, which should also correspond with peak seamount volcanic activity. Using a normal distribution random number generator, 1000 simulated age datasets are produced, where each age date is individually, randomly perturbed ± 0-3.5 Myr from its

corresponding actual (mean) age (assuming a total of 7 Ma of volcanic activity, as reported for other seamounts in the Pacific; Konter et al., 2009). Each simulated dataset is then backtracked using the above approach for all three APM models and combinations of models, from which peak densities and their corresponding coordinates (simulated Bend location estimate) are found. The aggregated simulated Bend locations can then be used to determine 95% covariance ellipses for each model and combined model. The results suggest the actual Bend location estimates have maximum uncertainties of ~2-3° latitude and ~1° longitude. Multiple simulations at n=100 and n=1000 produced estimates within error of each other.

Table S.4.1. Major element data, obtained via XRF at Michigan State University.

Sample	Group	SiO_2	TiO_2	Al_2O_3	Fe_2O_3	MnO	MgO	CaO	Na_2O	K_2O	P_2O_5	Sum	LOI
D02-06	1-Niu	45.97	2.54	13.40	10.06	0.14	6.01	15.57	2.46	0.67	0.36	97.18	2.66
D03-24	1-Niu	42.62	3.46	16.53	10.89	0.13	4.37	12.51	2.65	1.62	0.71	95.49	4.29
D04-01D	1-Niu	42.65	3.25	15.69	12.78	0.15	2.13	11.42	3.48	1.73	2.88	96.16	3.63
D05-08	1-Niu	38.79	3.60	15.59	14.84	0.19	5.24	12.35	1.64	1.13	1.77	95.14	4.61
D06-14	1-Niu	43.74	2.34	19.45	12.30	0.25	2.66	10.15	2.83	1.22	1.33	96.27	3.46
D09-14	1-Niu	37.90	3.34	13.55	15.18	0.16	5.40	12.65	1.42	1.56	2.67	93.83	5.97
D10-16	1-Niu	48.16	1.62	15.74	11.83	0.11	5.24	11.49	2.68	0.65	0.93	98.45	1.43
D10-32	1-Niu	42.91	2.69	15.88	13.38	0.16	5.35	12.73	2.08	0.84	0.92	96.94	2.83
D11-06	1-Niu	42.16	2.69	15.74	13.77	0.19	5.18	11.48	2.09	1.47	1.21	95.98	3.76
D13-01	1-Niu	41.85	2.89	17.11	14.04	0.17	4.88	11.30	1.96	0.97	0.79	95.96	3.86
D14-01	1-Niu	44.68	2.28	18.37	11.07	0.15	3.60	12.29	2.35	0.84	0.60	96.23	3.52
D18-11	1-Niu	45.66	1.95	17.04	11.88	0.21	4.49	9.37	4.17	1.93	0.55	97.25	2.50
D23-05	1-Niu	34.05	4.99	13.37	15.67	0.19	3.96	12.18	1.97	1.88	6.03	94.29	5.45
D24-14A	1-Niu	44.27	2.27	14.61	13.17	0.15	7.31	12.50	2.23	0.59	0.50	97.60	2.20
D07-30	1-Sil	45.07	2.99	15.54	11.46	0.11	4.95	12.66	2.44	1.52	1.19	97.93	1.91
D08-27	1-Sil	41.48	3.00	14.81	14.22	0.20	4.43	10.77	2.58	1.68	1.97	95.14	4.62
D15-17	1-Sil	46.49	2.55	16.78	12.43	0.11	4.86	10.39	2.81	1.08	0.52	98.02	1.84
D12-04	2	43.89	2.57	18.30	10.52	0.05	1.40	10.21	3.13	2.13	4.20	96.40	3.39
D19-08	2	49.77	2.97	18.93	10.13	0.09	1.22	6.66	3.92	2.31	1.29	97.29	2.49
D20-15	2	48.87	3.14	17.56	12.57	0.16	1.21	4.82	3.91	3.76	1.12	97.12	2.62
D21-26	3	46.44	1.37	15.67	12.68	0.19	7.63	11.58	3.05	0.54	0.24	99.39	0.47
D26-02	3	46.28	3.67	16.11	13.92	0.19	3.27	8.66	4.17	1.45	1.36	99.08	0.75
D28B-06	3	48.85	2.39	13.86	12.89	0.17	7.64	10.97	2.35	0.38	0.24	99.74	0.14
D33-32	3	42.33	2.18	14.22	13.12	0.11	6.37	12.93	2.78	0.45	2.14	96.63	3.23
D32-02	4	46.64	3.40	13.59	12.34	0.17	5.92	11.01	3.00	1.58	0.53	98.18	1.60
Standards													
RGM-1		73.74	0.27	13.75	1.87	0.04	0.26	0.98	4.39	4.32	0.05	99.67	0.19
RGM-1 GIVEN		73.45	0.27	13.72	1.86	0.036	0.27	1.15	4.07	4.3	0.048	99.17	
BHVO-1		49.36	2.73	13.44	12.35	0.17	7.25	11.44	2.28	0.53	0.28	99.83	0.03
BHVO-1 GIVEN		49.94	2.71	13.8	12.23	0.168	7.23	11.4	2.26	0.52	0.273	100.531	

Table S.4.2. Trace element data, obtained via LA-ICP-MS at Michigan State University.

Sample	Group	Sc	%σ	V	%σ	Cr	%σ	Co	%σ	Ni	%σ	Rb	%σ	Sr	%σ
D02-06	1-Niu	34.15	0.19%	275.1	0.98%	621.3	0.53%	52.94	0.07%	158.55	0.51%	10.17	0.52%	327.7	0.22%
D03-24	1-Niu	18.83	0.35%	259.2	1.48%	7.25	3.35%	31.44	0.42%	34.67	1.14%	37.20	0.21%	885.3	0.31%
D04-01D	1-Niu	18.45	4.70%	282.9	0.60%	81.23	1.05%	35.14	1.48%	54.42	0.71%	36.67	1.09%	747.6	0.79%
D05-08	1-Niu	27.67	0.44%	317.5	0.97%	43.03	0.45%	40.90	0.41%	55.92	0.63%	28.26	1.81%	766.9	0.91%
D06-14	1-Niu	3.35	4.55%	56.9	0.35%	*0.34*	*9.24%*	17.69	0.76%	25.04	2.28%	24.01	0.39%	1118.2	0.54%
D09-14	1-Niu	28.77	1.12%	321.4	0.32%	512.9	0.15%	44.20	0.74%	120.88	0.49%	33.79	1.07%	292.2	0.35%
D10-16	1-Niu	27.23	1.11%	192.6	1.03%	388.1	0.75%	31.25	0.58%	71.76	0.25%	13.96	0.79%	404.6	1.13%
D10-32	1-Niu	34.31	0.63%	277.2	0.35%	531.3	0.59%	46.45	0.22%	94.07	0.91%	18.57	0.57%	682.6	0.84%
D11-06	1-Niu	28.36	0.85%	250.8	0.17%	405.1	0.03%	43.24	1.16%	70.32	1.37%	31.71	1.80%	781.1	0.50%
D13-01	1-Niu	33.48	0.34%	318.2	0.97%	302.5	0.96%	46.05	0.94%	93.95	0.57%	19.25	0.53%	630.9	0.83%
D14-01	1-Niu	30.53	1.17%	268.9	0.34%	87.57	0.81%	37.63	1.24%	59.73	1.02%	14.70	3.64%	581.6	0.59%
D18-11	1-Niu	18.67	0.68%	172.4	1.48%	106.5	0.80%	35.50	1.64%	62.02	1.22%	53.82	0.49%	776.9	0.56%
D23-05	1-Niu	19.20	1.01%	214.8	0.24%	1.56	6.67%	38.22	1.15%	73.71	0.11%	43.77	0.65%	706.7	0.35%
D24-14A	1-Niu	34.98	1.50%	298.1	0.83%	528.5	1.34%	49.35	0.92%	191.54	1.17%	9.99	1.76%	527.5	1.21%
D07-30	1-Sil	32.37	1.32%	316.0	0.69%	39.91	2.61%	40.20	0.26%	64.67	1.22%	35.92	1.58%	516.9	0.82%
D08-27	1-Sil	28.85	1.08%	272.9	0.53%	533.8	0.29%	64.31	0.77%	133.25	0.20%	32.84	1.57%	614.0	0.30%
D15-17	1-Sil	31.39	0.23%	243.7	1.07%	165.0	0.71%	34.57	1.06%	67.08	0.31%	33.10	0.84%	335.4	0.37%
D12-04	2	24.05	1.40%	223.3	1.23%	156.1	1.08%	6.59	1.28%	51.22	0.91%	27.80	2.49%	615.8	1.01%
D19-08	2	26.38	0.70%	137.7	1.29%	169.7	0.75%	17.06	1.07%	45.29	0.72%	32.49	1.22%	638.7	0.70%
D20-15	2	22.73	1.28%	186.0	0.53%	146.5	0.25%	32.78	1.42%	90.68	0.59%	74.69	0.20%	694.3	0.83%
D21-26	3	31.80	2.06%	263.1	1.02%	362.2	0.52%	59.41	1.31%	197.15	0.61%	11.28	2.02%	379.5	1.26%
D26-02	3	17.43	0.98%	221.8	0.20%	4.23	4.58%	28.54	1.34%	24.40	0.84%	23.60	1.28%	649.7	0.87%
D28B-06	3	34.09	1.31%	297.8	1.02%	281.3	0.28%	46.58	0.82%	135.93	0.31%	5.74	4.93%	279.6	1.15%
D33-32	3	27.37	0.72%	273.7	0.64%	413.2	0.46%	43.56	1.37%	133.19	1.23%	13.67	2.06%	342.4	0.87%
D32-02	4	28.19	0.57%	290.5	1.57%	361.4	1.07%	45.72	0.47%	137.86	0.88%	31.30	0.72%	603.3	1.15%
Standards															
Average JB1a		27.769	1.07%	199.759	0.87%	416.667	1.13%	37.911	1.13%	139.941	1.38%	37.833	2.05%	440.729	0.93%
Average BHVO-1		31.387	2.27%	312.609	0.89%	282.055	1.12%	43.609	1.03%	116.799	1.04%	9.288	2.71%	395.011	0.65%

Sample data are the average of three replicate analyses, from which a relative standard deviation (%σ, n=3) is calculated. Italicized values are near detection limits.

Sr/Sr* and Eu/Eu* are calculated after Hart et al. (1999) as Sr/(0.5 Nd + 0.5 Sm) and Eu/(0.5 Sm + 0.5 Tb), respectively.

Table S.4.2. (Continued)

Sample	Y	%σ	Zr	%σ	Nb	%σ	Cs	%σ	Ba	%σ	La	%σ	Ce	%σ
D02-06	24.69	0.98%	140.5	0.87%	23.35	1.04%	0.351	3.99%	78.3	2.06%	15.33	1.22%	34.16	1.24%
D03-24	32.65	0.76%	316.5	0.31%	105.17	0.53%	0.482	2.09%	530.8	1.21%	64.41	0.30%	124.83	0.54%
D04-01D	52.34	0.66%	261.4	0.72%	81.65	1.46%	0.832	0.60%	396.1	0.74%	68.06	1.96%	106.14	2.25%
D05-08	39.79	0.43%	293.1	0.79%	121.99	0.43%	1.010	1.19%	578.0	1.35%	106.89	0.84%	171.40	0.64%
D06-14	43.87	0.75%	458.3	0.85%	156.88	0.40%	0.531	2.19%	601.5	0.81%	110.08	0.75%	201.64	0.47%
D09-14	29.71	0.70%	244.8	0.33%	54.01	0.55%	1.014	1.35%	131.3	0.21%	41.65	0.30%	81.90	0.33%
D10-16	20.45	0.99%	96.1	0.50%	21.38	1.01%	0.741	3.91%	64.3	1.10%	18.13	0.53%	34.97	1.47%
D10-32	31.79	1.02%	247.5	0.93%	69.63	0.44%	0.634	2.33%	370.2	1.39%	52.78	1.23%	97.64	1.26%
D11-06	36.02	0.22%	304.9	0.53%	108.68	0.19%	0.865	2.50%	518.5	0.31%	78.62	0.19%	147.84	0.58%
D13-01	29.62	0.49%	168.5	0.28%	51.15	0.44%	0.698	0.85%	268.9	0.56%	33.75	0.60%	68.07	0.84%
D14-01	26.53	1.69%	150.4	1.81%	58.20	0.77%	0.466	5.39%	953.4	0.62%	36.62	2.03%	68.94	0.72%
D18-11	30.35	1.20%	378.3	1.65%	128.82	0.53%	0.774	0.99%	497.9	0.53%	85.06	0.54%	151.03	0.73%
D23-05	83.55	1.30%	472.3	0.83%	134.99	0.26%	1.314	1.61%	664.6	0.70%	114.20	0.75%	190.18	0.55%
D24-14A	27.65	3.00%	157.0	1.80%	44.69	0.99%	0.461	3.20%	148.8	2.23%	32.39	1.61%	62.18	0.69%
D07-30	28.42	0.64%	220.0	0.96%	55.78	0.65%	1.683	0.79%	218.3	0.86%	39.67	0.51%	79.68	0.57%
D08-27	28.41	0.48%	227.1	0.61%	65.57	0.29%	1.241	0.55%	280.3	0.28%	42.29	1.16%	84.88	0.88%
D15-17	26.22	1.95%	138.1	0.92%	33.95	0.29%	2.658	0.29%	127.7	0.78%	17.63	0.36%	35.35	0.20%
D12-04	101.49	2.68%	340.9	2.90%	72.47	1.33%	0.888	1.96%	289.4	2.10%	95.58	2.75%	93.30	1.97%
D19-08	50.18	0.47%	317.4	0.83%	42.57	0.96%	0.907	1.23%	388.2	0.26%	45.42	0.97%	89.11	0.74%
D20-15	56.58	0.43%	453.8	0.18%	73.93	0.69%	1.341	0.56%	614.1	1.26%	66.83	0.68%	116.64	0.60%
D21-26	22.87	2.11%	86.3	1.09%	20.28	0.97%	0.444	1.51%	171.1	0.58%	18.81	1.22%	36.87	0.87%
D26-02	68.61	0.91%	368.8	0.52%	36.98	1.00%	0.279	3.29%	226.3	1.22%	39.91	0.96%	77.79	0.39%
D28B-06	28.84	1.56%	152.3	2.41%	11.41	0.98%	0.237	4.31%	39.0	0.79%	10.38	0.92%	25.80	0.77%
D33-32	37.95	1.22%	129.4	1.06%	9.82	0.68%	1.393	1.23%	34.2	1.00%	12.86	0.73%	25.29	0.38%
D32-02	29.37	1.05%	258.9	0.39%	44.40	0.93%	0.481	3.98%	365.2	0.49%	38.60	0.45%	79.56	0.61%
Standards														
Average														
JB1a	22.922	1.43%	137.221	0.88%	27.584	0.79%	1.239	1.79%	490.298	1.19%	38.123	0.68%	66.476	1.22%
Average														
BHVO-1	26.432	1.33%	174.262	0.92%	18.224	0.68%	0.099	6.53%	129.444	1.41%	15.787	0.84%	38.179	0.89%

Table S.4.2. (Continued)

Sample	Pr	%σ	Nd	%σ	Sm	%σ	Eu	%σ	Gd	%σ	Tb	%σ	Dy	%σ
D02-06	4.54	1.10%	20.29	0.57%	5.095	0.54%	1.785	0.63%	5.559	0.90%	0.830	1.09%	4.795	1.28%
D03-24	14.51	0.51%	56.38	0.25%	10.508	0.77%	3.210	0.37%	9.284	0.74%	1.188	0.62%	6.772	0.48%
D04-01D	13.037	1.46%	50.43	1.12%	9.468	0.13%	2.941	2.21%	8.779	1.74%	1.216	2.68%	6.973	2.14%
D05-08	19.85	0.26%	72.85	1.10%	12.097	0.87%	3.582	0.86%	10.497	1.04%	1.321	1.44%	7.406	1.92%
D06-14	22.52	0.64%	82.48	0.90%	13.810	1.61%	4.145	0.66%	11.574	0.92%	1.460	0.53%	8.472	1.01%
D09-14	10.09	0.78%	41.95	0.90%	8.659	1.05%	2.813	0.61%	8.202	1.84%	1.070	1.10%	5.863	0.35%
D10-16	4.23	1.36%	17.93	0.89%	4.403	0.70%	1.594	1.44%	4.703	0.96%	0.701	0.31%	3.916	0.26%
D10-32	11.35	0.72%	44.72	1.26%	8.556	0.87%	2.718	0.72%	8.082	1.73%	1.083	0.49%	6.247	1.40%
D11-06	16.51	1.16%	61.34	0.32%	10.543	1.79%	3.219	0.44%	9.266	0.69%	1.222	1.09%	6.972	1.28%
D13-01	8.18	0.41%	33.63	0.85%	6.846	1.79%	2.273	0.37%	6.747	0.66%	0.960	0.77%	5.747	1.44%
D14-01	7.96	0.67%	31.05	1.10%	6.069	2.39%	2.009	1.26%	5.838	0.92%	0.830	1.29%	4.823	2.01%
D18-11	15.89	0.57%	55.99	0.50%	9.045	1.39%	2.736	0.35%	7.699	0.63%	1.022	1.48%	5.902	1.96%
D23-05	23.25	0.63%	91.73	0.23%	16.543	0.92%	4.928	1.31%	15.060	1.20%	1.827	1.28%	10.830	0.75%
D24-14A	7.45	1.23%	29.97	0.80%	6.268	2.34%	2.053	0.54%	6.279	3.29%	0.887	1.44%	5.075	1.01%
D07-30	9.80	0.80%	40.23	1.56%	8.225	1.09%	2.588	0.52%	7.708	1.64%	1.036	1.95%	5.848	0.90%
D08-27	10.11	0.71%	41.07	0.30%	8.285	2.21%	2.604	0.80%	7.745	0.94%	1.021	1.10%	5.678	0.88%
D15-17	4.53	0.79%	19.75	0.64%	4.846	0.88%	1.707	1.52%	5.417	0.71%	0.817	1.40%	4.853	1.26%
D12-04	14.14	2.78%	56.90	2.26%	10.581	2.46%	3.337	1.35%	12.309	3.21%	1.591	3.09%	10.492	3.14%
D19-08	12.08	0.89%	53.31	0.50%	11.898	2.20%	3.839	0.58%	12.509	0.69%	1.675	0.75%	10.187	0.61%
D20-15	14.95	0.59%	61.76	0.56%	13.104	1.27%	3.890	0.84%	13.417	0.76%	1.749	1.08%	10.448	0.24%
D21-26	4.43	0.77%	18.08	1.63%	3.995	1.00%	1.382	0.81%	4.221	1.72%	0.672	0.77%	4.079	1.50%
D26-02	11.71	0.34%	54.15	0.36%	13.268	0.82%	4.281	0.99%	14.325	0.81%	1.913	1.09%	11.621	0.81%
D28B-06	3.81	1.74%	18.54	1.15%	5.282	1.13%	1.830	1.46%	6.108	2.07%	0.915	0.99%	5.462	2.40%
D33-32	3.71	1.35%	18.38	0.47%	5.106	2.53%	1.812	0.79%	6.204	0.66%	0.914	1.72%	5.486	0.64%
D32-02	9.93	0.19%	40.85	0.69%	8.564	0.87%	2.692	0.74%	8.167	0.93%	1.071	1.64%	5.975	0.44%
Standards														
Average JB1a	7.053	1.40%	26.409	0.80%	5.134	1.92%	1.492	1.46%	4.751	1.59%	0.707	1.25%	4.062	1.40%
Average BHVO-1	5.373	1.91%	25.039	1.36%	6.230	1.73%	2.085	1.41%	6.464	1.44%	0.923	1.47%	5.292	1.23%

Table S.4.2. (Continued)

Sample	Ho	%σ	Er	%σ	Tm	%σ	Yb	%σ	Lu	%σ	Hf	%σ	Ta	%σ	Pb	%σ
D02-06	0.901	0.70%	2.336	0.64%	0.322	0.36%	1.943	0.78%	0.268	2.05%	3.567	0.95%	1.577	0.91%	1.094	0.52%
D03-24	1.200	0.45%	3.225	1.12%	0.436	1.33%	2.722	0.37%	0.377	1.82%	6.897	0.43%	6.569	0.52%	4.222	0.34%
D04-01D	1.407	2.17%	3.824	2.18%	0.509	3.12%	3.063	1.69%	0.485	4.13%	6.025	1.04%	5.505	1.40%	3.024	3.76%
D05-08	1.337	0.75%	3.586	0.57%	0.482	0.76%	3.001	1.53%	0.434	0.70%	6.812	0.83%	7.688	0.40%	4.876	2.56%
D06-14	1.523	0.91%	4.230	0.87%	0.574	1.54%	3.650	1.03%	0.505	1.53%	8.716	1.73%	9.839	0.47%	6.918	1.07%
D09-14	1.017	0.68%	2.558	1.44%	0.329	1.04%	1.915	0.27%	0.266	1.43%	5.490	1.19%	3.389	0.39%	2.350	1.45%
D10-16	0.746	1.23%	1.866	0.84%	0.258	0.75%	1.497	0.44%	0.215	1.47%	2.440	1.66%	1.217	0.60%	1.461	0.87%
D10-32	1.143	1.05%	3.108	1.17%	0.421	0.91%	2.618	2.29%	0.362	1.94%	5.522	2.31%	4.414	1.05%	2.895	1.36%
D11-06	1.286	0.85%	3.507	1.27%	0.477	0.64%	3.025	1.38%	0.436	0.77%	6.324	1.00%	6.672	0.12%	4.322	2.00%
D13-01	1.094	0.80%	3.051	0.26%	0.419	1.45%	2.658	1.12%	0.376	0.93%	4.003	0.74%	3.265	0.21%	2.535	0.54%
D14-01	0.920	1.04%	2.501	1.78%	0.351	2.31%	2.210	1.42%	0.320	1.92%	3.456	1.96%	3.524	0.61%	2.300	1.98%
D18-11	1.079	1.39%	3.010	1.13%	0.428	1.65%	2.733	2.33%	0.392	1.22%	7.462	1.08%	8.330	0.14%	5.805	1.29%
D23-05	2.030	0.52%	6.099	1.67%	0.829	0.74%	5.419	0.40%	0.830	0.87%	10.549	0.59%	8.540	0.76%	4.743	0.48%
D24-14A	0.963	0.99%	2.552	2.01%	0.352	1.79%	2.157	2.55%	0.305	0.31%	3.846	2.51%	2.791	2.16%	2.593	2.70%
D07-30	1.045	0.54%	2.719	2.23%	0.356	1.13%	2.167	0.47%	0.304	3.03%	5.322	0.57%	3.665	0.98%	2.262	0.65%
D08-27	1.010	0.61%	2.621	0.96%	0.350	1.54%	2.111	0.90%	0.292	2.74%	5.208	0.41%	4.144	0.81%	2.082	1.51%
D15-17	0.942	0.30%	2.548	0.40%	0.347	1.41%	2.178	0.73%	0.306	1.02%	3.495	0.72%	2.327	1.20%	0.958	1.15%
D12-04	2.211	3.47%	6.978	3.69%	0.969	2.45%	6.374	2.73%	0.951	2.50%	7.182	2.32%	4.824	2.51%	2.732	1.38%
D19-08	1.823	0.67%	5.109	1.08%	0.677	0.85%	4.189	0.52%	0.564	0.53%	7.361	0.34%	2.559	0.91%	1.915	0.96%
D20-15	1.892	0.27%	5.419	0.30%	0.721	0.92%	4.582	0.91%	0.629	1.05%	10.275	0.98%	4.639	0.81%	3.129	2.10%
D21-26	0.828	0.60%	2.282	1.28%	0.328	0.79%	2.078	1.29%	0.299	0.93%	2.185	0.80%	1.257	0.19%	1.342	1.71%
D26-02	2.085	0.45%	6.011	0.53%	0.796	2.05%	4.956	1.24%	0.704	0.86%	8.846	1.48%	2.506	0.91%	3.048	0.49%
D28B-06	1.040	1.20%	2.806	2.94%	0.388	2.11%	2.392	1.66%	0.336	2.44%	3.851	2.38%	0.790	1.61%	1.098	3.01%
D33-32	1.067	1.59%	2.896	1.57%	0.395	2.01%	2.408	1.65%	0.356	1.99%	3.273	0.86%	0.633	0.45%	2.821	2.38%
D32-02	1.058	0.40%	2.694	0.32%	0.359	0.88%	2.100	0.14%	0.291	1.99%	6.131	0.70%	2.837	0.34%	3.657	1.04%
Standards																
Average JB1a	0.808	1.50%	2.196	1.51%	0.323	1.06%	2.091	1.98%	0.304	1.31%	3.466	0.83%	1.748	1.82%	6.443	2.39%
Average BHVO-1	0.977	1.31%	2.520	1.19%	0.337	1.69%	2.031	1.44%	0.279	2.63%	4.398	1.39%	1.202	1.86%	2.224	1.97%

Table S.4.2. (Continued)

Sample	Th	%σ	U	%σ	Sr/Sr*	Th/U	Eu/Eu*
D02-06	1.476	0.31%	0.590	1.41%	25.82	2.50	0.6025
D03-24	7.608	0.33%	1.734	0.33%	26.47	4.39	0.5490
D04-01D	6.559	0.38%	1.555	0.91%	24.96	4.22	0.5504
D05-08	13.327	0.25%	2.732	1.12%	18.06	4.88	0.5339
D06-14	14.386	1.17%	1.712	0.66%	23.23	8.40	0.5429
D09-14	4.364	0.62%	1.844	1.03%	11.55	2.37	0.5782
D10-16	2.494	0.64%	0.637	1.90%	36.23	3.91	0.6244
D10-32	6.093	0.86%	1.330	0.23%	25.62	4.58	0.5641
D11-06	8.974	0.38%	2.119	0.54%	21.73	4.23	0.5472
D13-01	3.376	0.37%	1.241	0.29%	31.17	2.72	0.5825
D14-01	4.380	1.33%	0.909	2.10%	31.34	4.82	0.5824
D18-11	12.485	1.05%	2.950	1.12%	23.89	4.23	0.5435
D23-05	11.977	0.97%	4.318	0.48%	13.05	2.77	0.5365
D24-14A	3.755	1.93%	1.051	1.39%	29.11	3.57	0.5739
D07-30	4.367	1.11%	2.293	1.03%	21.34	1.90	0.5589
D08-27	4.750	0.59%	1.791	1.10%	24.88	2.65	0.5597
D15-17	1.928	0.99%	0.679	0.80%	27.27	2.84	0.6028
D12-04	5.989	2.82%	1.889	1.67%	18.25	3.17	0.5482
D19-08	2.877	0.91%	0.876	1.04%	19.59	3.28	0.5657
D20-15	6.430	0.71%	1.780	0.75%	18.55	3.61	0.5238
D21-26	1.840	1.83%	0.448	1.75%	34.38	4.11	0.5922
D26-02	3.053	0.48%	1.446	1.04%	19.27	2.11	0.5639
D28B-06	0.943	0.92%	0.205	2.35%	23.48	4.59	0.5907
D33-32	0.787	1.51%	1.281	0.64%	29.15	0.61	0.6019
D32-02	4.263	0.12%	1.111	0.45%	24.42	3.84	0.5588
Standards							
Average JB1a	9.103	1.46%	1.603	2.63%			
Average BHVO-1	1.233	1.64%	0.408	4.57%			

Table S.4.3. Sample and standard isotopic data.

Sample	Group	$^{208}Pb/^{204}Pb$	2SE	$^{207}Pb/^{204}Pb$	2SE	$^{206}Pb/^{204}Pb$	2SE	$^{208}Pb^*/^{206}Pb^*$	$^{87}Sr/^{86}Sr$	2SE	$^{143}Nd/^{144}Nd$	2SE	εNd	$^{176}Hf/^{177}Hf$	2SE
D02-06	1-Niu	39.4093	7.00E-04	15.6198	3.00E-04	19.7808	3.00E-04	0.94849	0.703658	5.00E-06	0.512846	1.20E-05	4.1	0.282888	6.00E-06
D03-24	1-Niu	40.1725	6.00E-04	15.7016	2.00E-04	20.6274	3.00E-04	0.94497	0.702994	6.00E-06	0.512898	8.00E-06	5.1	0.282964	5.00E-06
D04-01D	1-Niu	40.2963	1.20E-03	15.6817	7.00E-04	20.3989	5.00E-04	0.97561	0.703448	6.00E-06	0.512841	1.10E-05	4	0.282932	3.00E-06
(TIMS replicate)		--	--	--	--	--	--	--	0.703465	1.30E-05	--	--	--	--	--
D05-08	1-Niu	42.0587	1.20E-03	15.7962	3.00E-04	21.4171	3.00E-04	1.03911	0.702978	6.00E-06	0.512794	5.00E-06	3	--	--
(rerun)		--	--	--	--	--	--	--	0.70298	1.60E-05	--	--	--	--	--
D05-08dup	1-Niu	42.0239	8.00E-04	15.7914	3.00E-04	21.3711	4.00E-04	1.04018	--	--	--	--	--	0.282877	5.00E-06
D06-14	1-Niu	40.7754	7.00E-04	15.7728	4.00E-04	21.0077	4.00E-04	0.96579	0.702986	6.00E-06	0.512823	5.00E-06	3.6	0.282898	4.00E-06
D09-14	1-Niu	40.3858	9.00E-04	15.6771	4.00E-04	20.2418	4.00E-04	0.99781	0.703331	7.00E-06	0.512876	4.00E-06	4.6	0.282956	4.00E-06
D10-16	1-Niu	39.6928	1.10E-03	15.6715	4.00E-04	20.0565	4.00E-04	0.95053	0.703119	6.00E-06	0.512851	7.00E-06	4.1	0.282941	5.00E-06
D10-32	1-Niu	40.8197	8.00E-04	15.7664	3.00E-04	21.0968	4.00E-04	0.96224	0.702963	7.00E-06	0.512856	5.00E-06	4.3	0.282946	5.00E-06
D10-32dup	1-Niu	40.7693	7.00E-04	15.7688	3.00E-04	21.0737	3.00E-04	0.95985	0.702944	5.00E-06	0.512855	5.00E-06	4.2	--	--
(rerun)		40.7423	1.00E-03	15.7658	3.00E-04	21.0691	4.00E-04	0.95793	--	--	--	--	--	--	--
D11-06	1-Niu	40.9641	1.00E-03	15.7405	5.00E-04	21.0713	4.00E-04	0.97661	0.702944	4.00E-06	0.512852	5.00E-06	4.2	0.282982	6.00E-06
D13-01	1-Niu	40.6004	1.00E-03	15.7664	3.00E-04	21.0621	3.00E-04	0.94644	0.703016	5.00E-06	0.512871	4.00E-06	4.5	0.283014	5.00E-06
(rerun)		--	--	--	--	--	--	--	0.703006	1.30E-05	--	--	--	--	--
D14-01	1-Niu	40.6768	1.10E-03	15.7202	4.00E-04	20.8045	4.00E-04	0.97428	0.703082	6.00E-06	0.512878	6.00E-06	4.7	0.282979	4.00E-06
D18-07	1-Niu	40.6248	7.00E-04	15.7217	5.00E-04	21.0122	4.00E-04	0.95255	0.702951	6.00E-06	0.512877	3.00E-06	4.7	0.28297	5.00E-06
D18-11	1-Niu	40.4366	8.00E-04	15.7186	3.00E-04	20.9178	3.00E-04	0.94409	0.703004	6.00E-06	0.51287	5.00E-06	4.5	0.282974	4.00E-06
D23-05	1-Niu	39.7766	5.00E-04	15.6804	2.00E-04	20.2018	3.00E-04	0.94555	0.703557	6.00E-06	0.512831	1.10E-05	3.8	0.282843	5.00E-06
D24-04	1-Niu	40.3419	8.00E-04	15.7501	3.00E-04	21.0868	4.00E-04	0.9225	0.703056	5.00E-06	0.512867	4.00E-06	4.5	0.282961	6.00E-06
D24-14A	1-Niu	40.7392	6.00E-04	15.7787	2.00E-04	21.2754	3.00E-04	0.94117	0.703165	6.00E-06	0.512844	4.00E-06	4	0.282947	7.00E-06
(rerun)		--	--	--	--	--	--	--	0.703147	9.00E-06	--	--	--	--	--
D27-35	1-Niu	40.8038	6.00E-04	15.8003	2.00E-04	21.6541	3.00E-04	0.91753	0.703207	7.00E-06	0.512839	3.20E-05	3.9	0.282921	6.00E-06
D27-57	1-Niu	40.5866	6.00E-04	15.786	2.00E-04	21.29	3.00E-04	0.92729	0.703336	6.00E-06	0.512837	4.00E-06	3.9	0.282902	1.00E-05
TUV-1	1-Niu	40.422	2.30E-03	15.754	7.00E-04	20.936	9.00E-04	0.94134	0.703069	4.00E-06	0.512858	4.00E-06	4.3	--	--
D22-23	1-Sil	39.0137	6.00E-04	15.6097	3.00E-04	19.3006	3.00E-04	0.95449	0.702777	6.00E-06	0.512949	7.00E-06	6.1	0.283012	5.00E-06
D07-30	1-Sil	40.1986	7.00E-04	15.6772	6.00E-04	20.897	4.00E-04	0.92524	0.702868	8.00E-06	0.51293	6.00E-06	5.7	0.282991	6.00E-06
D08-27	1-Sil	39.8599	6.00E-04	15.6193	3.00E-04	20.2878	3.00E-04	0.94573	0.702818	6.00E-06	0.512966	5.00E-06	6.4	0.283063	1.30E-05
(TIMS replicate)		--	--	--	--	--	--	--	0.702818	1.30E-05	--	--	--	--	--
D15-02	1-Sil	39.7581	8.00E-04	15.598	3.00E-04	20.2049	4.00E-04	0.94359	0.702691	7.00E-06	0.513021	4.00E-06	7.5	0.283098	5.00E-06
D15-17	1-Sil	39.6321	1.00E-03	15.587	3.00E-04	20.0949	3.00E-04	0.94153	0.702691	5.00E-06	0.513021	5.00E-06	7.5	0.283099	5.00E-06
(TIMS replicate)		--	--	--	--	--	--	--	0.702689	1.30E-05	--	--	--	--	--
D16-38cpx	1-Sil	39.8502	3.00E-03	15.6208	1.10E-03	20.2516	1.00E-03	0.94798	0.702706	1.00E-05	0.513021	5.00E-06	7.5	--	--
TUV-2	1-Sil	40.634	4.80E-03	15.596	1.80E-03	20.454	2.00E-03	1.00107	0.702795	3.00E-06	0.512952	4.00E-06	6.1	--	--
TUV-4	1-Sil	*38.84*	*2.13E-02*	*15.42*	*8.40E-03*	*19.26*	*1.04E-02*	0.9413	*0.702749*	*4.00E-06*	0.513004	1.00E-05	7.1	--	--

Table S.4.3. (Continued)

Sample	Group	$^{208}Pb/^{204}Pb$	2SE	$^{207}Pb/^{204}Pb$	2SE	$^{206}Pb/^{204}Pb$	2SE	$^{208}Pb^*/^{206}Pb^*$	$^{87}Sr/^{86}Sr$	2SE	$^{143}Nd/^{144}Nd$	2SE	εNd	$^{176}Hf/^{177}Hf$	2SE
TUV-5	1-Sil	39.564	1.20E-03	15.593	4.00E-04	20.126	6.00E-04	0.93254	0.70285	4.00E-06	0.513038	9.00E-06	7.8	--	--
D12-01	2	39.2965	7.00E-04	15.6445	4.00E-04	20.1363	4.00E-04	0.90694	0.702844	7.00E-06	0.513132	1.30E-05	9.6	0.283032	4.00E-06
D12-04	2	38.9807	1.20E-03	15.626	4.00E-04	19.7607	4.00E-04	0.90931	0.702777	9.00E-06	0.513055	1.40E-05	8.1	0.283022	4.00E-06
(rerun)		--	--	--	--	--	--	--	--	--	--	--	--	0.283023	4.00E-06
D19-03	2	38.9826	7.00E-04	15.6909	3.00E-04	20.5661	4.00E-04	0.84443	0.703047	6.00E-06	0.513218	1.60E-05	11.3	0.282896	5.00E-06
D19-08	2	38.8339	8.00E-04	15.6691	3.00E-04	20.0438	3.00E-04	0.87166	0.703024	5.00E-06	0.513029	1.50E-05	7.6	0.282887	3.00E-06
(TIMS replicate)		--	--	--	--	--	--	--	0.703029	1.10E-05	--	--	--	--	--
D20-15	2	39.1484	1.10E-03	15.7023	4.00E-04	20.5319	4.00E-04	0.86178	0.703178	8.00E-06	0.512939	1.50E-05	5.9	0.282875	3.00E-06
TUV-3	2	38.054	8.80E-03	15.541	4.00E-03	20.603	5.00E-03	0.75945	0.704775	3.00E-06	*0.5131*	*3.00E-04*	9.1	--	--
D21-19	3	38.4651	1.60E-03	15.5297	8.00E-04	18.7003	9.00E-04	0.95708	0.703546	6.00E-06	0.512974	3.00E-06	6.5	0.283137	7.00E-06
D21-26	3	38.7315	1.70E-03	15.5622	5.00E-04	19.0325	6.00E-04	0.95178	0.70369	5.00E-06	0.512932	8.00E-06	5.7	0.283105	7.00E-06
D26-02	3	38.4534	9.00E-04	15.5424	3.00E-04	18.711	3.00E-04	0.95474	0.704171	6.00E-06	0.512965	6.00E-06	6.4	0.283082	3.00E-06
D27-31	3	38.5771	5.00E-04	15.5448	2.00E-04	18.7676	2.00E-04	0.96211	0.703825	6.00E-06	0.513009	5.00E-06	7.2	0.283079	4.00E-05
D28B-06	3	38.394	8.00E-04	15.5212	3.00E-04	18.6141	2.00E-04	0.95831	0.704137	7.00E-06	0.512959	1.00E-05	6.3	0.283073	5.00E-06
(TIMS replicate)		--	--	--	--	--	--	--	0.704122	1.40E-05	--	--	--	--	--
D33-32	3	38.4409	9.00E-04	15.5125	3.00E-04	18.7813	4.00E-04	0.94634	0.703605	6.00E-06	0.512978	7.00E-06	6.6	0.283094	4.00E-06
D32-02	4	39.2571	1.60E-03	15.6307	5.00E-04	19.0508	5.00E-04	1.00393	0.705108	5.00E-06	0.512662	6.00E-06	0.5	0.282879	4.00E-06
Standards															
BCR-2		38.7426	8.00E-04	15.6237	3.00E-04	18.7601	3.00E-04	--	--	--	--	--	--	--	--
(rerun)		38.7205	6.00E-04	15.6168	3.00E-04	18.7547	3.00E-04	--	--	--	--	--	--	--	--
BCR-2 duplicate1		38.7397	7.00E-04	15.6238	3.00E-04	18.761	3.00E-04	--	0.705	6.00E-06	0.512629	4.00E-06	--	0.28287	4.00E-06
(rerun)		38.7262	2.00E-03	15.6208	6.00E-04	18.7629	5.00E-04	--	0.705009	6.00E-06	0.512635	4.00E-06	--	0.282871	4.00E-06
(rerun)		38.7164	7.00E-04	15.6124	3.00E-04	18.7596	3.00E-04	--	0.705013	8.00E-06	--	--	--	--	--
(rerun)		38.7089	7.00E-04	15.6158	3.00E-04	18.7572	3.00E-04	--	0.705025	1.20E-05	--	--	--	--	--
(rerun)		--	--	--	--	--	--	--	0.705013	5.00E-06	--	--	--	--	--
(rerun)		--	--	--	--	--	--	--	0.705008	5.00E-06	--	--	--	--	--
(rerun)		--	--	--	--	--	--	--	0.705016	6.00E-06	--	--	--	--	--
BCR-2 duplicate2		--	--	--	--	--	--	--	--	--	0.512626	1.20E-05	--	0.282863	3.00E-06
Average BCR-2 (2σ)		**38.7257**	**2.65E-02**	**15.6189**	**9.30E-03**	**18.7593**	**5.80E-03**	--	**0.705012**	**1.50E-05**	**0.51263**	**9.00E-06**	--	**0.282868**	**9.00E-06**
La Jolla Nd		--	--	--	--	--	--	--	--	--	0.511861	7.00E-06	--	--	--
(rerun)		--	--	--	--	--	--	--	--	--	0.511855	3.00E-06	--	--	--
(rerun)		--	--	--	--	--	--	--	--	--	0.511861	6.00E-06	--	--	--
Average La Jolla (2σ)		--	--	--	--	--	--	--	--	--	**0.511859**	**6.00E-06**	--	**--**	**--**
BHVO-1		38.3463	7.00E-04	15.5671	3.00E-04	18.7064	3.00E-04	--	--	--	--	--	--	--	--
BHVO-1 duplicate		38.3589	6.00E-04	15.5711	3.00E-04	18.7095	3.00E-04	--	0.70346	6.00E-06	0.512983	4.00E-06	--	--	--
Average BHVO-1 (2σ)		**38.3526**	**1.78E-02**	**15.5691**	**5.70E-03**	**18.7079**	**4.50E-03**	--	**--**	**--**	**--**	**--**	--	**--**	**--**

Table S.4.3. (Continued)

Sample	Group	$^{208}Pb/^{204}Pb$	2SE	$^{207}Pb/^{204}Pb$	2SE	$^{206}Pb/^{204}Pb$	2SE	$^{208}Pb^*/^{206}Pb^*$	$^{87}Sr/^{86}Sr$	2SE	$^{143}Nd/^{144}Nd$	2SE	εNd	$^{176}Hf/^{177}Hf$	2SE
BIR-1		38.4747	6.00E-04	15.6517	3.00E-04	18.8452	3.00E-04	--	0.703102	5.00E-06	0.513096	8.00E-06	--	0.283114	2.00E-05
(TIMS replicate)		--	--	--	--	--	--	--	0.703102	1.40E-05	--	--	--	--	--
BIR-1 duplicate		38.4729	1.00E-03	15.6506	4.00E-04	18.8451	4.00E-04	--	--	--	--	--	--	--	--
(rerun)		38.4732	8.00E-04	15.6517	3.00E-04	18.8469	3.00E-04	--	--	--	--	--	--	--	--
Average BIR-1 (2σ)		**38.4736**	**1.90E-03**	**15.6513**	**1.20E-03**	**18.8457**	**2.10E-03**	--	**0.703102**	**4.00E-07**	**--**	**--**	--	**--**	**--**
JMC475		--	--	--	--	--	--	--	--	--	--	--	--	0.282159	5.00E-06
(rerun)		--	--	--	--	--	--	--	--	--	--	--	--	0.282162	5.00E-06
(rerun)		--	--	--	--	--	--	--	--	--	--	--	--	0.282159	4.00E-06
Average JMC475 (2σ)		**--**	**--**	**--**	**--**	**--**	**--**	--	**--**	**--**	**--**	**--**	--	**0.28216**	**3.00E-06**

All sample data, unless noted otherwise, were obtained via Nu Plasma HR MC-ICP-MS. Samples in italic had a low yield and consequently produced a lower-precision ratio during analysis. Several sample and standard $^{87}Sr/^{86}Sr$ were replicated via Sector TIMS, marked "*TIMS replicate*". Some sample solutions (*"rerun"*) were reanalyzed to confirm consistent instrumental operating conditions. Uncertainties for single analyses are given as 2*standard error (2SE), and averages of multiple standard analyses are given as 2*standard deviations (2σ).

Table S.4.4. Age corrected (initial) isotopic ratios and forward-modeled isotopic data for a subset of samples.

Sample	Group	Age (Ma)	Error (2σ)	Phase/sample dated	$^{238}U/^{204}Pb$	$^{235}U/^{204}Pb$	$^{232}Th/^{204}Pb$	$^{87}Rb/^{86}Sr$	$^{147}Sm/^{144}Nd$	$^{176}Lu/^{177}Hf$
D02-06	1-Niu	74.57	0.28†	gm/D02-04	38.275	0.278	96.418	0.09	0.16	0.010
D03-24	1-Niu	61.57	0.50†	gm/D03-23	29.131	0.211	128.722	0.12	0.12	0.008
D04-01D	1-Niu	63.66	0.34†	plag/D04-01D	36.468	0.265	154.895	0.14	0.12	0.011
D11-06	1-Niu	52.89	0.25	hbl avg/D11-10 (n=2)	34.770	0.252	148.290	0.11	0.11	0.010
D13-01	1-Niu	50.52	0.20†	plag/D13-01	34.723	0.252	95.140	0.09	0.13	0.013
D14-01	1-Niu	49.82	0.18†	plag/D14-08	28.040	0.203	136.038	0.07	0.12	0.013
D18-07*	1-Niu	48.88	0.12†	hbl/D18-07	*33.131*	*0.240*	*131.908*	*0.20*	*0.10*	*0.007*
D18-11	1-Niu	48.91	0.07	hbl avg/D18-07,D18-23 (n=2)	36.037	0.262	153.632	0.20	0.10	0.007
D24-04*	1-Niu	47.37	0.11†	gm/D24-04	*33.131*	*0.240*	*131.908*	*0.05*	*0.13*	*0.011*
D24-14A	1-Niu	47.77	1.12	gm/D24-04.D24-11 (n=2)	28.751	0.209	103.454	0.05	0.13	0.011
D27-35*	1-Niu	42.24	0.82†	hbl/D27-35	*33.131*	*0.240*	*131.908*	*0.11*	0.12	0.011
D07-30	1-Sil	52.70	4.95	cpx, plag, gm avg/D07-09,D07-22b (n=5)	71.866	0.522	137.892	0.20	0.13	0.008
D15-02*	1-Sil	49.03	0.19†	gm/D15-02	*61.059*	*0.443*	*140.800*	*0.28*	*0.15*	*0.012*
D15-17	1-Sil	49.31	0.78	gm avg/D15-02,D15-12 (n=2)	50.251	0.365	143.708	0.28	0.15	0.012
D12-01*	2	91.46	0.22†	gm/D12-01	*40.598*	*0.295*	*136.893*	*0.13*	*0.12*	*0.018*
D12-04	2	89.46	0.41†	gm/D12-04	49.020	0.356	156.583	0.13	0.12	0.018
D19-03*	2	92.03	1.15†	plag/D19-03	*40.598*	*0.295*	*136.893*	*0.14*	*0.14*	*0.011*
D19-08	2	93.01	2.77	plag/D19-03,D19-12 (n=2)	32.449	0.235	107.317	0.14	0.14	0.011
D20-15	2	95.00	0.19†	plag/D20-15	40.326	0.293	146.779	0.30	0.13	0.009
D21-26	3	9.29	1.96	gm/D21-03,D21-19 (n=3)	23.670	0.172	97.935	0.08	*0.14*	0.019
D26-02‡	3	14.00	2.86	gm avg(tf)/D26-01,D26-03 (n=2)	33.644	0.244	71.560	0.10	0.15	0.011
D28B-06	3	13.31	1.18	gm, plag/D28B-01,D28B-04,D28B-05	13.270	0.096	61.322	0.06	*0.18*	0.012
D21-19*	3	9.29	1.96	gm/D21-03,D21-19 (n=3)	*23.528*	*0.171*	*76.939*	*0.08*	*0.14*	*0.019*
D27-31*	3	14.76	0.12†	plag/D27-31	*23.528*	*0.171*	*76.939*	*0.08*	*0.16*	*0.014*
D32-02	4	11.10	0.23	plag, gm/D32-01,D32-04 (n=2)	21.542	0.156	83.257	0.15	0.13	0.007
D33-32	4	12.24	0.13	plag/D33-05	39.823	0.289	24.645	0.11	0.17	0.015
The following do not have an age date, so assumed ages are assigned. Shifting ages ±15 Ma produces ratios within analytical error except for Pb.										
D05-08	1-Niu	55			39.727	0.288	195.230	0.10	0.10	0.009
D05-08dup	1-Niu	55			39.727	0.288	195.230	0.10	0.10	0.009
D06-14	1e	55			17.548	0.127	148.536	0.06	0.11	0.008
D08-27	1-Sil	55			60.997	0.443	162.983	0.15	0.13	0.008
D09-14	1-Niu	50			55.648	0.404	132.644	0.33	0.13	0.007
D10-16	1-Niu	50			30.936	0.224	121.963	0.10	0.15	0.012
D10-32	1-Niu	50			32.571	0.236	150.339	0.08	0.12	0.009
D23-05	1-Niu	45			64.567	0.469	180.385	0.17	0.11	0.011

- Initial isotopic ratios for a subset of samples were calculated using parent/daughter ratios from the sample data. For the full isotopic dataset, see Table 2. The initial ratios were then forward-modeled using fixed parent-daughter ratios from Nebel et al. (2013), except for $^{87}Rb/^{86}Sr$ (Sun and McDonough, 1989) and approximate ages (50 Ma for Group 1, 90 Ma for Group 2, 15 Ma for Groups 3 and 4). To find modeled $^{232}Th/^{204}Pb$ and $^{235}U/^{204}Pb$, ^{232}Th abundances were assumed using age-corrected MORB Th/U (Sun and McDonough, 1989) and age-corrected $^{238}U/^{235}U$, and assuming μ = 28.6. The ratios used include: μ =28.6, $^{87}Rb/^{86}Sr$ = 0.851, $^{147}Sm/^{144}Nd$ = 0.22, $^{176}Lu/^{177}Hf$ = 0.031. Parent/daughter ratios for $^{207}Pb/^{204}Pb$, and $^{208}Pb/^{204}Pb$ were derived from the modeled μ value and assuming a MORB Th/U ratio (Sun and McDonough, 1989). Using Nd and Hf parent/daughter ratios calculated from Sun and McDonough (1989) MORB abundances produced forward-modeled ratios identical within error of the Nebel et al. (2013) ratios. The low μ of the MORB estimate does not reproduce any Pb isotopic results. Decay constants used are 238U=1.55125e-10 yr^-1, 235U=9.8571e-10yr^-1, 232Th=4.948e-11 yr^-1, 87Rb=1.42e-11 yr^-1, 147Sm=6.54e-12 yr^-1, 176Lu=1.867e-11 yr^-1 (White 2014; Mattinson 2010).

- Samples marked with a (*) do not have trace element data available. Instead, parent-daughter ratio estimates (italicized) are determined from a sample from the same dredge, or an average of compositional data from the sample group/subgroup were used.

†Errors reported are standard deviation (σ) for a single analysis. All other errors are standard deviation of two or more seamount ages (see Supplemental Ages, Konrad et al., submitted).

‡Age determinations for D26 samples did not form a consistent plateau, but yielded ages in good agreement with age of Samoan activity in adjacent volcanoes (~12-15 Ma). Details are provided in Supplemental Ages.

- Forward-modeled $^{176}/^{177}Hf$ and $^{143}Nd/^{144}Nd$ ratios (using modeled ratios from Sun and McDonough, 1989) are not displayed in the Supplemental Figures. Instead, these are used to confirm that they reproduce the modeled data using the ratios published by Nebel et al. (2013).

- Age data are $^{40}Ar/^{39}Ar$ plateau ages from Konrad et al. (submitted). Where possible, ages from the same sample and/or mineral phase ages are favored over sample-dredge ages and/or groundmass ages. Where noted as "avg" in the phase/sample information column, ages shown are seamount averages and error represents 2σ of the average. Correspondingly, errors are given as 2σ. Single age 2σ errors (†) are from Konrad et al. (submitted). A (tf) indicates where a total fusion age was used; no plateau age vailable. Individual sample ages for Rurutu Group 1 (also used in the Bend locator model) are found in Figure 6. Individual ages for seamounts in the other groups may be found in Konrad et al. (submitted). Phases used include groundmass (gm), plagioclase (plag), hornblende (hbl), and clinopyroxene (cpx).

Table S.4.4. (Continued)

Sample	$^{206}Pb/^{204}Pb$ meas	2SE	$^{206}Pb/^{204}Pb$ initial	$^{206}Pb/^{204}Pb$ modeled	$^{207}Pb/^{204}Pb$ meas	2SE	$^{207}Pb/^{204}Pb$ initial	$^{207}Pb/^{204}Pb$ modeled
D02-06	19.7808	3.0E-04	19.3355	19.6682	15.6198	3.0E-04	15.5986	15.6151
D03-24	20.6274	3.0E-04	20.3478	20.6223	15.7016	2.4E-04	15.6884	15.7019
D04-01D	20.3989	4.6E-04	20.0370	20.3208	15.6817	6.8E-04	15.6646	15.6786
D11-06	21.0713	4.3E-04	20.7848	21.0205	15.7405	3.8E-04	15.7270	15.7386
D13-01	21.0621	3.0E-04	20.7889	21.0139	15.7664	3.2E-04	15.7536	15.7646
D14-01	20.8045	4.3E-04	20.5869	20.8088	15.7202	4.0E-04	15.7099	15.7208
D18-07*	*21.0122*	3.7E-04	*20.7600*	*20.9777*	*15.7217*	4.7E-04	*15.7098*	*15.7205*
D18-11	20.9178	3.3E-04	20.6433	20.8611	15.7186	2.9E-04	15.7057	15.7164
D24-04*	*21.0868*	4.0E-04	*20.8425*	*21.0534*	*15.7501*	3.2E-04	*15.7386*	*15.7489*
D24-14A	21.2754	2.8E-04	21.0615	21.2743	15.7787	2.1E-04	15.7686	15.7791
D27-35*	21.6541	3.3E-04	21.4363	21.6243	15.8003	2.4E-04	15.7901	15.7993
D07-30	20.8970	3.8E-04	20.3071	20.5419	15.6772	6.1E-04	15.6494	15.6609
D15-02*	*20.2049*	3.9E-04	*19.7387*	*19.9571*	*15.5980*	3.0E-04	*15.5761*	*15.5868*
D15-17	20.0949	3.3E-04	19.7090	19.9286	15.5870	3.3E-04	15.5689	15.5796
D12-01*	*20.1363*	3.6E-04	*19.5562*	*19.9649*	*15.6445*	3.6E-04	*15.6167*	*15.6378*
D12-04	19.7607	4.2E-04	19.0757	19.4753	15.6260	4.0E-04	15.5932	15.6138
D19-03*	*20.5661*	3.6E-04	*19.9823*	*20.3936*	*15.6909*	2.9E-04	*15.6630*	*15.6842*
D19-08	20.0438	3.1E-04	19.5722	19.9879	15.6691	3.0E-04	15.6465	15.6680
D20-15	20.5319	4.0E-04	19.9332	20.3578	15.7023	4.1E-04	15.6736	15.6955
D21-26	19.0325	5.9E-04	18.9984	19.0396	15.5622	5.4E-04	15.5606	15.5625
D26-02‡	18.7110	3.1E-04	18.6379	18.7001	15.5424	3.0E-04	15.5390	15.5419
D28B-06	18.6141	2.5E-04	18.5866	18.6458	15.5212	2.9E-04	15.5199	15.5227
D21-19*	*18.7003*	9.2E-04	*18.6663*	*18.7076*	*15.5297*	7.4E-04	*15.5282*	*15.5301*
D27-31*	*18.7676*	2.2E-04	*18.7136*	*18.7792*	*15.5448*	1.9E-04	*15.5423*	*15.5453*
D32-02	19.0508	5.4E-04	19.0136	19.0629	15.6307	5.5E-04	15.6289	15.6312
D33-32	18.7813	3.5E-04	18.7056	18.7600	15.5125	2.6E-04	15.5090	15.5116
The following do not have an age date, so assumed ages are assigned. Shifting ages ±15 Ma produces ratios within analytical error except for Pb.								
D05-08	21.4171	2.7E-04	21.0767	21.3218	15.7962	2.5E-05	15.7801	15.7922
D05-08dup	21.3711	3.6E-04	21.0307	21.2758	15.7914	2.7E-04	15.7754	15.7874
D06-14	21.0077	3.9E-04	20.8573	21.1024	15.7728	3.5E-04	15.7657	15.7778
D08-27	20.2878	3.0E-04	19.7652	20.0102	15.6193	2.6E-04	15.5946	15.6067
D09-14	20.2418	3.7E-04	19.8085	20.0312	15.6771	3.7E-04	15.6567	15.6676
D10-16	20.0565	3.7E-04	19.8156	20.0383	15.6715	3.8E-04	15.6602	15.6711
D10-32	21.0968	3.7E-04	20.8432	21.0659	15.7664	3.3E-04	15.7545	15.7654
D23-05	20.2018	2.6E-04	19.7495	19.9498	15.6804	2.1E-04	15.6591	15.6690

Table S.4.4. (Continued)

Sample	$^{208}Pb/^{204}Pb$ meas	2SE	$^{208}Pb/^{204}Pb$ initial	$^{208}Pb/^{204}Pb$ modeled	$^{87}Sr/^{86}Sr$ meas	2SE	$^{87}Sr/^{86}Sr$ initial	$^{87}Sr/^{86}Sr$ modeled (S&D)
D02-06	39.4093	6.6E-04	39.0529	39.4839	0.703658	4.7E-06	0.703506	0.703596
D03-24	40.1725	6.3E-04	39.7797	40.1355	0.702994	5.7E-06	0.702868	0.702943
D04-01D	40.2963	1.2E-03	39.8077	40.1756	0.703448	6.1E-06	0.703318	0.703395
D11-06	40.9641	1.0E-03	40.5756	40.8811	0.702944	4.2E-06	0.702836	0.702900
D13-01	40.6004	1.0E-03	40.3623	40.6541	0.703016	4.7E-06	0.702913	0.702974
D14-01	40.6768	1.1E-03	40.3410	40.6288	0.703082	6.2E-06	0.702980	0.703040
D18-07*	*40.6248*	7.0E-04	*40.3054*	*40.5877*	*0.702951*	5.6E-06	*0.702851*	*0.702910*
D18-11	40.4366	8.2E-04	40.0643	40.3469	0.703004	6.1E-06	0.702904	0.702963
D24-04*	*40.3419*	7.6E-04	*40.0323*	*40.3060*	*0.703056*	5.2E-06	*0.702960*	*0.703017*
D24-14A	40.7392	6.3E-04	40.4944	40.7704	0.703165	5.8E-06	0.703067	0.703125
D27-35*	40.8038	6.2E-04	40.5278	40.7718	0.703207	6.6E-06	0.703121	0.703172
D07-30	40.1986	7.5E-04	39.8385	40.1430	0.702868	8.0E-06	0.702760	0.702824
D15-02*	*39.7581*	8.0E-04	*39.4161*	*39.6994*	*0.702691*	7.3E-06	*0.702591*	*0.702650*
D15-17	39.6321	9.6E-04	39.2810	39.5659	0.702691	4.8E-06	0.702590	0.702650
D12-01*	*39.2965*	6.9E-04	*38.6756*	*39.2045*	*0.702844*	6.7E-06	*0.702658*	*0.702768*
D12-04	38.9807	1.2E-03	38.2861	38.8034	0.702774	8.6E-06	0.702591	0.702700
D19-03*	*38.9826*	7.5E-04	*38.3578*	*38.8900*	*0.703047*	5.7E-06	*0.702859*	*0.702970*
D19-08	38.8339	7.9E-04	38.3389	38.8768	0.703020	5.4E-06	0.702830	0.702943
D20-15	39.1484	1.1E-03	38.4568	39.0062	0.703181	7.8E-06	0.702987	0.703102
D21-26	38.7315	1.7E-03	38.6865	38.7401	0.703690	5.1E-06	0.703671	0.703682
D26-02‡	38.4534	9.1E-04	38.4038	38.4846	0.704171	6.1E-06	0.704142	0.704159
D28B-06	38.3940	8.3E-04	38.3536	38.4304	0.704137	6.6E-06	0.704110	0.704126
D21-19*	*38.4651*	1.6E-03	*38.4298*	*38.4834*	*0.703546*	6.2E-06	*0.703527*	*0.703538*
D27-31*	*38.5771*	4.9E-04	*38.5209*	*38.6061*	*0.703825*	5.9E-06	*0.703795*	*0.703813*
D32-02	39.2571	1.6E-03	39.2114	39.2754	0.705108	5.3E-06	0.705086	0.705099
D33-32	38.4409	8.9E-04	38.4260	38.4966	0.703605	5.9E-06	0.703580	0.703595
The following do not have an age date, so assumed ages are assigned. Shifting ages ±15 Ma produces ratios within analytical error except for Pb.								
D05-08	42.0587	1.2E-03	41.5267	41.8445	0.702978	5.5E-06	0.702866	0.702932
D05-08dup	42.0239	7.5E-04	41.4919	41.8096				
D06-14	40.7754	7.3E-04	40.3706	40.6884	0.702986	5.7E-06	0.702874	0.702940
D08-27	39.8599	6.3E-04	39.4157	39.7335	0.702818	6.0E-06	0.702706	0.702772
D09-14	40.3858	8.9E-04	40.0572	40.3461	0.703331	6.6E-06	0.703229	0.703289
D10-16	39.6928	1.1E-03	39.3907	39.6795	0.703119	5.8E-06	0.703017	0.703077
D10-32	40.8197	8.5E-04	40.4473	40.7361	0.702963	7.3E-06	0.702861	0.702921
D23-05	39.7766	5.0E-04	39.3745	39.6344	0.703557	6.2E-06	0.703465	0.703520

Table S.4.4. (Continued)

Sample	$^{143}Nd/^{144}Nd$ meas	2SE	$^{143}Nd/^{144}Nd$ initial	$^{143}Nd/^{144}Nd$ modeled (Nebel)	$^{143}Nd/^{144}Nd$ modeled (S&D)	176Hf/ 177Hf meas	2SE	$^{176}Hf/^{177}Hf$ initial	$^{176}Hf/^{177}Hf$ modeled (Nebel)	$^{176}Hf/^{177}Hf$ modeled (S&D)
D02-06	0.512846	1.2E-05	0.512769	0.512877	0.512870	0.282888	6.0E-06	0.282873	0.282916	0.282920
D03-24	0.512898	7.9E-06	0.512851	0.512939	0.512934	0.282964	5.0E-06	0.282955	0.282991	0.282994
D04-01D	0.512841	1.1E-05	0.512792	0.512884	0.512878	0.282932	2.9E-06	0.282919	0.282956	0.282959
D11-06	0.512852	5.2E-06	0.512814	0.512890	0.512886	0.282982	6.0E-06	0.282972	0.283003	0.283005
D13-01	0.512871	4.2E-06	0.512829	0.512901	0.512897	0.283014	4.8E-06	0.283001	0.283031	0.283033
D14-01	0.512878	5.6E-06	0.512838	0.512909	0.512905	0.282979	4.2E-06	0.282967	0.282996	0.282998
D18-07*	*0.512877*	3.0E-06	*0.512845*	*0.512915*	*0.512911*	*0.282970*	2.6E-06	*0.282963*	*0.282991*	*0.282993*
D18-11	0.512870	5.3E-06	0.512837	0.512908	0.512903	0.282974	3.7E-06	0.282967	0.282996	0.282998
D24-04*	*0.512867*	3.8E-06	*0.512827*	*0.512895*	*0.512891*	*0.282961*	3.2E-06	*0.282951*	*0.282978*	*0.282980*
D24-14A	0.512844	4.2E-06	0.512803	0.512872	0.512868	0.282947	6.7E-06	0.282937	0.282965	0.282967
D27-35*	0.512839	3.2E-05	0.512807	0.512868	0.512864	0.282921	3.2E-06	0.282912	0.282937	0.282939
D07-30	0.512930	5.8E-06	0.512886	0.512961	0.512957	0.282991	6.0E-06	0.282983	0.283013	0.283016
D15-02*	*0.513021*	3.6E-06	*0.512972*	*0.513042*	*0.513038*	*0.283098*	2.7E-06	*0.283087*	*0.283116*	*0.283118*
D15-17	0.513021	4.7E-06	0.512971	0.513042	0.513038	0.283099	5.0E-06	0.283088	0.283117	0.283119
D12-01*	*0.513132*	1.3E-05	*0.513062*	*0.513193*	*0.513186*	*0.283032*	2.0E-06	*0.283001*	*0.283054*	*0.283058*
D12-04	0.513055	1.4E-05	0.512987	0.513116	0.513108	0.283022	4.0E-06	0.282991	0.283043	0.283047
D19-03*	*0.513218*	1.6E-05	*0.513134*	*0.513266*	*0.513258*	*0.282896*	2.6E-06	*0.282878*	*0.282931*	*0.282935*
D19-08	0.513029	1.5E-05	0.512943	0.513077	0.513069	0.282887	3.4E-06	0.282869	0.282923	0.282927
D20-15	0.512939	1.5E-05	0.512855	0.512992	0.512984	0.282875	3.3E-06	0.282860	0.282915	0.282920
D21-26	0.512932	8.1E-06	0.512924	0.512937	0.512937	0.283105	7.0E-06	0.283102	0.283107	0.283108
D26-02‡	0.512965	5.9E-06	0.512950	0.512971	0.512969	0.283082	3.4E-06	0.283079	0.283087	0.283088
D28B-06	0.512959	1.0E-05	0.512943	0.512963	0.512961	0.283073	5.0E-06	0.283070	0.283078	0.283078
D21-19*	*0.512974*	3.3E-06	*0.512965*	*0.512979*	*0.512978*	*0.283137*	3.6E-06	*0.283134*	*0.283139*	*0.283140*
D27-31*	*0.513009*	5.0E-06	*0.512993*	*0.513015*	*0.513013*	*0.283079*	2.1E-05	*0.283075*	*0.283083*	*0.283084*
D32-02	0.512662	6.2E-06	0.512653	0.512669	0.512668	0.282879	3.7E-06	0.282877	0.282884	0.282884
D33-32	0.512978	6.7E-06	0.512964	0.512982	0.512981	0.283094	3.5E-06	0.283091	0.283098	0.283098
The following do not have an age date, so assumed ages are assigned. Shifting ages ±15 Ma produces ratios within analytical error except for Pb.										
D05-08	0.512794	5.4E-06	0.512757	0.512836	0.512831	0.282877	2.5E-06	0.282868	0.282899	0.282902
D05-08dup										
D06-14	0.512823	4.7E-06	0.512785	0.512864	0.512859	0.282898	3.8E-06	0.282890	0.282922	0.282924
D08-27	0.512966	5.4E-06	0.512921	0.513000	0.512995	0.283063	1.3E-05	0.283055	0.283087	0.283089
D09-14	0.512876	4.4E-06	0.512834	0.512906	0.512901	0.282956	3.7E-06	0.282949	0.282978	0.282981
D10-16	0.512851	7.0E-06	0.512800	0.512872	0.512868	0.282941	5.0E-06	0.282930	0.282959	0.282961
D10-32	0.512856	4.6E-06	0.512817	0.512888	0.512884	0.282946	5.0E-06	0.282938	0.282967	0.282969
D23-05	0.512831	1.1E-05	0.512797	0.512862	0.512858	0.282843	4.5E-06	0.282834	0.282860	0.282862

Table S.4.5. Leaching experiment results.

		$^{208}Pb/^{204}Pb$	2SE	$^{207}Pb/^{204}Pb$	2SE	$^{206}Pb/^{204}Pb$	2SE	Approximate undiluted voltage in cut
D05-08	**Leachate 1**	40.3081	2.0E-03	15.7571	8.1E-04	20.7608	9.7E-04	97.5
	Leachate 2	40.4589	3.3E-03	15.7617	1.1E-03	20.8437	1.2E-03	13.25
	Leachate 3	--	--	--	--	--	--	--
	Leachate 4	40.7571	7.9E-03	15.7734	3.1E-03	20.9445	4.2E-03	2.75
	Sample	42.8683	2.3E-03	15.8050	9.2E-04	21.6696	1.0E-03	10.75
D20-15	**Leachate 1**	39.0642	1.8E-03	15.6947	7.0E-04	20.4123	7.5E-04	47.5
	Leachate 2	38.9005	2.8E-03	15.6947	1.2E-03	20.2729	1.3E-03	17.75
	Leachate 3	--	--	--	--	--	--	--
	Leachate 4	38.8555	3.4E-03	15.6943	1.1E-03	20.2234	1.4E-03	6.25
	Sample	39.1442	1.7E-03	15.6991	7.6E-04	20.5301	7.9E-04	28.75

Each leach step was performed using 1 mL ~6N double-distilled HCl for ~1 hour on 500-600 mg crushed sample. A final 12 hour leach was then performed to bring the total time spent in leach to ~16 hours to best replicate the conditions of the main sample set. This leach fraction was not expected to contain significant amount of Pb and was discarded. The leachate was then pipetted into a separate, clean Teflon beaker. The sample was rinsed 3x with 18MΩ water, which was drawn off of the sample each time and added to the leachate to ensure the entire leachate fraction was captured. The leaches were then processed through Pb separation and cleanup chemistry and analyzed as described in the Supplemental Methods. Since Leachate 3 was not analyzed for either sample and represents a relatively small fraction of total sample Pb, it is not considered in this estimate.

Table S.4.6. Mixing model parameters.

	HIMU	MORB	EM1	FOZO
$^{143}Nd/^{144}Nd$	0.512909	0.51327	0.512509	0.51282
$^{206}Pb/^{204}Pb$	21.652	17.72	17.804	19
$^{207}Pb/^{204}Pb$	15.821	15.5	15.4728	15.55
$^{208}Pb/^{204}Pb$	40.534	37.91	39.001	38.9
$^{87}Sr/^{86}Sr$	0.702817	0.70215	0.704511	0.704
$^{176}Hf/^{177}Hf$	0.282885	0.28326	0.282718	0.2828
Nd (ppm)	38.13	12.03	46.14	32.67
Pb (ppm)	2.29	0.57	4.34	1.68
Sr (ppm)	542.18	129	603.00	506.17
Hf (ppm)	4.95	2.79	7.11	5.27

MORB is from Chauvel and Blichert-Toft (2001)and Gale et al. (2013), HIMU from Woodhead (1996), EM1 from Eisele et al., (2002), EM2 from Jackson et al. (2007), and FOZO is from Hart et al. (1992), Hauri and Hart (1994), and trace elements, assumed to be similar to the FOZO/C Louisville hotspot, are from Vanderkluysen et al. (2014).

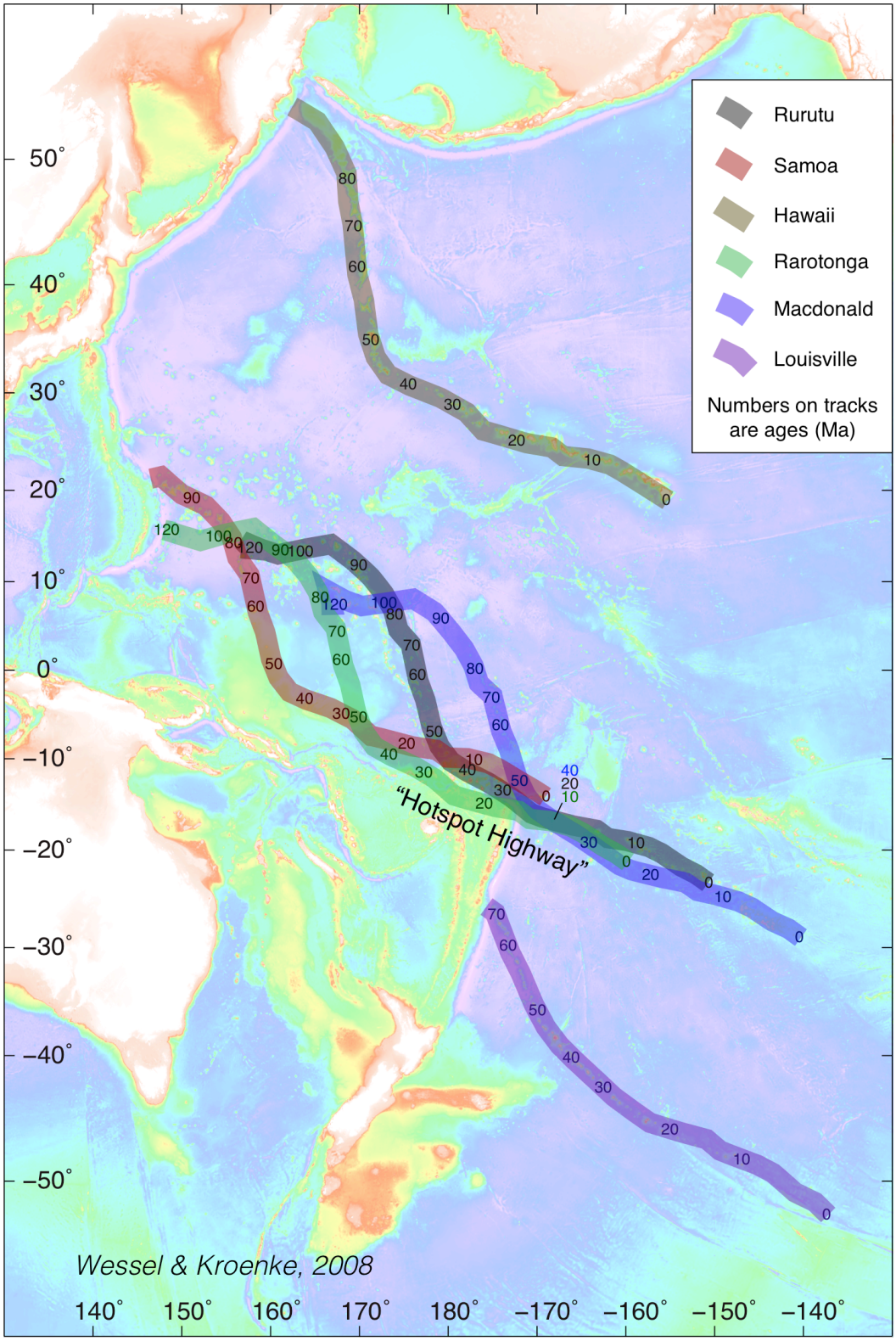

Supplemental Figure S.4.1. Map of the Pacific Ocean showing the track overlap in the Hotspot Highway. Hawaiian-Emperor and Louisville tracks also shown for reference.

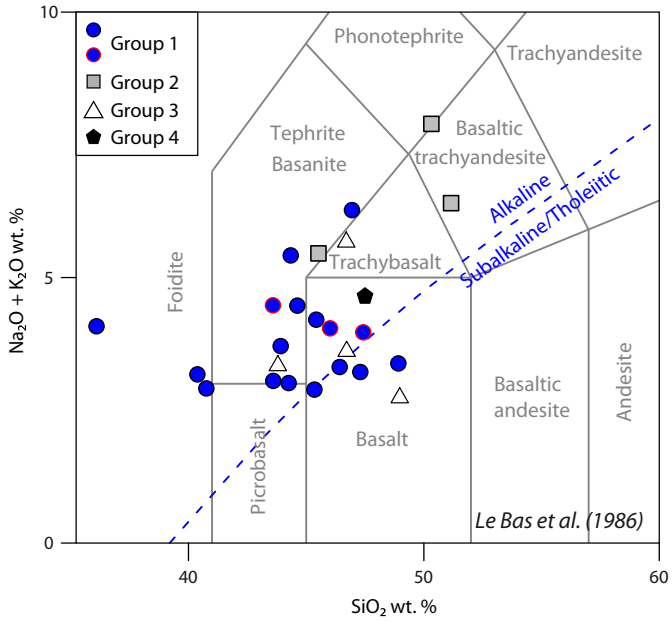

Supplemental Figure S.4.2. Total alkali-silica (TAS) diagram.

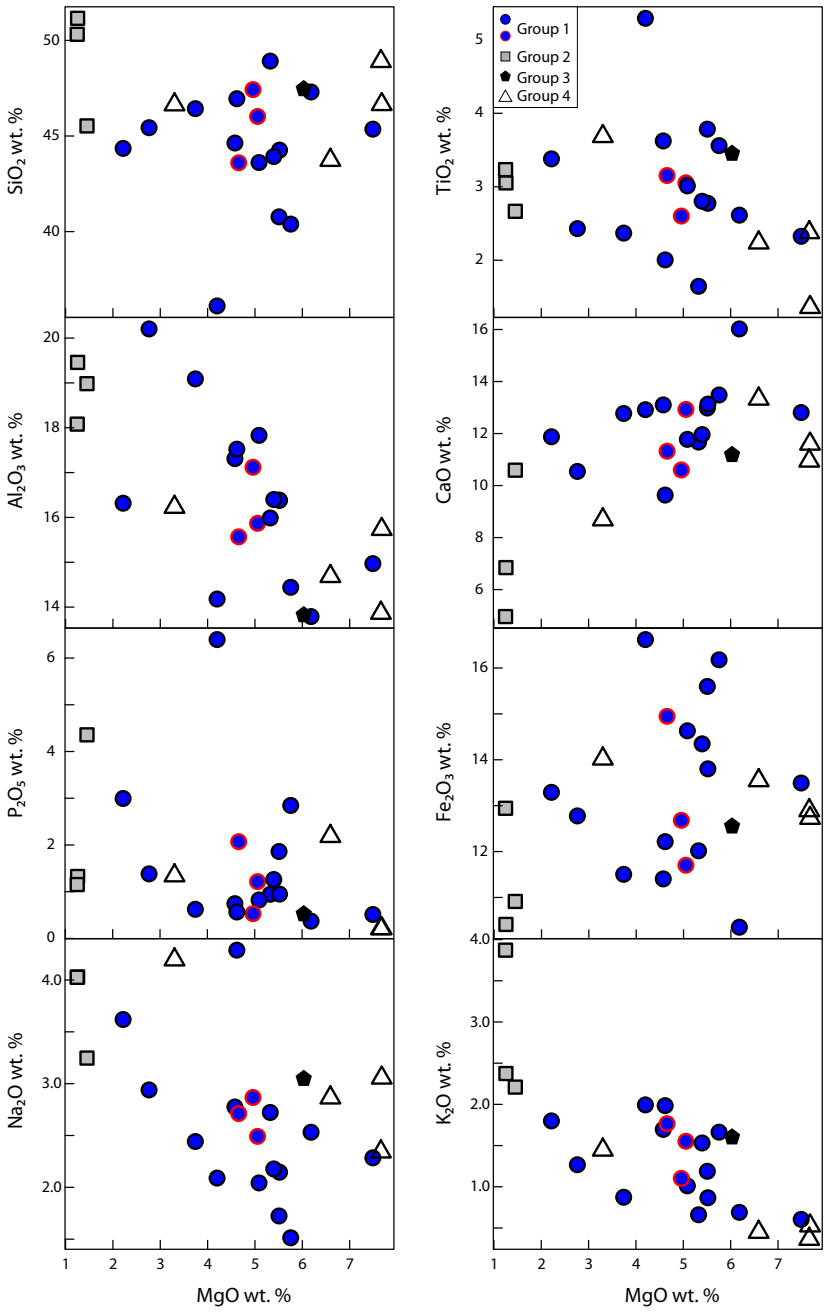

Supplemental Figure S.4.3. MgO plots for various major elements.

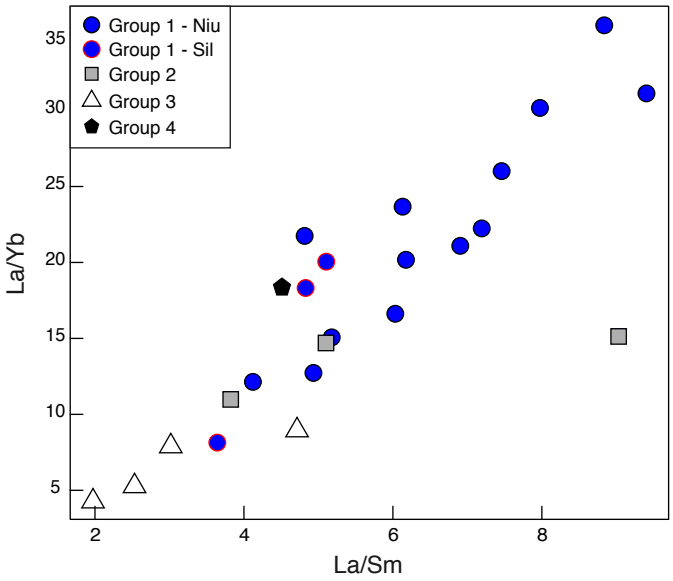

Supplemental Figure S.4.4. La/Yb vs. La/Sm ratios of the RR1310 samples. Ratios represent absolute elemental compositions; no normalization was used. Group 1 (Rurutu) are enriched and plot with typical OIB compositions. Group 2 plot in the depleted third of samples for La/Yb, with one outlier suggesting an anomalous Sm depletion resulting in an unusually enriched La/Sm ratio. Group 3 are the most depleted of the sample set, while Group 4, as a true Samoan composition, plots within the OIB-typical field defined by the Group 1 samples.

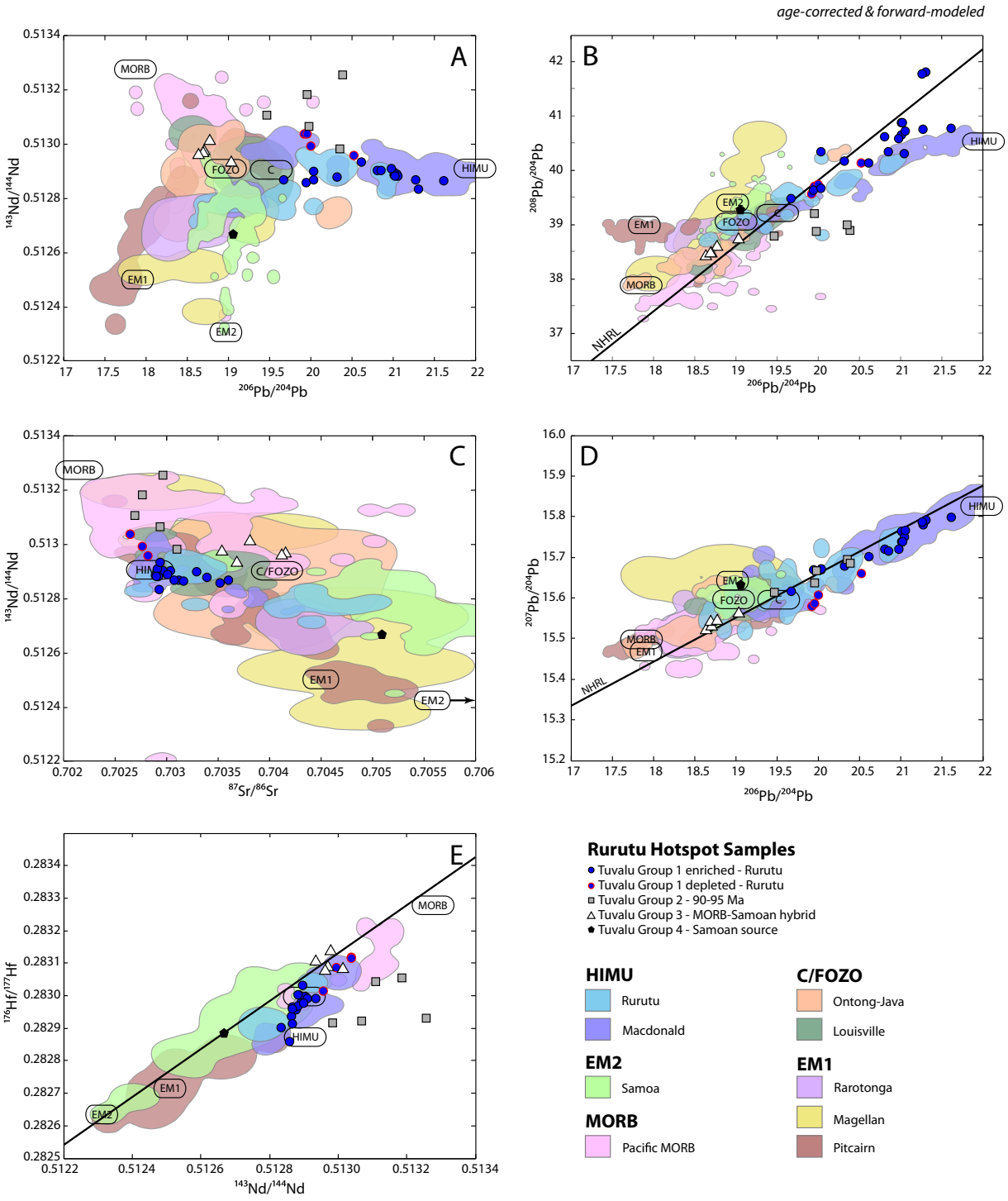

Supplemental Figure S.4.5. Age-corrected and forward-modeled isotopic data plotted against the background data used in Figure 4. Niu and Sil trends remain after age correction and forward modeling, suggesting the trends are primary to the magmas.

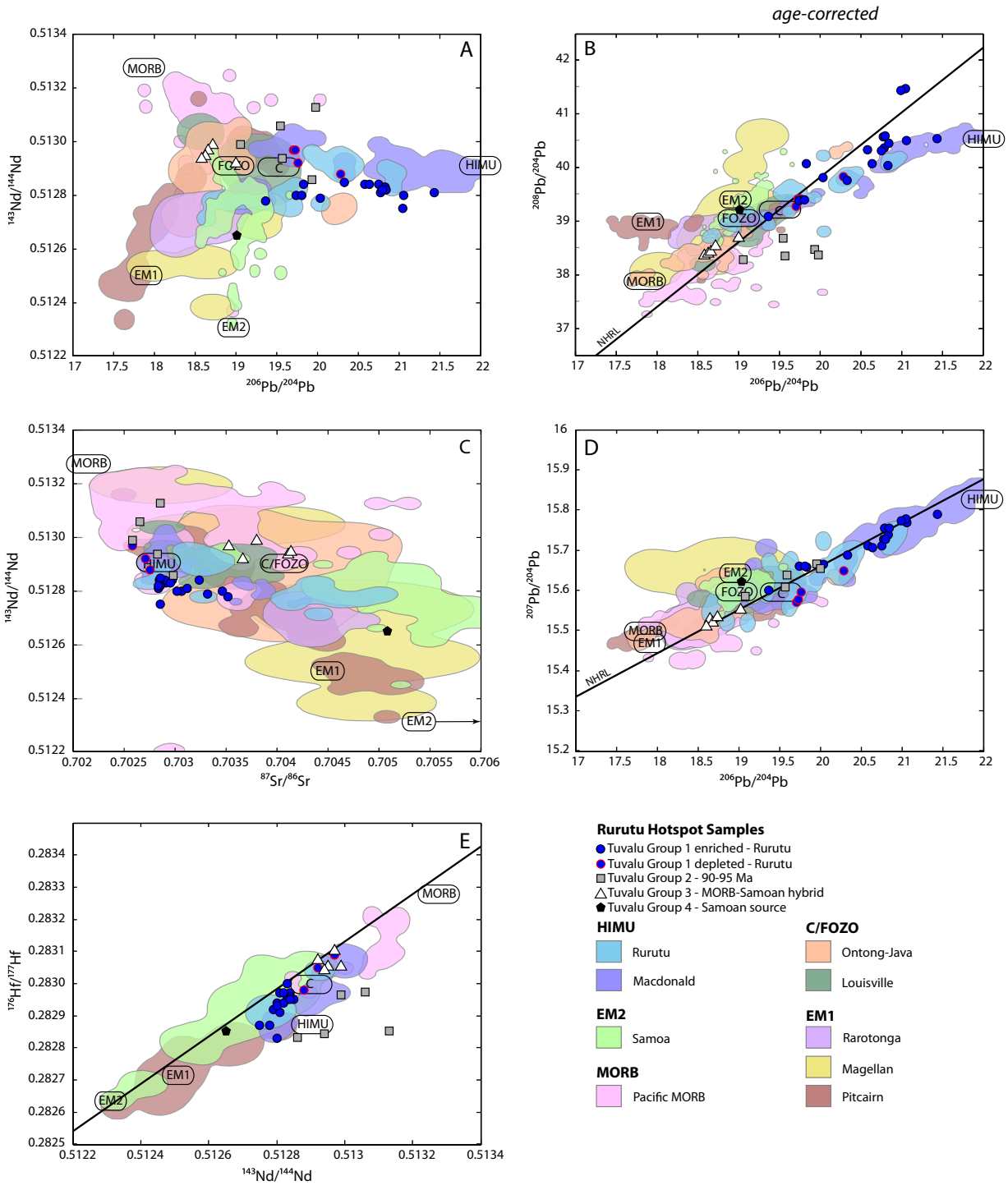

Supplemental Figure S.4.6. Age-corrected isotopic data plotted against background data used in Figure 4, showing Niu and Sil trends remain after correction back to an initial ratio.

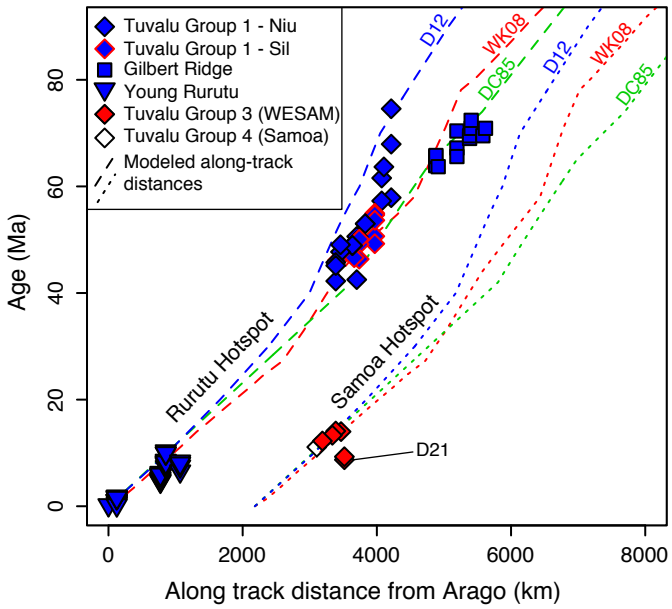

Supplemental Figure S.4.7. Along-track distance vs. age plot for all existing Rurutu hotspot and Samoan seamounts identified in this study. Rurutu data sources: Konter et al. (2008), Koppers et al. (2003), Staudigel et al. (1991). Model fits include WK08, DC85, and D12 projected from Arago Seamount (Rurutu), and Vailulu'u Seamount (Samoa).

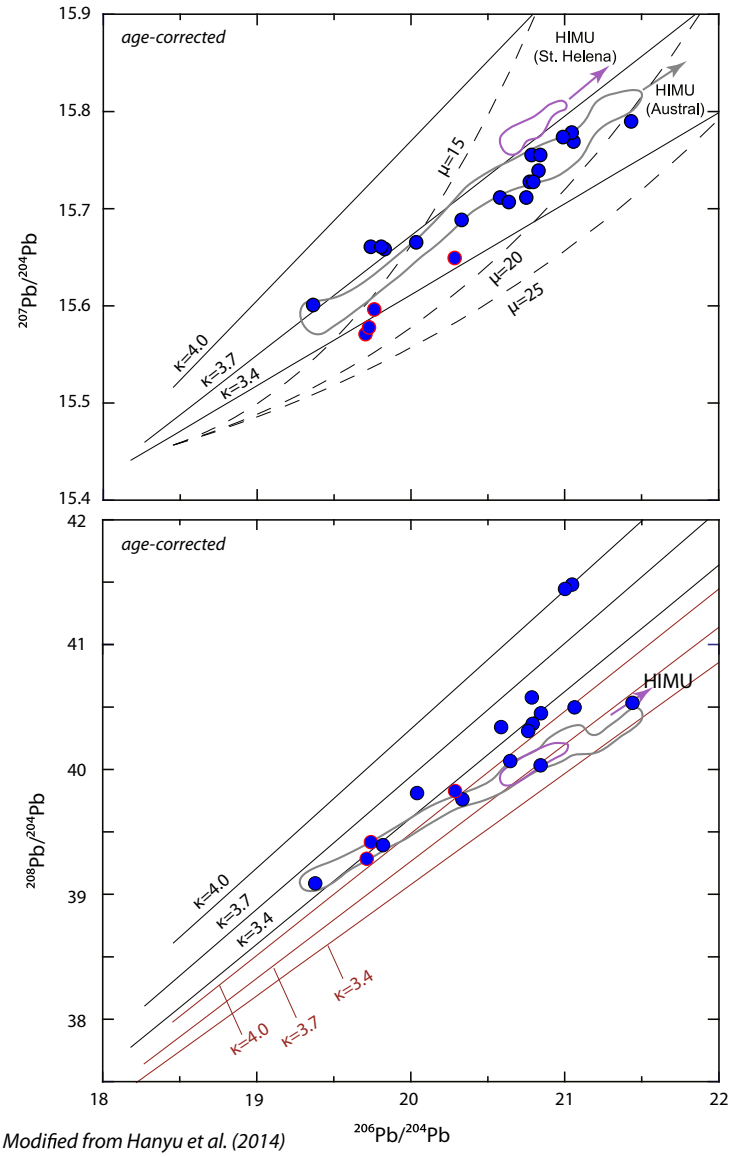

Modified from Hanyu et al. (2014)

Supplemental Figure S.4.8. Comparison of Group 1 isotopic data to the μ-κ ingrowth model of Hanyu et al. (2014). Rurutu compositions display greater κ variability than that found in traditional HIMU, suggesting some Rurutu magmas probably assimilated heterogeneous, variably Th/U-enriched (via zones of allanite and/or monazite) sections of hydrothermally altered oceanic crust gabbros.

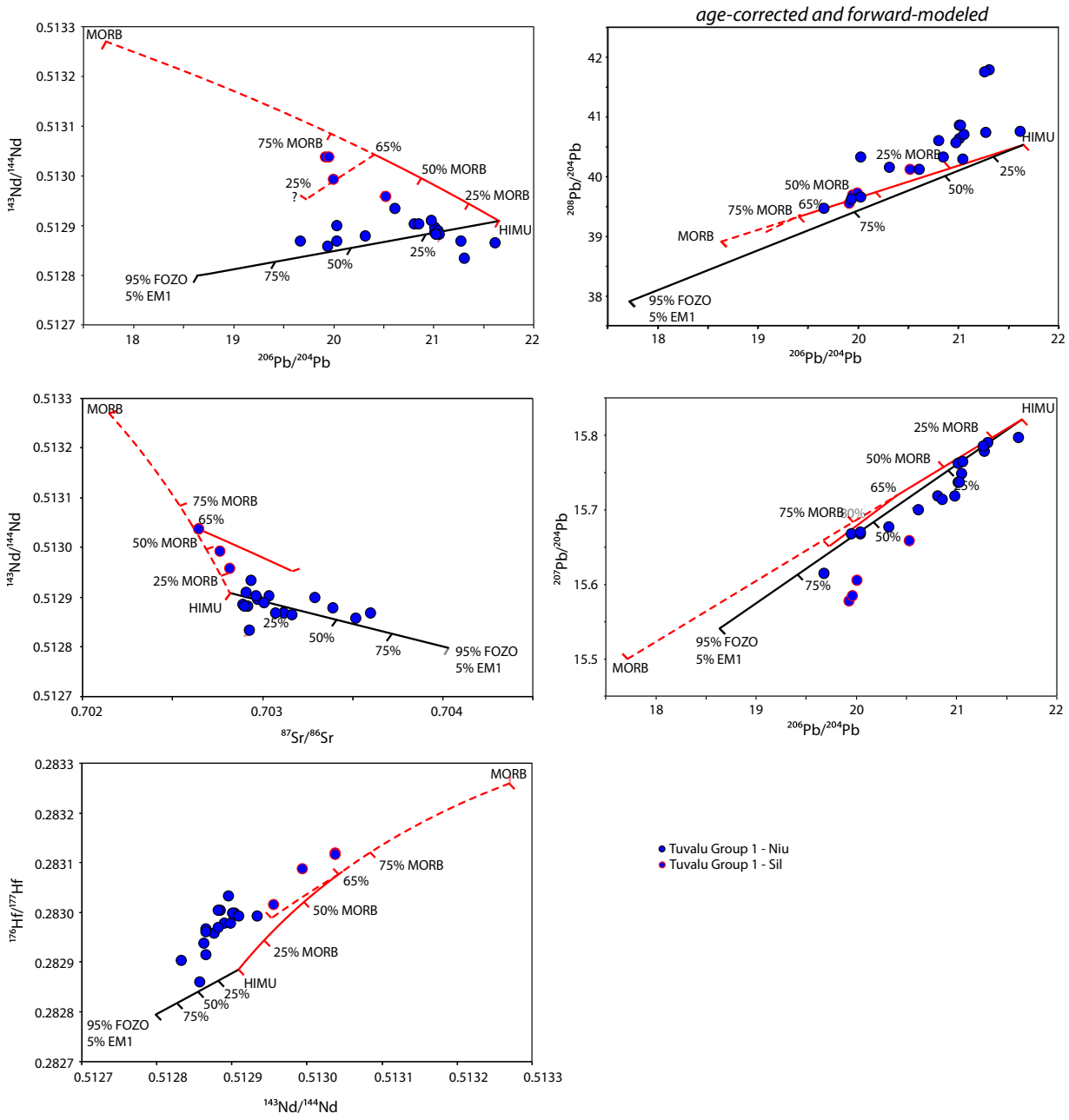

Supplemental Figure S.4.9. Possible mixing models for a four-component system in different isotope axes (emphasizing $^{143}Nd/^{144}Nd$ vs. $^{206}Pb/^{204}Pb$). Note the poor fit in $^{207}Pb/^{204}Pb$ vs. $^{206}Pb/^{204}Pb$ for the Sil trend, which plots below the NHRL and the Niu trend.

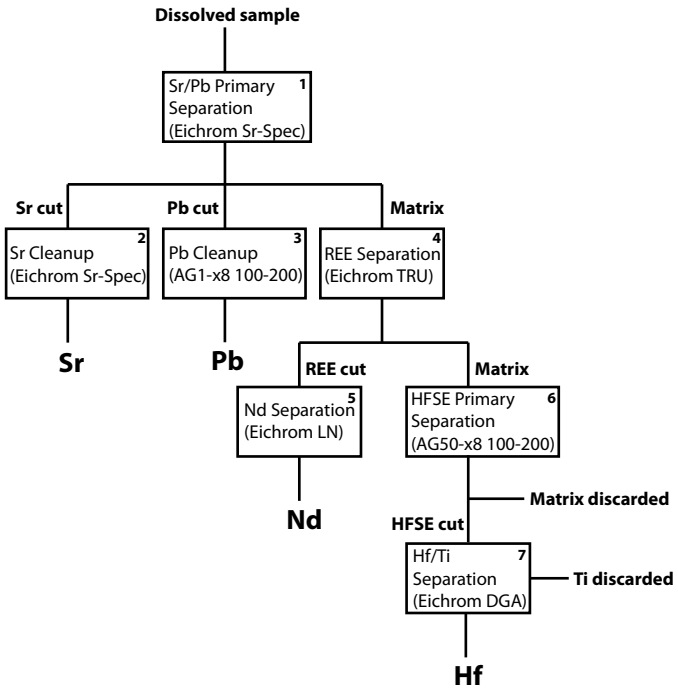

Supplemental Figure S.4.10. Flow chart illustrating the single-digestion elemental separation sequence, described in further detail in Supplemental Methods.

Supplemental Ages - Summary

Sample Information			Plateau							Inverse Isochron					Total Fusion		
Sample Name	Material	Seamount	Age ± 2σ (i)	± 2σ (f)	^{39}Ar	K/Ca ± 2σ	MSWD	n	N	Age ± 2σ (i)	± 2σ (f)	^{40}Ar/^{39}Ar intercept ± 2σ	SF	MSWD	Age ± 2σ (i)	± 2σ (f)	K/Ca ± 2σ
RR1310-D12-01	Groundmass	Fialua	**91.46 ± 0.22 Ma**	± 2.05 Ma	31%	0.481 ± 0.068	3.09	14	33	92.08 ± 0.75 Ma	± 2.19 Ma	225.08 ± 70.94	1%	2.73	86.81 ± 0.17 Ma	± 1.94 Ma	0.646 ± 0.025
RR1310-D12-04	Groundmass	Fialua	**89.46 ± 0.41 Ma**	± 2.04 Ma	29%	0.36 ± 0.032	3.8	19	35	88.41 ± 0.85 Ma	± 2.15 Ma	303.89 ± 6.11	41%	2.75	82.18 ± 0.20 Ma	± 1.85 Ma	0.369 ± 0.013
RR1310-D19-03	Plagioclase	Pae							24						89.35 ± 0.19 Ma	± 2.00 Ma	0.034 ± 0.000
RR1310-D19-03	Plagioclase	Pae							24						89.36 ± 0.27 Ma	± 2.01 Ma	0.035 ± 0.000
RR1310-D19-03	Plagioclase	Pae	**92.03 ± 1.15 Ma**	± 2.35 Ma	95%	0.029 ± 0.002	2.09	10	14	91.77 ± 1.58 Ma	± 2.58 Ma	324.6 ± 82.21	16%	2.2	92.49 ± 0.99 Ma	± 2.29 Ma	0.029 ± 0.002
RR1310-D19-12	Plagioclase	Pae	**93.99 ± 0.43 Ma**	± 2.14 Ma	52%	0.047 ± 0.002	2	14	26	94.03 ± 0.53 Ma	± 2.16 Ma	293.72 ± 18.93	30%	2.18	93.35 ± 0.29 Ma	± 2.10 Ma	0.047 ± 0.001
RR1310-D20-10	Plagioclase	Foumatua	**94.06 ± 0.20 Ma**	± 2.11 Ma	48%	0.064 ± 0.001	0.16	6	24	94.04 ± 0.23 Ma	± 2.11 Ma	302.36 ± 30.39	3%	0.15	93.81 ± 0.19 Ma	± 2.10 Ma	0.065 ± 0.001
RR1310-D20-15	Plagioclase	Foumatua	**95.00 ± 0.19 Ma**	± 2.13 Ma	77%	0.079 ± 0.001	1.1	13	24	95.18 ± 0.51 Ma	± 2.18 Ma	206.03 ± 113.09	1%	1.15	94.99 ± 0.19 Ma	± 2.13 Ma	0.08 ± 0.001
RR1310-D21-03	Groundmass	Nukulaelae	**10.42 ± 0.05 Ma**	± 0.24 Ma	42%	0.006 ± 0.007	1.49	5	29	10.38 ± 0.16 Ma	± 0.28 Ma	325.26 ± 113.62	14%	1.79	15.65 ± 0.06 Ma	± 0.36 Ma	0.055 ± 0.000
RR1310-D21-19	Groundmass	Nukulaelae	**8.81 ± 0.10 Ma**	± 0.22 Ma	86%	0.038 ± 0.002	0.54	29	36	8.87 ± 0.16 Ma	± 0.25 Ma	293.82 ± 3.49	66%	0.52	8.49 ± 0.13 Ma	± 0.23 Ma	0.027 ± 0.000
RR1310-D21-19	Groundmass	Nukulaelae	**8.64 ± 0.16 Ma**	± 0.25 Ma	81%	0.032 ± 0.002	0.46	27	36	8.6 ± 0.27 Ma	± 0.33 Ma	300.14 ± 23.02	48%	0.47	8.54 ± 0.17 Ma	± 0.26 Ma	0.023 ± 0.000
RR1310-D26-01	Groundmass	West Niulakita							36						12.99 ± 0.03 Ma	± 0.29 Ma	0.153 ± 0.002
RR1310-D26-03	Groundmass	West Niulakita							34						15.01 ± 0.03 Ma	± 0.34 Ma	0.177 ± 0.002
RR1310-D27-31	Groundmass	East Niulakita	**13.46 ± 0.05 Ma**	± 0.31 Ma	56%	0.211 ± 0.011	0.65	8	36	13.1 ± 0.78 Ma	± 0.84 Ma	303.4 ± 17.43	5%	0.61	13.53 ± 0.05 Ma	± 0.31 Ma	0.185 ± 0.002
RR1310-D27-31	Plagioclase	East Niulakita	**14.76 ± 0.12 Ma**	± 0.35 Ma	34%	0.02 ± 0.002	1.54	7	24	15.05 ± 0.23 Ma	± 0.41 Ma	287.12 ± 5.95	27%	0.33	15.96 ± 0.08 Ma	± 0.37 Ma	0.03 ± 0.000
RR1310-D27-32	Plagioclase	East Niulakita							21						17.56 ± 0.08 Ma	± 0.40 Ma	0.006 ± 0.000
RR1310-D27-33	Groundmass	East Niulakita							31						13.75 ± 0.04 Ma	± 0.31 Ma	0.198 ± 0.000
RR1310-D27-42	*Groundmass*	*East Niulakita*	***14.76 ± 0.05 Ma***	***± 0.34 Ma***	*54%*	*0.177 ± 0.017*	*0.87*	*14*	*31*	***14.76 ± 0.08 Ma***	***± 0.34 Ma***	*328.37 ± 3.93*	*25%*	*1.58*	*15.16 ± 0.05 Ma*	*± 0.34 Ma*	*0.152 ± 0.000*
RR1310-D32-01	Groundmass	Lafetoga	**11.18 ± 0.06 Ma**	± 0.26 Ma	35%	0.428 ± 0.077	1.69	4	28	11.08 ± 0.18 Ma	± 0.31 Ma	309.53 ± 22.95	11%	1.43	10.68 ± 0.07 Ma	± 0.25 Ma	0.355 ± 0.002
RR1310-D32-04	Plagioclase	Lafetoga	**11.02 ± 0.04 Ma**	± 0.25 Ma	77%	0.033 ± 0.000	0.64	18	24	11.04 ± 0.07 Ma	± 0.26 Ma	286.28 ± 31.60	17%	0.66	11.05 ± 0.04 Ma	± 0.25 Ma	0.033 ± 0.000
RR1310-D33-05	Plagioclase	Tuscarora	**12.24 ± 0.13 Ma**	± 0.31 Ma	36%	0.005 ± 0.000	0.58	10	21	12.13 ± 0.21 Ma	± 0.34 Ma	318.44 ± 30.32	25%	0.32	12.64 ± 0.08 Ma	± 0.30 Ma	0.006 ± 0.000

All age are normalized to the FCT-2 sanidine age of 28.201 (Kuiper et al., 2008)

Italic samples indicate the plateau values are recalculated using the inverse isochron intercept for $^{40}Ar/^{39}Ar$.
(i) indicatede internal uncertainty and (f) indicates full external uncertainty
n=steps used in calculating plateau age; N=total steps in the heating spectrum
SF = Spreading factor

Supplemental Ages. $^{40}Ar/^{39}Ar$ age data for Tuvalu seamounts not included in Konrad et al. (submitted).

OSU Argon Geochronology Lab
CEOAS Oregon State University, Corvallis, USA

RR1310-D12-01 > Groundmass > RURUTU (13-INT-08)
TUVALU > RURUTU HOTSPOT
14-OSU-02 (2A32-14) > Incremental Heating > Kevin Konrad

Information on Analysis and Constants Used in Calculations

Project = **RURUTU (13-INT-08)**
Sample = **RR1310-D12-01**
Material = **Groundmass**
Location = **Rurutu Hotspot**
Region = **Tuvalu**
Analyst = **Kevin Konrad**
Irradiation = **14-OSU-02 (2A32-14)**
Position = **X: 0 | Y: 0 | Z/H: 37.3 mm**
FCT-NM Age = **28.201 ± 0.023 Ma**
FCT-NM Reference = **Kuiper et al. (2008)**
FCT-NM 40Ar/39Ar Ratio = **8.85384 ± 0.00841**
FCT-NM J-value = **0.00177521 ± 0.00000169**
Air Shot 40Ar/36Ar = **303.8680 ± 0.4436**
Air Shot MDF = **0.99310653 ± 0.00067761 (LIN)**
Experiment Type = **Incremental Heating**
Extraction Method = **Bulk Laser Heating**
Heating = **77 sec**
Isolation = **10.00 min**
Instrument = **ARGUS-VI-D**
Preferred Age = **Plateau Age**
Age Classification = **Eruption Age**
IGSN = Undefined
Rock Class = Undefined
Lithology = **Basalt**
Lat-Lon = Undefined - Undefined
Age Equations = **Min et al. (2000)**
Negative Intensities = **Allowed**
Collector Calibrations = **40Ar 36Ar**
Decay 40K = **5.530 ± 0.048 E-10 1/a**
Decay 39Ar = **2.940 ± 0.016 E-07 1/h**
Decay 37Ar = **8.230 ± 0.012 E-04 1/h**
Decay 36Cl = **2.257 ± 0.015 E-06 1/a**
Decay 40K(EC,β⁺) = **0.580 ± 0.009 E-10 1/a**
Decay 40K(β⁻) = **4.950 ± 0.043 E-10 1/a**
Atmospheric 40/36(a) = **295.50**
Atmospheric 38/36(a) = **0.1869**
Production 39/37(ca) = **0.0006756 ± 0.0000089**
Production 38/37(ca) = **0.0000718 ± 0.0000092**
Production 36/37(ca) = **0.0002663 ± 0.0000004**
Production 40/39(k) = **0.003823 ± 0.000102**
Production 38/39(k) = **0.012031 ± 0.000019**
Production 36/38(cl) = **262.80 ± 1.71**
Scaling Ratio K/Ca = **0.430**
Abundance Ratio 40K/K = **1.1700 ± 0.0100 E-04**
Atomic Weight K = **39.0983 ± 0.0001 g**

Results	40(a)/36(a) ± 2σ	40(r)/39(k) ± 2σ	Age ± 2σ (Ma)	MSWD	39Ar(k) (%,n)	K/Ca ± 2σ
Age Plateau		29.22457 ± 0.04352	**91.46 ± 0.22**	3.09	31.10	0.48 ± 0.07
Error Mean		± 0.15%	**± 0.24%**	0%	14	
			Full External Error ± 2.05	1.78	2σ Confidence Limit	
			Analytical Error ± 0.13	1.7565	Error Magnification	
Total Fusion Age		27.70066 ± 0.01390	**86.81 ± 0.17**		33	0.65 ± 0.02
		± 0.05%	**± 0.19%**			
			Full External Error ± 1.94			
			Analytical Error ± 0.04			
Normal Isochron	**210.40 ± 83.21**	29.46779 ± 0.24120	**92.20 ± 0.76**	2.76	31.10	
Error Chron	**± 39.55%**	± 0.82%	**± 0.82%**	0%	14	
			Full External Error ± 2.19	1.82	2σ Confidence Limit	
			Analytical Error ± 0.74	1.6602	Error Magnification	
Inverse Isochron	**225.08 ± 70.94**	29.42637 ± 0.24064	**92.08 ± 0.75**	2.73	31.10	
Error Chron	**± 31.52%**	± 0.82%	**± 0.82%**	0%	14	
			Full External Error ± 2.19	1.82	2σ Confidence Limit	
			Analytical Error ± 0.73	1.6535	Error Magnification	
				1%	Spreading Factor	

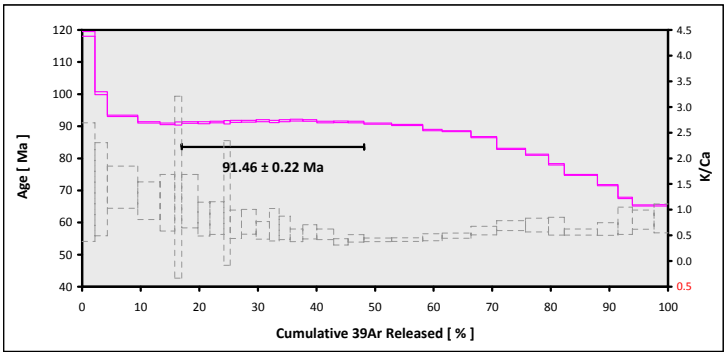

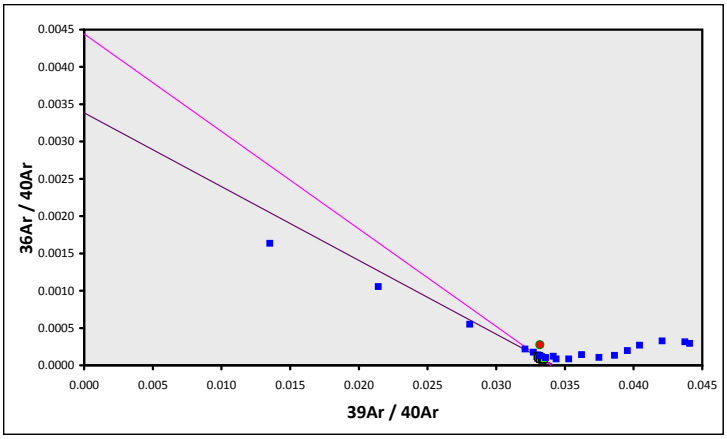

14D27566.one-pager.xls printed at 18-10-2016 (16:18)
ArArCALC v2.7.0 -- Beta Version

Supplemental Ages (Continued). $^{40}Ar/^{39}Ar$ age data for Tuvalu seamounts not included in Konrad et al. (submitted).

OSU Argon Geochronology Lab
CEOAS Oregon State University, Corvallis, USA

RR1310-D12-04 > Groundmass > RURUTU (13-INT-08)
TUVALU > RURUTU HOTSPOT
14-OSU-02 (2A34-14) > Incremental Heating > Kevin Konrad

Information on Analysis and Constants Used in Calculations

Project = **RURUTU (13-INT-08)**
Sample = **RR1310-D12-04**
Material = **Groundmass**
Location = **Rurutu Hotspot**
Region = **Tuvalu**
Analyst = **Kevin Konrad**
Irradiation = **14-OSU-02 (2A34-14)**
Position = **X: 0 | Y: 0 | Z/H: 39.5 mm**
FCT-NM Age = **28.201 ± 0.023 Ma**
FCT-NM Reference = **Kuiper et al (2008)**
FCT-NM 40Ar/39Ar Ratio = **8.86645 ± 0.00842**
FCT-NM J-value = **0.00177268 ± 0.00000168**
Air Shot 40Ar/36Ar = **335.0000 ± 2.0100**
Air Shot MDF = **0.97048429 ± 0.00142445 (LIN)**
Experiment Type = **Incremental Heating**
Extraction Method = **Bulk Laser Heating**
Heating = **77 sec**
Isolation = **10.00 min**
Instrument = **ARGUS-VI-D**
Preferred Age = **Plateau Age**
Age Classification = **Eruption Age**
IGSN = Undefined
Rock Class = Undefined
Lithology = **Basalt**
Lat-Lon = Undefined - Undefined
Age Equations = **Min et al. (2000)**
Negative Intensities = **Allowed**
Collector Calibrations = **40Ar 36Ar**
Decay 40K = **5.530 ± 0.048 E-10 1/a**
Decay 39Ar = **2.940 ± 0.016 E-07 1/h**
Decay 37Ar = **8.230 ± 0.012 E-04 1/h**
Decay 36Cl = **2.257 ± 0.015 E-06 1/a**
Decay 40K(EC,β⁺) = **0.580 ± 0.009 E-10 1/a**
Decay 40K(β⁻) = **4.950 ± 0.043 E-10 1/a**
Atmospheric 40/36(a) = **295.50**
Atmospheric 38/36(a) = **0.1869**
Production 39/37(ca) = **0.0006756 ± 0.0000089**
Production 38/37(ca) = **0.0000718 ± 0.0000092**
Production 36/37(ca) = **0.0002663 ± 0.0000004**
Production 40/39(k) = **0.003823 ± 0.000102**
Production 38/39(k) = **0.012031 ± 0.000019**
Production 36/38(cl) = **262.80 ± 1.71**
Scaling Ratio K/Ca = **0.430**
Abundance Ratio 40K/K = **1.1700 ± 0.0100 E-04**
Atomic Weight K = **39.0983 ± 0.0001 g**

Results	40(a)/36(a) ± 2σ	40(r)/39(k) ± 2σ	Age ± 2σ (Ma)	MSWD	39Ar(k) (%,n)	K/Ca ± 2σ
Age Plateau		28.61080 ± 0.12152	**89.46 ± 0.41**	3.80	28.92	0.360 ± 0.032
Error Mean		± 0.42%	**± 0.45%**	0%	19	
			Full External Error ± 2.04	1.67	2σ Confidence Limit	
			Analytical Error ± 0.37	1.9488	Error Magnification	
Total Fusion Age		26.22792 ± 0.04411	**82.18 ± 0.20**		35	0.369 ± 0.013
		± 0.17%	**± 0.25%**			
			Full External Error ± 1.85			
			Analytical Error ± 0.14			
Normal Isochron	**303.90 ± 6.13**	28.25850 ± 0.27485	**88.39 ± 0.85**	2.79	28.92	
Error Chron	**± 2.02%**	± 0.97%	**± 0.97%**	0%	19	
			Full External Error ± 2.15	1.69	2σ Confidence Limit	
			Analytical Error ± 0.84	1.6696	Error Magnification	
Inverse Isochron	**303.89 ± 6.11**	28.26520 ± 0.27380	**88.41 ± 0.85**	2.75	28.92	
Error Chron	**± 2.01%**	± 0.97%	**± 0.96%**	0%	19	
			Full External Error ± 2.15	1.69	2σ Confidence Limit	
			Analytical Error ± 0.84	1.6588	Error Magnification	
				41%	Spreading Factor	

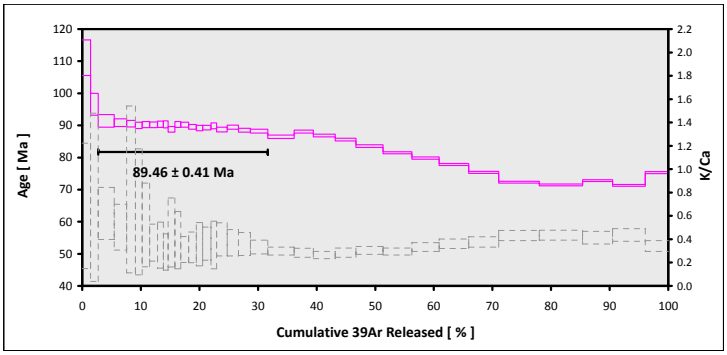

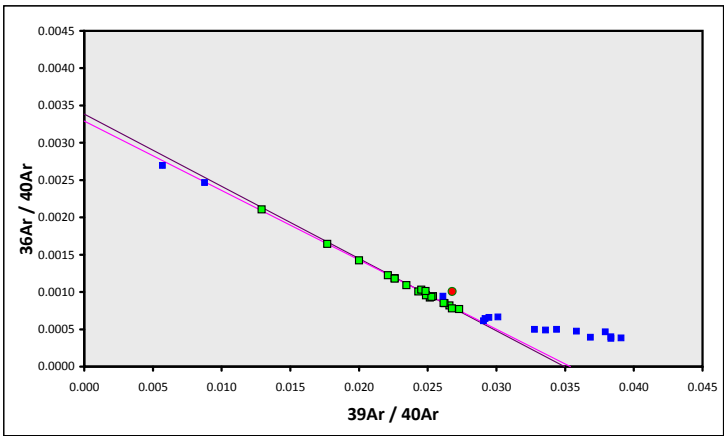

14D27661.one-pager.xls printed at 18-10-2016 (16:18)
ArArCALC v2.7.0 -- Beta Version

Supplemental Ages (Continued). $^{40}Ar/^{39}Ar$ age data for Tuvalu seamounts not included in Konrad et al. (submitted).

OSU Argon Geochronology Lab
CEOAS Oregon State University, Corvallis, USA

RR1310-D19-03 > Plagioclase > RURUTU (13-INT-08)
TUVALU > RURUTU HOTSPOT
14-OSU-02 (2A10-14) > Incremental Heating > Kevin Konrad

Information on Analysis and Constants Used in Calculations

Project = **RURUTU (13-INT-08)**
Sample = **RR1310-D19-03**
Material = **Plagioclase**
Location = **Rurutu Hotspot**
Region = **Tuvalu**
Analyst = **Kevin Konrad**
Irradiation = **14-OSU-02 (2A10-14)**
Position = **X: 0 | Y: 0 | Z/H: 14 mm**
FCT-NM Age = **28.201 ± 0.023 Ma**
FCT-NM Reference = **Kuiper et al. 2008**
FCT-NM 40Ar/39Ar Ratio = **8.83481 ± 0.00839**
FCT-NM J-value = **0.00177903 ± 0.00000169**
Air Shot 40Ar/36Ar = **304.0520 ± 0.3953**
Air Shot MDF = **0.99295922 ± 0.00065762 (LIN)**
Experiment Type = **Incremental Heating**
Extraction Method = **Bulk Laser Heating**
Heating = **0 sec**
Isolation = **6.00 min**
Instrument = **ARGUS-VI-D**
Preferred Age = Undefined
Age Classification = Undefined
IGSN = Undefined
Rock Class = Undefined
Lithology = **Basalt**
Lat-Lon = Undefined - Undefined
Age Equations = **Min et al. (2000)**
Negative Intensities = **Allowed**
Collector Calibrations = **40Ar 36Ar**
Decay 40K = **5.530 ± 0.048 E-10 1/a**
Decay 39Ar = **2.940 ± 0.016 E-07 1/h**
Decay 37Ar = **8.230 ± 0.012 E-04 1/h**
Decay 36Cl = **2.257 ± 0.015 E-06 1/a**
Decay 40K(EC,β⁺) = **0.580 ± 0.009 E-10 1/a**
Decay 40K(β⁻) = **4.950 ± 0.043 E-10 1/a**
Atmospheric 40/36(a) = **295.50**
Atmospheric 38/36(a) = **0.1869**
Production 39/37(ca) = **0.0006756 ± 0.0000089**
Production 38/37(ca) = **0.0000718 ± 0.0000092**
Production 36/37(ca) = **0.0002663 ± 0.0000004**
Production 40/39(k) = **0.003823 ± 0.000102**
Production 38/39(k) = **0.012031 ± 0.000019**
Production 36/38(cl) = **262.80 ± 1.71**
Scaling Ratio K/Ca = **0.430**
Abundance Ratio 40K/K = **1.1700 ± 0.0100 E-04**
Atomic Weight K = **39.0983 ± 0.0001 g**

Results	40(a)/36(a) ± 2σ	40(r)/39(k) ± 2σ	Age ± 2σ (Ma)	MSWD	39Ar(k) (%,n)	K/Ca ± 2σ
Age Plateau Cannot Calculate						
Total Fusion Age		28.47055 ± 0.03200 ± 0.11%	**89.35 ± 0.19 ± 0.22%** Full External Error ± 2.00 Analytical Error ± 0.10		24	0.0335 ± 0.0001
Normal Isochron Cannot Calculate						
Inverse Isochron Cannot Calculate						

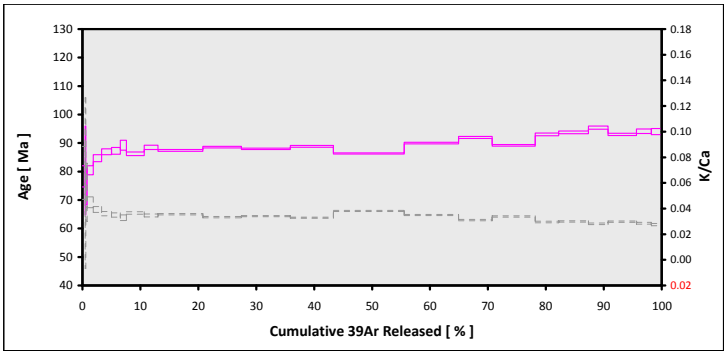

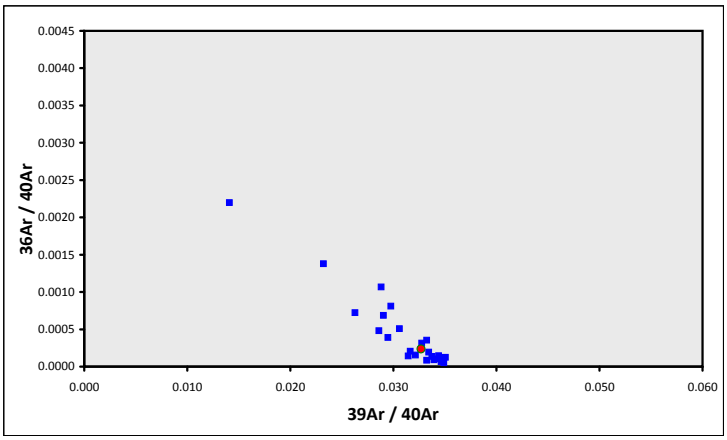

14D23574.one-pager.xls printed at 18-10-2016 (16:20)
ArArCALC v2.7.0 -- Beta Version

Supplemental Ages (Continued). $^{40}Ar/^{39}Ar$ age data for Tuvalu seamounts not included in Konrad et al. (submitted).

OSU Argon Geochronology Lab
CEOAS Oregon State University, Corvallis, USA

RR1310-D19-03 > Plagioclase > RURUTU (13-INT-08)
TUVALU > RURUTU HOTSPOT
14-OSU-02 (2A10-14) > Incremental Heating > Kevin Konrad

Information on Analysis and Constants Used in Calculations

Project = **RURUTU (13-INT-08)**
Sample = **RR1310-D19-03**
Material = **Plagioclase**
Location = **Rurutu Hotspot**
Region = **Tuvalu**
Analyst = **Kevin Konrad**
Irradiation = **14-OSU-02 (2A10-14)**
Position = **X: 0 | Y: 0 | Z/H: 14 mm**
FCT-NM Age = **28.201 ± 0.023 Ma**
FCT-NM Reference = **Kuiper et al. (2008)**
FCT-NM 40Ar/39Ar Ratio = **8.83481 ± 0.00839**
FCT-NM J-value = **0.00177903 ± 0.00000169**
Air Shot 40Ar/36Ar = **304.0540 ± 0.3922**
Air Shot MDF = **0.99295762 ± 0.00065645 (LIN)**
Experiment Type = **Incremental Heating**
Extraction Method = **Bulk Laser Heating**
Heating = **0 sec**
Isolation = **6.00 min**
Instrument = **ARGUS-VI-D**
Preferred Age = Undefined
Age Classification = Undefined
IGSN = Undefined
Rock Class = Undefined
Lithology = **Basalt**
Lat-Lon = Undefined - Undefined
Age Equations = **Min et al. (2000)**
Negative Intensities = **Allowed**
Collector Calibrations = **40Ar 36Ar**
Decay 40K = **5.530 ± 0.048 E-10 1/a**
Decay 39Ar = **2.940 ± 0.016 E-07 1/h**
Decay 37Ar = **8.230 ± 0.012 E-04 1/h**
Decay 36Cl = **2.257 ± 0.015 E-06 1/a**
Decay 40K(EC,β⁺) = **0.580 ± 0.009 E-10 1/a**
Decay 40K(β⁻) = **4.950 ± 0.043 E-10 1/a**
Atmospheric 40/36(a) = **295.50**
Atmospheric 38/36(a) = **0.1869**
Production 39/37(ca) = **0.0006756 ± 0.0000089**
Production 38/37(ca) = **0.0000718 ± 0.0000092**
Production 36/37(ca) = **0.0002663 ± 0.0000004**
Production 40/39(k) = **0.003823 ± 0.000102**
Production 38/39(k) = **0.012031 ± 0.000019**
Production 36/38(cl) = **262.80 ± 1.71**
Scaling Ratio K/Ca = **0.430**
Abundance Ratio 40K/K = **1.1700 ± 0.0100 E-04**
Atomic Weight K = **39.0983 ± 0.0001 g**

Results	40(a)/36(a) ± 2σ	40(r)/39(k) ± 2σ	Age ± 2σ (Ma)	MSWD	39Ar(k) (%,n)	K/Ca ± 2σ
Age Plateau Cannot Calculate						
Total Fusion Age		28.47433 ± 0.06838 ± 0.24%	**89.36 ± 0.27 ± 0.30%** Full External Error ± 2.01 Analytical Error ± 0.21		24	0.0348 ± 0.0003
Normal Isochron Cannot Calculate						
Inverse Isochron Cannot Calculate						

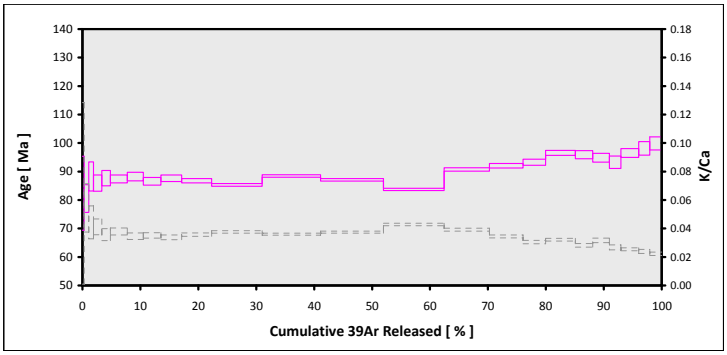

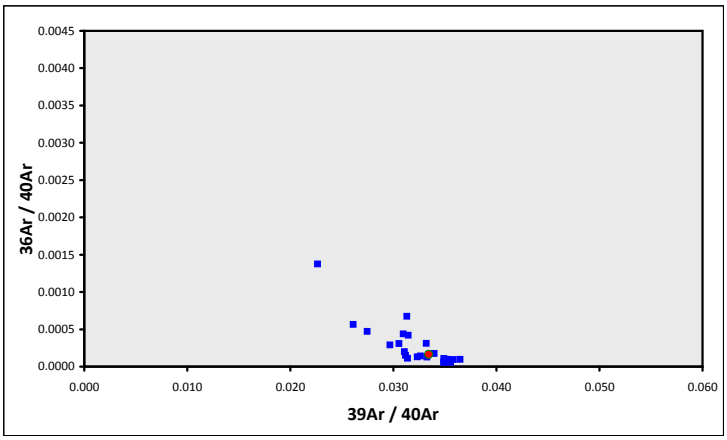

14D23610.one-pager.xls printed at 18-10-2016 (16:20)
ArArCALC v2.7.0 -- Beta Version

Supplemental Ages (Continued). $^{40}Ar/^{39}Ar$ age data for Tuvalu seamounts not included in Konrad et al. (submitted).

OSU Argon Geochronology Lab
CEOAS Oregon State University, Corvallis, USA

RR1310-D19-03 > Plagioclase > RURUTU (13-INT-08)
TUVALU > RURUTU HOTSPOT
14-OSU-02 (2A10-14) > Incremental Heating > Kevin Konrad

Information on Analysis and Constants Used in Calculations

Project = **RURUTU (13-INT-08)**
Sample = **RR1310-D19-03**
Material = **Plagioclase**
Location = **Rurutu Hotspot**
Region = **Tuvalu**
Analyst = **Kevin Konrad**
Irradiation = **14-OSU-02 (2A10-14)**
Position = **X: 0 | Y: 0 | Z/H: 14 mm**
FCT-NM Age = **28.201 ± 0.023 Ma**
FCT-NM Reference = **Kuiper et al. (2008)**
FCT-NM 40Ar/39Ar Ratio = **8.83481 ± 0.00839**
FCT-NM J-value = **0.00177903 ± 0.00000169**
Air Shot 40Ar/36Ar = **303.8240 ± 0.4527**
Air Shot MDF = **0.99314179 ± 0.00068157 (LIN)**
Experiment Type = **Incremental Heating**
Extraction Method = **Bulk Laser Heating**
Heating = **0 sec**
Isolation = **6.00 min**
Instrument = **ARGUS-VI-D**
Preferred Age = **Plateau Age**
Age Classification = **Eruption Age**
IGSN = Undefined
Rock Class = Undefined
Lithology = **Basalt**
Lat-Lon = Undefined - Undefined
Age Equations = **Min et al. (2000)**
Negative Intensities = **Allowed**
Collector Calibrations = **40Ar 36Ar**
Decay 40K = **5.530 ± 0.048 E-10 1/a**
Decay 39Ar = **2.940 ± 0.016 E-07 1/h**
Decay 37Ar = **8.230 ± 0.012 E-04 1/h**
Decay 36Cl = **2.257 ± 0.015 E-06 1/a**
Decay 40K(EC,β⁺) = **0.580 ± 0.009 E-10 1/a**
Decay 40K(β⁻) = **4.950 ± 0.043 E-10 1/a**
Atmospheric 40/36(a) = **295.50**
Atmospheric 38/36(a) = **0.1869**
Production 39/37(ca) = **0.0006756 ± 0.0000089**
Production 38/37(ca) = **0.0000718 ± 0.0000092**
Production 36/37(ca) = **0.0002663 ± 0.0000004**
Production 40/39(k) = **0.003823 ± 0.000102**
Production 38/39(k) = **0.012031 ± 0.000019**
Production 36/38(cl) = **262.80 ± 1.71**
Scaling Ratio K/Ca = **0.430**
Abundance Ratio 40K/K = **1.1700 ± 0.0100 E-04**
Atomic Weight K = **39.0983 ± 0.0001 g**

Results	40(a)/36(a) ± 2σ	40(r)/39(k) ± 2σ	Age ± 2σ (Ma)	MSWD	39Ar(k) (%,n)	K/Ca ± 2σ
Age Plateau		29.34862 ± 0.37296	**92.03 ± 1.15**	2.09	95.08	0.0288 ± 0.0023
Error Mean		± 1.27%	**± 1.25%**	3%	10	
			Full External Error ± 2.35	1.94	2σ Confidence Limit	
			Analytical Error ± 1.14	1.4445	Error Magnification	
Total Fusion Age		29.49631 ± 0.32001	**92.49 ± 0.99**		14	0.0293 ± 0.0018
		± 1.08%	**± 1.07%**			
			Full External Error ± 2.29			
			Analytical Error ± 0.98			
Normal Isochron	**292.01 ± 91.64**	29.49267 ± 0.53822	**92.47 ± 1.65**	2.39	95.08	
No Convergence	**± 31.38%**	± 1.82%	**± 1.79%**	1%	10	
			Full External Error ± 2.64	2.00	2σ Confidence Limit	
			Analytical Error ± 1.65	1.5463	Error Magnification	
Inverse Isochron	**324.60 ± 82.21**	29.26376 ± 0.51289	**91.77 ± 1.58**	2.20	95.08	
Error Chron	**± 25.33%**	± 1.75%	**± 1.72%**	2%	10	
			Full External Error ± 2.58	2.00	2σ Confidence Limit	
			Analytical Error ± 1.57	1.4827	Error Magnification	
				16%	Spreading Factor	

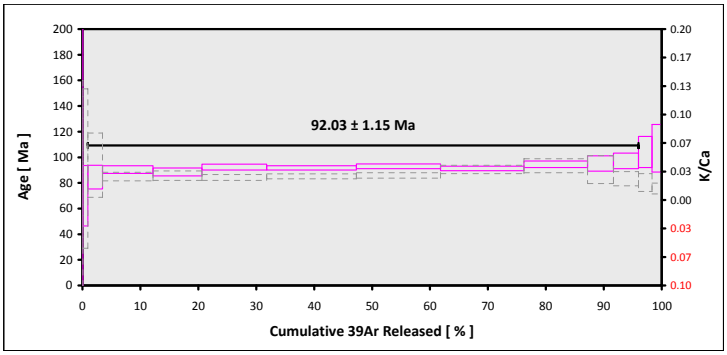

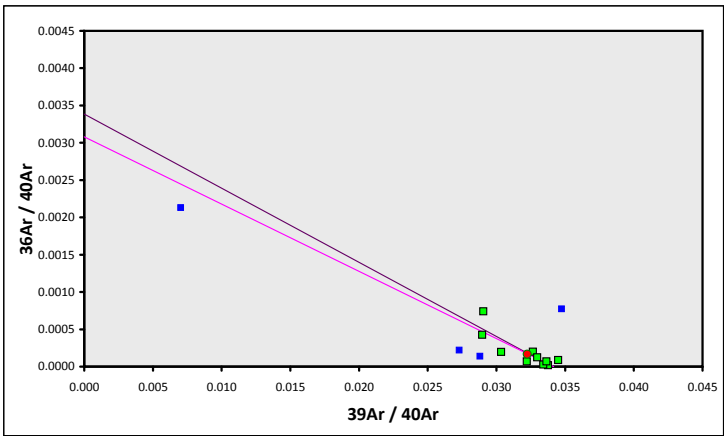

14D27825.one-pager.xls printed at 18-10-2016 (16:20)
ArArCALC v2.7.0 -- Beta Version

Supplemental Ages (Continued). $^{40}Ar/^{39}Ar$ age data for Tuvalu seamounts not included in Konrad et al. (submitted).

OSU Argon Geochronology Lab
CEOAS Oregon State University, Corvallis, USA

RR1310-D19-12 > Plagioclase > RURUTU (13-INT-08)
TUVALU > RURUTU HOTSPOT
14-OSU-02 (2A11-14) > Incremental Heating > Kevin Konrad

Information on Analysis and Constants Used in Calculations

Project = **RURUTU (13-INT-08)**
Sample = **RR1310-D19-12**
Material = **Plagioclase**
Location = **Rurutu Hotspot**
Region = **Tuvalu**
Analyst = **Kevin Konrad**
Irradiation = **14-OSU-02 (2A11-14)**
Position = **X: 0 | Y: 0 | Z/H: 15.5 mm**
FCT-NM Age = **28.201 ± 0.023 Ma**
FCT-NM Reference = **Kuiper et al. (2008)**
FCT-NM 40Ar/39Ar Ratio = **8.82973 ± 0.00839**
FCT-NM J-value = **0.00178005 ± 0.00000169**
Air Shot 40Ar/36Ar = **303.8280 ± 0.4527**
Air Shot MDF = **0.99313858 ± 0.00068156 (LIN)**
Experiment Type = **Incremental Heating**
Extraction Method = **Bulk Laser Heating**
Heating = **0 sec**
Isolation = **6.00 min**
Instrument = **ARGUS-VI-D**
Preferred Age = **Plateau Age**
Age Classification = **Eruption Age**
IGSN = Undefined
Rock Class = Undefined
Lithology = **Basalt**
Lat-Lon = Undefined - Undefined
Age Equations = **Min et al. (2000)**
Negative Intensities = **Allowed**
Collector Calibrations = **40Ar 36Ar**
Decay 40K = **5.530 ± 0.048 E-10 1/a**
Decay 39Ar = **2.940 ± 0.016 E-07 1/h**
Decay 37Ar = **8.230 ± 0.012 E-04 1/h**
Decay 36Cl = **2.257 ± 0.015 E-06 1/a**
Decay 40K(EC,β⁺) = **0.580 ± 0.009 E-10 1/a**
Decay 40K(β⁻) = **4.950 ± 0.043 E-10 1/a**
Atmospheric 40/36(a) = **295.50**
Atmospheric 38/36(a) = **0.1869**
Production 39/37(ca) = **0.0006756 ± 0.0000089**
Production 38/37(ca) = **0.0000718 ± 0.0000092**
Production 36/37(ca) = **0.0002663 ± 0.0000004**
Production 40/39(k) = **0.003823 ± 0.000102**
Production 38/39(k) = **0.012031 ± 0.000019**
Production 36/38(cl) = **262.80 ± 1.71**
Scaling Ratio K/Ca = **0.430**
Abundance Ratio 40K/K = **1.1700 ± 0.0100 E-04**
Atomic Weight K = **39.0983 ± 0.0001 g**

Results	40(a)/36(a) ± 2σ	40(r)/39(k) ± 2σ	Age ± 2σ (Ma)	MSWD	39Ar(k) (%,n)	K/Ca ± 2σ
Age Plateau		29.97061 ± 0.13036	**93.99 ± 0.43**	2.00	51.97	0.0474 ± 0.0023
Error Mean		± 0.43%	**± 0.46%**	2%	14	
			Full External Error ± 2.14	1.78	2σ Confidence Limit	
			Analytical Error ± 0.40	1.4154	Error Magnification	
Total Fusion Age		29.76231 ± 0.07804	**93.35 ± 0.29**		26	0.0469 ± 0.0011
		± 0.26%	**± 0.32%**			
			Full External Error ± 2.10			
			Analytical Error ± 0.24			
Normal Isochron	**282.36 ± 22.25**	30.14585 ± 0.19059	**94.52 ± 0.61**	2.96	51.97	
No Convergence	**± 7.88%**	± 0.63%	**± 0.64%**	0%	14	
			Full External Error ± 2.19	1.82	2σ Confidence Limit	
			Analytical Error ± 0.58	1.7200	Error Magnification	
Inverse Isochron	**293.72 ± 18.93**	29.98418 ± 0.16404	**94.03 ± 0.53**	2.18	51.97	
Error Chron	**± 6.44%**	± 0.55%	**± 0.56%**	1%	14	
			Full External Error ± 2.16	1.82	2σ Confidence Limit	
			Analytical Error ± 0.50	1.4749	Error Magnification	
				30%	Spreading Factor	

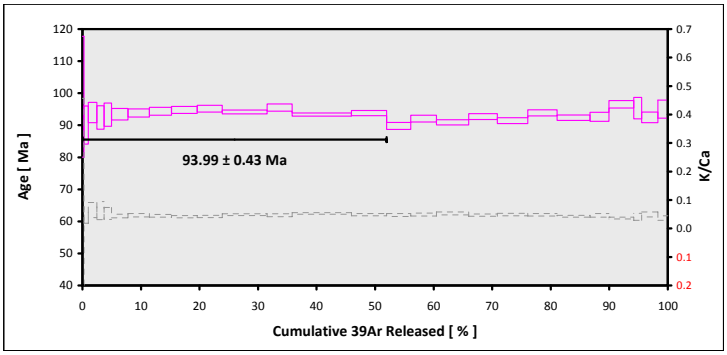

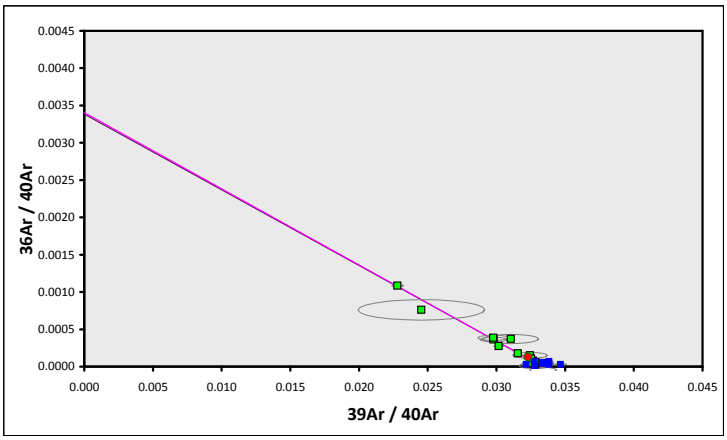

14D27789.one-pager.xls printed at 18-10-2016 (16:20)
ArArCALC v2.7.0 -- Beta Version

Supplemental Ages (Continued). $^{40}Ar/^{39}Ar$ age data for Tuvalu seamounts not included in Konrad et al. (submitted).

OSU Argon Geochronology Lab
CEOAS Oregon State University, Corvallis, USA

RR1310-D20-10 > Plagioclase > RURUTU (13-INT-08)
TUVALU > RURUTU HOTSPOT
14-OSU-02 (2A7-14) > Incremental Heating > Kevin Konrad

Information on Analysis and Constants Used in Calculations

Project = **RURUTU (13-INT-08)**
Sample = **RR1310-D20-10**
Material = **Plagioclase**
Location = **Rurutu Hotspot**
Region = **Tuvalu**
Analyst = **Kevin Konrad**
Irradiation = **14-OSU-02 (2A7-14)**
Position = **X: 0 | Y: 0 | Z/H: 10 mm**
FCT-NM Age = **28.201 ± 0.023 Ma**
FCT-NM Reference = **Kuiper et al. (2008)**
FCT-NM 40Ar/39Ar Ratio = **8.85259 ± 0.00841**
FCT-NM J-value = **0.00177546 ± 0.00000169**
Air Shot 40Ar/36Ar = **303.8830 ± 0.4163**
Air Shot MDF = **0.99309452 ± 0.00066635 (LIN)**
Experiment Type = **Incremental Heating**
Extraction Method = **Bulk Laser Heating**
Heating = **0 sec**
Isolation = **6.00 min**
Instrument = **ARGUS-VI-D**
Preferred Age = **Plateau Age**
Age Classification = **Eruption Age**
IGSN = Undefined
Rock Class = Undefined
Lithology = **Basalt**
Lat-Lon = Undefined - Undefined
Age Equations = **Min et al. (2000)**
Negative Intensities = **Allowed**
Collector Calibrations = **40Ar 36Ar**
Decay 40K = **5.530 ± 0.048 E-10 1/a**
Decay 39Ar = **2.940 ± 0.016 E-07 1/h**
Decay 37Ar = **8.230 ± 0.012 E-04 1/h**
Decay 36Cl = **2.257 ± 0.015 E-06 1/a**
Decay 40K(EC,β⁺) = **0.580 ± 0.009 E-10 1/a**
Decay 40K(β⁻) = **4.950 ± 0.043 E-10 1/a**
Atmospheric 40/36(a) = **295.50**
Atmospheric 38/36(a) = **0.1869**
Production 39/37(ca) = **0.0006756 ± 0.0000089**
Production 38/37(ca) = **0.0000718 ± 0.0000092**
Production 36/37(ca) = **0.0002663 ± 0.0000004**
Production 40/39(k) = **0.003823 ± 0.000102**
Production 38/39(k) = **0.012031 ± 0.000019**
Production 36/38(cl) = **262.80 ± 1.71**
Scaling Ratio K/Ca = **0.430**
Abundance Ratio 40K/K = **1.1700 ± 0.0100 E-04**
Atomic Weight K = **39.0983 ± 0.0001 g**

Results	40(a)/36(a) ± 2σ	40(r)/39(k) ± 2σ	Age ± 2σ (Ma)	MSWD	39Ar(k) (%,n)	K/Ca ± 2σ
Age Plateau Overestimated		30.07325 ± 0.02936 ± 0.10%	**94.06 ± 0.20 ± 0.21%**	0.16	48.06	0.064 ± 0.001
			Full External Error ± 2.11	98%	6	
			Analytical Error ± 0.09	2.26	2σ Confidence Limit	
				1.0000	Error Magnification	
Total Fusion Age		29.98936 ± 0.02431 ± 0.08%	**93.81 ± 0.19 ± 0.20%**		24	0.065 ± 0.001
			Full External Error ± 2.10			
			Analytical Error ± 0.07			
Normal Isochron Overestimated	**300.15 ± 30.41 ± 10.13%**	30.06853 ± 0.04992 ± 0.17%	**94.05 ± 0.23 ± 0.25%**	0.16	48.06	
			Full External Error ± 2.11	96%	6	
			Analytical Error ± 0.15	2.41	2σ Confidence Limit	
				1.0000	Error Magnification	
Inverse Isochron Overestimated	**302.36 ± 30.39 ± 10.05%**	30.06417 ± 0.04993 ± 0.17%	**94.04 ± 0.23 ± 0.25%**	0.15	48.06	
			Full External Error ± 2.11	96%	6	
			Analytical Error ± 0.15	2.41	2σ Confidence Limit	
				1.0000	Error Magnification	
				3%	Spreading Factor	

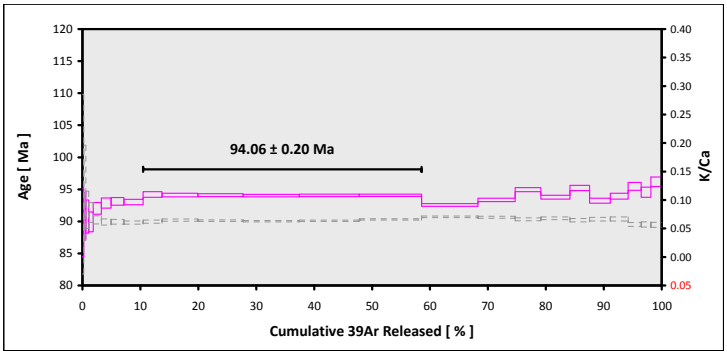

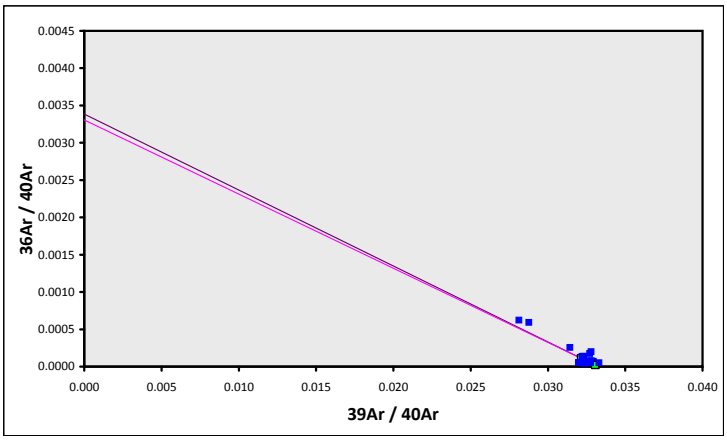

14D27268.one-pager.xls printed at 18-10-2016 (16:21)
ArArCALC v2.7.0 -- Beta Version

Supplemental Ages (Continued). $^{40}Ar/^{39}Ar$ age data for Tuvalu seamounts not included in Konrad et al. (submitted).

OSU Argon Geochronology Lab
CEOAS Oregon State University, Corvallis, USA

RR1310-D20-15 > Plagioclase > RURUTU (13-INT-08)
TUVALU > RURUTU HOTSPOT
14-OSU-02 (2A8-14) > Incremental Heating > Kevin Konrad

Information on Analysis and Constants Used in Calculations

Project = **RURUTU (13-INT-08)**
Sample = **RR1310-D20-15**
Material = **Plagioclase**
Location = **Rurutu Hotspot**
Region = **Tuvalu**
Analyst = **Kevin Konrad**
Irradiation = **14-OSU-02 (2A8-14)**
Position = **X: 0 | Y: 0 | Z/H: 11.5 mm**
FCT-NM Age = **28.201 ± 0.023 Ma**
FCT-NM Reference = **Kuiper et al. (2008)**
FCT-NM 40Ar/39Ar Ratio = **8.84520 ± 0.00840**
FCT-NM J-value = **0.00177694 ± 0.00000169**
Air Shot 40Ar/36Ar = **303.8790 ± 0.4163**
Air Shot MDF = **0.99309772 ± 0.00066636 (LIN)**
Experiment Type = **Incremental Heating**
Extraction Method = **Bulk Laser Heating**
Heating = **0 sec**
Isolation = **6.00 min**
Instrument = **ARGUS-VI-D**
Preferred Age = **Plateau Age**
Age Classification = **Eruption Age**
IGSN = Undefined
Rock Class = Undefined
Lithology = **Basalt**
Lat-Lon = Undefined - Undefined
Age Equations = **Min et al. (2000)**
Negative Intensities = **Allowed**
Collector Calibrations = **40Ar 36Ar**
Decay 40K = **5.530 ± 0.048 E-10 1/a**
Decay 39Ar = **2.940 ± 0.016 E-07 1/h**
Decay 37Ar = **8.230 ± 0.012 E-04 1/h**
Decay 36Cl = **2.257 ± 0.015 E-06 1/a**
Decay 40K(EC,β⁺) = **0.580 ± 0.009 E-10 1/a**
Decay 40K(β⁻) = **4.950 ± 0.043 E-10 1/a**
Atmospheric 40/36(a) = **295.50**
Atmospheric 38/36(a) = **0.1869**
Production 39/37(ca) = **0.0006756 ± 0.0000089**
Production 38/37(ca) = **0.0000718 ± 0.0000092**
Production 36/37(ca) = **0.0002663 ± 0.0000004**
Production 40/39(k) = **0.003823 ± 0.000102**
Production 38/39(k) = **0.012031 ± 0.000019**
Production 36/38(cl) = **262.80 ± 1.71**
Scaling Ratio K/Ca = **0.430**
Abundance Ratio 40K/K = **1.1700 ± 0.0100 E-04**
Atomic Weight K = **39.0983 ± 0.0001 g**

Results	40(a)/36(a) ± 2σ	40(r)/39(k) ± 2σ	Age ± 2σ (Ma)	MSWD	39Ar(k) (%,n)	K/Ca ± 2σ
Age Plateau		30.35500 ± 0.02533 ± 0.08%	**95.00 ± 0.19 ± 0.20%**	1.10	77.39	0.079 ± 0.001
			Full External Error ± 2.13	35%	13	
			Analytical Error ± 0.08	1.82	2σ Confidence Limit	
				1.0486	Error Magnification	
Total Fusion Age		30.35164 ± 0.02405 ± 0.08%	**94.99 ± 0.19 ± 0.20%**		24	0.080 ± 0.001
			Full External Error ± 2.13			
			Analytical Error ± 0.07			
Normal Isochron	**285.33 ± 241.20 ± 84.53%**	30.35849 ± 0.16211 ± 0.53%	**95.01 ± 0.52 ± 0.55%**	1.21	77.39	
			Full External Error ± 2.18	27%	13	
			Analytical Error ± 0.49	1.85	2σ Confidence Limit	
				1.1014	Error Magnification	
Inverse Isochron	**206.03 ± 113.09 ± 54.89%**	30.41431 ± 0.15592 ± 0.51%	**95.18 ± 0.51 ± 0.53%**	1.15	77.39	
Clustered Points			Full External Error ± 2.18	32%	13	
			Analytical Error ± 0.48	1.85	2σ Confidence Limit	
				1.0708	Error Magnification	
				1%	Spreading Factor	

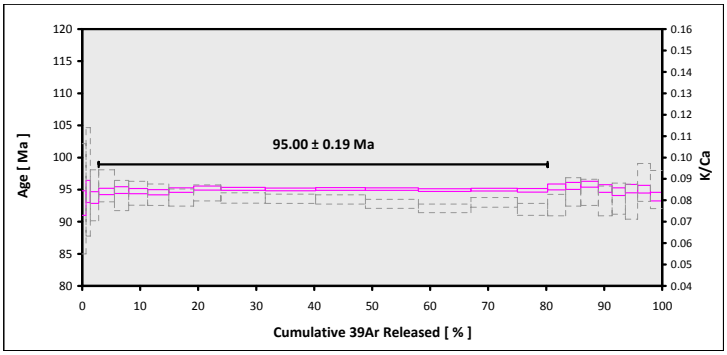

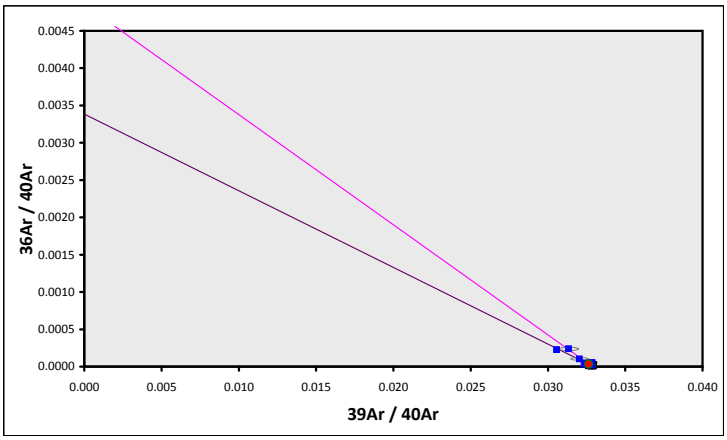

14D27334.one-pager.xls printed at 18-10-2016 (16:21)
ArArCALC v2.7.0 -- Beta Version

Supplemental Ages (Continued). $^{40}Ar/^{39}Ar$ age data for Tuvalu seamounts not included in Konrad et al. (submitted).

OSU Argon Geochronology Lab
CEOAS Oregon State University, Corvallis, USA

RR1310-D21-03 > Groundmass > KONRAD (13-INT-08)
TUVALU > RURUTU HOTSPOT
15-OSU-04 (4A19-15) > Incremental Heating > Kevin Konrad

Information on Analysis and Constants Used in Calculations

Project = **KONRAD (13-INT-08)**
Sample = **RR1310-D21-03**
Material = **Groundmass**
Location = **Rurutu Hotspot**
Region = **Tuvalu**
Analyst = **Kevin Konrad**
Irradiation = **15-OSU-04 (4A19-15)**
Position = **X: 0 | Y: 0 | Z/H: 26.87 mm**
FCT-NM Age = **28.201 ± 0.023 Ma**
FCT-NM Reference = **Kuiper et al (2008)**
FCT-NM 40Ar/39Ar Ratio = **8.93418 ± 0.01519**
FCT-NM J-value = **0.00175924 ± 0.00000299**
Air Shot 40Ar/36Ar = **304.4600 ± 0.5541**
Air Shot MDF = **0.99263320 ± 0.00072600 (LIN)**
Experiment Type = **Incremental Heating**
Extraction Method = **Bulk Laser Heating**
Heating = **77 sec**
Isolation = **3.00 min**
Instrument = **ARGUS-VI-D**
Preferred Age = **Plateau Age**
Age Classification = **Unknown**
IGSN = Undefined
Rock Class = Undefined
Lithology = **Basalt**
Lat-Lon = Undefined - Undefined
Age Equations = **Min et al. (2000)**
Negative Intensities = **Allowed**
Collector Calibrations = **36Ar**
Decay 40K = **5.530 ± 0.048 E-10 1/a**
Decay 39Ar = **2.940 ± 0.016 E-07 1/h**
Decay 37Ar = **8.230 ± 0.012 E-04 1/h**
Decay 36Cl = **2.257 ± 0.015 E-06 1/a**
Decay 40K(EC,β⁺) = **0.580 ± 0.009 E-10 1/a**
Decay 40K(β⁻) = **4.950 ± 0.043 E-10 1/a**
Atmospheric 40/36(a) = **295.50**
Atmospheric 38/36(a) = **0.1869**
Production 39/37(ca) = **0.0006756 ± 0.0000089**
Production 38/37(ca) = **0.0000718 ± 0.0000092**
Production 36/37(ca) = **0.0002663 ± 0.0000004**
Production 40/39(k) = **0.003823 ± 0.000102**
Production 38/39(k) = **0.012031 ± 0.000019**
Production 36/38(cl) = **262.80 ± 1.71**
Scaling Ratio K/Ca = **0.430**
Abundance Ratio 40K/K = **1.1700 ± 0.0100 E-04**
Atomic Weight K = **39.0983 ± 0.0001 g**

Results	40(a)/36(a) ± 2σ	40(r)/39(k) ± 2σ	Age ± 2σ (Ma)	MSWD	39Ar(k) (%,n)	K/Ca ± 2σ
Age Plateau		3.28630 ± 0.01107 ± 0.34%	**10.42 ± 0.05 ± 0.48%**	1.49	42.13	0.0063 ± 0.0070
		Full External Error ± 0.24		20%	5	
		Analytical Error ± 0.04		2.41	2σ Confidence Limit	
				1.2197	Error Magnification	
Total Fusion Age		4.94229 ± 0.00916 ± 0.19%	**15.65 ± 0.06 ± 0.39%**		29	0.0546 ± 0.0003
		Full External Error ± 0.36				
		Analytical Error ± 0.03				
Normal Isochron	**335.24 ± 125.23 ± 37.36%**	3.26663 ± 0.05596 ± 1.71%	**10.36 ± 0.18 ± 1.74%**	2.16	42.13	
No Convergence		Full External Error ± 0.30		9%	5	
		Analytical Error ± 0.18		2.63	2σ Confidence Limit	
				1.4710	Error Magnification	
Inverse Isochron	**325.26 ± 113.62 ± 34.93%**	3.27379 ± 0.04823 ± 1.47%	**10.38 ± 0.16 ± 1.51%**	1.79	42.13	
		Full External Error ± 0.28		15%	5	
		Analytical Error ± 0.15		2.63	2σ Confidence Limit	
				1.3397	Error Magnification	
				14%	Spreading Factor	

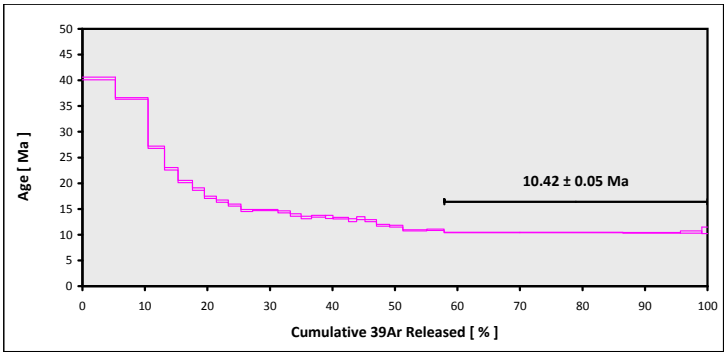

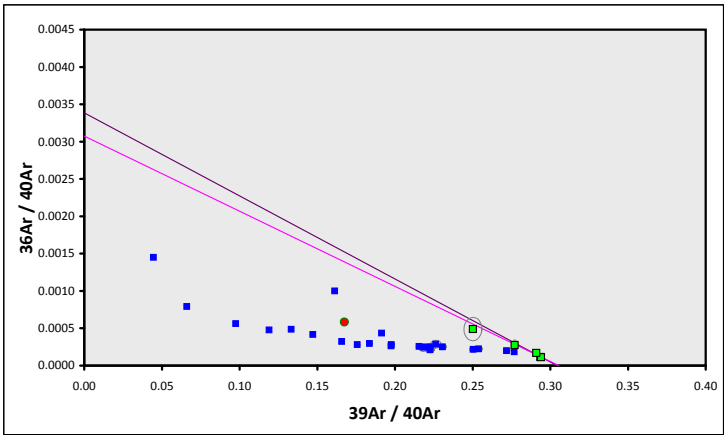

16D05772.one-pager.xls printed at 18-10-2016 (16:41)
ArArCALC v2.7.0 -- Beta Version

Supplemental Ages (Continued). $^{40}Ar/^{39}Ar$ age data for Tuvalu seamounts not included in Konrad et al. (submitted).

OSU Argon Geochronology Lab
CEOAS Oregon State University, Corvallis, USA

RR1310-D21-19 > Groundmass > RURUTU (13-INT-08)
TUVALU > RURUTU HOTSPOT
14-OSU-02 (2A56-14) > Incremental Heating > Kevin Konrad

Information on Analysis and Constants Used in Calculations

Project = **RURUTU (13-INT-08)**
Sample = **RR1310-D21-19**
Material = **Groundmass**
Location = **Rurutu Hotspot**
Region = **Tuvalu**
Analyst = **Kevin Konrad**
Irradiation = **14-OSU-02 (2A56-14)**
Position = **X: 0 | Y: 0 | Z/H: 66.3 mm**
FCT-NM Age = **28.201 ± 0.023 Ma**
FCT-NM Reference = **Kuiper et al. 2008**
FCT-NM 40Ar/39Ar Ratio = **9.16993 ± 0.00844**
FCT-NM J-value = **0.00171401 ± 0.00000158**
Air Shot 40Ar/36Ar = **304.0670 ± 0.3922**
Air Shot MDF = **0.99294722 ± 0.00065642 (LIN)**
Experiment Type = **Incremental Heating**
Extraction Method = **Bulk Laser Heating**
Heating = **77 sec**
Isolation = **10.00 min**
Instrument = **ARGUS-VI-D**
Preferred Age = **Plateau Age**
Age Classification = **Eruption Age**
IGSN = Undefined
Rock Class = Undefined
Lithology = **Basalt**
Lat-Lon = Undefined - Undefined
Age Equations = **Min et al. (2000)**
Negative Intensities = **Allowed**
Collector Calibrations = **40Ar 36Ar**
Decay 40K = **5.530 ± 0.048 E-10 1/a**
Decay 39Ar = **2.940 ± 0.016 E-07 1/h**
Decay 37Ar = **8.230 ± 0.012 E-04 1/h**
Decay 36Cl = **2.257 ± 0.015 E-06 1/a**
Decay 40K(EC,β⁺) = **0.580 ± 0.009 E-10 1/a**
Decay 40K(β⁻) = **4.950 ± 0.043 E-10 1/a**
Atmospheric 40/36(a) = **295.50**
Atmospheric 38/36(a) = **0.1869**
Production 39/37(ca) = **0.0006756 ± 0.0000089**
Production 38/37(ca) = **0.0000718 ± 0.0000092**
Production 36/37(ca) = **0.0002663 ± 0.0000004**
Production 40/39(k) = **0.003823 ± 0.000102**
Production 38/39(k) = **0.012031 ± 0.000019**
Production 36/38(cl) = **262.80 ± 1.71**
Scaling Ratio K/Ca = **0.430**
Abundance Ratio 40K/K = **1.1700 ± 0.0100 E-04**
Atomic Weight K = **39.0983 ± 0.0001 g**

Results	40(a)/36(a) ± 2σ	40(r)/39(k) ± 2σ	Age ± 2σ (Ma)	MSWD	39Ar(k) (%,n)	K/Ca ± 2σ
Age Plateau		2.79372 ± 0.05111 ± 1.83%	**8.64 ± 0.16 ± 1.83%**	0.46	81.36	0.0315 ± 0.0023
			Full External Error ± 0.25	99%	27	
			Analytical Error ± 0.16	1.55	2σ Confidence Limit	
				1.0000	Error Magnification	
Total Fusion Age		2.76193 ± 0.05589 ± 2.02%	**8.54 ± 0.17 ± 2.03%**		36	0.0235 ± 0.0002
			Full External Error ± 0.26			
			Analytical Error ± 0.17			
Normal Isochron	**298.14 ± 22.60 ± 7.58%**	2.76670 ± 0.08810 ± 3.18%	**8.56 ± 0.27 ± 3.18%**	0.49	81.36	
			Full External Error ± 0.33	98%	27	
			Analytical Error ± 0.27	1.57	2σ Confidence Limit	
				1.0000	Error Magnification	
Inverse Isochron	**300.14 ± 23.02 ± 7.67%**	2.78010 ± 0.08779 ± 3.16%	**8.60 ± 0.27 ± 3.16%**	0.47	81.36	
			Full External Error ± 0.33	99%	27	
			Analytical Error ± 0.27	1.57	2σ Confidence Limit	
				1.0000	Error Magnification	
				48%	Spreading Factor	

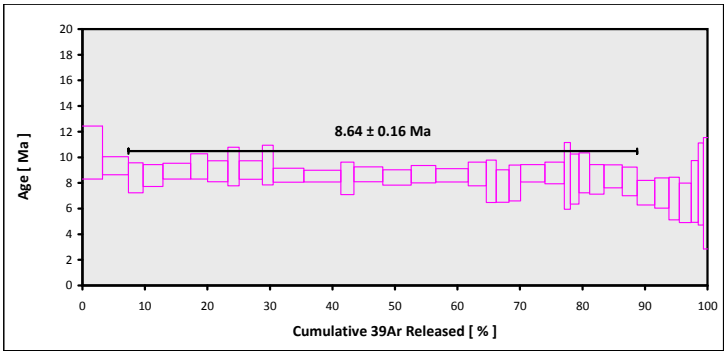

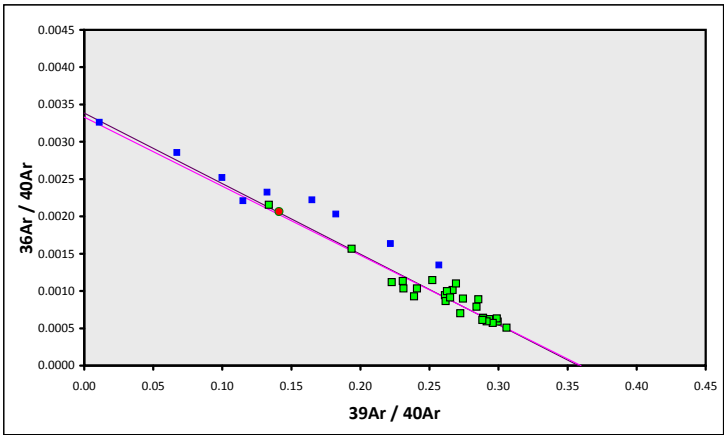

14D23685.one-pager.xls printed at 18-10-2016 (16:21)
ArArCALC v2.7.0 -- Beta Version

Supplemental Ages (Continued). $^{40}Ar/^{39}Ar$ age data for Tuvalu seamounts not included in Konrad et al. (submitted).

OSU Argon Geochronology Lab
CEOAS Oregon State University, Corvallis, USA

RR1310-D21-19 > Groundmass > RURUTU (13-INT-08)
TUVALU > RURUTU HOTSPOT
14-OSU-02 (2A56-14) > Incremental Heating > Kevin Konrad

Information on Analysis and Constants Used in Calculations

Project = **RURUTU (13-INT-08)**
Sample = **RR1310-D21-19**
Material = **Groundmass**
Location = **Rurutu Hotspot**
Region = **Tuvalu**
Analyst = **Kevin Konrad**
Irradiation = **14-OSU-02 (2A56-14)**
Position = **X: 0 | Y: 0 | Z/H: 66.3 mm**
FCT-NM Age = **28.201 ± 0.023 Ma**
FCT-NM Reference = **Kuiper et al. 2008**
FCT-NM 40Ar/39Ar Ratio = **9.16993 ± 0.00844**
FCT-NM J-value = **0.00171401 ± 0.00000158**
Air Shot 40Ar/36Ar = **304.0210 ± 0.3952**
Air Shot MDF = **0.99298403 ± 0.00065769 (LIN)**
Experiment Type = **Incremental Heating**
Extraction Method = **Bulk Laser Heating**
Heating = **77 sec**
Isolation = **10.00 min**
Instrument = **ARGUS-VI-D**
Preferred Age = **Plateau Age**
Age Classification = **Eruption Age**
IGSN = Undefined
Rock Class = Undefined
Lithology = **Basalt**
Lat-Lon = Undefined - Undefined
Age Equations = **Min et al. (2000)**
Negative Intensities = **Allowed**
Collector Calibrations = **40Ar 36Ar**
Decay 40K = **5.530 ± 0.048 E-10 1/a**
Decay 39Ar = **2.940 ± 0.016 E-07 1/h**
Decay 37Ar = **8.230 ± 0.012 E-04 1/h**
Decay 36Cl = **2.257 ± 0.015 E-06 1/a**
Decay 40K(EC,β⁺) = **0.580 ± 0.009 E-10 1/a**
Decay 40K(β⁻) = **4.950 ± 0.043 E-10 1/a**
Atmospheric 40/36(a) = **295.50**
Atmospheric 38/36(a) = **0.1869**
Production 39/37(ca) = **0.0006756 ± 0.0000089**
Production 38/37(ca) = **0.0000718 ± 0.0000092**
Production 36/37(ca) = **0.0002663 ± 0.0000004**
Production 40/39(k) = **0.003823 ± 0.000102**
Production 38/39(k) = **0.012031 ± 0.000019**
Production 36/38(cl) = **262.80 ± 1.71**
Scaling Ratio K/Ca = **0.430**
Abundance Ratio 40K/K = **1.1700 ± 0.0100 E-04**
Atomic Weight K = **39.0983 ± 0.0001 g**

Results	40(a)/36(a) ± 2σ	40(r)/39(k) ± 2σ	Age ± 2σ (Ma)	MSWD	39Ar(k) (%,n)	K/Ca ± 2σ
Age Plateau		2.84847 ± 0.03206 (± 1.13%)	**8.81 ± 0.10 (± 1.14%)**	0.54	85.97	0.0378 ± 0.0021
			Full External Error ± 0.22	98%	29	
			Analytical Error ± 0.10	1.53	2σ Confidence Limit	
				1.0000	Error Magnification	
Total Fusion Age		2.74551 ± 0.04085 (± 1.49%)	**8.49 ± 0.13 (± 1.50%)**		36	0.0267 ± 0.0002
			Full External Error ± 0.23			
			Analytical Error ± 0.13			
Normal Isochron	**293.95 ± 3.47 (± 1.18%)**	2.86273 ± 0.05073 (± 1.77%)	**8.85 ± 0.16 (± 1.78%)**	0.56	85.97	
			Full External Error ± 0.25	97%	29	
			Analytical Error ± 0.16	1.54	2σ Confidence Limit	
				1.0000	Error Magnification	
Inverse Isochron	**293.82 ± 3.49 (± 1.19%)**	2.86811 ± 0.05096 (± 1.78%)	**8.87 ± 0.16 (± 1.78%)**	0.52	85.97	
			Full External Error ± 0.25	98%	29	
			Analytical Error ± 0.16	1.54	2σ Confidence Limit	
				1.0000	Error Magnification	
				66%	Spreading Factor	

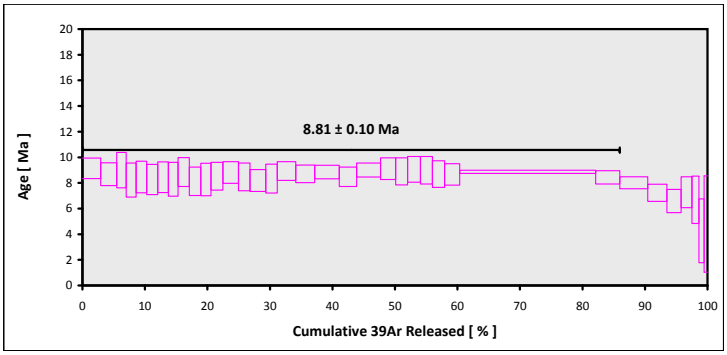

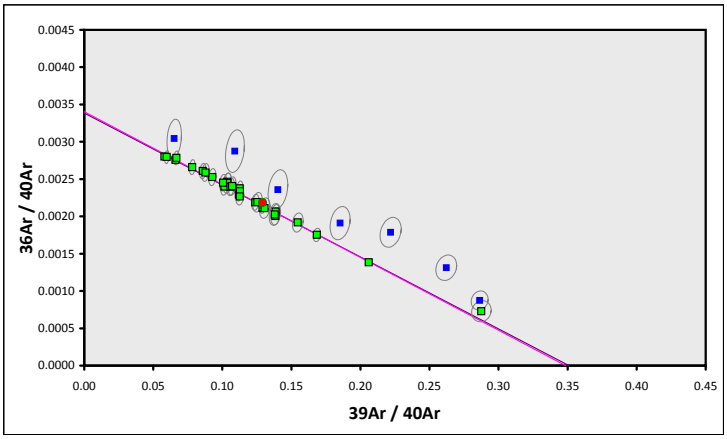

14D23486.one-pager.xls printed at 18-10-2016 (16:21)
ArArCALC v2.7.0 -- Beta Version

Supplemental Ages (Continued). $^{40}Ar/^{39}Ar$ age data for Tuvalu seamounts not included in Konrad et al. (submitted).

OSU Argon Geochronology Lab
CEOAS Oregon State University, Corvallis, USA

RR1310-D26-01 > Groundmass > RURUTU (13-INT-08)
SAMOA > RURUTU HOTSPOT
14-OSU-02 (2A26-14) > Incremental Heating > Kevin Konrad

Information on Analysis and Constants Used in Calculations

Project = **RURUTU (13-INT-08)**
Sample = **RR1310-D26-01**
Material = **Groundmass**
Location = **Rurutu Hotspot**
Region = **Samoa**
Analyst = **Kevin Konrad**
Irradiation = **14-OSU-02 (2A26-14)**
Position = **X: 0 | Y: 0 | Z/H: 30.2 mm**
FCT-NM Age = **28.201 ± 0.023 Ma**
FCT-NM Reference = **Kuiper et al. (2008)**
FCT-NM 40Ar/39Ar Ratio = **8.82587 ± 0.00838**
FCT-NM J-value = **0.00178083 ± 0.00000169**
Air Shot 40Ar/36Ar = **304.0270 ± 0.4074**
Air Shot MDF = **0.99297922 ± 0.00066241 (LIN)**
Experiment Type = **Incremental Heating**
Extraction Method = **Bulk Laser Heating**
Heating = **77 sec**
Isolation = **10.00 min**
Instrument = **ARGUS-VI-D**
Preferred Age = Undefined
Age Classification = Undefined
IGSN = Undefined
Rock Class = Undefined
Lithology = **Basalt**
Lat-Lon = Undefined - Undefined
Age Equations = **Min et al. (2000)**
Negative Intensities = **Allowed**
Collector Calibrations = **40Ar 36Ar**
Decay 40K = **5.530 ± 0.048 E-10 1/a**
Decay 39Ar = **2.940 ± 0.016 E-07 1/h**
Decay 37Ar = **8.230 ± 0.012 E-04 1/h**
Decay 36Cl = **2.257 ± 0.015 E-06 1/a**
Decay 40K(EC,β⁺) = **0.580 ± 0.009 E-10 1/a**
Decay 40K(β⁻) = **4.950 ± 0.043 E-10 1/a**
Atmospheric 40/36(a) = **295.50**
Atmospheric 38/36(a) = **0.1869**
Production 39/37(ca) = **0.0006756 ± 0.0000089**
Production 38/37(ca) = **0.0000718 ± 0.0000092**
Production 36/37(ca) = **0.0002663 ± 0.0000004**
Production 40/39(k) = **0.003823 ± 0.000102**
Production 38/39(k) = **0.012031 ± 0.000019**
Production 36/38(cl) = **262.80 ± 1.71**
Scaling Ratio K/Ca = **0.430**
Abundance Ratio 40K/K = **1.1700 ± 0.0100 E-04**
Atomic Weight K = **39.0983 ± 0.0001 g**

Results	40(a)/36(a) ± 2σ	40(r)/39(k) ± 2σ	Age ± 2σ (Ma)	MSWD	39Ar(k) (%,n)	K/Ca ± 2σ
Age Plateau Cannot Calculate						
Total Fusion Age		4.04917 ± 0.00568 ± 0.14%	**12.99 ± 0.03 ± 0.24%** Full External Error ± 0.29 Analytical Error ± 0.02		36	0.153 ± 0.002
Normal Isochron Cannot Calculate						
Inverse Isochron Cannot Calculate						

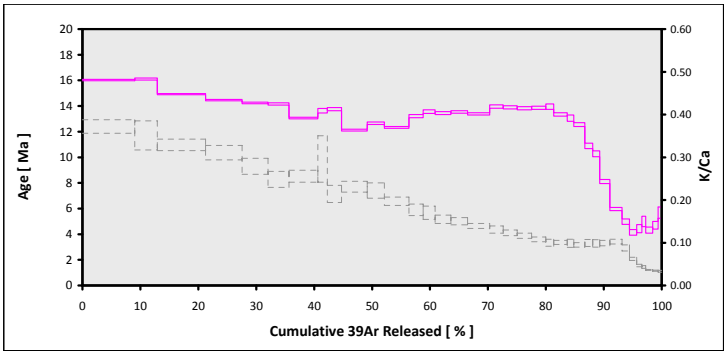

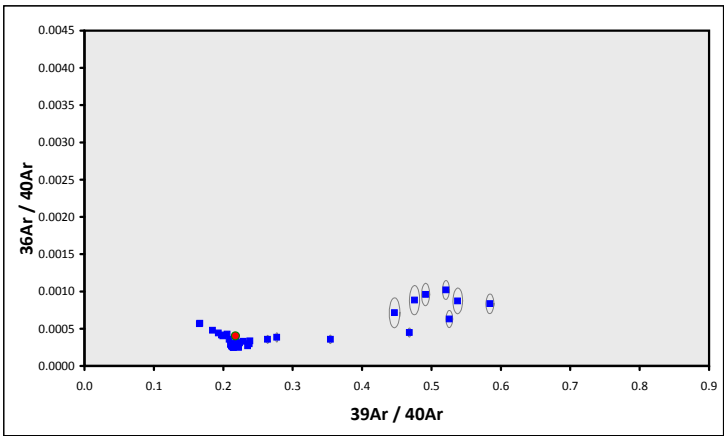

14D26196.one-pager.xls printed at 18-10-2016 (16:22)
ArArCALC v2.7.0 -- Beta Version

Supplemental Ages (Continued). $^{40}Ar/^{39}Ar$ age data for Tuvalu seamounts not included in Konrad et al. (submitted).

OSU Argon Geochronology Lab
CEOAS Oregon State University, Corvallis, USA

RR1310-D26-03 > Groundmass > RURUTU (13-INT-08)
SAMOA > RURUTU HOTSPOT
14-OSU-02 (2A55-14) > Incremental Heating > Kevin Konrad

Information on Analysis and Constants Used in Calculations

Project = **RURUTU (13-INT-08)**
Sample = **RR1310-D26-03**
Material = **Groundmass**
Location = **Rurutu Hotspot**
Region = **Samoa**
Analyst = **Kevin Konrad**
Irradiation = **14-OSU-02 (2A55-14)**
Position = **X: 0 | Y: 0 | Z/H: 65.1 mm**
FCT-NM Age = **28.201 ± 0.023 Ma**
FCT-NM Reference = **Kuiper et al. (2008)**
FCT-NM 40Ar/39Ar Ratio = **9.15042 ± 0.00842**
FCT-NM J-value = **0.00171767 ± 0.00000158**
Air Shot 40Ar/36Ar = **303.9340 ± 0.4103**
Air Shot MDF = **0.99305367 ± 0.00066382 (LIN)**
Experiment Type = **Incremental Heating**
Extraction Method = **Bulk Laser Heating**
Heating = **77 sec**
Isolation = **10.00 min**
Instrument = **ARGUS-VI-D**
Preferred Age = Undefined
Age Classification = Undefined
IGSN = Undefined
Rock Class = Undefined
Lithology = **Basalt**
Lat-Lon = Undefined - Undefined
Age Equations = **Min et al. (2000)**
Negative Intensities = **Allowed**
Collector Calibrations = **40Ar 36Ar**
Decay 40K = **5.530 ± 0.048 E-10 1/a**
Decay 39Ar = **2.940 ± 0.016 E-07 1/h**
Decay 37Ar = **8.230 ± 0.012 E-04 1/h**
Decay 36Cl = **2.257 ± 0.015 E-06 1/a**
Decay 40K(EC,β⁺) = **0.580 ± 0.009 E-10 1/a**
Decay 40K(β⁻) = **4.950 ± 0.043 E-10 1/a**
Atmospheric 40/36(a) = **295.50**
Atmospheric 38/36(a) = **0.1869**
Production 39/37(ca) = **0.0006756 ± 0.0000089**
Production 38/37(ca) = **0.0000718 ± 0.0000092**
Production 36/37(ca) = **0.0002663 ± 0.0000004**
Production 40/39(k) = **0.003823 ± 0.000102**
Production 38/39(k) = **0.012031 ± 0.000019**
Production 36/38(cl) = **262.80 ± 1.71**
Scaling Ratio K/Ca = **0.430**
Abundance Ratio 40K/K = **1.1700 ± 0.0100 E-04**
Atomic Weight K = **39.0983 ± 0.0001 g**

Results	40(a)/36(a) ± 2σ	40(r)/39(k) ± 2σ	Age ± 2σ (Ma)	MSWD	39Ar(k) (%,n)	K/Ca ± 2σ
Age Plateau Cannot Calculate						
Total Fusion Age		4.85346 ± 0.00505 ± 0.10%	**15.01 ± 0.03 ± 0.21%** Full External Error ± 0.34 Analytical Error ± 0.02		34	0.177 ± 0.002
Normal Isochron Cannot Calculate						
Inverse Isochron Cannot Calculate						

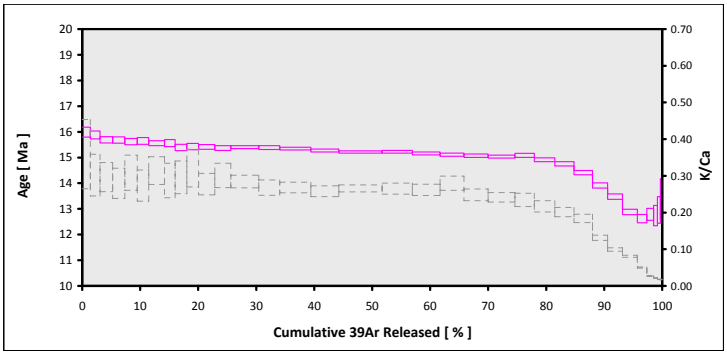

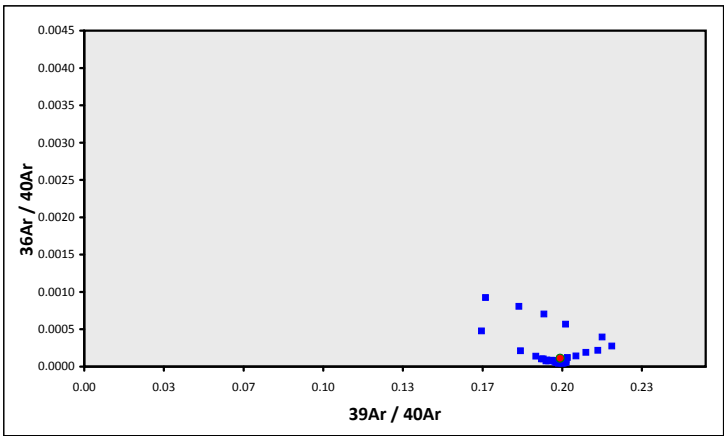

14D26843.one-pager.xls printed at 18-10-2016 (16:22)
ArArCALC v2.7.0 -- Beta Version

Supplemental Ages (Continued). $^{40}Ar/^{39}Ar$ age data for Tuvalu seamounts not included in Konrad et al. (submitted).

OSU Argon Geochronology Lab
CEOAS Oregon State University, Corvallis, USA

RR1310-D27-31 > Plagioclase > RURUTU (13-INT-08)
SAMOA > RURUTU HOTSPOT
14-OSU-02 (2A18-14) > Incremental Heating > Kevin Konrad

Information on Analysis and Constants Used in Calculations

Project = **RURUTU (13-INT-08)**
Sample = **RR1310-D27-31**
Material = **Plagioclase**
Location = **Rurutu Hotspot**
Region = **Samoa**
Analyst = **Kevin Konrad**
Irradiation = **14-OSU-02 (2A18-14)**
Position = **X: 0 | Y: 0 | Z/H: 23 mm**
FCT-NM Age = **28.201 ± 0.023 Ma**
FCT-NM Reference = **Kuiper et al. (2008)**
FCT-NM 40Ar/39Ar Ratio = **8.81735 ± 0.00838**
FCT-NM J-value = **0.00178255 ± 0.00000169**
Air Shot 40Ar/36Ar = **303.9990 ± 0.4165**
Air Shot MDF = **0.99300163 ± 0.00066610 (LIN)**
Experiment Type = **Incremental Heating**
Extraction Method = **Bulk Laser Heating**
Heating = **77 sec**
Isolation = **6.00 min**
Instrument = **ARGUS-VI-D**
Preferred Age = **Plateau Age**
Age Classification = **Eruption Age**
IGSN = Undefined
Rock Class = Undefined
Lithology = **Basalt**
Lat-Lon = Undefined - Undefined
Age Equations = **Min et al. (2000)**
Negative Intensities = **Allowed**
Collector Calibrations = **40Ar 36Ar**
Decay 40K = **5.530 ± 0.048 E-10 1/a**
Decay 39Ar = **2.940 ± 0.016 E-07 1/h**
Decay 37Ar = **8.230 ± 0.012 E-04 1/h**
Decay 36Cl = **2.257 ± 0.015 E-06 1/a**
Decay 40K(EC,β⁺) = **0.580 ± 0.009 E-10 1/a**
Decay 40K(β⁻) = **4.950 ± 0.043 E-10 1/a**
Atmospheric 40/36(a) = **295.50**
Atmospheric 38/36(a) = **0.1869**
Production 39/37(ca) = **0.0006756 ± 0.0000089**
Production 38/37(ca) = **0.0000718 ± 0.0000092**
Production 36/37(ca) = **0.0002663 ± 0.0000004**
Production 40/39(k) = **0.003823 ± 0.000102**
Production 38/39(k) = **0.012031 ± 0.000019**
Production 36/38(cl) = **262.80 ± 1.71**
Scaling Ratio K/Ca = **0.430**
Abundance Ratio 40K/K = **1.1700 ± 0.0100 E-04**
Atomic Weight K = **39.0983 ± 0.0001 g**

Results	40(a)/36(a) ± 2σ	40(r)/39(k) ± 2σ	Age ± 2σ (Ma)	MSWD	39Ar(k) (%,n)	K/Ca ± 2σ
Age Plateau		4.59666 ± 0.03591 (± 0.78%)	**14.76 ± 0.12 (± 0.80%)**	1.54	33.98	0.0204 ± 0.0015
		Full External Error ± 0.35		16%	7	
		Analytical Error ± 0.11		2.15	2σ Confidence Limit	
				1.2416	Error Magnification	
Total Fusion Age		4.97305 ± 0.02428 (± 0.49%)	**15.96 ± 0.08 (± 0.52%)**		24	0.0303 ± 0.0002
		Full External Error ± 0.37				
		Analytical Error ± 0.08				
Normal Isochron	**287.14 ± 5.95 (± 2.07%)**	4.68937 ± 0.07200 (± 1.54%)	**15.05 ± 0.23 (± 1.54%)**	0.34	33.98	
		Full External Error ± 0.41		89%	7	
		Analytical Error ± 0.23		2.26	2σ Confidence Limit	
				1.0000	Error Magnification	
Inverse Isochron	**287.12 ± 5.95 (± 2.07%)**	4.68990 ± 0.07193 (± 1.53%)	**15.05 ± 0.23 (± 1.54%)**	0.33	33.98	
		Full External Error ± 0.41		89%	7	
		Analytical Error ± 0.23		2.26	2σ Confidence Limit	
				1.0000	Error Magnification	
				27%	Spreading Factor	

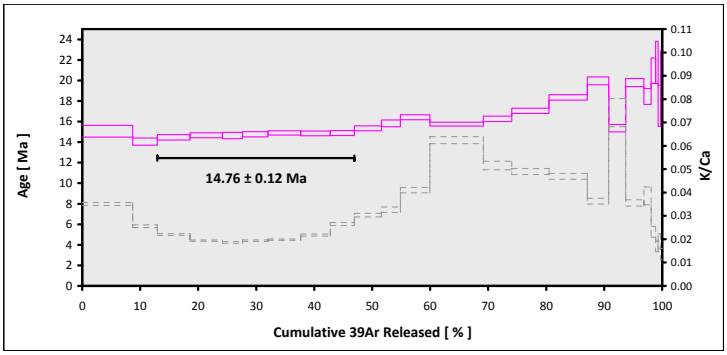

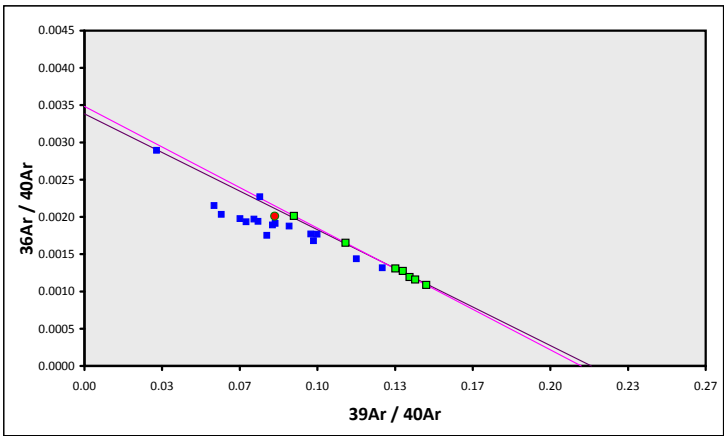

14D26361.one-pager.xls printed at 18-10-2016 (16:22)
ArArCALC v2.7.0 -- Beta Version

Supplemental Ages (Continued). $^{40}Ar/^{39}Ar$ age data for Tuvalu seamounts not included in Konrad et al. (submitted).

OSU Argon Geochronology Lab
CEOAS Oregon State University, Corvallis, USA

RR1310-D27-31 > Groundmass > RURUTU (13-INT-08)
SAMOA > RURUTU HOTSPOT
14-OSU-02 (2A31-14) > Incremental Heating > Kevin Konrad

Information on Analysis and Constants Used in Calculations

Project = **RURUTU (13-INT-08)**
Sample = **RR1310-D27-31**
Material = **Groundmass**
Location = **Rurutu Hotspot**
Region = **Samoa**
Analyst = **Kevin Konrad**
Irradiation = **14-OSU-02 (2A31-14)**
Position = **X: 0 | Y: 0 | Z/H: 35.7 mm**
FCT-NM Age = **28.201 ± 0.023 Ma**
FCT-NM Reference = **Kuiper et al. (2008)**
FCT-NM 40Ar/39Ar Ratio = **8.84584 ± 0.00840**
FCT-NM J-value = **0.00177681 ± 0.00000169**
Air Shot 40Ar/36Ar = **304.0070 ± 0.3952**
Air Shot MDF = **0.99299523 ± 0.00065772 (LIN)**
Experiment Type = **Incremental Heating**
Extraction Method = **Bulk Laser Heating**
Heating = **77 sec**
Isolation = **10.00 min**
Instrument = **ARGUS-VI-D**
Preferred Age = **Plateau Age**
Age Classification = **Eruption Age**
IGSN = Undefined
Rock Class = Undefined
Lithology = **Basalt**
Lat-Lon = Undefined - Undefined
Age Equations = **Min et al. (2000)**
Negative Intensities = **Allowed**
Collector Calibrations = **40Ar 36Ar**
Decay 40K = **5.530 ± 0.048 E-10 1/a**
Decay 39Ar = **2.940 ± 0.016 E-07 1/h**
Decay 37Ar = **8.230 ± 0.012 E-04 1/h**
Decay 36Cl = **2.257 ± 0.015 E-06 1/a**
Decay 40K(EC,β⁺) = **0.580 ± 0.009 E-10 1/a**
Decay 40K(β⁻) = **4.950 ± 0.043 E-10 1/a**
Atmospheric 40/36(a) = **295.50**
Atmospheric 38/36(a) = **0.1869**
Production 39/37(ca) = **0.0006756 ± 0.0000089**
Production 38/37(ca) = **0.0000718 ± 0.0000092**
Production 36/37(ca) = **0.0002663 ± 0.0000004**
Production 40/39(k) = **0.003823 ± 0.000102**
Production 38/39(k) = **0.012031 ± 0.000019**
Production 36/38(cl) = **262.80 ± 1.71**
Scaling Ratio K/Ca = **0.430**
Abundance Ratio 40K/K = **1.1700 ± 0.0100 E-04**
Atomic Weight K = **39.0983 ± 0.0001 g**

Results	40(a)/36(a) ± 2σ	40(r)/39(k) ± 2σ	Age ± 2σ (Ma)	MSWD	39Ar(k) (%,n)	K/Ca ± 2σ
Age Plateau		4.20364 ± 0.01517 (± 0.36%)	**13.46 ± 0.05 (± 0.41%)**	0.65	56.34	0.211 ± 0.011
		Full External Error ± 0.31		72%	8	
		Analytical Error ± 0.05		2.07	2σ Confidence Limit	
				1.0000	Error Magnification	
Total Fusion Age		4.22648 ± 0.01372 (± 0.32%)	**13.53 ± 0.05 (± 0.37%)**		36	0.185 ± 0.002
		Full External Error ± 0.31				
		Analytical Error ± 0.04				
Normal Isochron	**303.34 ± 17.43 (± 5.75%)**	4.09289 ± 0.24628 (± 6.02%)	**13.10 ± 0.79 (± 6.00%)**	0.61	56.34	
		Full External Error ± 0.84		72%	8	
		Analytical Error ± 0.79		2.15	2σ Confidence Limit	
				1.0000	Error Magnification	
Inverse Isochron	**303.40 ± 17.43 (± 5.74%)**	4.09229 ± 0.24483 (± 5.98%)	**13.10 ± 0.78 (± 5.96%)**	0.61	56.34	
		Full External Error ± 0.84		72%	8	
		Analytical Error ± 0.78		2.15	2σ Confidence Limit	
				1.0000	Error Magnification	
				5%	Spreading Factor	

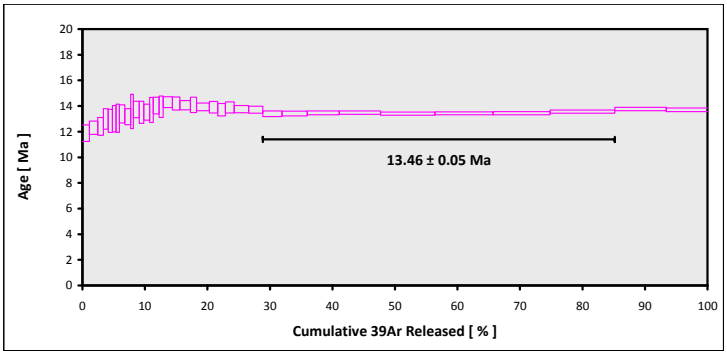

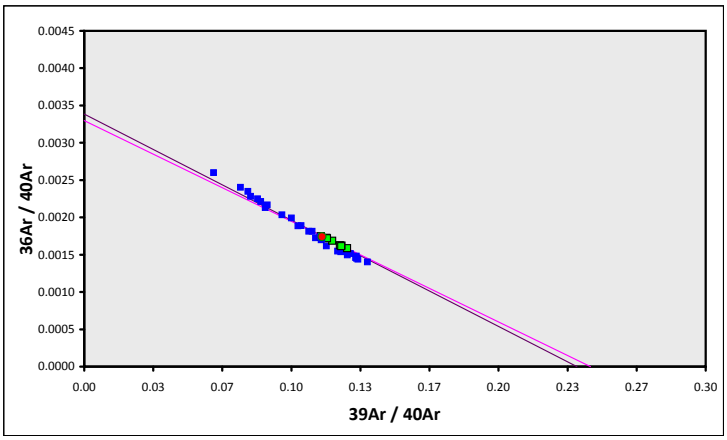

14D23437.one-pager.xls printed at 18-10-2016 (16:22)
ArArCALC v2.7.0 -- Beta Version

Supplemental Ages (Continued). $^{40}Ar/^{39}Ar$ age data for Tuvalu seamounts not included in Konrad et al. (submitted).

OSU Argon Geochronology Lab
CEOAS Oregon State University, Corvallis, USA

RR1310-D27-32 > Plagioclase > KONRAD (13-INT-08)
PACIFIC OCEAN > SAMOA
15-OSU-06 (6A7-15) > Incremental Heating > Kevin Konrad

Information on Analysis and Constants Used in Calculations

Project = **KONRAD (13-INT-08)**
Sample = **RR1310-D27-32**
Material = **Plagioclase**
Location = **Samoa**
Region = **Pacific Ocean**
Analyst = **Kevin Konrad**
Irradiation = **15-OSU-06 (6A7-15)**
Position = **X: 0 | Y: 0 | Z/H: 15.67 mm**
FCT-NM Age = **28.201 ± 0.023 Ma**
FCT-NM Reference = **Kuiper et al (2008)**
FCT-NM 40Ar/39Ar Ratio = **8.75579 ± 0.01226**
FCT-NM J-value = **0.00179509 ± 0.00000251**
Air Shot 40Ar/36Ar = **304.7630 ± 0.4206**
Air Shot MDF = **0.99239165 ± 0.00066564 (LIN)**
Experiment Type = **Incremental Heating**
Extraction Method = **Bulk Laser Heating**
Heating = **77 sec**
Isolation = **1.50 min**
Instrument = **ARGUS-VI-D**
Preferred Age = Undefined
Age Classification = Undefined
IGSN = Undefined
Rock Class = Undefined
Lithology = **Basalt**
Lat-Lon = Undefined - Undefined
Age Equations = **Min et al. (2000)**
Negative Intensities = **Allowed**
Collector Calibrations = **36Ar**
Decay 40K = **5.530 ± 0.048 E-10 1/a**
Decay 39Ar = **2.940 ± 0.016 E-07 1/h**
Decay 37Ar = **8.230 ± 0.012 E-04 1/h**
Decay 36Cl = **2.257 ± 0.015 E-06 1/a**
Decay 40K(EC,β⁺) = **0.580 ± 0.009 E-10 1/a**
Decay 40K(β⁻) = **4.950 ± 0.043 E-10 1/a**
Atmospheric 40/36(a) = **295.50**
Atmospheric 38/36(a) = **0.1869**
Production 39/37(ca) = **0.0006756 ± 0.0000089**
Production 38/37(ca) = **0.0000718 ± 0.0000092**
Production 36/37(ca) = **0.0002663 ± 0.0000004**
Production 40/39(k) = **0.003823 ± 0.000102**
Production 38/39(k) = **0.012031 ± 0.000019**
Production 36/38(cl) = **262.80 ± 1.71**
Scaling Ratio K/Ca = **0.430**
Abundance Ratio 40K/K = **1.1700 ± 0.0100 E-04**
Atomic Weight K = **39.0983 ± 0.0001 g**

Results	40(a)/36(a) ± 2σ	40(r)/39(k) ± 2σ	Age ± 2σ (Ma)	MSWD	39Ar(k) (%,n)	K/Ca ± 2σ
Age Plateau Cannot Calculate						
Total Fusion Age		5.43556 ± 0.02045 ± 0.38%	**17.56 ± 0.08 ± 0.47%** Full External Error ± 0.40 Analytical Error ± 0.07		21	0.0064 ± 0.0000
Normal Isochron Cannot Calculate						
Inverse Isochron Cannot Calculate						

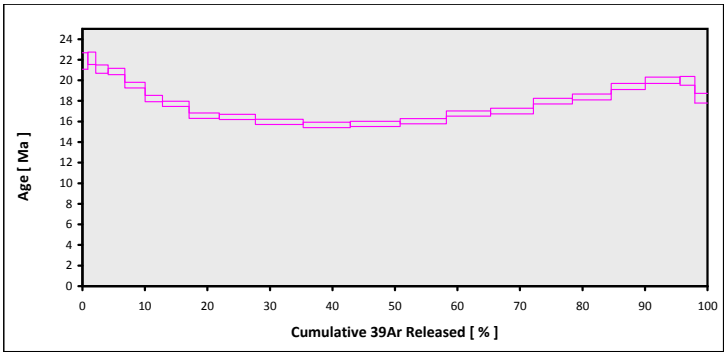

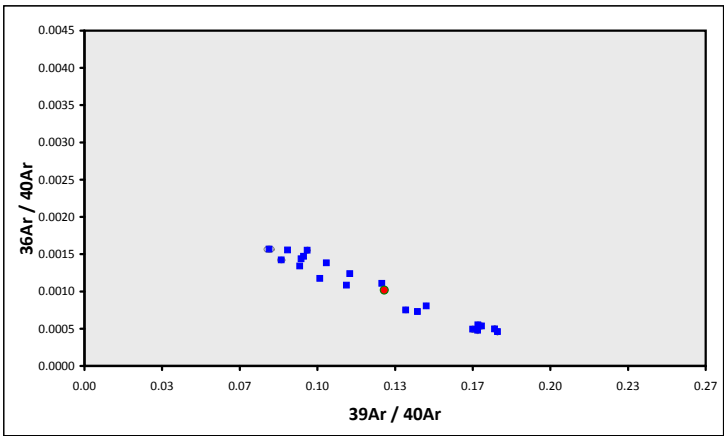

16D10094.one-pager.xls printed at 18-10-2016 (16:41)
ArArCALC v2.7.0 -- Beta Version

Supplemental Ages (Continued). $^{40}Ar/^{39}Ar$ age data for Tuvalu seamounts not included in Konrad et al. (submitted).

OSU Argon Geochronology Lab
CEOAS Oregon State University, Corvallis, USA

RR1310-D27-33 > Groundmass > KONRAD (13-INT-08)
PACIFIC OCEAN > SAMOA
15-OSU-06 (6A19-15) > Incremental Heating > Kevin Konrad

Information on Analysis and Constants Used in Calculations

Project = **KONRAD (13-INT-08)**
Sample = **RR1310-D27-33**
Material = **Groundmass**
Location = **Samoa**
Region = **Pacific Ocean**
Analyst = **Kevin Konrad**
Irradiation = **15-OSU-06 (6A19-15)**
Position = **X: 0 | Y: 0 | Z/H: 40.66 mm**
FCT-NM Age = **28.201 ± 0.023 Ma**
FCT-NM Reference = **Kuiper et al (2008)**
FCT-NM 40Ar/39Ar Ratio = **9.21005 ± 0.01234**
FCT-NM J-value = **0.00170655 ± 0.00000229**
Air Shot 40Ar/36Ar = **304.7610 ± 0.4206**
Air Shot MDF = **0.99239324 ± 0.00066565 (LIN)**
Experiment Type = **Incremental Heating**
Extraction Method = **Bulk Laser Heating**
Heating = **77 sec**
Isolation = **3.00 min**
Instrument = **ARGUS-VI-D**
Preferred Age = Undefined
Age Classification = Undefined
IGSN = Undefined
Rock Class = Undefined
Lithology = **Basalt**
Lat-Lon = Undefined - Undefined
Age Equations = **Min et al. (2000)**
Negative Intensities = **Allowed**
Collector Calibrations = **36Ar**
Decay 40K = **5.530 ± 0.048 E-10 1/a**
Decay 39Ar = **2.940 ± 0.016 E-07 1/h**
Decay 37Ar = **8.230 ± 0.012 E-04 1/h**
Decay 36Cl = **2.257 ± 0.015 E-06 1/a**
Decay 40K(EC,β⁺) = **0.580 ± 0.009 E-10 1/a**
Decay 40K(β⁻) = **4.950 ± 0.043 E-10 1/a**
Atmospheric 40/36(a) = **295.50**
Atmospheric 38/36(a) = **0.1869**
Production 39/37(ca) = **0.0006756 ± 0.0000089**
Production 38/37(ca) = **0.0000718 ± 0.0000092**
Production 36/37(ca) = **0.0002663 ± 0.0000004**
Production 40/39(k) = **0.003823 ± 0.000102**
Production 38/39(k) = **0.012031 ± 0.000019**
Production 36/38(cl) = **262.80 ± 1.71**
Scaling Ratio K/Ca = **0.430**
Abundance Ratio 40K/K = **1.1700 ± 0.0100 E-04**
Atomic Weight K = **39.0983 ± 0.0001 g**

Results	40(a)/36(a) ± 2σ	40(r)/39(k) ± 2σ	Age ± 2σ (Ma)	MSWD	39Ar(k) (%,n)	K/Ca ± 2σ
Age Plateau Cannot Calculate						
Total Fusion Age		4.47380 ± 0.00662 ± 0.15%	**13.75 ± 0.04 ± 0.31%** Full External Error ± 0.31 Analytical Error ± 0.02		31	0.198 ± 0.000
Normal Isochron Cannot Calculate						
Inverse Isochron Cannot Calculate						

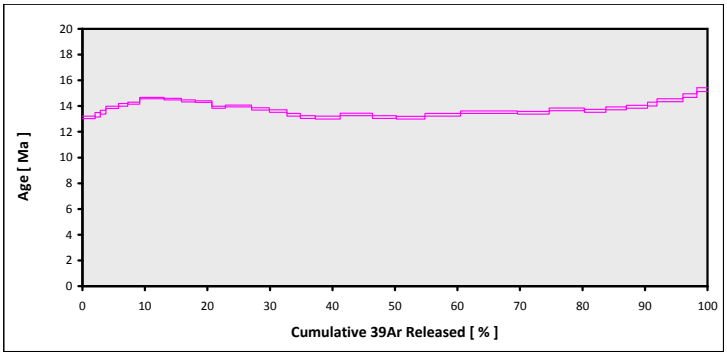

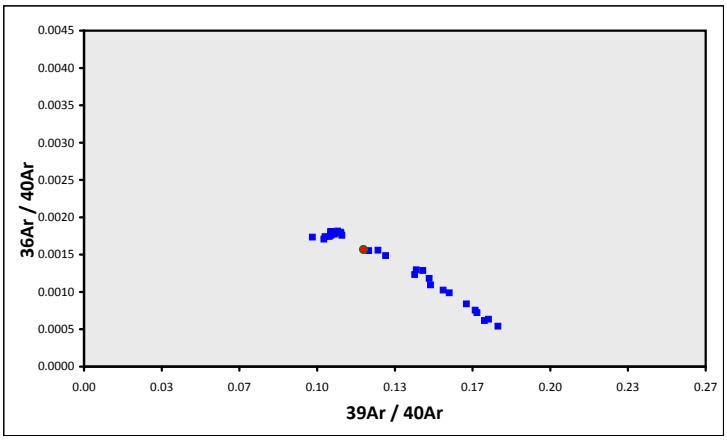

16D10221.one-pager.xls printed at 18-10-2016 (16:41)
ArArCALC v2.7.0 -- Beta Version

Supplemental Ages (Continued). $^{40}Ar/^{39}Ar$ age data for Tuvalu seamounts not included in Konrad et al. (submitted).

OSU Argon Geochronology Lab
CEOAS Oregon State University, Corvallis, USA

RR1310-D27-42 > Groundmass > KONRAD (13-INT-08)
PACIFIC OCEAN > SAMOA
15-OSU-06 (6A16-15) > Incremental Heating > Kevin Konrad

Information on Analysis and Constants Used in Calculations

Project = **KONRAD (13-INT-08)**
Sample = **RR1310-D27-42**
Material = **Groundmass**
Location = **Samoa**
Region = **Pacific Ocean**
Analyst = **Kevin Konrad**
Irradiation = **15-OSU-06 (6A16-15)**
Position = **X: 0 | Y: 0 | Z/H: 34.96 mm**
FCT-NM Age = **28.201 ± 0.023 Ma**
FCT-NM Reference = **Kuiper et al (2008)**
FCT-NM 40Ar/39Ar Ratio = **9.08112 ± 0.01226**
FCT-NM J-value = **0.00173078 ± 0.00000234**
Air Shot 40Ar/36Ar = **304.7550 ± 0.4175**
Air Shot MDF = **0.99239802 ± 0.00066444 (LIN)**
Experiment Type = **Incremental Heating**
Extraction Method = **Bulk Laser Heating**
Heating = **77 sec**
Isolation = **3.00 min**
Instrument = **ARGUS-VI-D**
Preferred Age = **Plateau Age**
Age Classification = **Eruption Age**
IGSN = Undefined
Rock Class = Undefined
Lithology = **Basalt**
Lat-Lon = Undefined - Undefined
Age Equations = **Min et al. (2000)**
Negative Intensities = **Allowed**
Collector Calibrations = **36Ar**
Decay 40K = **5.530 ± 0.048 E-10 1/a**
Decay 39Ar = **2.940 ± 0.016 E-07 1/h**
Decay 37Ar = **8.230 ± 0.012 E-04 1/h**
Decay 36Cl = **2.257 ± 0.015 E-06 1/a**
Decay 40K(EC,β⁺) = **0.580 ± 0.009 E-10 1/a**
Decay 40K(β⁻) = **4.950 ± 0.043 E-10 1/a**
Atmospheric 40/36(a) = **328.40 ± 1.94**
Atmospheric 38/36(a) = **0.1869**
Production 39/37(ca) = **0.0006756 ± 0.0000089**
Production 38/37(ca) = **0.0000718 ± 0.0000092**
Production 36/37(ca) = **0.0002663 ± 0.0000004**
Production 40/39(k) = **0.003823 ± 0.000102**
Production 38/39(k) = **0.012031 ± 0.000019**
Production 36/38(cl) = **262.80 ± 1.71**
Scaling Ratio K/Ca = **0.430**
Abundance Ratio 40K/K = **1.1700 ± 0.0100 E-04**
Atomic Weight K = **39.0983 ± 0.0001 g**

Results	40(a)/36(a) ± 2σ	40(r)/39(k) ± 2σ	Age ± 2σ (Ma)	MSWD	39Ar(k) (%,n)	K/Ca ± 2σ
Age Plateau		4.73590 ± 0.00827 (± 0.17%)	**14.76 ± 0.05 (± 0.32%)**	0.87	54.08	0.177 ± 0.017
		Full External Error ± 0.34		58%	14	
		Analytical Error ± 0.03		1.78	2σ Confidence Limit	
				1.0000	Error Magnification	
Total Fusion Age		4.86395 ± 0.00721 (± 0.15%)	**15.16 ± 0.05 (± 0.31%)**		31	0.152 ± 0.000
		Full External Error ± 0.34				
		Analytical Error ± 0.02				
Normal Isochron	**328.19 ± 3.97 (± 1.21%)**	4.73652 ± 0.02107 (± 0.44%)	**14.76 ± 0.08 (± 0.52%)**	1.61	54.08	
		Full External Error ± 0.34		8%	14	
		Analytical Error ± 0.07		1.82	2σ Confidence Limit	
				1.2685	Error Magnification	
Inverse Isochron	**328.37 ± 3.93 (± 1.20%)**	4.73584 ± 0.02084 (± 0.44%)	**14.76 ± 0.08 (± 0.51%)**	1.58	54.08	
		Full External Error ± 0.34		9%	14	
		Analytical Error ± 0.06		1.82	2σ Confidence Limit	
				1.2583	Error Magnification	
				25%	Spreading Factor	

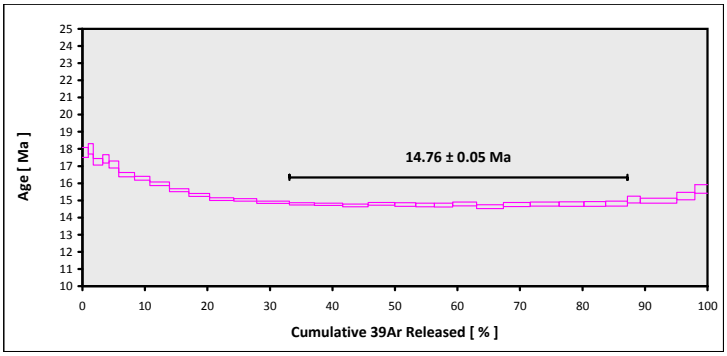

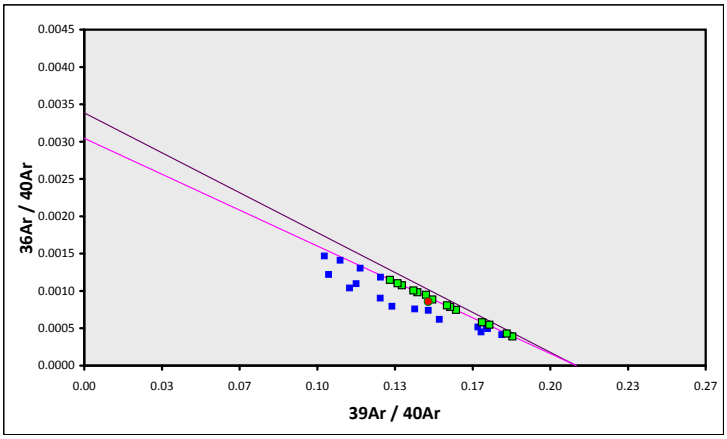

16D10267.one-pager.xls printed at 18-10-2016 (16:41)
ArArCALC v2.7.0 -- Beta Version

Supplemental Ages (Continued). $^{40}Ar/^{39}Ar$ age data for Tuvalu seamounts not included in Konrad et al. (submitted).

OSU Argon Geochronology Lab
CEOAS Oregon State University, Corvallis, USA

RR1310-D32-01 > Groundmass > KONRAD (13-INT-08)
PACIFIC OCEAN > SAMOA
15-OSU-06 (6A8-15) > Incremental Heating > Kevin Konrad

Information on Analysis and Constants Used in Calculations

Project = **KONRAD (13-INT-08)**
Sample = **RR1310-D32-01**
Material = **Groundmass**
Location = **Samoa**
Region = **Pacific Ocean**
Analyst = **Kevin Konrad**
Irradiation = **15-OSU-06 (6A8-15)**
Position = **X: 0 | Y: 0 | Z/H: 18.03 mm**
FCT-NM Age = **28.201 ± 0.023 Ma**
FCT-NM Reference = **Kuiper et al (2008)**
FCT-NM 40Ar/39Ar Ratio = **8.78639 ± 0.01230**
FCT-NM J-value = **0.00178883 ± 0.00000250**
Air Shot 40Ar/36Ar = **326.5000 ± 3.6568**
Air Shot MDF = **0.97623272 ± 0.00259361 (LIN)**
Experiment Type = **Incremental Heating**
Extraction Method = **Bulk Laser Heating**
Heating = **77 sec**
Isolation = **3.00 min**
Instrument = **ARGUS-VI-D**
Preferred Age = **Plateau Age**
Age Classification = **Eruption Age**
IGSN = Undefined
Rock Class = Undefined
Lithology = **Basalt**
Lat-Lon = Undefined - Undefined
Age Equations = **Min et al. (2000)**
Negative Intensities = **Allowed**
Collector Calibrations = **36Ar**
Decay 40K = **5.530 ± 0.048 E-10 1/a**
Decay 39Ar = **2.940 ± 0.016 E-07 1/h**
Decay 37Ar = **8.230 ± 0.012 E-04 1/h**
Decay 36Cl = **2.257 ± 0.015 E-06 1/a**
Decay 40K(EC,β⁺) = **0.580 ± 0.009 E-10 1/a**
Decay 40K(β⁻) = **4.950 ± 0.043 E-10 1/a**
Atmospheric 40/36(a) = **295.50**
Atmospheric 38/36(a) = **0.1869**
Production 39/37(ca) = **0.0006756 ± 0.0000089**
Production 38/37(ca) = **0.0000718 ± 0.0000092**
Production 36/37(ca) = **0.0002663 ± 0.0000004**
Production 40/39(k) = **0.003823 ± 0.000102**
Production 38/39(k) = **0.012031 ± 0.000019**
Production 36/38(cl) = **262.80 ± 1.71**
Scaling Ratio K/Ca = **0.430**
Abundance Ratio 40K/K = **1.1700 ± 0.0100 E-04**
Atomic Weight K = **39.0983 ± 0.0001 g**

Results	40(a)/36(a) ± 2σ	40(r)/39(k) ± 2σ	Age ± 2σ (Ma)	MSWD	39Ar(k) (%,n)	K/Ca ± 2σ
Age Plateau		3.46599 ± 0.01693 (± 0.49%)	**11.18 ± 0.06 (± 0.56%)**	1.69	34.55	0.428 ± 0.077
		Full External Error ± 0.26		17%	4	
		Analytical Error ± 0.05		2.63	2σ Confidence Limit	
				1.2984	Error Magnification	
Total Fusion Age		3.31197 ± 0.02071 (± 0.63%)	**10.68 ± 0.07 (± 0.68%)**		28	0.355 ± 0.002
		Full External Error ± 0.25				
		Analytical Error ± 0.07				
Normal Isochron	**309.48 ± 22.80 (± 7.37%)**	3.43421 ± 0.05369 (± 1.56%)	**11.07 ± 0.18 (± 1.58%)**	1.43	34.55	
		Full External Error ± 0.31		24%	4	
		Analytical Error ± 0.17		3.00	2σ Confidence Limit	
				1.1960	Error Magnification	
Inverse Isochron	**309.53 ± 22.95 (± 7.41%)**	3.43438 ± 0.05399 (± 1.57%)	**11.08 ± 0.18 (± 1.59%)**	1.43	34.55	
		Full External Error ± 0.31		24%	4	
		Analytical Error ± 0.17		3.00	2σ Confidence Limit	
				1.1977	Error Magnification	
				11%	Spreading Factor	

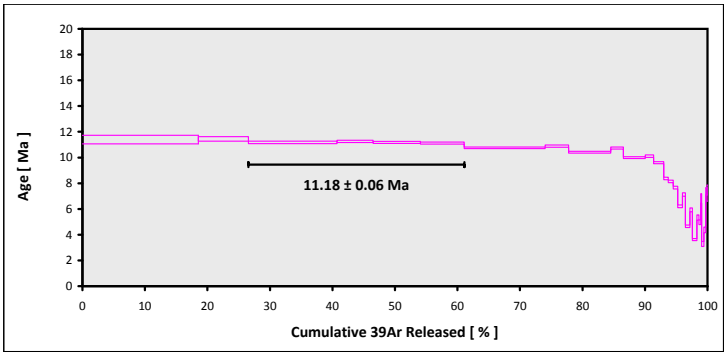

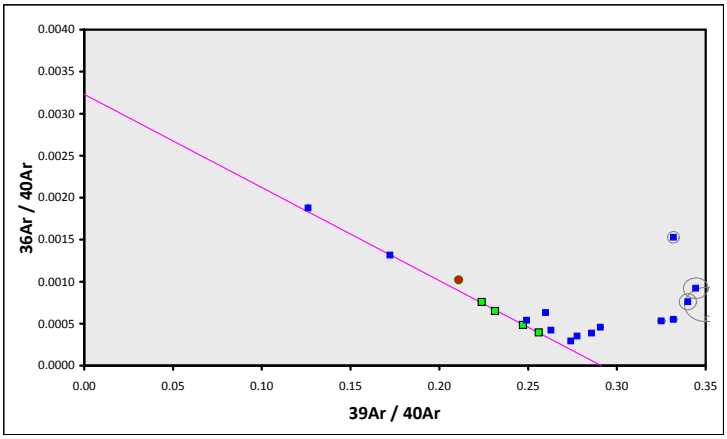

16D16524.one-pager.xls printed at 18-10-2016 (16:43)
ArArCALC v2.7.0 -- Beta Version

Supplemental Ages (Continued). $^{40}Ar/^{39}Ar$ age data for Tuvalu seamounts not included in Konrad et al. (submitted).

OSU Argon Geochronology Lab
CEOAS Oregon State University, Corvallis, USA

RR1310-D32-04 > Plagioclase > RURUTU (13-INT-08)
SAMOA > RURUTU HOTSPOT
14-OSU-02 (2A50-14) > Incremental Heating > Kevin Konrad

Information on Analysis and Constants Used in Calculations

Project = **RURUTU (13-INT-08)**
Sample = **RR1310-D32-04**
Material = **Plagioclase**
Location = **Rurutu Hotspot**
Region = **Samoa**
Analyst = **Kevin Konrad**
Irradiation = **14-OSU-02 (2A50-14)**
Position = **X: 0 | Y: 0 | Z/H: 59.7 mm**
FCT-NM Age = **28.201 ± 0.023 Ma**
FCT-NM Reference = **Kuiper et al. (2008)**
FCT-NM 40Ar/39Ar Ratio = **9.06949 ± 0.00843**
FCT-NM J-value = **0.00173300 ± 0.00000161**
Air Shot 40Ar/36Ar = **304.0580 ± 0.4074**
Air Shot MDF = **0.99295442 ± 0.00066235 (LIN)**
Experiment Type = **Incremental Heating**
Extraction Method = **Bulk Laser Heating**
Heating = **0 sec**
Isolation = **6.00 min**
Instrument = **ARGUS-VI-D**
Preferred Age = **Plateau Age**
Age Classification = **Eruption Age**
IGSN = Undefined
Rock Class = Undefined
Lithology = **Basalt**
Lat-Lon = Undefined - Undefined
Age Equations = **Min et al. (2000)**
Negative Intensities = **Allowed**
Collector Calibrations = **40Ar 36Ar**
Decay 40K = **5.530 ± 0.048 E-10 1/a**
Decay 39Ar = **2.940 ± 0.016 E-07 1/h**
Decay 37Ar = **8.230 ± 0.012 E-04 1/h**
Decay 36Cl = **2.257 ± 0.015 E-06 1/a**
Decay 40K(EC,β⁺) = **0.580 ± 0.009 E-10 1/a**
Decay 40K(β⁻) = **4.950 ± 0.043 E-10 1/a**
Atmospheric 40/36(a) = **295.50**
Atmospheric 38/36(a) = **0.1869**
Production 39/37(ca) = **0.0006756 ± 0.0000089**
Production 38/37(ca) = **0.0000718 ± 0.0000092**
Production 36/37(ca) = **0.0002663 ± 0.0000004**
Production 40/39(k) = **0.003823 ± 0.000102**
Production 38/39(k) = **0.012031 ± 0.000019**
Production 36/38(cl) = **262.80 ± 1.71**
Scaling Ratio K/Ca = **0.430**
Abundance Ratio 40K/K = **1.1700 ± 0.0100 E-04**
Atomic Weight K = **39.0983 ± 0.0001 g**

Results	40(a)/36(a) ± 2σ	40(r)/39(k) ± 2σ	Age ± 2σ (Ma)	MSWD	39Ar(k) (%,n)	K/Ca ± 2σ
Age Plateau		3.52793 ± 0.01107 (± 0.31%)	**11.02 ± 0.04 (± 0.36%)**	0.64	76.91	0.0326 ± 0.0004
		Full External Error ± 0.25		86%	18	
		Analytical Error ± 0.03		1.69	2σ Confidence Limit	
				1.0000	Error Magnification	
Total Fusion Age		3.53527 ± 0.01067 (± 0.30%)	**11.05 ± 0.04 (± 0.35%)**		24	0.0327 ± 0.0002
		Full External Error ± 0.25				
		Analytical Error ± 0.03				
Normal Isochron	**282.62 ± 31.05 (± 10.99%)**	3.53170 ± 0.02244 (± 0.64%)	**11.03 ± 0.07 (± 0.66%)**	0.92	76.91	
		Full External Error ± 0.26		55%	18	
		Analytical Error ± 0.07		1.71	2σ Confidence Limit	
				1.0000	Error Magnification	
Inverse Isochron	**286.28 ± 31.60 (± 11.04%)**	3.53375 ± 0.02229 (± 0.63%)	**11.04 ± 0.07 (± 0.66%)**	0.66	76.91	
		Full External Error ± 0.26		84%	18	
		Analytical Error ± 0.07		1.71	2σ Confidence Limit	
				1.0000	Error Magnification	
				17%	Spreading Factor	

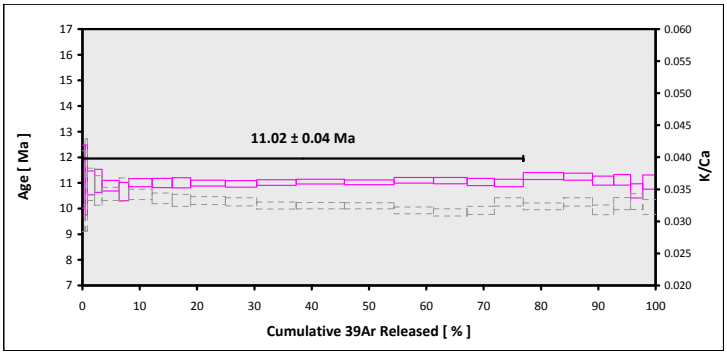

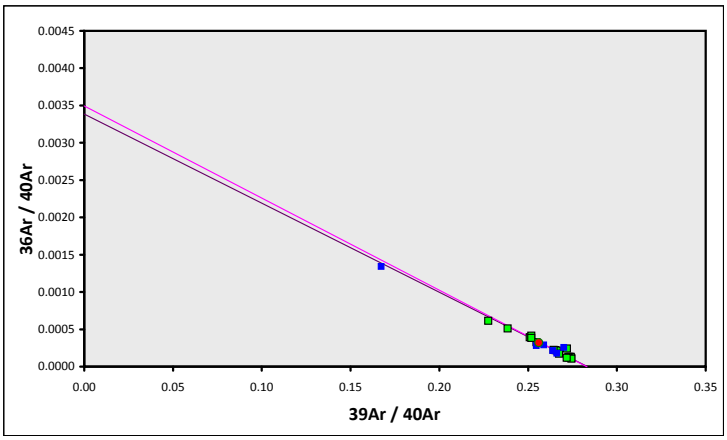

14D25827.one-pager.xls printed at 18-10-2016 (16:23)
ArArCALC v2.7.0 -- Beta Version

Supplemental Ages (Continued). $^{40}Ar/^{39}Ar$ age data for Tuvalu seamounts not included in Konrad et al. (submitted).

OSU Argon Geochronology Lab
CEOAS Oregon State University, Corvallis, USA

RR1310-D33-05 > Plagioclase > KONRAD (13-INT-08)
PACIFIC OCEAN > SAMOA
15-OSU-06 (6A27-15) > Incremental Heating > Kevin Konrad

Information on Analysis and Constants Used in Calculations

Project = **KONRAD (13-INT-08)**
Sample = **RR1310-D33-05**
Material = **Plagioclase**
Location = **Samoa**
Region = **Pacific Ocean**
Analyst = **Kevin Konrad**
Irradiation = **15-OSU-06 (6A27-15)**
Position = **X: 0 | Y: 0 | Z/H: 54.46 mm**
FCT-NM Age = **28.201 ± 0.023 Ma**
FCT-NM Reference = **Kuiper et al (2008)**
FCT-NM 40Ar/39Ar Ratio = **9.58415 ± 0.01227**
FCT-NM J-value = **0.00163994 ± 0.00000210**
Air Shot 40Ar/36Ar = **304.6670 ± 0.7007**
Air Shot MDF = **0.99246813 ± 0.00080183 (LIN)**
Experiment Type = **Incremental Heating**
Extraction Method = **Bulk Laser Heating**
Heating = **0 sec**
Isolation = **1.50 min**
Instrument = **ARGUS-VI-D**
Preferred Age = **Plateau Age**
Age Classification = **Eruption Age**
IGSN = Undefined
Rock Class = Undefined
Lithology = **Basalt**
Lat-Lon = Undefined - Undefined
Age Equations = **Min et al. (2000)**
Negative Intensities = **Allowed**
Collector Calibrations = **36Ar**
Decay 40K = **5.530 ± 0.048 E-10 1/a**
Decay 39Ar = **2.940 ± 0.016 E-07 1/h**
Decay 37Ar = **8.230 ± 0.012 E-04 1/h**
Decay 36Cl = **2.257 ± 0.015 E-06 1/a**
Decay 40K(EC,β⁺) = **0.580 ± 0.009 E-10 1/a**
Decay 40K(β⁻) = **4.950 ± 0.043 E-10 1/a**
Atmospheric 40/36(a) = **295.50**
Atmospheric 38/36(a) = **0.1869**
Production 39/37(ca) = **0.0006756 ± 0.0000089**
Production 38/37(ca) = **0.0000718 ± 0.0000092**
Production 36/37(ca) = **0.0002663 ± 0.0000004**
Production 40/39(k) = **0.003823 ± 0.000102**
Production 38/39(k) = **0.012031 ± 0.000019**
Production 36/38(cl) = **262.80 ± 1.71**
Scaling Ratio K/Ca = **0.430**
Abundance Ratio 40K/K = **1.1700 ± 0.0100 E-04**
Atomic Weight K = **39.0983 ± 0.0001 g**

Results	40(a)/36(a) ± 2σ	40(r)/39(k) ± 2σ	Age ± 2σ (Ma)	MSWD	39Ar(k) (%,n)	K/Ca ± 2σ
Age Plateau		4.14301 ± 0.04337 (± 1.05%)	**12.24 ± 0.13 (± 1.07%)**	0.58	36.40	0.0052 ± 0.0001
			Full External Error ± 0.31	82%	10	
			Analytical Error ± 0.13	1.94	2σ Confidence Limit	
				1.0000	Error Magnification	
Total Fusion Age		4.27807 ± 0.02651 (± 0.62%)	**12.64 ± 0.08 (± 0.67%)**		21	0.0056 ± 0.0000
			Full External Error ± 0.30			
			Analytical Error ± 0.08			
Normal Isochron	**312.40 ± 29.88 (± 9.56%)**	4.11528 ± 0.06721 (± 1.63%)	**12.16 ± 0.20 (± 1.65%)**	0.41	36.40	
No Convergence			Full External Error ± 0.34	91%	10	
			Analytical Error ± 0.20	2.00	2σ Confidence Limit	
				1.0000	Error Magnification	
Inverse Isochron	**318.44 ± 30.32 (± 9.52%)**	4.10396 ± 0.06949 (± 1.69%)	**12.13 ± 0.21 (± 1.71%)**	0.32	36.40	
			Full External Error ± 0.34	96%	10	
			Analytical Error ± 0.20	2.00	2σ Confidence Limit	
				1.0000	Error Magnification	
				25%	Spreading Factor	

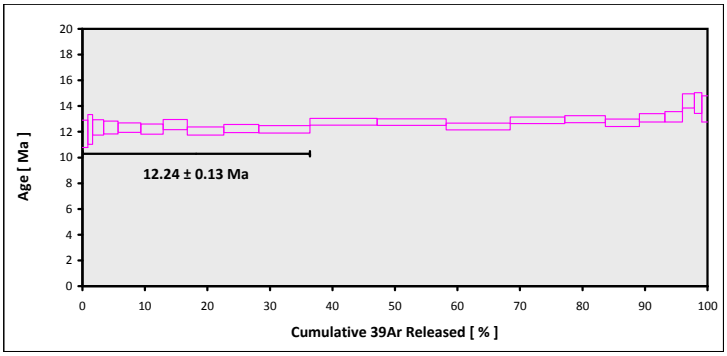

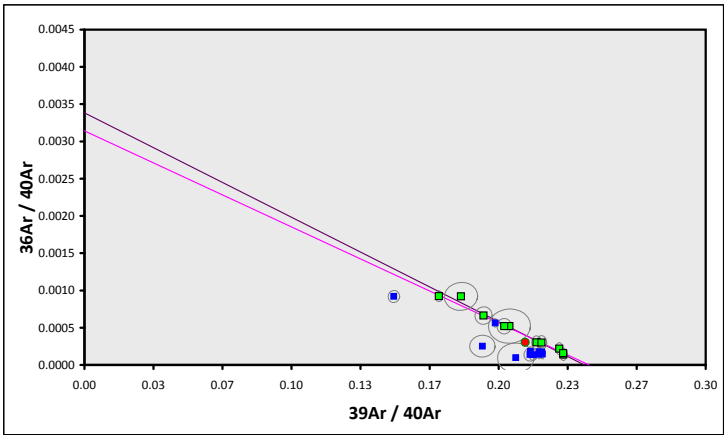

16D13681.one-pager.xls printed at 18-10-2016 (16:43)
ArArCALC v2.7.0 -- Beta Version

Supplemental Ages (Continued). $^{40}Ar/^{39}Ar$ age data for Tuvalu seamounts not included in Konrad et al. (submitted).

A.4.7. References

Allègre, C., Duprè, B., Lewin, E., 1986. Thorium/uranium ratio of the Earth. Chem. Geol. 56, 219–227.

Alt, J.C., 1995. Subseafloor Processes and Mid-Ocean Ridge Hydrothermal Systems, in: Seafloor Hydrothermal Systems: Physical, Chemical, Biological, and Geological Interactions, Geophysical Monograph 91. pp. 85–114.

Bach, W., Peucker-Ehrenbrink, Hart, S.R., Blusztajn, J., 2003. Geochemistry of hydrothermally altered oceanic crust: DSDP/ODP Hole 504B - Implications for seawater-crust exchange budgets and Sr-Pb-isotopic evolution of the mantle. Geochemistry, Geophys. Geosystems 4, 40–55.

Chauvel, C., Hofmann, A.W., Vidal, P., 1992. HIMU-EM: The French Polynesian connection. Earth Planet. Sci. Lett. 110, 99–119.

Connelly, J.N., Ulfbeck, D.G., Thrane, K., Bizzarro, M., Housh, T., 2006. A method for purifying Lu and Hf for analyses by MC-ICP-MS using TODGA resin. Chem. Geol. 233, 126–136. doi:10.1016/j.chemgeo.2006.02.020

Doubrovine, P. V., Steinberger, B., Torsvik, T.H., 2012. Absolute plate motions in a reference frame defined by moving hot spots in the Pacific, Atlantic, and Indian oceans. J. Geophys. Res. Solid Earth 117. doi:10.1029/2011JB009072

Duncan, R.A., Clague, D.A., 1985. Pacific plate motion recorded by linear volcanic chains, in: The Ocean Basins and Margins. Springer US, Boston MA. doi:10.1007/978-1-4613-2351-8_3

Eisele, J., Sharma, M., Galer, S.J.G., Blichert-Toft, J., Devey, C.W., Hofmann, A.W., 2002. The role of sediment recycling in EM-1 inferred from Os, Pb, Hf, Nd, Sr isotope and trace element systematics of the Pitcairn hotspot. Earth Planet. Sci. Lett. 196, 197–212.

Hanan, B.B., Blichert-Toft, J., Kingsley, R., Schilling, J.-G., 2000. Depleted Iceland mantle plume geochemical signature: Artifact of multicomponent mixing? Geochemistry, Geophys. Geosystems 1, n/a-n/a. doi:10.1029/1999GC000009

Hanan, B.B., Graham, D.W., 1996. Lead and Helium Isotope Evidence from Oceanic Basalts for a Common Deep Source of Mantle Plumes. Science (80-.). 272, 991–995.

Hanan, B.B., Schilling, J.-G., 1989. Easter Microplate Evolution: Pb Isotope Evidence. J. Geophys. Res. 94, 7432–7448.

Hanano, D., Scoates, J.S., Weis, D., 2009. Alteration mineralogy and the effect of acid-leaching on the Pb isotope systematics of ocean-island basalts. Am. Mineral. 94, 17–26.

Hanyu, T., Kawabata, H., Tatsumi, Y., Kimura, J.-I., Hyodo, H., Sato, K., Miyazaki, T., Chang, Q., Hirahara, Y., Takahashi, T., Senda, R., Nakai, S., 2014. Isotope evolution in the HIMU reservoir beneath St. Helena: Implications for the mantle recycling of U and Th. Geochim. Cosmochim. Acta. doi:10.1016/j.gca.2014.03.016

Hart, S.R., Blusztajn, J., Dick, H.J.B., Meyer, P.S., Muehlenbachs, K., 1999. The fingerprint of seawater circulation in a 500-meter section of ocean-crust gabbros. Geochim.

Cosmochim. Acta 63, 4059–4080.

Hart, S.R., Hauri, E.H., Oschmann, L.A., Whitehead, J.A., 1992. Mantle plumes and entrainment: Isotopic evidence. Science (80-.). 256, 517–520.

Hauri, E.H., Hart, S.R., 1994. Constraints on melt migration from mantle plumes: A trace element study of peridotite xenoliths from Savai'i, Western Samoa. J. Geophys. Res. 99, 24301–24321. doi:10.1029/94JB01553

Horwitz, E.P., Chiarizia, R., Dietz, M.L., Diamond, H., Nelson, D.M., 1993. Separation and preconcentration of actinides from acidic media by extraction chromatography. Anal. Chim. Acta 281, 361–372.

Jackson, M.G., Hart, S.R., Koppers, A.A.P., Staudigel, H., Konter, J.G., Blusztajn, J., Kurz, M.D., Russell, J.A., 2007. The return of subducted continental crust in Samoan lavas. Nature 448, 684–687. doi:10.1038/nature06048

Konter, J.G., Hanan, B.B., Blichert-Toft, J., Koppers, A.A.P., Plank, T., Staudigel, H., 2008. One hundred million years of mantle geochemical history suggest the retiring of mantle plumes is premature. Earth Planet. Sci. Lett. 275, 285–295. doi:10.1016/j.epsl.2008.08.023

Konter, J.G., Staudigel, H., Blichert-Toft, J., Hanan, B.B., Polvé, M., Davies, G.R., Shimizu, N., Schiffman, P., 2009. Geochemical stages at Jasper Seamount and the origin of intraplate volcanoes. Geochemistry, Geophys. Geosystems 10. doi:10.1029/2008GC002236

Konter, J.G., Storm, L.P., 2014. High precision 87Sr/86Sr measurements by MC-ICP-MS, simultaneously solving for Kr interferences and mass-based fractionation. Chem. Geol. 385, 26–34. doi:10.1016/j.chemgeo.2014.07.009

Koppers, A.A.P., Staudigel, H., Pringle, M.S., Wijbrans, J.R., 2003. Short-lived and discontinuous intraplate volcanism in the South Pacific: Hot spots or extensional volcanism? Geochemistry, Geophys. Geosystems 4. doi:10.1029/2003GC000533

Liew, T.C., Hofmann, A.W., 1990. Th-U-Pb evolution of the MORB mantle and upper continental crust, in: Seventh International Conference on Geochronology, Cosmochronology and Isotope Geology.

Mattinson, J.M., 2010. Analysis of the relative decay constants of 235U and 238U by multi-step CA-TIMS measurements of closed-system natural zircon systems. Chem. Geol. 275, 186–198.

Nebel, O., Arculus, R.J., Westrenen, W. van, Woodhead, J.D., Jenner, F.E., Nebel-Jacobsen, Y.J., Wille, M., Eggins, S.M., 2013. Coupled Hf–Nd–Pb isotope co-variations of HIMU oceanic island basalts from Mangaia , Cook-Austral islands, suggest an Archean source component in the mantle transition zone. Geochim. Cosmochim. Acta 112, 87–101.

Pin, C., Francisco, J., Zalduegui, S., 1997. Sequential separation of light rare-earth elements , thorium and uranium by miniaturized extraction chromatography: Application to isotopic analyses of silicate rocks. Anal. Chim. Acta 339, 79–89.

Rooney, T.O., Hart, W.K., Hall, C.M., Ayalew, D., Ghiorso, M.S., Hidalgo, P., Yirgu, G., 2012. Peralkaline magma evolution and the tephra record in the Ethiopian Rift. Contrib. to

Mineral. Petrol. 164, 407–426. doi:10.1007/s00410-012-0744-6

Rooney, T.O., Morell, K.D., Hidalgo, P., Fraceschi, P., 2015. Magmatic consequences of the transition from orthogonal to oblique subduction in Panama. Geochemistry, Geophys. Geosystems 16, 4178–4208. doi:10.1002/2015GC006150.Received

Salters, V.J.M., Mallick, S., Hart, S.R., Langmuir, C.E., Stracke, A., 2011. Domains of depleted mantle: New evidence from hafnium and neodymium isotopes. Geochemistry, Geophys. Geosystems 12. doi:10.1029/2011GC003617

Silva, I.G.N., Weis, D., Barling, J., Scoates, J.S., 2009. Leaching systematics and matrix elimination for the determination of high-precision Pb isotope compositions of ocean island basalts. Geochemistry, Geophys. Geosystems 10.

Staudigel, H., Plank, T., White, W.M., Schmincke, H.-U., 1996. Geochemical fluxes during seafloor alteration of the basaltic upper oceanic crust: DSDP Sites 417 and 418, in: Subduction Top to Bottom. pp. 19–38.

Vervoort, J.D., Blichert-Toft, J., 1999. Evolution of the depleted mantle: Hf isotope evidence from juvenile rocks through time. Geochim. Cosmochim. Acta 63, 533–556.

Wessel, P., Kroenke, L.W., 2008. Pacific absolute plate motion since 145 Ma: An assessment of the fixed hot spot hypothesis. J. Geophys. Res. 113, B06101. doi:10.1029/2007JB005499

Wessel, P., Smith, W.H.F., Scharroo, R., Luis, J., Wobbe, F., 2013. Generic Mapping Tools: Improved Version Released. Eos (Washington. DC). 94, 409–410.

White, W.M., 2014. Isotope Geochemistry.

White, W.M., Albarède, F., Telouk, P., 2000. High-precision analysis of Pb isotope ratios by multi-collector. Chem. Geol. 167, 257–270.

Woodhead, J.D., 1996. Extreme HIMU in an oceanic setting: the geochemistry of Mangaia Island (Polynesia) , and temporal evolution of the Cook-Austral hotspot. J. Volcanol. Geotherm. Res. 72, 1–19.